# The Effect of CLN3 Disease on Organellar Characteristics

## Thesis

# The effect of CLN3 disease on organellar characteristics

Emily Coode, BSc, MSc

A Thesis submission to The Open University
for the degree of Doctor of Philosophy

Faculty of Science, Technology, Engineering
and Mathematics

School of Life, Health and Chemical Sciences

May 2021

**Declaration**

I declare that the work presented in this thesis is my own original work and does not contain any material submitted for any other qualification at the Open University, or any other University. Contributions made by other researchers are fully acknowledged in relevant parts of the thesis.

**Abstract**

CLN3 disease, or juvenile dementia, is a lysosomal storage disorder with largely neurological symptoms. Towards the end of their lives, individuals with CLN3 disease develop a cardiac phenotype, which has not yet been systematically studied. On a cellular level, mutations in *CLN3* have been shown to disrupt the endo-lysosomal system. However, the function of the CLN3 protein, which is localised on the lysosomal membrane, is still unknown.

Positioning of lysosomes is affected by the physiological state of a cell and can be changed in diseases. This study developed a powerful assay for the automated analysis of lysosomal movement and positioning. This assay was then applied to study different cell lines with mutations in their *CLN3* gene, specifically a CLN3 knockout HeLa cell line and patient-derived fibroblasts with two different CLN3 mutations. Lysosomal movement was found to be reduced in CLN3 patient fibroblasts. Additionally, the calcium signalling, mitochondrial membrane potential and responses to oxidative stress were characterised in the cells. These were found to be not affected by the mutations in CLN3.

Another part of this study aimed to characterise changes in the structure and function of cardiac myocytes in CLN3 disease. This was approached in two ways: Firstly, changes in the structure of ventricular cardiac myocytes were investigated in hearts from mice with a common mutation causing CLN3 disease. Hearts from animals of three different ages were analysed, and changes in the mitochondria were found. Surprisingly, only little of the storage material, characteristic for lysosomal storage disorders, was found. Secondly, iPSC-derived cardiac myocytes were to be used to study changes in the cell's function.

**Acknowledgements**

First and foremost, I would like to thank my supervisors Katja and Martin. There are no words to express my gratitude for your guidance and support throughout the PhD. I have learnt a huge amount from both of you and truly appreciate the encouragement you've given me to develop confidence and resilience both in the laboratory and in other aspects of research, such as communication. In addition to work, I have fond memories of the funny conversations and the walks to the pub.

I'm fortunate to have spent the last few years surrounded by so many friendly, supportive, and inspiring people in LHCS. I would like to thank everyone who has contributed to the great community, stopped for a chat in the office or labs, or asked a question in one of my presentations. There are too many people to list, but I appreciate every single one of you (and especially Emily!). Thanks to admin and finance for keeping things running smoothly. I also could not have asked for better lab support; thank you Brett, George and Julia for patiently assisting with the endless queries, being approachable and all of the friendly conversations over the years. I would also like to thank Igor and Radka for their excellent assistance with the electron microscopy work.

Outside of The Open University, I've been exceptionally fortunate to meet many inspiring researchers through the NCL Foundation and The European Calcium Society. The NCL Foundation's dedication to research and wonderful annual Young Investigators meetings have been inspirational and invaluable in development of the project and in the connection to the wider researcher community led by Herman and Frank. The European Calcium Society is a brilliantly welcoming community and I have been so fortunate to join the junior board in 2020 and 'meet' so many amazing people through that work.

I would also like to acknowledge all of the laboratories I've visited and learnt from: Prof Chris Denning, Prof Tristan McKay, and their excellent teams. As well as those who have shared resources, advice, and support via post and email over the years: Professor Jens Schwamborn, Dr Emyr Lloyd-Evans, Dr Helen Waller-Evans, Dr Guido Hermey, Professor Sara Mole and Prof Jonathan Cooper. I would also like to thank Professor Fraser McDonald and Professor Dirk Bister at King's College London for their support of the project.

And finally, thank you to my family and friends for understanding and trusting my decision to pursue a PhD, for their patience when I've been consumed by work and for enjoying the pretty lysosome images - or at least, being supportive of my enjoyment of them!

**Conference items and publications**

Publications

Rietdorf K, Coode EE, Schulz A, Wibbeler E, Bootman MD, Ostergaard JR (2019) Cardiac pathology in neuronal ceroid lipofuscinoses (NCL): More than a mere co-morbidity' Biophys Acta Mol Basis Dis.

International conference participation

Oral presentations

2020 6th JNCL Young Investigator Symposium (International, online)

2019 5th JNCL Young Investigator Symposium (Utrecht, Netherlands)

2019 Gordon Research Seminar: Lysosomal Diseases (Texas, US)

2018 4th JNCL Young Investigator Symposium (London, UK)

2017 3rd JNCL Young Investigator Symposium (Hamburg, Germany)

Posters

2019 Gordon Research Conference: Lysosomal Diseases (Texas, US)

2018 NCL London 2018 (London, UK)

**Table of Contents**

**List of Figures**

**List of Tables**

**Abbreviations**

| | |
|---|---|
| µm | micrometer |
| µM | micromolar |
| ATP | adenosine triphosphate |
| $Ca^{2+}$ | Calcium ion |
| CaCl | calcium chloride |
| CM | cardiac myocyte |
| $dH_2O$ | double distilled water |
| DMEM | Dulbecco's Modified Eagle Medium |
| DMSO | dimethyl sulphoxide |
| DPBS | Dulbecco's phosphate-buffered saline |
| ECG | electrocardiogram |
| EDTA | Ethylenediaminetetraacetic acid |
| EGTA | ethylene glycol-bis (β-aminoethyl ether)-N,N,N',N'-tetraacetic acid |
| FBS | foetal bovine serum |
| FITC | Fluorescein isothiocyanate |
| GFP | green fluorescent protein |
| HEPES | 4-(2-hydroxyethyl)-1-piperazineethanesulfonic acid |
| iPSC | induced pluripotent stem cell |
| iPSC-CM | induced pluripotent stem cell derived cardiac myocyte |
| KCl | Potassium chloride |
| LAMP-1 | lysosomal-associated membrane protein 1 |
| LIF | Leica Image File |
| $MgCl_2$ | Magnesium chloride |
| $MgSO_4$ | magnesium sulphate |
| ml | millilitre |
| mM | millimolar |
| ms | millisecond |
| mTOR | mechanistic target of rapamycin |
| NaCl | Sodium chloride |
| $NaH_2PO_4H_20$ | sodium dihydrogen phosphate monohydrate |
| $NaHCO_3$ | Sodium bicarbonate |
| NaOH | Sodium hydroxide |
| NCLs | Neuronal Ceroid Lipofuscinoses |
| NRVMs | Neonatal rat ventricular myocytes |

| | |
|---|---|
| PBS | phosphate-buffered saline |
| Pen/Strep | Penicillin-Streptomycin |
| rpm | rotations per minute |
| S.E.M | Standard error of mean |
| TIF | Tagged Image File |

# 1 Introduction

## 1.1 The Neuronal Ceroid Lipofuscinoses

The Neuronal Ceroid Lipofuscinoses (NCLs) are hereditary lysosomal storage diseases, characterised by an accumulation of fluorescent proteins in cells (Palmer et al., 2013). The NCLs broadly share clinical symptoms of a progressive dementia, although specific symptoms, onset and prognosis depend on the subtype. NCL diseases are classified by gene, although the age at which the first symptoms emerge is still taken into consideration. In some NCLs such as CLN1, age of onset may vary from infantile to adult (Schulz and Kohlschutter, 2013).

## 1.2 Juvenile NCL: CLN3 disease

The most common NCL is CLN3 disease, which has a typical age of onset between 4 and 8 years old (Schulz et al., 2013). CLN3 disease is also referred to as Juvenile NCL (JNCL) and in this subtype, age of onset is consistently in juvenile years (Schulz and Kohlschutter, 2013). In some cases, CLN3 disease may be referred to as Batten disease, a name which is also used for other NCLs. Throughout this report, the juvenile NCL will be referred to as CLN3.

## 1.3 Clinical progression and prognosis

One of the earliest indicators of CLN3 disease is eyesight deterioration, which is often the trigger for referral and eventual diagnosis of CLN3 in a patient (Ouseph et al., 2016). Previously, eyesight deterioration has been discussed in context as a precursor to the onset of other CLN3 symptoms (Schulz et al., 2013). However, a recent clinical study has indicated that cognitive decline is already present at age of diagnosis and this may therefore be present alongside eyesight deterioration (Kuper et al., 2018). Another early symptom is a behaviour and mood change, followed by the start of progressively worsening seizures. The final dementia like symptoms include a decline in motor function and speech. Finally, cardiac symptoms emerge, typically in the second decade, towards the end of life (Schulz et al., 2013).

While the majority of CLN3 patients will deteriorate at a similar pace and the onset of symptoms follows an expected pattern, there are cases of protracted CLN3, where age of onset is later, progression is slower and death is later (Sarpong et al., 2009). Statistical analysis of data from around 60 CLN3 patients found that gender differences and the disease emerged on average 1 year later in females, but in the 226 recorded patient deaths, the average was 1 year earlier in females (Cialone et al., 2012). The same study also found that female patients were reported to have a more rapid deterioration in quality of life due to CLN3 symptoms (Cialone et al., 2012). The genetic variation in CLN3 disease is also linked to the disease progression, with less common mutations being responsible for protracted or delayed CLN3 cases (Sarpong et al., 2009, Licchetta et al., 2015, Cortese et al., 2014).

## 1.4 The *CLN3* gene and CLN3 protein

The *CLN3* gene is located on chromosome 16 (16p2.1.) (Mole, 2017). There are a number of mutations responsible for CLN3 disease, however the most common is a 1.02kb deletion of exons 7 and 8 is responsible for ~74% homozygous cases and ~22% heterozygous cases paired with a rarer mutation. The remaining ~4% have a combination of rare mutations (Cotman and Staropoli, 2012). The progression of CLN3 may depend on the mutation responsible and patients with the rarer mutations may follow a protracted course when compared to the 1.02kb deletion (Sarpong et al., 2009, Licchetta et al., 2015, Cortese et al., 2014). CLN3 disease is an autosomal recessive genetic disorder, which means that both inherited genes are mutated, and the presence of a normal gene renders the individual a carrier, with no CLN3 phenotype.

It has been proposed that some CLN3 protein function remains in CLN3 patients with the 1.02kb deletion (Kitzmuller et al., 2008). However, this has been directly refuted by a further study which claims that the results are an artefact of inadequate methods (Chan et al., 2008). Without deviating too far into a discussion of genetics, there is clearly some debate over the mouse models and the methods used to investigate them. More recently, the significance of genetic background in CLN3 mouse models has been investigated to compare the neurological phenotype closest to CLN3 (Kovacs and Pearce, 2015).

The *CLN3* gene encodes the CLN3 protein, also known as battenin, which is primarily found located on the lysosomes, but has also been identified in Golgi, mitochondria, lipid rafts and in neurons, also in the synapse (Kyttala et al., 2006). Lysosomes are intracellular organelles known primarily for their role in engulfing, digesting and clearing waste material from the cell, as part of the processes of endocytosis and autophagic flux (Ballabio, 2016, Walkley, 2009). Interestingly, CLN3 protein expression may not be static; a study in baby hamster kidney cells found that lysosomal location was altered by osmotic stress. An increase in osmotic stress increased CLN3 protein expression in lysosomes, particularly around the nucleus (Getty et al., 2013).

The CLN3 protein has been hypothesised to have 6 transmembrane domains and may function as a transporter, due to the similarities between the SLC29 family of transporters and several of the major facilitator superfamily (Cotman and Staropoli, 2012). The SLC29 family of proteins transport nucleosides and nucleobases and are found in a range of cell types, with two being characterised on plasma membranes and perinuclear membranes (Baldwin et al., 2004). The MFS proteins are a large family of transporters which carry a range of materials including sugars, amino acids, inorganic anions and cations and more (Cotman and Staropoli, 2012). A direct link has been established between MFS proteins and the NCLs, as mutations encoding the lysosomal transporter MFSD8 is responsible for the late-infantile NCL, CLN7 (Kousi et al., 2009).

## 1.5 The cellular effects of CLN3 disease

The key cellular pathology of CLN3 disease is the abnormal accumulation of lipofuscin, which gives its name to the NCLs. In addition to the accumulation in NCL, lipofuscin is described as a normal product of cellular senescence and accumulation is expected with age in healthy cells (Katz and Robison, 2002). There is currently no consensus on the exact origin of lipofuscin, even in healthy cells, but the most accepted theory is a failure in degradation of mitochondria via the autolysosomal pathway (Marani et al., 2009). Lipofuscin is not identical in composition in all cells, depending on type, animal and origin, for example the ageing process of senescence, or a disease such as the NCLs (Katz and Robison, 2002, Marani et al., 2009). Other cellular effects include a disruption in $Ca^{2+}$ handling and upregulation of autophagy (Chandrachud et al., 2015).

## 1.6 Models of CLN3 disease

There are many CLN3 models available from patient derived or CRISPR-engineered stem cells, to simple model organisms such as zebrafish, yeast and *Drosophila* for genetic analysis, as well as more complex animal models such as mouse and pig.

In addition to the wide range of cells and animals available, there are multiple CLN3 mutations. Due to the prevalence of the 1.02kb deletion in CLN3 patients, this mutation is desirable for studying in a model of CLN3 as it captures the disease as it is expressed in the majority of cases and therefore holds the greatest impact. Nonetheless, the rarer mutations are important, especially as the disease course is known to be altered, which could improve understanding of CLN3 as a whole, including the function of the gene/ protein. Furthermore, as a rare disease which is still anecdotally difficult to obtain a diagnosis for, the rarer mutations may be more common in populations that currently have poor awareness and diagnosis of CLN3. Regardless, when considering an area of CLN3 which is poorly researched such as the heart, the starting point will be the common 1.02kb deletion in order to contribute the greatest value and achieve comparison to the studies in other cell types.

The use of patient cells in CLN3 research enables a range of assays requiring only cell culture for cultivation. Patient cells have a significant advantage over animal models, as they represent the human disease without the complication of variation between species. Patient derived cells do not require interference to knock-in the mutation as the genotype is already present and identical to the patient. Additionally, iPSC technology allows the possibility of access to a wide range of cell types from a living patient without invasive biopsy. On the other hand, a limitation of patient cells is the difficulty of acquiring a control cell line from and age- and gender-matched healthy donor. The relatively new gene editing technology CRISPR Cas9 does provide the possibility of obtaining an isogenic control for the CLN3 cells by repairing the mutation. The creation of CLN3 cells from a healthy donor, ideally a healthy sibling of the patient, or rescue of patient cells could in either case

would generate a good control, removing concerns over variation between cell lines and genetic background.

For all cell culture models of disease there are two major flaws; the lack of longitudinal changes related to the development of CLN3 in a living being, and the full complexity of an organ, including multiple cell types. For example, the heart would be comprised of cardiac myocytes, as well as fibroblasts. Animal models address both the lack of longitudinal changes and provide whole organs to study. This is especially relevant for the heart, as an animal model will include the full conduction system. Therefore, a mouse model captures not only the cellular pathology in the cardiac myocytes, but provides an option to measure the system as a whole, which could be relevant in CLN3 patients as the symptoms can include arrhythmias and could be a result of aberrant pacing through the sinus and atrioventricular nodes (Reske-Nielsen E, 1981, Ostergaard JR, 2011). Animal models are therefore a valuable tool for research; but for research purposes they may be best used alongside human cells in order to make full use of the advantages of both models and to address their weaknesses.

## 1.7 Induced pluripotent stem cells (iPSCs)

First successfully published in 2006, the ability to differentiate human fibroblasts into a different cell type by inducing pluripotency is a powerful research tool (Takahashi and Yamanaka, 2006). iPSCs allow researchers to culture human patient cells carrying the desired mutations, which can then be differentiated to the cell types found within an organ of interest, such as the heart.

iPSC derived cardiac myocytes (iPSC-CMs) were studied and had action potential and ion channel characteristics comparable to adult cardiac myocytes; but a greater number of action potentials, spontaneous beating and other subtle differences in electrophysiological properties (Ma et al., 2011). A similar study confirmed that although successfully able to observe disease phenotypes in the iPSC-CMs, once again spontaneous beating and alterations to electrophysiological properties indicated immaturity (Hoekstra et al., 2012). Arrangement of t-tubules is important in ventricular myocytes and is important for the global $Ca^{2+}$ transient (Bootman et al., 2011) although these are a key feature which are under-developed in iPSC-CMs (Cadet and Kamp, 2017). A review of iPSC derived cardiac myocytes in research, although acknowledging the immaturity of the iPSC-CMs, summarises and describes the successful analysis of several congenital diseases including dysfunctions of ion channel intracellular communication and intrinsic cardiomyocyte dysfunction such as Cardiomyopathy (Yang et al., 2015). However, a study of ageing iPSC-CMs was able to identify markers such as lipofuscin from day 18 in culture, more pronounced at day 24, suggesting a window in which iPSC-CMs are able to mature to a certain extent in culture (Kim et al., 2013).

Based on literature, iPSCs cannot be expected to behave exactly as adult cardiac myocytes, but for the vast majority of diseases are a suitable model to capture changes alongside an appropriate

model (Ma et al., 2011, Hoekstra et al., 2012, Yang et al., 2015). The challenge will be identifying the CLN3 markers in iPSC-CMs. iPSC technology has been used in the generation of cell types for several lysosomal storage disorders. While the strengths of iPSC derived cells are acknowledged, concerns are raised such as the possible influence of disease metabolism on the differentiation process, the lack of matching control and the possible limitations arising from the relative immaturity of the cells (Borger et al., 2017). For CLN3, an iPSC-derived neuronal cell line containing homozygous 1.02kb deletion has been established and presents the expected CLN3 cellular pathology (Lojewski et al., 2014).

## 1.8 Mouse models

There are two primary models of the common 1.02kb deletion in mice, a knock-out and knock-in. The global knock-out mouse was generated by partial deletion of exon 1 and complete deletion of exons 2-6, denoted as *Cln3*$^{-/-}$ and the resulting mouse has a CLN3 phenotype (Mitchison et al., 1999). The global knock-in mouse model inserts a ~1kb deletion at exons 7-8 in order to mimic the deletion in the human disease, denoted *Cln3*$^{\Delta ex7/8}$ and again the CLN3 phenotype was observed in the mice (Cotman et al., 2002). At present, both models are generally accepted, however the knock-in *Cln3*$^{\Delta ex7/8}$ mouse model is considered to be the closest genetically (Staropoli et al., 2012). Subsequent publications have reiterated the CLN3 phenotype such as vision loss and markers including vacuolated peripheral blood lymphocytes in blood identifiable in this mouse model, which has been inbred and provides a good match to human patients (Staropoli et al., 2012, Brenneman et al., 2017).

Contrary to expectation, behavioural analysis of male and female mice of multiple genetic backgrounds, from models *Cln3*$^{\Delta ex7/8}$ and *Cln3*$^{-/-}$, found that *Cln3*$^{-/-}$ was most suitable in capturing the CLN3 cognitive phenotype, specifying the male and genetic background 129S6/SvEv (Kovacs and Pearce, 2015). However, it is important to consider that this study was exclusively based on behavioural analysis which is severely limiting in relevance to research into the functional effect on organs and subtle cellular changes which may not express as a behavioural phenotype. Furthermore, the recommendation to use the male mouse based on earlier onset of symptoms may not be taking into consideration the known differences between male and female mice, which is reflected in the human course of CLN3 disease (Staropoli et al., 2012, Cialone et al., 2012). Taking this into consideration, it would seem inappropriate to dismiss the female mouse model. Moreover, it is widely discussed and acknowledged in the research community that heart dysfunction outside of CLN3 disease is affected by sex, for example physiological differences between the sexes cause twice as many incidences of heart failure with preserved ejection fraction in women compared to men (Eisenberg et al., 2018). Considering that sex is implicated in the progression of CLN3 disease, and that decline in heart function in non-CLN3 patients is linked to sex, studies of the heart in CLN3 should not be exclusively limited to a single sex.

## 1.9 The heart in CLN3 disease

Cardiac symptoms of CLN3 have been described in clinical research multiple times in studies of individuals or groups of patients (Reske-Nielsen E, 1981, Michielsen et al., 1984, Tomiyasu et al., 2000, Ostergaard JR, 2011, Dilaveris P, 2014). Figure 1 and Figure 2 illustrate the range of cardiac abnormalities which are identified in the studies discussed below.

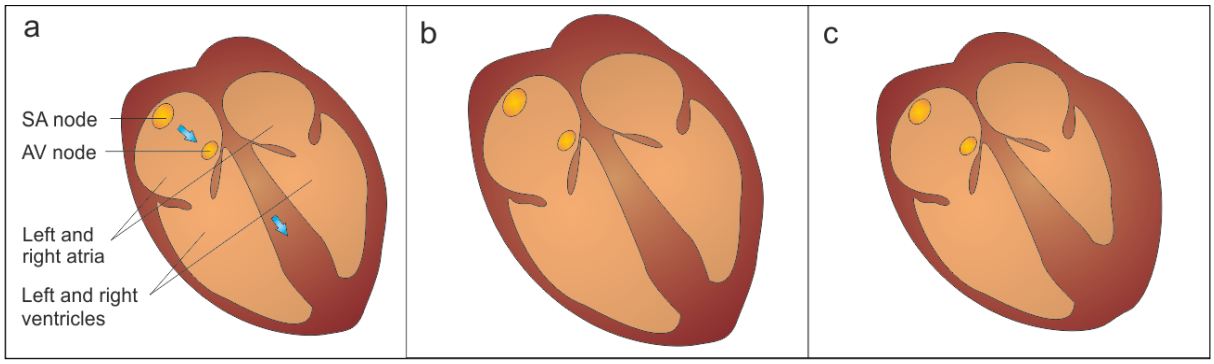


**Figure 1. The mammalian heart and changes in CLN3.** (a) Simple illustration of the heart and its chambers. Action potentials originate from the sinoatrial node (SA), pass through the atrioventricular node (AV) and then travel through the heart as illustrated by the blue arrows. CLN3 can cause; (b) cardiac hypertrophy, an enlarged heart, and (c) left ventricular hypertrophy, an increase in mass on the left ventricle.

One of the earliest papers (referring to CLN3 as 'Juvenile Amaurotic Idiocy') examined a combination of ECG history where available and post-mortem results on 13 CLN3 patients and describes a range of cardiac disorders. These included; cardiac enlargement, abnormal p-waves, increased atrial and diastolic pressure, bradycardia and a right bundle branch block Figure 1 (Reske-Nielsen E, 1981). This paper was published in 1981, based on the 13 patients who died over 7 years. The authors state that death is typically around age 20, although current papers suggest that CLN3 patients can live for a decade beyond this, which may reflect the more advanced knowledge and healthcare available to CLN3 patients (Schulz et al., 2013). Therefore, as patients live longer after the onset of cardiac symptoms, it is of greater importance that these symptoms are addressed and quality of life can be improved.

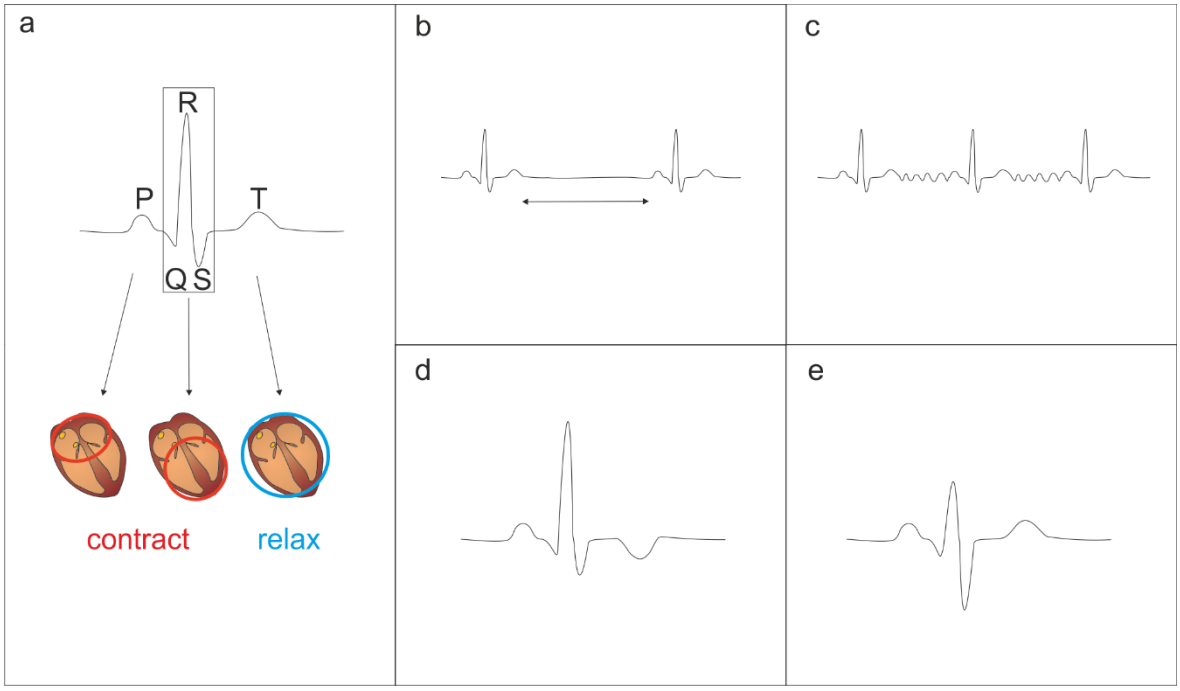


**Figure 2. Electrocardiograms illustrating changes in CLN3.** (a) A normal electrocardiogram showing the P wave as atrial contraction (systole), QRS wave as ventricular contraction (systole) and T wave as relaxation (diastole). An illustration of some changes in CLN3; (b) bradycardia, (c) atrial flutter, (d) inverted T wave and (e) right bundle branch block.

A study of 29 CLN3 patients found cardiac abnormalities from age 14, increasing with age. For example, an inverted T wave was identified in no patients aged <14 years, 15% patients aged 14-19 and 86% aged >19 years (Ostergaard JR, 2011). Other findings included hypertrophy of the left ventricle, bradycardia, atrioventricular block, atrial flutter and sinus arrest. During the study, the cause of death in 2 of 10 patients was heart failure at the age of 26-27 and the authors recommend monitoring CLN3 patients, with increased regularity from the age of 18 (Ostergaard JR, 2011).

A nationwide study of people aged between 14 and 35 years, provides some insight into cardiac abnormalities within the normal population (Chandra et al., 2014). This study found inverted T waves in only 2.8% of their non-athlete group, far lower than the incidences described in CLN3 patients. Interestingly, the study did show that some abnormalities were not uncommon, such as sinus bradycardia in 26.1% and isolated left ventricular hypertrophy in 24.7% of the young non-athlete participants (Chandra et al., 2014).

A case study describes a hemodynamically unstable 32 year old CLN3 patient, with a low blood pressure and heart rate of only 36 beats per minute. An echocardiogram showed severe abnormalities, in addition to hypertrophy of the left ventricle. The authors report that a pacemaker not only improved alertness, but also improved dysphagia, a difficulty in swallowing (Dilaveris P, 2014). While this is only one patient, there is a strong indication that treatment of underlying

cardiac abnormalities can improve quality of life and have an impact beyond the direct cardiac symptoms.

In addition to the clinical reports, cardiac abnormalities are described in animal models. For example, an enlarged heart and abnormal shape in comparison to the control was also observed in the zebrafish model of CLN3, although functional effects were not further investigated by the authors (Wager et al., 2016). In the CLN3$^{\Delta ex7/8}$ mouse model, the average weight of the heart was found to be greater than the control at 20 weeks, however there was no significant effect on heart function (Staropoli et al., 2012). While there was no obvious phenotype in the mouse model, the lipopigment accumulation observed in the mouse cardiac cells is comparable to the accumulation observed in human disease (Reske-Nielsen E, 1981, Staropoli et al., 2012).

Although cardiac dysfunction is not at the forefront of CLN3 research and even the symptoms are not widely reported, there is plenty of evidence showing that CLN3 affects the heart, which may be of greater significance as patients live longer with improved care and the possible therapeutic intervention. Therefore, research must consider the effect of CLN3 on the heart to improve quality of life and reduce the risk of death from heart failure.

## 1.10 CLN3 research in the cell

In the single cell, $Ca^{2+}$ interacts with a variety of proteins to inhibit or initiate a range of events (Bootman, 2012). These can include differentiation, transcription of genes and in muscle cells, contraction (Bootman, 2012). Cardiac myocytes are the muscle cells responsible for the contraction of the heart. Contraction of the heart pumps blood through the chambers and into the body and lungs. To be effective, timing has to be strictly paced by an electrical impulse originating from the sinoatrial node. Excitation-contraction coupling is the process through which the electrical impulse triggers the contraction; mediated by $Ca^{2+}$ release (Bers, 2008). The arrival of the action potential causes depolarisation of the cardiac myocytes, an opening of the L-type voltage-gated $Ca^{2+}$ channels and subsequent release of $Ca^{2+}$, which in turn activates the ryanodine receptors and causes a larger $Ca^{2+}$ release from the sarcoplasmic reticulum (Fearnley et al., 2011). The contraction itself is a result of $Ca^{2+}$ binding to troponin, shortening the muscle fibres in order to cause a contraction of the entire chamber when all cardiac myocytes in a chamber contract simultaneously (Eisner et al., 2017).

If excitation-contraction coupling is altered, the resulting cardiac changes can be responsible for a range of cardiac diseases (Bootman, 2012). Consequently, $Ca^{2+}$ has a significant role in the heart. To summarise; during systole, the heart contracts and the cytosolic $Ca^{2+}$ concentration is increased. During diastole, the drop in the cytosolic $Ca^{2+}$ concentration causes troponin to release from the myofilaments and the heart muscle relaxes (Eisner et al., 2017).

Fluorescent indicators can be used to measure $Ca^{2+}$ in living cells, enabling characterisation of $Ca^{2+}$ signalling such as $Ca^{2+}$ release during an action potential or spontaneous activity observed in excitable cells like cardiac myocytes (Bootman et al., 2013).

Changes in the calcium signalling have been described for several diseases. These can, for example be changes in the ER $Ca^{2+}$ content and ER $Ca^{2+}$ release characteristics, as commonly found in heart dysfunctions (Roderick et al., 2007), changes in the $Ca^{2+}$ entry following the emptying of the endoplasmic reticulum (ER) in cellular immune functions (Shaw and Feske, 2012) and persistent increase in the cytosolic $Ca^{2+}$ concentration found in Alzheimer's disease and affecting the memory formation (Berridge, 2014).. These alterations to calcium signalling, alongside changes in the lysosomal $Ca^{2+}$ concentration, have been described for several neurodegenerative disorders. For example, patient cells from the lysosomal storage disorder Niemann-Pick disease type C (Feng and Yang, 2016, Lloyd-Evans, 2016). While cells from patients with mucolipoidosis IV, based on a mutation in the TRP-ML1 channel, showed an increased lysosomal $Ca^{2+}$ concentration (Ruas et al., 2010). Cerebellar cells from the *Cln3*$^{\Delta ex7/8}$ mouse model showed an elevated lysosomal $Ca^{2+}$ concentration and an increased $Ca^{2+}$ leak from cells (Chandrachud et al., 2015).

CLN3 is classed as a lysosomal storage disorder, which is a group of diseases in which lysosomes are unable to process waste material normally, resulting in an accumulation of lysosomes containing only partially digested waste products.

Lysosomes are also established intracellular $Ca^{2+}$ stores. Despite their large number, their small size means that the total lysosomal calcium concentration is similar in magnitude to that stored in the ER ~500µM (Lloyd-Evans, 2016). However, a small $Ca^{2+}$ release from lysosomes is capable of triggering $Ca^{2+}$ release from the much larger ER and therefore can have a significant impact on $Ca^{2+}$ signalling (Calcraft et al., 2009). Lysosomes also play a role in cell signalling via mechanisms such as mTORC1 (Ballabio, 2016). Lysosomal storage disorders are known to primarily affect vulnerable cell types such as neurons and this is reported as being due to the signalling events and the lack of new cells due to terminal differentiation (Walkley, 2009).

In the cell, lysosomes are numerous and not static. Position of lysosomes is understood to be linked to BORC, a complex of 8 subunits involved in the kinesin dependent movement (Pu et al., 2015). Lysosomes are known to travel along microtubules and in some conditions, including lysosomal storage disorders, are known to collect at the nucleus (Pu et al., 2016). Interestingly, an increased expression of the CLN3 protein has been linked to lysosomes at the perinuclear location in the condition of osmotic stress (Getty et al., 2013). Unfortunately, due to the lack of specificity of CLN3 antibodies, this is difficult to measure (Nelson et al., 2017). However, it is still a finding that would be interesting to correlate with other stress conditions, age, $Ca^{2+}$ activity and finally the size, movement and other characteristics of lysosomes themselves.

In the heart, autophagic flux has been found to be down regulated with age, associated with an increase in waste material such as lipofuscin and damaged mitochondria which in turn is linked to the increased weakness and risk of disease in an ageing heart (Shirakabe et al., 2016). Autophagy is also closely regulated by changes in the $Ca^{2+}$ concentration, which is considered an important signalling process (Bootman et al., 2018). Autophagosome accumulation has been observed in CLN3 cerebellar cells and the link between $Ca^{2+}$ and autophagy is further strengthened by the reversal of this accumulation by $Ca^{2+}$ chelation (Chandrachud et al., 2015). Another study in cerebellar cells from the *Cln3*$^{\Delta ex7/8}$ mouse model found that an upregulation in autophagy (Cao et al., 2006). However, to our knowledge, nobody has so far undertaken a detailed characterisation of the autophagic flux in CLN3 cells.

Mitochondria are organelles found in the cytoplasm, contained within a double membrane and containing separate DNA which contributes to encoding mitochondrial proteins. These organelles utilise fatty acids and carbohydrates to produce ATP as an energy source for a range of cellular activities (Cooper, 2000). Mitochondria are a $Ca^{2+}$ store and this function is closely linked to autophagy; namely that a reduced $Ca^{2+}$ uptake is known to trigger autophagy (Bootman et al., 2018).

Accumulation of mitochondrial subunit c is a well characterised marker of CLN3 disease affected cells, as a component of lipofuscin (Kominami et al., 1992). However, in addition to the accumulation of defective subunits, a change in mitochondrial function as a whole is implicated in CLN3 disease. A decrease of mitochondrial function has been found in *CLN3*$^{-/-}$ mice (Luiro et al., 2006). In the CLN3$^{\Delta ex7/8}$ model, mitochondria were found to be elongated while a decreased level of intracellular ATP and increased death as a result of oxidative stress indicates further mitochondrial abnormalities (Fossale et al., 2004).

# 2 Chapter 2: Materials and Methods

## 2.1 Materials

The materials used in this thesis are detailed in Table 1, including supplier number and application. For materials relating to the culture and differentiation of induced pluripotent stem cells, these can be found in Chapter 8.

**Table 1. Materials**: supplier, catalogue number (Cat. #) and application.

| Description | Supplier | Cat. # | Application |
|---|---|---|---|
| Dulbecco's Modified Eagle Medium (DMEM) high glucose, GlutaMAX™ | Fisher/Gibco | 61965-026 | Cell culture |
| Penicillin-Streptomycin (10,000 U/mL) | Fisher/Gibco | 15140-122 | Cell culture |
| Fetal Bovine Serum | Sigma | F7524 | Cell culture |
| Dulbecco's Phosphate Buffered Saline (DPBS) -$CaCl_2$ -$MgCl_2$ | Fisher/Gibco | 21600-010 | Cell culture |
| 0.25% Trypsin EDTA (1X) | Fisher/Gibco | 25200-056 | Cell culture |
| HBSS (1X) +$CaCl_2$ +$MgCl_2$ | Fisher/Gibco | 14025-050 | Loading/imaging |
| FluoroBrite DMEM | Fisher/Gibco | A18967-01 | Loading/imaging |
| GlutaMAX -I (100X) | Fisher/Gibco | 35050-038 | Loading/imaging |
| Dimethyl sulfoxide | Sigma | 276855-100ML | Solvent |
| Pluronic™ F-127, low UV absorbance | Fisher/Invitrogen | P6867 | Solvent |
| Cal-520 AM | AAT Bioquest | 21130 | Indicator |
| Rhod-2, AM, cell permeant | Fisher/Invitrogen | R1244 | Indicator |
| LysoTracker™ Red DND-99 | Fisher/Invitrogen | L7528 | Probe |
| LysoTracker™ Green DND-26 | Fisher/Invitrogen | L7526 | Probe |
| CellLight™ Lysosomes-GFP, BacMam 2.0 | Fisher/Invitrogen | C10596 | Probe |
| CellLight™ Lysosomes-RFP, BacMam 2.0 | Fisher/Invitrogen | C10504 | Probe |

| | | | |
|---|---|---|---|
| Tubulin Tracker™ Green (Oregon Green™ 488 Taxol, bis-acetate) | Fisher/Invitrogen | T34078 | Probe |
| MitoTracker™ Green FM | Fisher/Invitrogen | M7514 | Probe |
| Hoechst | Fisher/ Pierce | 62249 | Probe |
| TMRE | Sigma | 87917 | Indicator |
| ROS Brite™ 570 | Stratech | 16000-AAT | Indicator |
| Adenosine 5'-triphosphate disodium salt hydrate | Sigma | A2383-10G | Treatment |
| Nocodazole ≥99% (TLC) | Sigma | M1404-10MG | Treatment |
| Carbonyl cyanide 4-(trifluoromethoxy)phenylhydrazone (FCCP) | abcam | ab120081 | Treatment |
| tert-butyl hydroperoxide (TBHP) | abcam | ab113851 | Treatment |
| Hydrogen peroxide solution 30 % (w/w) in $H_2O$ | Sigma | H1009-100ML | Treatment |
| BAPTA-AM | Cambridge Bioscience (Biotium) | BT50000 | Treatment |
| di-bromo BAPTA-AM | Cambridge Bioscience (Biotium) | BT50004 | Treatment |
| EGTA-AM | Fisher/Invitrogen | E1219 | Treatment |
| Paraformaldehyde (PFA) | Sigma | 158127 | Immunostaining |
| Methanol | Fisher | 11367996 | Immunostaining |
| Triton X-100 | Sigma | T9284-100ML | Immunostaining |
| Tween 20 | Sigma | P5927-500ML | Immunostaining |
| Glycine (powder) | Fisher | 10061073 | Immunostaining |
| Bovine Serum Albumin Powder, Fraction V | Fisher | 11403164 | Immunostaining |
| VECTASHIELD® HardSet™ Antifade Mounting Medium with DAPI | Vector Laboratories | H-1500-10 | Immunostaining |
| VECTASHIELD® HardSet™ Antifade Mounting Medium with Phalloidin | Vector Laboratories | H-1600-10 | Immunostaining |

| | | | |
|---|---|---|---|
| Anti-LAMP-2 (human) monoclonal primary antibody | Developmental Studies Hybridoma Bank | H4B4 | Immunostaining |
| Alexa Fluor® 568 goat-anti-mouse IgG (H+L) | Fisher/Invitrogen | A11031 | Immunostaining |

The medium and buffers that were used in cell culture and experiments are described in Table 2.

**Table 2. Buffer and medium**: components and application.

| **Buffer/medium** | **Supplementation/formulation** | **Application** |
|---|---|---|
| Dulbecco's Modified Eagle Medium (DMEM) high glucose, GlutaMAX™ | 10% FBS and 1% Pen/Strep (100 U/mL) | Cell culture |
| DPBS -$CaCl_2$ -$MgCl_2$ | NaOH (1M stock added dropwise to pH 7.3) | Cell culture, immunostaining |
| FluoroBrite DMEM | GlutaMAX (2 mM), HEPES and NaOH (1M stock added dropwise to pH 7.3) | Loading and imaging |
| Imaging Buffer | Distilled water, with NaCl (12.1 mM), KCl (0.54 mM), $MgCl_2$ (0.08 mM), CaCl (1.8 mM), NaHC03 (0.6 mM), EGTA (1 mM), D-glucose (5.5 mM), HEPES (2.5 mM) and NaOH (1M stock added dropwise to pH 7.3) | Loading and imaging |
| HBSS +$CaCl_2$ +$MgCl_2$ | NaOH (1M stock added dropwise to pH 7.3) | Loading and imaging |

## 2.2 Methods

The experiments were conducted in live or fixed cells and these were cultured according to the methods detailed below.

The details of each individual experiment including the loading of indicators or probes, and the treatments of cells, was detailed in the methods section of each chapter.

### 2.2.1 Cell culture

All cell culture was carried out in sterile conditions, using a laminar airflow hood and cells were screened for mycoplasma at 3 monthly intervals to ensure that there was no undetected contamination. The cells were incubated in a 37°C/ 5% $CO_2$ humidified cell culture incubator.

Neonatal Rat Ventricular Myocytes (NRVMs) were briefly used for analysis in Chapter 4 and these were isolated according to (Masoud, 2018). Briefly, neonatal rats aged between 2 – 4 days were sacrificed, their hearts immediately removed and placed in ice-cold buffer. The hearts were cut into ~1 $mm^3$ with a scalpel and then digested in an enzyme solution (pancreatin, DNAse I and collagenase). The enzyme solution was exchanged several times and the solution was passed through 100 µm cell strainers. After centrifugation and removal of the supernatant, the cells were placed in a T175 flask for 1 hour to allow the fibroblasts to adhere and therefore be removed from the solution. The final centrifugation and resuspension of the pellet in plating medium resulted in a primary NRVM culture which was plated on laminin-coated coverslips and maintained until they were used in imaging experiments.

The culture of induced pluripotent stem cells (iPSCs) is described in full in Chapter 9. Additionally, the culture of active and inactive Mouse Embryonic Fibroblasts (MEFs and iMEFs) is detailed in Chapter 9, as these were used in the culture of some iPSC lines.

The methods for the culture of HeLa and fibroblast cell lines (Table 3) are detailed below.

**Table 3. HeLa and fibroblast cell lines**

| Cell type | Mutation | Source |
|---|---|---|
| HeLa cells | Wild Type (WT) | Dr Guido Hermey at University Medical Centre Hamburg-Eppendorf |
| | CLN3 KO | |
| Human fibroblast cells | Wild Type (WT) | Coriell Institute (GM05399) "apparently healthy individual" |
| | $CLN3^{\Delta ex7/8}$ | Prof. Mole at University College London (UCL) |
| | CLN3 D416G | Dr Waller-Evans at Cardiff University (originating from UCL) |

#### *2.2.1.1 Thawing frozen cells*

To thaw frozen cells, a 15 ml falcon tube was prepared with 9ml of cell culture medium in the hood. The cryovials was collected from storage (-80°C freezer or liquid nitrogen) or transport container with dry ice upon arrival. The vial was rapidly thawed in a pre-heated 37°C water bath until a small chunk of ice remained in the centre of the vial. The vial was then cleaned with ethanol and transferred to the cell culture hood, where 1ml of cell culture medium from the pre-prepared 15 ml falcon was dropped into the vial to thaw the remaining ice. The 2 ml of cell-containing solution was then transferred to the 8ml remaining in the falcon and centrifuged at 1200 rpm for 5 minutes. The supernatant was carefully aspirated, and the pellet was gently resuspended in cell culture medium before transfer to a plate or flask and into the incubator. Cells were monitored for attachment and growth, with change or medium or passage as required.

#### *2.2.1.2 Expansion and maintenance of cell culture*

Cell were cultured in flasks or plates to maintain and expand the culture. For the expansion and maintenance of the culture, cells were grown in T25 flasks (for routine passaging) and T75 (to expand and generate stocks for freezing).

The cells were passaged when they reached approximately 80% confluency. Media was removed, and the cells were gently washed once with 5ml PBS. Immediately after the removal of the PBS, 0.25% Trypsin-EDTA was added to the flask (1 ml for a T25 or 6-well plate or 3 ml for a T75) which was incubated for approximately 2-3 minutes. When the cells had a rounded appearance, observed through the light microscope, the cells were detached by tapping the flask against the bench. When all cells were in suspension, media was added (5 ml for T25 or 12 ml for T75) to inactive the trypsin.

The cell suspension was then divided between flasks for continued growth or plates for experimental work, as required. To prepare cells for imaging experiments, they were seeded on uncoated glass coverslips of either 16mm diameter for 12 well plates, or 14mm diameter for 24 well plates, 2 days prior to the experiment.

#### *2.2.1.3 Freezing cells for long term storage*

To prepare cell pellets for long term storage, the cells were detached with trypsin as described above, and the suspension was centrifuged at 1200 rpm for 5 minutes. The pellet was then diluted in freezing medium (90% FBS, 10% DMSO) and transferred to cryovials in 1ml aliquots and placed in a freezing chamber in a -80°C freezer before transfer to liquid nitrogen for long term frozen storage. The freezing procedure was carried out rapidly, to minimise the time that the cells were in contact with the DMSO at room temperature.

### 2.2.2 Imaging experiments

The protocols for the use of specific probes, indicators or treatments are detailed in each chapter.

Cells were seeded on uncoated glass coverslips of either 16mm diameter for 12 well plates, or 14mm diameter for 24 well plates, approximately 48 hours before the day of experiment or fixation, to allow for growth and recovery from dissociation.

### 2.2.3 Live cell imaging

For live cell imaging, the coverslips were transferred to an imaging chamber and maintained in an appropriate loading buffer or culture medium as shown in Figure 3.

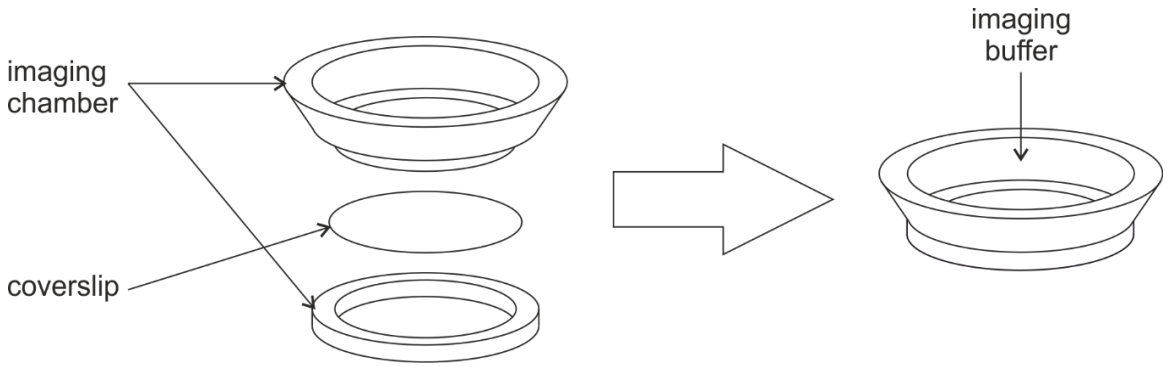


**Figure 3. Imaging chamber assembly.** The coverslip was sealed into the chamber with Dow Corning High Vacuum grease to prevent leaking of imaging buffer. Imaging buffer was added to the chamber to prevent cells drying out and to load fluorescent indicators or other compounds.

Images were acquired using a Leica DMI 6000 SD fluorescence microscope fitted with the following objectives: 5x, 10x, 20x air objectives and a 63x oil immersion objective and the filter cubes shown in Figure 4. The numerical aperture of the objective was 1.4. Image capture was carried out using the Leica Application Suite software.


**Figure 4. Filter cubes fitted to Leica DMI6000 fluorescence microscope.** Excitation filters with bandpass (BP) for excitation wavelength (nm).

All images were saved to the hard drive in LIF (Leica Image File) format and for analysis, imported into ImageJ where they were subsequently be stored as a TIF (Tagged Image File) to avoid loss of information, or in another format such as PNG (Portable Network Graphics) for illustration purposes.

### 2.2.4 Immunostaining

For immunofluorescence, the plated cells were removed from the cell culture laboratory and immediately washed with DPBS and fixed using ice-cold methanol. The protocol was carried out as detailed in Table 4. All stages were carried out at room temperature (unless otherwise stated) and the plates were incubated on a plate shaker. From the secondary antibody (Ab) stage onwards, the coverslips were protected from light with a foil covering. If a fluorescent probe (such as CellLight) was present prior to the fixation, all stages were performed in subdued light conditions and protected from light during incubation. After the final wash stage, the coverslips were removed from the plate and mounted to glass microscope slides using mounting medium. The mounting medium contained DAPI, and for one experiment in Chapter 4, mounting medium with phalloidin was used. The coverslips were dried for an hour at room temperature and either imaged immediately or refrigerated overnight.

**Table 4. Immunofluorescence protocol**

| Stage | Time | Solution |
|---|---|---|
| **Wash** | 3x | DPBS |
| **Fixation** | 15 min (on ice) | Methanol |
| **Wash** | 3x | Washing solution: 0.1% Tween-20 in DPBS |
| **Block** | 45 min | Blocking solution: 1% BSA in DPBS |
| **Primary Ab** | 60 min | LAMP2 1/500 in blocking solution |
| **Wash** | 3x | Washing solution |
| **Secondary Ab** | 45 min | Goat anti-mouse 1/500 in blocking solution |
| **Wash** | 3x | Washing solution |
| **Mounting** | 1 hour + | VECTASHIELD mounting medium |

### 2.2.5 Electron microscopy

For electron microscopy of heart tissue (Chapter 7), fixed and frozen mouse hearts were kindly supplied by Professor Jonathan Cooper. The sections were prepared for electron microscopy by Dr Igor Kraev and Dr Radka Gromnicova in the Electron Microscopy Suite at The Open University. The images were collected using the Transmission Electron Microscope (JEM 1400) and analysed in ImageJ. The tissue samples were processed for TEM imaging according to (Gromnicova et al., 2013).

## 2.3 Summary of statistics

Defining the n number for statistical analysis was depended upon the experiment being carried out. Replicates were typically either:

- Multiple images of several regions (Figure 5A) per coverslip, with multiple cells (Figure 5B). In this case, N is the average value per cell and equals the number of cells analysed. This definition was used for the analysis carried out in Chapter 6 and Chapter 8.
- One experiment per coverslip, with multiple cells in a single region (Figure 5B)

The raw data from quantified images or regions was collected and stored in Excel, with basic calculations such as average of multiple replicates, background subtraction carried out in Excel.

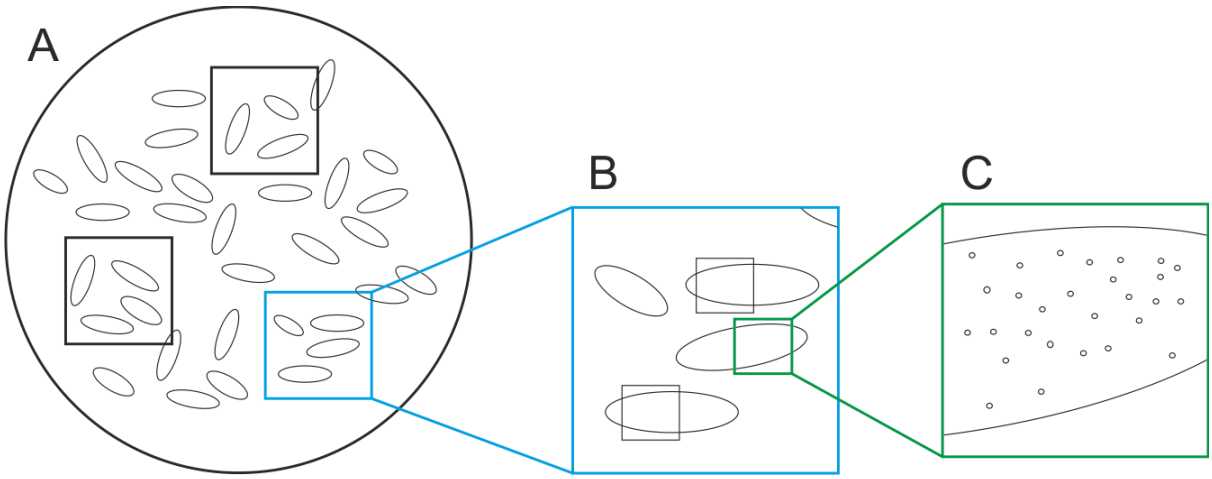


**Figure 5. Selection of regions for imaging and analysis.** (A) Cells were grown on glass coverslips and imaged in chambers (live cells) or on slides (fixed cells). (B) Images of cells were taken across regions on the coverslip. (C) A whole cell or region of interest (ROI) within a cell was selected for quantification.

The statistical analysis and graphical presentation of the data was carried out using GraphPad PRISM 9 using the tests set out in Figure 6. Initially, outlier analysis was carried out to remove any outliers from the dataset with the exception of the lysosome movement analysis in Chapters 4 and 5. To determine whether the data was normally distributed, the D'Agostino & Pearson test and Shapiro-Wilk tests were carried out, with the latter being useful for the assessment of small datasets. The comparison of 2, or ≥3 datasets was carried out using the appropriate parametric or non-parametric test as set out in Figure 6.

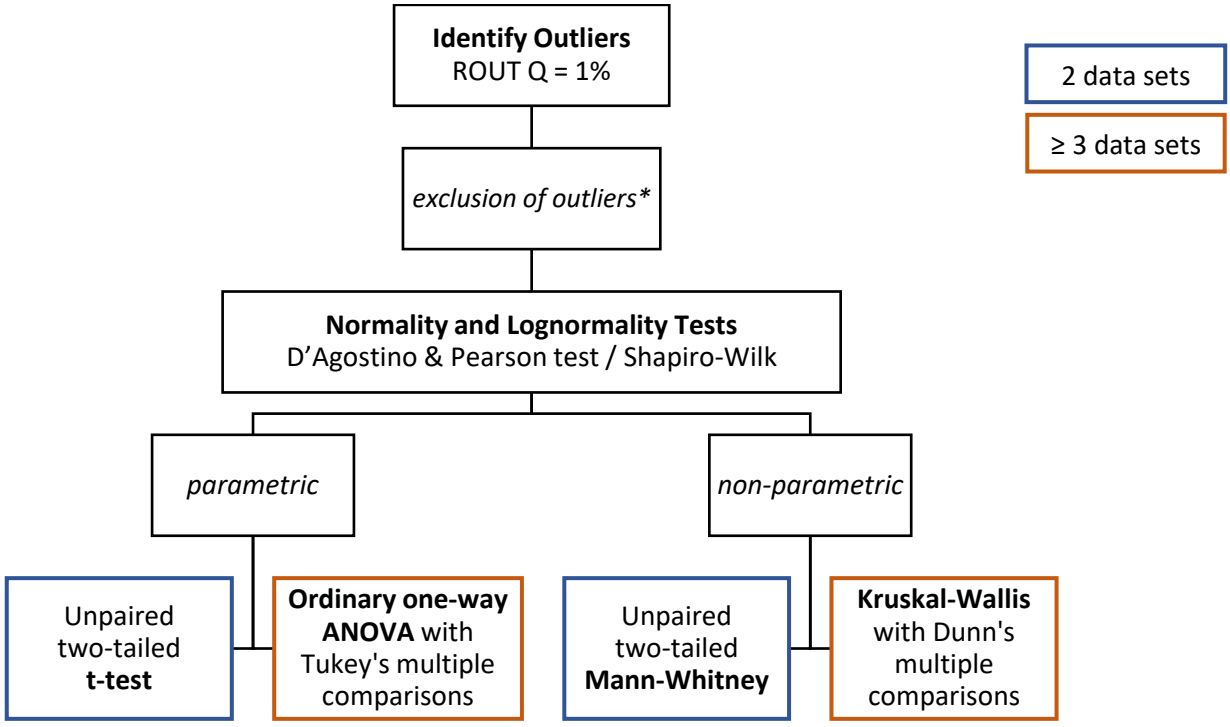


**Figure 6. Flow diagram of statistics applied to each dataset.** All statistical tests were carried out in GraphPad Prism 9. *Outlier analysis was not applied to the data for lysosome movement (chapters 4 and 5).

For some experiments, additional analysis was carried out using GraphPad Prism. These included: simple linear regression, slope, and area under the curve for XY plots such as signal over time. Where these additional analyses provided additional readouts, the replicates were plotted in a Column table and analysed using the appropriate test as in Figure 6.

Data was typically presented as charts in which the bar represents the mean and the error bar shows the ±S.E.M. For many figures, scatter points were also presented to illustrate the replicates per bar.

# 3 An analysis of lysosome probes and their appropriateness for experimental purposes

## 3.1 Introduction

### 3.1.1 Lysosomes in CLN3 disease

In Chapter 1, CLN3 disease was introduced as a lysosomal storage disorder, caused by a mutation of the *CLN3* gene resulting in expression of a mutant form of the CLN3 protein. The CLN3 protein is reportedly expressed on lysosomes (Kyttala et al., 2006). A major characteristic of CLN3 disease is the accumulation of lipofuscin within affected cells, which has been described as a likely failure in the interaction between lysosomes and autophagosomes during autophagy (Marani et al., 2009). Although lysosomes play an essential part in autophagic catabolism, they also have an acknowledged role in cellular signal transduction pathways, such as calcium signalling (Walkley, 2009, Ballabio, 2016, Lloyd-Evans, 2016). Many of the normal lysosome activities, including $Ca^{2+}$ signalling and autophagy, were recognised as defective in a study of CLN3 disease (Chandrachud et al., 2015).

Given the location of the CLN3 protein and the documented effects of CLN3 disease on lysosome function, the ability to image lysosomes with fluorescence microscopy was critical to this project. There are several currently available options for fluorescent lysosome probes, with differing fluorescence characteristics and mechanisms of organelle labelling. The two most commonly used approaches for labelling lysosomes are to exploit the distinctive low pH of these organelles to cause probes to accumulate and/or fluoresce, or to genetically target probes to the lysosome. The following criteria were essential considerations in the selection of a lysosome probe in this study:

- Whether a probe could be used for live-cell imaging, with fixed cells, or for both live and fixed cells.
- Confirming that a probe was specific for lysosomes was crucial for analysis of lysosome activity based on the imaging experiments.
- The fluorescence properties of a probe, particularly the excitation and emission wavelengths, intensity, and stability of signal.

### 3.1.2 Comparison of lysosome probes for fluorescence microscopy

To image lysosomes with fluorescence microscopy there are a range of commercially available lysosome probes with varying mechanisms of labelling:

- LysoTracker Green DND-26 (LysoTracker green)
- LysoTracker Red DND-99 (LysoTracker red)

- CellLight Lysosomes-GFP BacMam 2.0 (CellLight green)
- CellLight Lysosomes-RFP BacMam 2.0 (CellLight red)
- Anti-LAMP2 antibody + Alexa Fluor® 568 (anti-LAMP2 antibody)

The lysosome-associated membrane proteins 1 and 2 (LAMP1 and LAMP2) are glycoproteins found in abundance on the lysosome membrane (Eskelinen, 2006). Immunostaining for LAMP proteins is widely considered to be a valid method for examining the location of lysosomes. However, a major limitation of antibody staining is the necessity for cells to be fixed, which means that this approach cannot be used for dynamic measurements with live cells. In this study, endogenous LAMP proteins were used as the standard for lysosome labelling to examine the specificity of the LysoTracker and CellLight lysosomal probes.

The LysoTracker probes exploit the low pH of the lysosome to achieve specific lysosome labelling (ThermoFisher, 2021b). The fluorescence of these synthetic probes increases to detectable levels when the fluorophore is protonated in the acidic compartment of the lysosomes. The CellLight baculovirus constructs lead to the expression of fluorescently-tagged LAMP1 in living cells (ThermoFisher, 2021a). Unlike the LysoTracker stains, the fluorescence of fluorescently-tagged LAMP1 is pH independent. Furthermore, as shown in this chapter, the expressed fluorescently-tagged LAMP1 protein is retained post permeabilisation and fixation, which makes the CellLight method potentially more versatile than LysoTracker. On the other hand, the baculovirus-based probes rely upon successful transduction of the cells, which can have variable efficiencies in different cell lines. Further potential disadvantages of the CellLight approach are the many hours required for the fluorescence to develop, and that the over-expressed fluorescently-tagged LAMP1 protein may be incorrectly targeted or may interfere with the normal function of native LAMP1 in the cell.

As stated above, this study utilised the immunofluorescence of endogenous LAMP proteins, identified via a specific antibody, to assess the specificity of lysosome labelling. With the appropriate controls (including 'secondary antibody only' to rule out non-specific binding), LAMP2 immunostaining delineated the specific subcellular localisation of the LAMP2 protein without requirement for overexpression and provided the means to validate the use of other lysosomal probes for dynamic measurements in living cells.

**Aim 1: to identify a specific probe for imaging of lysosomes in living cells.**

Objectives:

- Establish protocols for LysoTracker, CellLight, and LAMP2 labelling in fibroblasts and HeLa cells.

- Characterise the specificity of the probes using co-localisation.

**Aim 2: to characterise the specific lysosome probes for their use in live cell imaging experiments**

Objectives:

- Establish efficient image processing to remove or reduce background signals from fluorescence images.
- Characterise the photostability of the probes in live-cell imaging experiments.

## 3.2 Methods

The methods for cell culture, details of fluorescence imaging, and the preparation of chambers for fluorescence imaging of live cells and slides for fixed cells are described in Chapter 2. All solutions containing fluorophores (e.g. LysoTracker and secondary antibody solutions) or cells labelled with/expressing fluorophores (such as LysoTracker, CellLight or immunofluorescence) were handled in subdued light conditions to avoid photobleaching.

### 3.2.1 Loading or expressing lysosome probes in live cells

The names, sources, and functional properties of the lysosomal probes used in this study are shown in Table 5.

**Table 5. Details of lysosome probes.**

| Probe name | Supplier (Catalogue #) | Mechanism of labelling | Wavelength |
|---|---|---|---|
| LysoTracker™ Green DND-26 | Invitrogen™ (L7526) | Accumulation of probe in lysosomes leading to enhanced fluorescence through protonation of fluorophore at low pH | 504/511 nm |
| LysoTracker™ Red DND-99 | Invitrogen™ (L7528) | | 577/590 nm |
| CellLight™ Lysosomes-GFP BacMam 2.0 | Invitrogen™ (C10507) | Transduction with baculovirus for expression of fluorescently-labelled LAMP1 | 488/510 nm |
| CellLight™ Lysosomes-RFP BacMam 2.0 | Invitrogen™ (C10597) | | 555/584 nm |
| Anti-LAMP2 (human) antibody | Developmental Studies Hybridoma Bank (H4B4) | Monoclonal primary antibody; anti-LAMP2 | N/A |
| Alexa Fluor® 568 goat-anti-mouse IgG (H+L) | Invitrogen (A11031) | Immunostaining with cross-adsorbed secondary antibody | 578/603 nm |

#### *3.2.1.1 LysoTracker*

The LysoTracker probes were loaded into living cells 30 minutes prior to imaging. LysoTracker was stored as small aliquots of a 1 mM stock solution to avoid frequent freeze-thaw cycles. Immediately prior to loading, an aliquot was thawed and diluted in imaging buffer (warmed to room temperature) to achieve the working concentration of 50 nM. A coverslip coated with cells at approximately 70% confluency was removed from a 12-well plate and placed in an imaging

chamber. The coverslip was washed gently with room temperature imaging buffer to remove traces of cell culture medium, and the LysoTracker solution was subsequently added to the chamber to start the incubation. The imaging chamber was incubated at room temperature, protected from light, for 30 minutes. Subsequently, the LysoTracker solution was exchanged for fresh imaging buffer and the chamber was immediately placed on the microscope stage to commence imaging.

#### *3.2.1.2 CellLight*

The CellLight probes were introduced to the cells via transduction with baculovirus to induce expression of GFP- or RFP-tagged LAMP1. Cells were grown to approximately 70% confluency on imaging coverslips placed in 6-well plates. The virus particles were diluted in cell culture medium to the required titre before being added to the cells. A 6-well plate was retrieved from the incubator and the virus-containing solution was gently added to the medium surrounding the cells. The 6-well plate was then returned to the incubator to allow expression of the fluorescently-tagged protein. At a specific time, the solution containing the virus particles was aspirated from the cells and replaced with fresh medium. The cells were then returned to the incubator. Immediately prior to imaging, a coverslip from the virus-treated 6-well plate was placed in an imaging chamber and gently superfused with room temperature imaging buffer to remove the cell culture medium.

For co-loading of LysoTracker and CellLight, cells expressing CellLight were loaded with LysoTracker as detailed above. LysoTracker Red was combined with CellLight GFP, while LysoTracker Green was combined with CellLight RFP.

#### *3.2.1.3 Anti-LAMP2 antibody*

To label cells with the anti-LAMP2 antibody, immunostaining was carried out following the protocol described in Chapter 2. The secondary antibody was selected for species reactivity, with the corresponding Alexa Fluor that did not overlap in excitation/emission wavelengths with the lysosomal probes being examined. A control for non-specific binding of the secondary antibody was included each time an immunostaining experiment was performed. After immunostaining, the coverslips were mounted on slides for imaging.

For comparison of CellLight and LAMP2 antibody staining, coverslips expressing CellLight were fixed, permeabilised and immunostained. CellLight GFP was used in combination with a secondary antibody conjugated with Alexa Fluor® 568.

### 3.2.2 Imaging lysosome probes with fluorescence microscopy

Imaging was performed using a Leica DMI600 fluorescence microscope and a 63x oil immersion objective. The LysoTracker probes were imaged with an exposure time of 20 - 50 ms, while the

CellLight probes were imaged with an exposure time of 100 - 150 ms. The differences in exposure time reflect the fact that the BacMam-based labelling was not as intense as the LysoTracker probe and required more excitation for an optimal signal.

The lysosomal probes used in this study were imaged using typical 'green' or 'red' filter sets as depicted in Table 6. To co-localise the signals from two probes within the same cell, the probes were imaged as a green/red pairs in order to detect each probe in separate channels. This method relied upon fluorophore detection at the expected channel and an absence of bleed-through to the other channel, which would interfere with the results.

**Table 6. Excitation and emission wavelengths of the fluorophores of each lysosomal probe.** The excitation/emission reported by the manufacturers are listed for each probe, in the column referring to the respective channels of the Leica fluorescence microscope used for detection.

| | **Green channel** | **Red channel** |
|---|---|---|
| LysoTracker™ Green DND-26 | 504/511 nm | No signal |
| LysoTracker® Red DND-99 | No signal | 577/590 nm |
| CellLight™ Lysosomes-GFP | 488/510 nm | No signal |
| CellLight™ Lysosomes-RFP | No signal | 555/584 nm |
| Secondary Ab Alexa Fluor® 568 | No signal | 578/603 nm |

Since a key aim of this work was to compare the cellular distribution and utility of lysosomal probes, it was necessary to perform co-localisation experiments using green and red pairs of the indicators. Table 6 depicts the imaging channels with which the various lysosomal probes should optimally correspond with. Any fluorescence emission that is detected in the non-expected channel could interfere with co-localisation analyses. To ensure that the light emitted by the fluorophores was not detected outside of the expected wavelengths, the probes were imaged with both green and red channels. The expected outcome was that the fluorescence would be detected in one channel and absent on the other (denoted 'expected channel' and 'empty channel', respectively). For this analysis, the probes were loaded individually into cells on coverslips and imaged using both channels to determine whether there was any fluorescence bleed through into the empty channel. To image the empty channels, an exposure time of 150 ms was used. This was the maximal exposure time used in this study, and it was required for the least bright probe (CellLight Lysosomes-RFP).

Using a relatively long exposure time of 150 ms increased the likelihood of detecting any apparent bleed through.

The lysosome probes used in this study were selected to represent a range of mechanisms to label lysosomes and were not all compatible across live and fixed cell experiments. While both LysoTracker and CellLight were loaded into live cells, antibody staining required fixed and permeabilised cells. An attempt was made to use both LysoTracker and CellLight probes with LAMP2 immunocytochemistry. LysoTracker fluorescence was detrimentally affected by fixation and lost during permeabilisation. Whereas, CellLight retained its signal after fixation and permeabilisation. Therefore, the most versatile probes for staining live, fixed and permeabilised cells was CellLight, as shown in 7.

**Table 7. Summary of the utility of different lysosomal probes for live and fixed cell experiments.** LysoTracker and CellLight can be readily used to label living cells. Only CellLight is suitable for both living cell and fixed cell experiments.

| Probe | Live cells | | Fixed & permeabilised cells | |
|---|---|---|---|---|
| | Labelling | Imaging | Labelling | Imaging |
| LysoTracker | ✓ | ✓ | | |
| CellLight | ✓ | ✓ | | ✓ |
| Anti-LAMP2 | | | ✓ | ✓ |

Fluorescence imaging was carried out by collecting a series of images for a specified duration. The interval between subsequent images in a series was set to the minimal value possible (to obtain the most rapid sequence) unless otherwise stated.

### 3.2.3 Methods for the analysis of lysosome images

Analysis of the fluorescence images was carried out using tools and plugins within ImageJ. Data obtained from the images were transferred to Microsoft Excel for additional calculation, if necessary, and to GraphPad Prism for statistical analysis and presentation. The example panels shown in Figure 8 and Figure 11 were created using a combination of 'Split Channels' and 'Merge Channels' and the relevant images were saved as .jpeg files for import to Corel Draw. To plot the fluorescence profile across the cell images, the ImageJ 'line' tool was used to specify a line across the diameter of cells, and intensity of the pixels along the line was measured using the 'Plot Profile'

tool. The profile intensity data was transferred to GraphPad Prism, with the independent variable being distance (pixels) and the dependent variable being pixel intensity (gray value). Distances reported in pixels were subsequently converted to µm.

To measure the specific fluorescence intensity of lysosomal probes within whole cells in a field of view, the 'background signal' observed in non-cellular areas was subtracted from the fluorescence intensity recorded from the image area containing cells. For this, the mean gray value was measured for a small extracellular area of the image. The cells within the image were outlined by tracing around their circumference and duplicated using the ImageJ 'Polygon selections' tool. The area outside of the traced cell was removed (set to 0 intensity) with 'Clear Outside' function. The mean gray value was measured for the entire area of each cropped cell.

Co-localisation analysis was used to determine the extent to which two probes overlapped within cells. For this, the images collected using the red and green channels were separated from the stack with the ImageJ plugin 'Split Channels'. To quantitate co-localisation of the lysosomal probe fluorescence, the 'Just Another Co-localisation Plugin' (JACoP) for ImageJ was used. This plugin returned the Pearson's co-efficient, which is directly proportional the degree of co-localisation.

Photobleaching analysis was carried out using 'Intensity v Time Monitor' plugin within ImageJ and exported, with time as the independent variable and the mean gray value of cellular fluorescence as the dependent variable.

## 3.3 Results

### 3.3.1 Optimisation of loading conditions

LysoTracker had a straightforward loading protocol, achieved within the parameters suggested by the manufacturer. Conversely, CellLight required considerable optimisation for each cell line, as recommended by the manufacturer. On initial testing, the GFP form of the BacMam expression vector construct showed a brighter and clearer signal than the RFP version. Therefore, optimisation was carried out with CellLight Lysosomes-GFP to achieve good transduction efficiency and good signal to noise. The signal to noise ratio refers to the difference between the signal from the fluorophore, localised to its intended target (signal) and the background fluorescence (noise). For the optimisation of CellLight, signal to noise was assessed in a qualitative manner, based on the appearance of fluorescence signal in the images. Initially, the protocol recommended by the manufacturer was tested with fibroblasts, but no fluorescence was observed during imaging. Thereafter, the viral transduction protocol was sequentially altered, and several different conditions were tested (Table 8).

Although the manufacturer suggested that CellLight viral particles had “minimal toxicity”, it was still considered beneficial to reduce the length of time during which the cells were exposed to the particles. Since the principal purpose of this study was to characterise lysosomes within individual cells, the quality of lysosome staining within each cell was more important than the total number of cells transduced. The CellLight reagent was a single particles, so there were no separate negative controls for associated reagents.

**Table 8. Optimisation of CellLight protocol.** Manufacturer recommended conditions, range of testing and results for optimal expression of CellLight to indicate lysosomes. The CellLight stock solution contained $1 \times 10^8$ particles/ml solution.

| Parameters | Manufacturer recommended conditions | Range of conditions tested for optimisation of CellLight expression |
|---|---|---|
| Concentration of viral particles | 0.2 µl/ 1,000 cells | 0.1-5 µl/ 1,000 cells |
| Cell seeding density | <70% | 50-80% in 96- and 12-well plates |
| Volume of medium | N/A | 0.05-0.1 ml (96-well) 0.5-1 ml (12-well) |
| Incubation times | 16 hr with particles | 8-16 hours with particles, followed by 18-42 hours in fresh medium |
| Plate shaking | N/A | No shaking, 15 minutes or 1 hour RT |

The most relevant parameters for improved fluorescence signal and image clarity were found to be the concentration of viral particles and incubation time, as illustrated in Figure 7. At 18 hours post-addition of the viral particles, a relatively strong signal was observed in cells that had been exposed to the highest concentrations of particles (Figure 7A – C). However, for the cells at 42 hours post-addition of viral particles, there was a detectable signal at even the lowest viral particle concentration (Figure 7D – F). Moreover, there was a greater image clarity with the longer incubation time; the lysosomes were more easily resolvable compared to the more diffused fluorescence observed with 18 hours' incubation.

While the cells appeared to have a healthy morphology and normal growth with extended exposure to the particles, the particles did not need to be present for the entire duration of incubation to improve expression. Therefore, the particles could be incubated overnight (~8 - 12 hours), washed off using fresh culture medium, and the cells incubated for a further day and a half (~30 - 34 hours) before imaging. These timings were used to reduce the exposure of the cells to the viral particles with no evident detriment to GFP-expression, indicating that the cells were able to rapidly take up the particles, and once internalised the majority of the incubation time was required for the vector-encoded protein to be expressed.

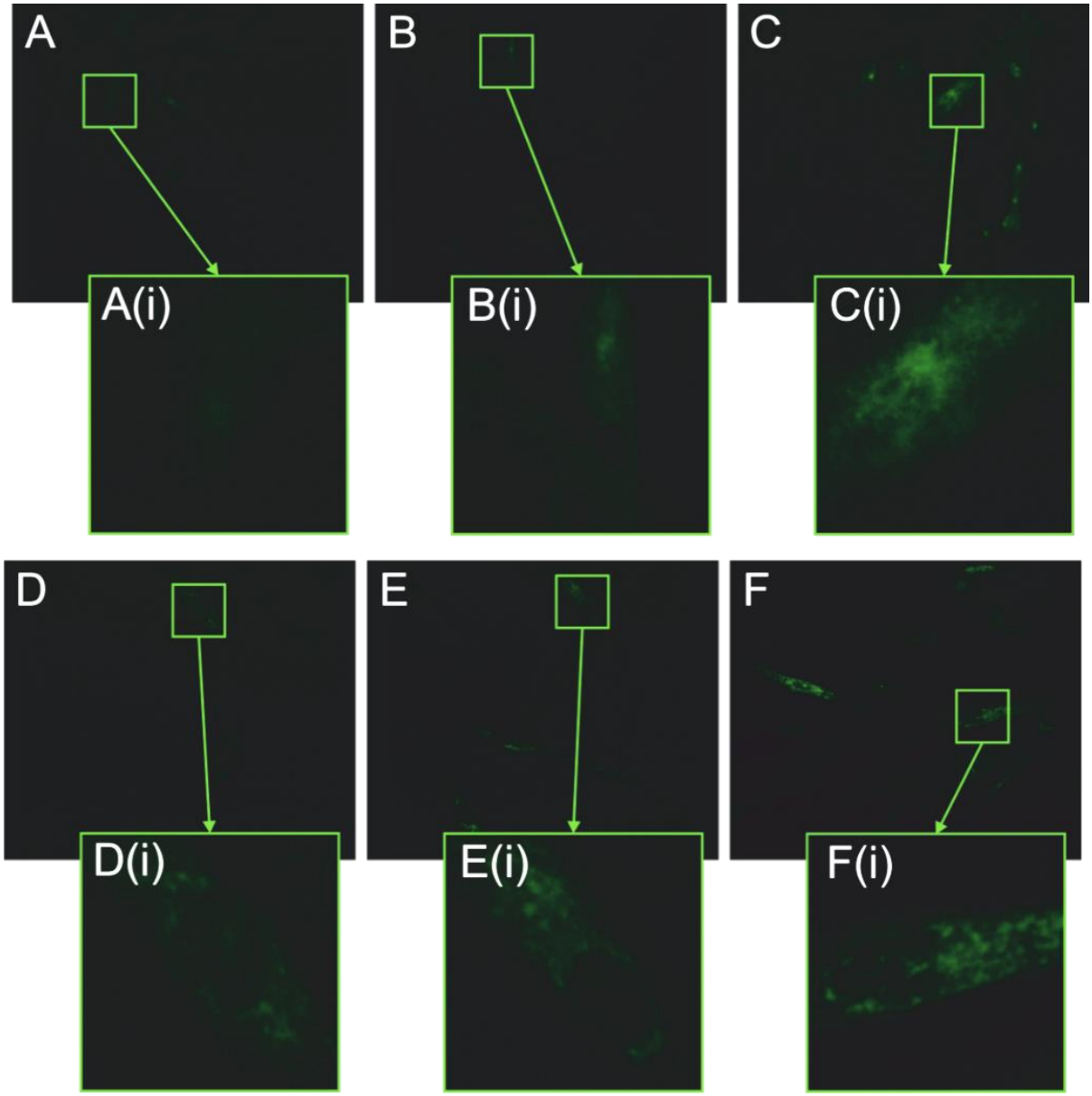


**Figure 7. Optimisation of CellLight™ Lysosomes-GFP, BacMam 2.0 loading.** Fibroblast cells were grown on glass coverslips in 96-well plates as described in Chapter 2. The cells were transduced with CellLight™ Lysosomes-GFP using the following conditions: 18-hour incubation (A-C) or 42-hour incubation (D-F) with 0.5 µl (A and D), 2.5 µl (B and E), or 5 µl (C and F) of the viral particle stock per ml of medium. The CellLight stock solution contained $1 \times 10^8$ particles/mL solution.

Table 9 lists that optimised conditions that were established for CellLight™ Lysosomes-GFP expression. The key parameters that affect the quality of images were concentration of viral particles, incubation time, and the use of plate shaking. The latter may have aided in the dispersal of the viral particles as it reduced the appearance of extremely bright, rounded cells that appeared to have been overloaded with particles, while the majority of surrounding cells failed to express any GFP signal.

**Table 9. Optimisation of CellLight protocol for fibroblast cells.** The CellLight stock solution contained $1 \times 10^8$ particles/mL solution.

| Parameter | Range of conditions tested for optimisation | Optimal conditions for high quality images |
|---|---|---|
| Concentration of viral particles | 0.1-5 µl/ 1,000 cells | ≤2.5 µl |
| Cell seeding density | 50-80% in 96- and 12-well plates | No visible difference |
| Volume of medium | 0.05-0.1 ml (96-well)<br>0.5-1 ml (12-well) | No visible difference |
| Incubation times | 8-16 hours with particles<br>18-42 hours in fresh medium | 8 hours with particles followed by ≤42 hours in fresh medium |
| Plate shaking | No shaking, 15 minutes or 1 hour RT | 15 minutes RT or,<br>2-3 minutes tapping |

Following the optimisation of CellLight Lysosomes-GFP expression in fibroblasts, the protocol was tested in HeLa cells. HeLa cells initially appeared to have significantly better transduction efficiency and a stronger signal in a shorter time. However, a challenge associated with these cells was their high proliferation rate which meant that the seeding density and incubation time were limited to avoid over-confluency.

The optimal conditions for CellLight Lysosomes-GFP expression in HeLa cells are presented in Table 10. In essence, the HeLa cell conditions were altered to account for the cell seeding density required to maintain a healthy culture up to the point of imaging. While fibroblasts were passaged and allowed 24 hours to settle prior to addition of the particles, HeLa cells were seeded and given some time to adhere (~4-6 hours) before addition of the particles, which were then allowed an overnight incubation before exchange for fresh medium. The HeLa cells were then incubated for a further 24 hours before imaging.

**Table 10. Optimisation of CellLight protocol for HeLa cells.** The CellLight stock solution contained $1 \times 10^8$ particles/mL solution.

| Parameter | Range of conditions tested for optimisation | Optimal conditions for high quality images |
|---|---|---|
| Concentration of viral particles | 2.5-5 µl/ 1,000 cells | 2.5 µl |
| Cell seeding density | 50-70% | 60% |
| Volume of medium | 0.05-0.1 ml (96-well) 0.5-1 ml (12-well) | 1 ml (12-well) |
| Incubation time | 8-16 hours with particles<br>16-42 hours in fresh medium | 16 hours particles<br>≤30 hours medium |
| Plate shaking | No shaking, 2-3 minutes tapping, shaking; 15 min or 1hr RT | 15 min RT<br>or 2-3 minutes tapping |

Following the optimisation using CellLight Lysosomes-GFP, the HeLa cells were transduced with CellLight Lysosomes-RFP using the optimal conditions detailed in Table 10. In comparison to CellLight Lysosomes-GFP, the RFP signal was less intense and therefore required a greater exposure time to visualise the lysosomes, but the expression otherwise replicated that of the GFP vector.

Fixed cells were stained for LAMP2 using a specific antibody and a fluorescently-tagged secondary antibody (Table 5) as described in Chapter 2. Essentially, immunofluorescence was carried out using methanol fixation and permeabilisation in a single step, with clear LAMP2 staining achieved with a 1/500 dilution of the primary and secondary antibodies.

### 3.3.2 Testing for imaging channel specificity

As described above, the lysosomal probes (Table 5) were detected using a fluorescence microscope with the relevant red or green channel being selected depending upon their excitation and emission wavelengths (6). Due to the broad excitation and emission spectra of some fluorophores, there is a possibility with fluorescence imaging that signals may not be solely restricted to one channel. This is commonly referred to crosstalk or referred to as 'bleed-through.' Alternatively, an apparent fluorescence signal could be obtained through other means such as background fluorescence from the buffer or autofluorescence from the cells, or noise from the imaging system.

Since bleed-through between fluorescence channels can confound the interpretation of colocalization analysis, it was important to determine whether there was an issue with the

lysosomal probes used in this study. The potential for bleed-through was examined through loading/expressing individual lysosomal probes, followed by quantitative and qualitative analyses of images obtained using both red and green channels. For example, LysoTracker red was loaded into cells using standard conditions, and the cells were imaged using both green and red channels (Figure 8). The expected outcome was the presence of significant signal in the red channel associated with the excitation and emission wavelengths of the probe. The key unknown was the amount of fluorescence evident in the green channel.

Typical images acquired from cells expressing the different lysosomal probes using both green and red channels are shown in Figure 8. The LysoTracker Red probe fluorescence was evident in both green and red channels, with a punctate appearance in both channels that is consistent with labelling of lysosomes. In contrast, fluorescence from the red secondary antibody used for LAMP2 detection displayed a punctate appearance in the red channel, but a diffuse signal in the green channel. The diffuse signal observed in the green channel when imaging the red secondary antibody did not resemble lysosome staining and may have resulted from a high background fluorescence caused by the immunostaining protocol. The CellLight transduction expressed the cleanest signals, with no evident bleed-through between the channels. Additionally, the LysoTracker Green probe did not display bleed-through to the red channel, unlike the red variant of the product. While images such as those shown in Figure 8 provide qualitative guidance about channel bleed-through, they are not quantitative because sensitive imaging cameras are able to detect modest signals and the electronics of an imaging system can enhance the signals for display purposes.

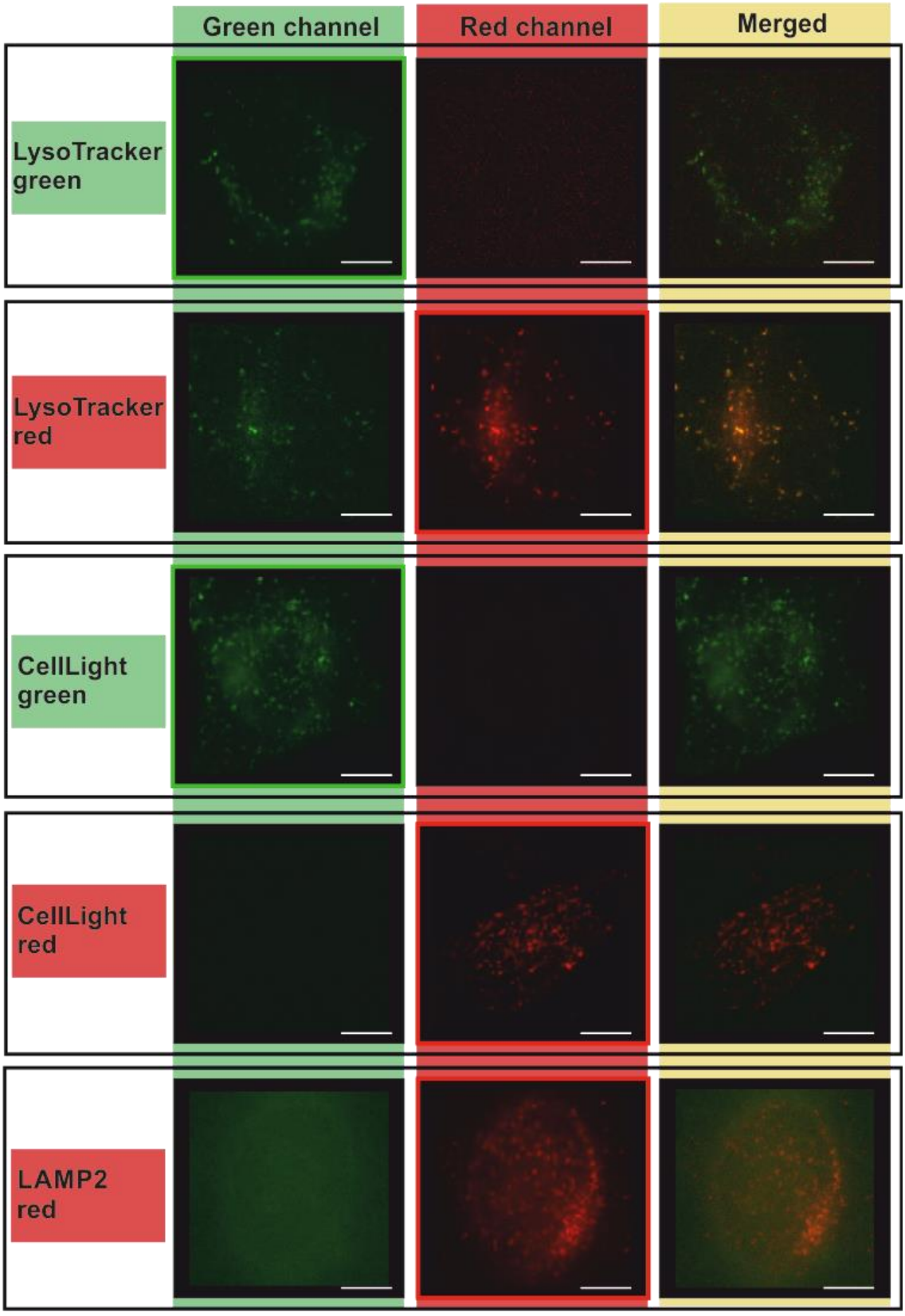


**Figure 8. Images showing HeLa cells loaded with LysoTracker, expressing CellLight, or immunostained with LAMP2 antibody.** Images of HeLa cells labelled with each probe were captured with green and red channels, as illustrated alongside the merged images. The scale bar is 10 µM on all images.

Images such as those shown in Figure 8 were quantified to measure the fluorescence intensity within both the green and red channels for each lysosome probe. The quantification shown in Figure 9 compared the fluorescence recorded by the green and red channels when cells were loaded with the probes in pairs (Figure 9A) or individually (Figure 9B). Figure 9A shows that each pair of probes has similar levels of fluorescence signal under the conditions used. The parity of signal between the various probes is helpful in ensuring that co-localisation analysis is meaningful. Whilst there was some variation in the fluorescence intensity, each channel had a mean gray value of between 50 to 150 and there was no significant difference between the paired channels when loaded.

Whilst the data shown in Figure 9A indicate similar levels of fluorescence arising the in the green and red channels when pairs of probes are used, they do not inform about any potential bleed through between channels. The quantitation of each probe on its own is required to determine bleed through (Figure 9B). As anticipated, substantial fluorescence intensity was observed with the 'expected channel' that matched a lysosomal probe's specified excitation and emission wavelengths, and this was significantly greater than that in the 'empty channel'. The mean gray values of the empty channels were between 4 and 10 for all lysosomal probes, except for the red secondary antibody used for LAMP2 detection, where the empty green channel had a mean gray value of 25. Nonetheless, in each case, the fluorescence intensity of the expected channel was significantly greater than in the paired empty channel. This was even true for LysoTracker Red, which visually appeared to show bleed-through to the green channel (Figure 8). These data indicate that although there was some bleed through between the green and red channels for all the probes tested (Figure 8 and Figure 9B), it was a small fraction of the signal observed when pairs of probes were used together (Figure 9A).

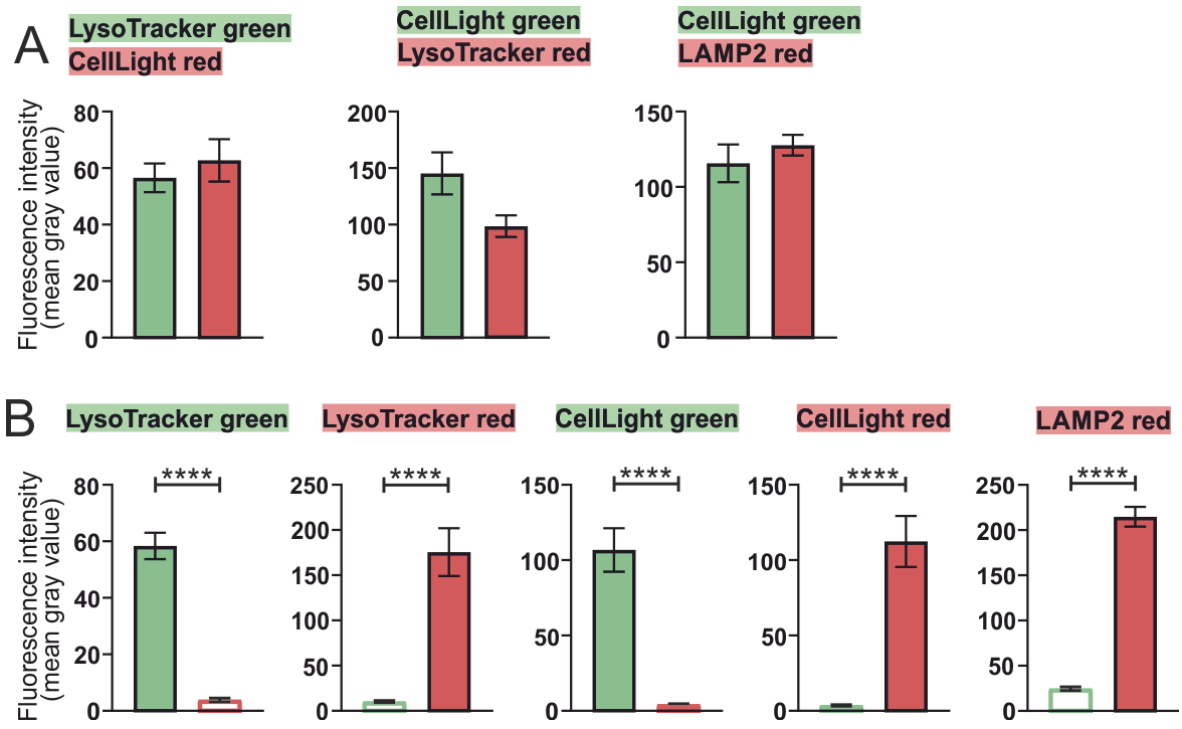


**Figure 9. Fluorescence intensity of lysosome probes in HeLa cells when imaged using the green and red channels of the Leica microscope.** The fluorescence in images of cells labelled with each lysosome probe is shown for the green channel (green bars) and red channel (red bars). The cells were labelled with: (A) multiplexed probes, or (B) individual probes. These data were analysed with a Mann-Whitney test where **** indicates $p \leq 0.0001$ and $n = 27$ images per condition (9 images from 3 coverslips, on 3 days).

A negative control that was always imaged alongside the anti-LAMP2 antibody staining was cells permeabilised and fixed cells incubated with the secondary antibody only. For every immunostaining that was carried out, additional coverslips were treated as a negative control in which the only deviation from the immunostaining protocol was the absence of the primary antibody, which was replaced with diluent only (blocking buffer) during the primary antibody stage. The images achieved from this negative control showed weak fluorescence signals in the green channel and the absence of any discernible intracellular structures in the red channel (Figure 4). The weak green fluorescence obtained from imaging the red-labelled secondary antibody-only cells is likely to reflect cellular autofluorescence (Figure 10).

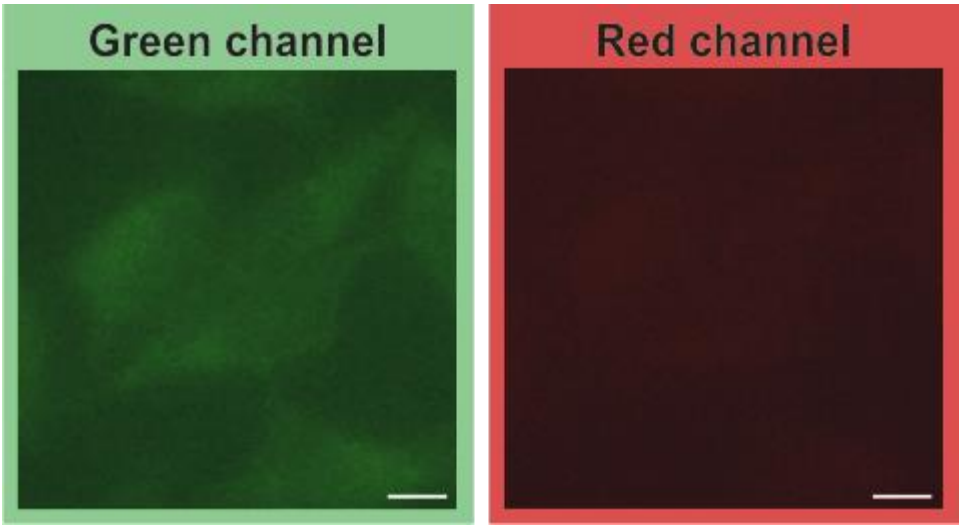


**Figure 10. Images of HeLa cells labelled with the anti-LAMP2 secondary antibody only (red secondary antibody).** The fixed, permeabilised and immunostained cells were imaged using the green and red channels of the Leica microscope. The scale bar is 10 µm.

### 3.3.3 Co-localisation of lysosome probes to assess specificity

With LysoTracker being lost from cells after permeabilisation, and the anti-LAMP2 antibody requiring permeabilisation for staining, CellLight represented a lysosome probe that was available as a comparison for both live and fixed cells.

Experiments were undertaken in which cells were co-labelled with LysoTracker and CellLight to explore their subcellular distributions. However, whereas LysoTracker loaded into in all the cells on a coverslip, CellLight only caused fluorescently-tagged LAMP1 expression in relatively fewer cells that were successfully transduced. Figure 11 shows a field of cells that was transduced with CellLight Lysosomes-GFP and subsequently incubated with LysoTracker Red. All of the cells were observed to have punctate red fluorescence consistent with LysoTracker Red labelling the lysosomes, but fewer cells were found to show green fluorescence. Merging the green and red fluorescence images yields yellow pixel colouration for those cells in which CellLight Lysosomes-GFP was expressed. Similarly, transducing cells with CellLight Lysosomes-RFP and subsequently incubating with LysoTracker Green produced yellow pixels in those cells where both probes were evident.

These data indicate that lysosomal probes of different colours can be multiplexed and can either identify the lysosomes in all the cells in a field of view (LysoTracker probes) or relatively fewer transduced cells (CellLight). Moreover, the clear single-colour staining of the LysoTracker-only cells shows that there was little bleed-through between the green and red channels in these experiments.

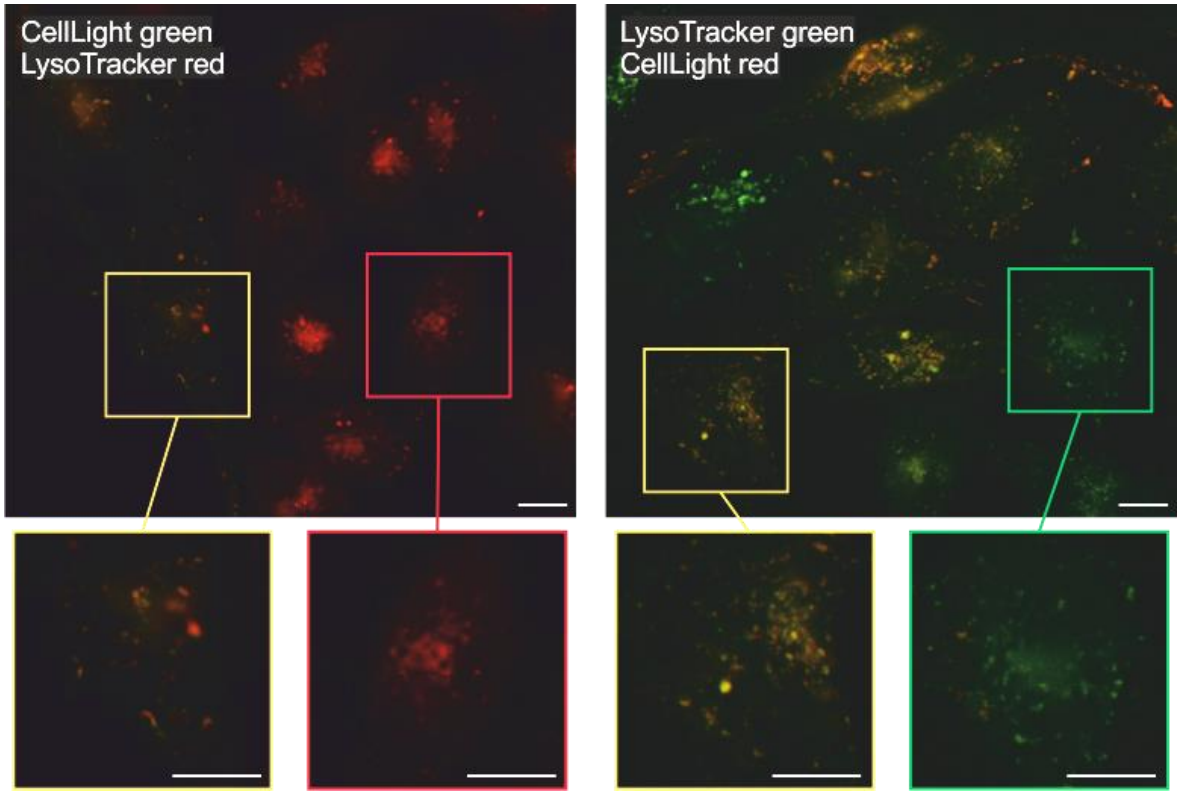


**Figure 11. HeLa cells on coverslips loaded with LysoTracker and transduced with CellLight.** Left: CellLight Lysosomes-GFP was expressed by some cells on the coverslip, while all cells were loaded with LysoTracker red, resulting in a population of partially yellow (labelled with CellLight and LysoTracker) and partially red (LysoTracker only). Right: LysoTracker green was loaded in all cells on the coverslip, while some cells expressed CellLight Lysosomes-RFP, resulting in a population of partially yellow (labelled with LysoTracker and CellLight) and partially green (LysoTracker only).

To quantify the co-localisation of the probes, LysoTracker green was compared against CellLight Lysosomes-RFP and LysoTracker red was compared against CellLight Lysosomes-GFP. The CellLight probes lead to the significant LAMP1 protein translation, which means that they carry a risk of incorrect localisation associated with protein over-expression. Therefore, the CellLight probes were also compared against the immunofluorescence staining of the endogenous LAMP2 protein. This was carried out using CellLight Lysosomes-GFP and immunostaining of an anti-LAMP2 antibody with a red (Alexa Fluor® 568) secondary antibody (hereafter denoted 'LAMP2 red'). For each pairing, the green and red channels, alongside the composite image, are displayed in Figure 12. Additionally, the fluorescence profile was plotted along a line drawn through the cells (depicted on each composite image). The peaks indicate the greater fluorescence of a labelled lysosome and the overlapping peaks across the profile showed that the lysosomes were at the same location in each red and green image.

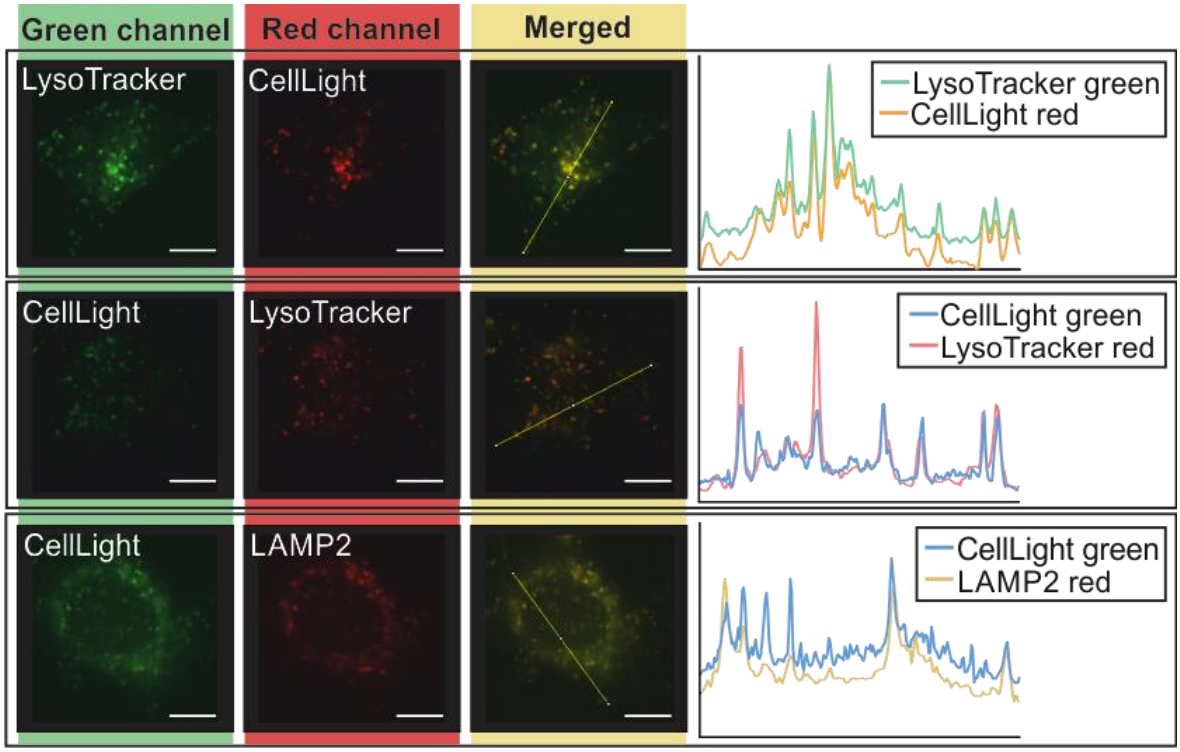


**Figure 12. HeLa cells co-labelled with lysosome probes: green, red, and merged images with plotted fluorescence profile.** The combinations are: LysoTracker green with CellLight red, CellLight green with LysoTracker red, and CellLight green with LAMP2 antibody (red secondary). The fluorescence profile of each channel was plotted using the yellow line depicted in the merged image. The scale bar is 10 µm.

The co-localisation of lysosome labelling was assessed using Pearson's co-efficient, where a value of 1 represents a perfect co-localisation of the above-background pixels between the images, and 0 indicates no overlap of fluorescent signals in the images. Pearson's coefficient was calculated from images of cells labelled with each probe: (1) individually, in cells on separate coverslips, and (2) multiplexed, in pairs, using the green and red channels of the Leica microscope for both (1) and (2). The rationale for analysing Pearson's coefficient in cells with a single probe as well as with multiplexed probes was to examine potential for miscalculation of colocalization due to bleed-through or background signals. As discussed earlier, the lysosomal probes were each designed to be detected within a single microscope channel based upon the associated fluorophore (6), and therefore, any apparent co-localisation occurring when cells contained only a single probe could be attributed to bleed-through or background fluorescence. As such, the analyses of cells containing a single probe represented a negative control to investigate the influence of potential extraneous signals.

The Pearson's co-efficient for the lysosomal probes when they were singularly present within cells is shown in Figure 11. It is evident that there was some difference in the apparent co-localisation

of these lysosomal probes. LysoTracker Green, CellLight green, and CellLight red were found to have the least apparent co-localisation.

**Table 11. Analysis of apparent co-localisation of the lysosome probes in HeLa cells.** The Pearson's co-efficient was calculated by individually loading (LysoTracker), expressing (CellLight), or immunostaining (LAMP2) each lysosome probe, followed by imaging the cells using the green and red channels of the Leica microscope.

| Lysosome probe | Pearson's co-efficient (mean ±S.E.M.) |
|---|---|
| LysoTracker Green | 0.16 ± 0.02 |
| LysoTracker Red | 0.45 ± 0.03 |
| CellLight green | 0.14 ± 0.01 |
| CellLight red | 0.11 ± 0.01 |
| LAMP2 with red secondary antibody | 0.44 ± 0.02 |

Co-localisation was quantitated for the following multiplexed pairings: LysoTracker Green with CellLight red (Figure 13A), LysoTracker Red with CellLight Green (Figure 13B) and CellLight green with LAMP2 immunostaining (Figure 13C). The Pearson's coefficients determined by imaging cells containing these lysosomal probe pairings are plotted alongside the quantification of the corresponding negative controls taken from Figure 11. The pairing of LysoTracker Green and CellLight red yielded a Pearson's co-efficient of 0.76 ± 0.02, which was significantly greater than that observed with either probe alone (Figure 13A and Figure 11). The significant difference in co-localisation between the images of cells containing individual probes and those of the multiplexed probes suggested that the co-localisation reflected a high proportion of vesicles labelled by both probes. The quantitation of co-localisation for CellLight green in combination with LysoTracker Red indicated a significantly greater co-localisation between the multiplexed probes (Pearson's co-efficient of 0.80 ± 0.02) compared to either probe alone (Figure 11). LysoTracker Red probe had a notably higher apparent co-localisation by itself (Pearson's co-efficient of 0.45 ± 0.03), suggesting some signal bleed-through associated with the probe (as noted in Figure 8) present in the images captured using the green channel wavelength. Nonetheless, the assessment of both LysoTracker and CellLight combinations (Figure 13A and B) suggests that the majority of the fluorescent signals were present at the same location, indicative of the probes labelling the same structures within the cells.

The comparison of CellLight green and LAMP2 immunostaining with the red secondary antibody yielded the strongest co-localisation with a Pearson's co-efficient of 0.89 ± 0.01 (Figure 13C), which was significantly greater than that observed with either lysosomal probe alone (Figure 13). There was a notable apparent co-localisation occurring with LAMP2 staining only, indicating that some bleed-through or background fluorescence from the red Alexa Fluor 568-labelled secondary antibody was detected in the green channel.

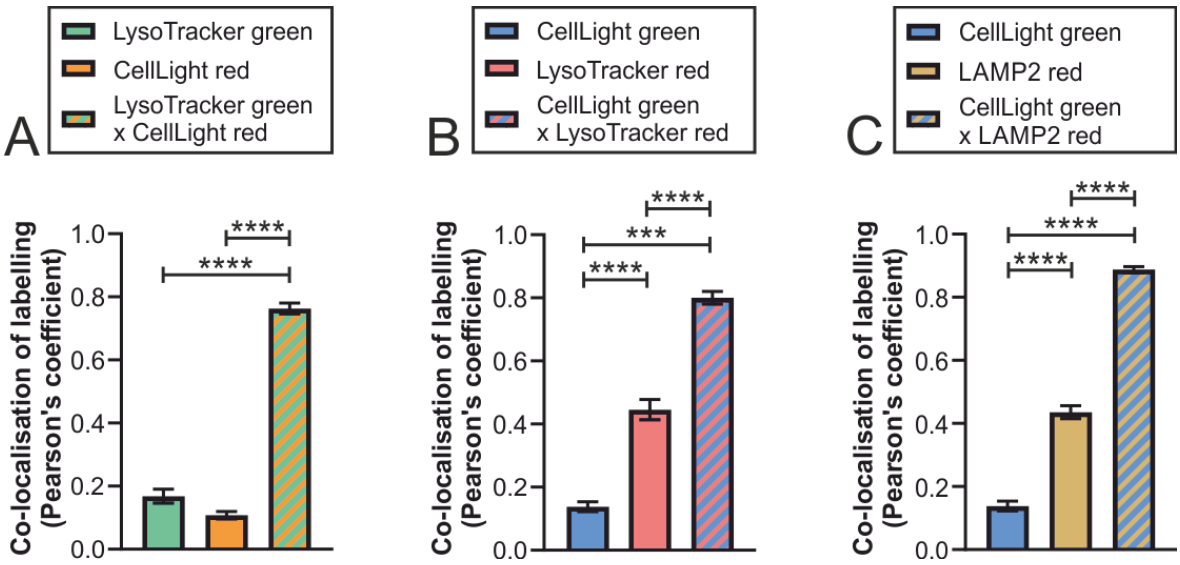


**Figure 13. Co-localisation of green and red channels with and without lysosome labelling in HeLa cells.** The probes were loaded individually and in pairs, as indicated. Each individual probe and pair of probes were imaged with both red and green channels to assess for any effect of bleed-through, and the corresponding Pearson's coefficient was calculated. (A) LysoTracker Green (LTg), and CellLight red (CLr), (B) LysoTracker Red (LTr) and CellLight green (CLg) and (C) CellLight green (CLg) and anti-LAMP2 antibody with red secondary (LAMP2r). These data were analysed with Kruskal-Wallis test and multiple comparisons, where *** indicates $p \leq 0.001$ and **** indicates $p \leq 0.0001$ and n = 27 images per condition (9 images from 3 coverslips, on 3 days).

Given that LAMP2 is expressed on lysosomal membranes (Schwake et al., 2013). The LAMP2 immunostaining observed in this study provides the best marker for validation of lysosomal labelling by the other probes. The significant Pearson's coefficients observed when LAMP2 immunostaining was compared with the CellLight indicators (Figure 13 and Table 12) validates the BacMam probes as lysosomal indictors. In turn, the significant Pearson's coefficients observed when CellLight indicators were compared with the LysoTracker probes (Figure 13 and Table 12) validates the acutely-loaded LysoTracker reagents as lysosomal indicators.

**Table 12. Analysis of co-localisation of the lysosome probes in HeLa cells.** The Pearson's co-efficient was calculated by co-loading (LysoTracker), co-expressing (CellLight), or immunostaining (LAMP2), followed by imaging the cells using the green and red channels of the Leica microscope.

| Lysosome probe pair | Pearson's co-efficient (mean ±S.E.M.) |
|---|---|
| LysoTracker Green/CellLight red | 0.76 ± 0.02 |
| CellLight green/LysoTracker Red | 0.80 ± 0.02 |
| CellLight green/LAMP2 (red secondary antibody) | 0.89 ± 0.01 |

### 3.3.4 Assessment of background fluorescence associated with the LysoTracker and CellLight lysosome probes

With their specificity for lysosomes confirmed, both the LysoTracker and CellLight probes were considered to be appropriate for use in lysosome imaging experiments. The specificity of the probes was crucial in order to reliably analyse lysosomes. However, specificity was not the only consideration when selecting a probe for lysosome imaging experiments: the quality of the images obtained with each probe could influence the analysis, especially when analyses were automated with the use of software such as ImageJ.

Fluorescent probes such as LysoTracker and CellLight have different characteristics which may influence the resulting image quality. These can include:

- **Bleed-through**, which was examined in Figure 8.
- **Intensity of fluorescence**, as illustrated in Figure 9.
- **Background signal**, referring to fluorescence not associated with the lysosomes, which may originate from various sources such as unbound fluorophores in the buffer solution, or even enhanced background introduced by the labelling method (e.g., cell fixation).
- **Noise**, which is generally a property of an imaging system, and can appear as a random, frame-by-frame grainy or speckled texture in the background of an image. Noise can be more profound for indicators with limited brightness.

A key part of the analysis and quantification of images is the selection of regions, or segmentation of cells, or intracellular structures. Manual analysis has a number of drawbacks including the risk of

human error or subjectivity, as well as the inability to generate a high number of replicates in a short period of time, compared to that achieved with automated processing and analysis. Therefore, software-driven automated analysis, such as through the use of ImageJ plugins is highly desirable, although this comes with its own complications. For example, a noisy background that contains regions of a bright pixels that encompass a similar area and shape to lysosomes may be incorrectly identified by automated segmentation algorithms and included in the analysis. Erroneous segmentation associated with automated analysis can be considerably reduced if the images being processed are of high quality (i.e., good resolution and signal intensity), with minimal background noise, and consistent labelling. The use of automated image analysis is discussed in greater depth in Chapter 4.

Prior to quantification, images of cells with labelled lysosomes were processed with the ImageJ function 'Subtract Background.' Removal of background signal from the images enhanced the automated segmentation of the lysosomes. The effect of background subtraction on an original image of LysoTracker fluorescence within a HeLa cell is shown in Figure 14. The original image evidently has numerous discrete lysosomes, but the image also had an elevated background signal which was most prominent in the cloudy appearance in the centre. The 'Subtract Background' function in ImageJ was used to clean the background with minimal impact on the lysosome fluorescence. This plugin was based on the removal of background signal in relation to the size of the object to be detected, originally described by (Sternberg, 1983). Therefore, it was important that lysosome size was considered when removing background and this was achieved through careful observation of lysosomes in the images and adjustment of the 'rolling ball radius'. A rolling ball radius of 100 or 50 pixels reduced the background to an extent but did not entirely eliminate the cloudy background. With a rolling ball radius of 1, 5 or 10 pixels, the cloudy background was fully eliminated. However, a rolling ball radius 1 pixel was considered too extreme as the size and shape of the lysosomes was impacted. Ultimately, a rolling ball radius of 5 pixels was used as the appropriate radius for the background subtraction in this study, as this method eliminated the background signal while retaining the clearest lysosome signal.

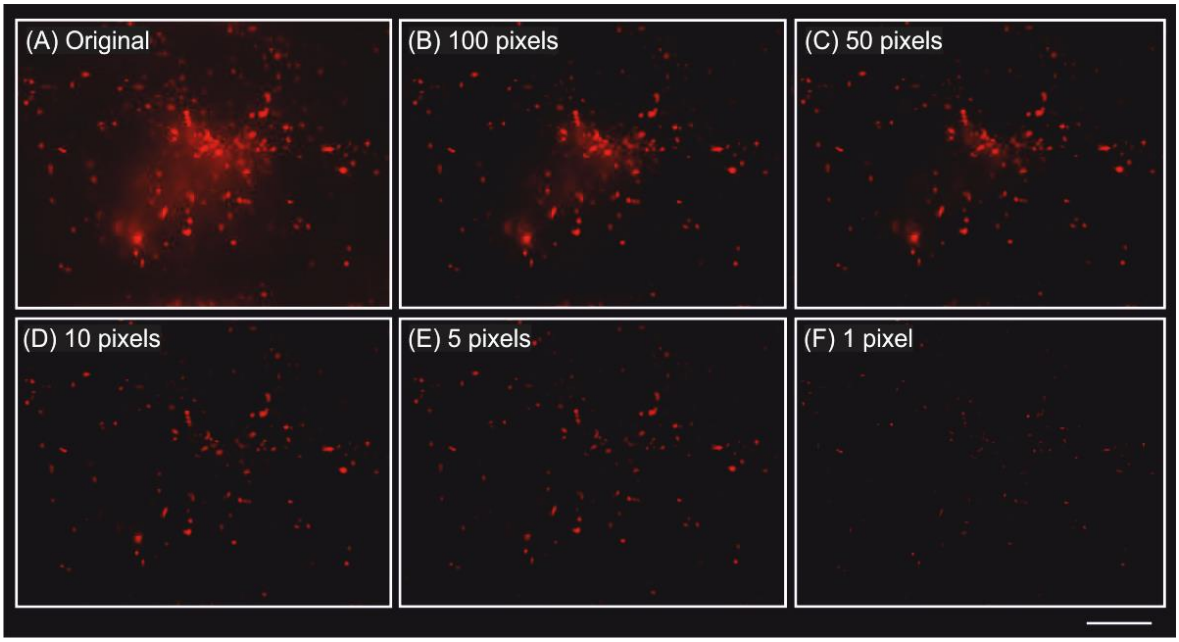


**Figure 14. Background subtraction applied to an image of a LysoTracker labelled HeLa cell.** Background subtraction was performed using the ImageJ rolling ball plugin with the rolling ball radius set to 100, 50, 10, 5 or 1 pixels (px). The scale bar is 10 µm.

To compare the image quality achieved with the use of LysoTracker and CellLight, the probes were loaded or expressed in HeLa cells on separate coverslips and were imaged using the fluorescence microscope. From these images, regions of lysosome signal or non-lysosome background were selected, and the fluorescence intensity measured as mean gray value (Figure 15). In all of the images of cells labelled with LysoTracker or CellLight, the pixels had a significantly greater fluorescent signal (mean gray value) localised to the lysosomes than found in the background regions. As the background fluorescence was comparatively low, this was plotted separately on an expanded scale (Figure 15B) to more clearly illustrate the comparison of background signals associated with each probe. While the background signals observed with LysoTracker and CellLight were not statistically significant, the background signal was noticeably lower in the images of LysoTracker-loaded cells than in those expressing CellLight (Figure 15B).

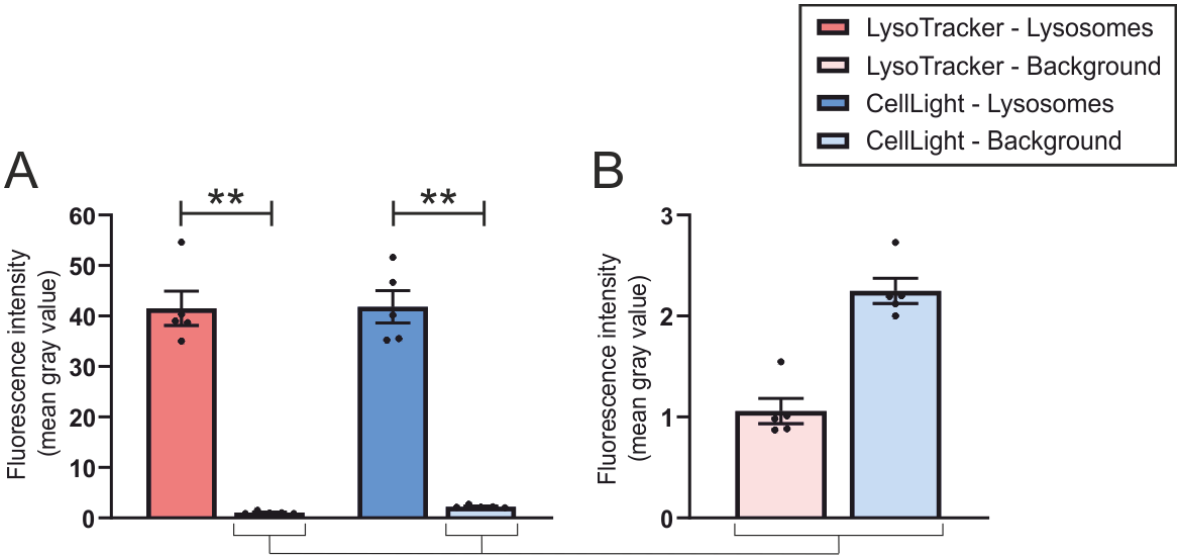


**Figure 15. Fluorescence intensity of labelled lysosomes and background regions in sample images.** (A) Lysosome and background fluorescence (mean gray value) plotted from the images of cells labelled with LysoTracker or CellLight. These data were analysed using a Kruskal-Wallis test with multiple comparisons, where ** = $p \leq 0.01$ and n = 5 regions of lysosome or background fluorescence from 5 images. (B) Fluorescence intensity of background signal measurements only. The data are presented as mean ± S.E.M. with individual values plotted.

Figure 15 illustrates that there was a robust and consistent fluorescence from lysosome with both LysoTracker and CellLight indicators that was substantially greater than the background signal. However, despite the relatively low background signal when using these lysosomal probes, an issue became apparent due to noise. This was particularly prominent in the recordings of lysosome movement, which are further discussed in Chapter 4.

To visualise the noise in the images, background regions were sampled from images of cells loaded with LysoTracker or CellLight, as shown in Figure 16. The images of these background regions initially looked similar, but increasing the contrast using ImageJ revealed a clear difference, as shown in Figure 16B and Figure 16D. The fluorescence profile depicted in Figure 16E represents the pixel intensities along a diagonal line from the bottom left to the top right corners of each background image, to capture the variation in signal in a quantitative manner. The number of peaks represented the frequency of variation in the signal across the distance measured, while the height highlighted the intensity of the signal. The plotted profile across the background of the image from LysoTracker-loaded cells had few peaks or troughs with little height, on an otherwise flat baseline (Figure 16). Comparatively, the background in the image from CellLight-expressing cells had a far greater number of peaks of considerable height.

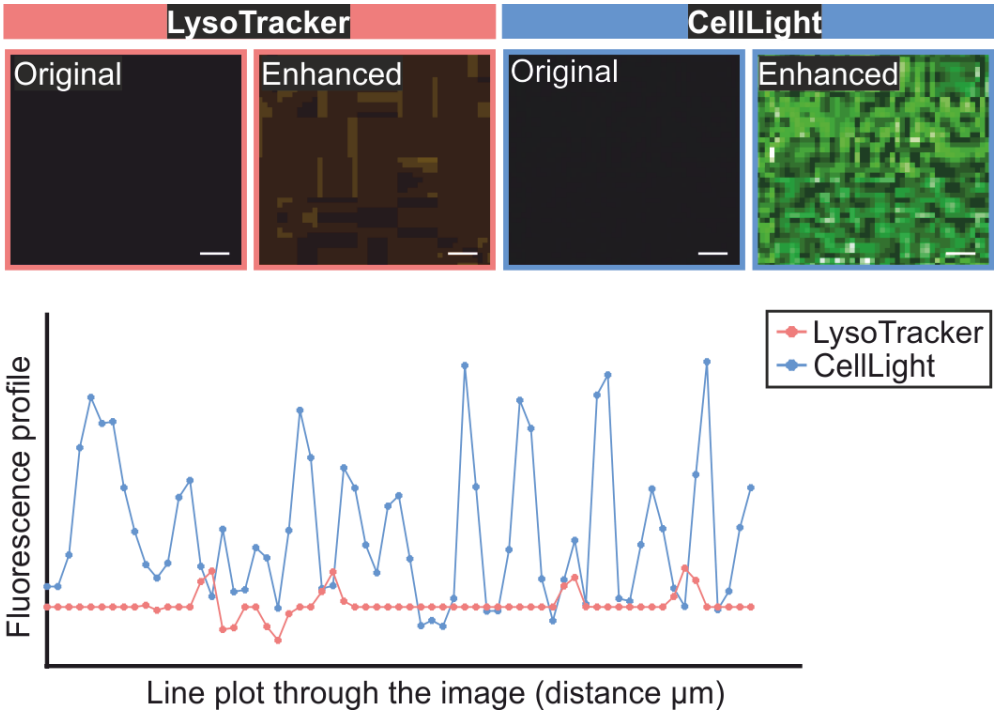


**Figure 16. Example background signals from HeLa cells labelled with LysoTracker (red) or CellLight-GFP, after background subtraction with rolling ball radius set to 5 pixels.** The top panels show regions of background from images of LysoTracker loaded or CellLight expressing cells; with both original and contrast-enhanced versions of each. The scale bar represents 1 µm in all images. The fluorescence profile was plotted using a line drawn across the images diagonally (a distance of 10 µm) to illustrate the relative variation in the gray value between the images of each indicator.

The data in Figure 16 clearly show that LysoTracker-treated coverslips had the least variable background signal, after the rolling ball background subtraction had been applied. Whilst the average background pixel intensity for both LysoTracker and CellLight is low compared to the lysosomal fluorescence of both probes, the variation in background noise seen with CellLight raises an issue with lysosome segmentation. Specifically, it became apparent that variable background noise, such as that shown in Figure 3E, was the reason for the random detection of 'lysosome-like' particles by the segmentation algorithm in cells labelled with CellLight. This is further discussed in Chapter 5, in the context of the automated segmentation and tracking of lysosomes.

### 3.3.5 Photostability of fluorescent lysosome probes during imaging

In addition to the specificity and quality of fluorescence staining, the stability of the signal is an important criterion for live cell imaging, particularly for experiments using time series imaging. The stability of the fluorescent signal from probes such as LysoTracker and CellLight was partially dependent on the rate of photobleaching during exposure to the microscope light source. The exposure time set to capture an image, and the number of images in a series, were both factors in the rate of photobleaching. The probes with a weaker signal require a longer exposure time per image to achieve good signal-to-noise. For time series experiments, such as recording lysosome movement (discussed further in Chapter 4), the probes were subject to repeated exposure.

Images of LysoTracker displayed a strong signal with minimal background, but the intensity of the signal reduced rapidly during exposure, as shown in Figure 17. The lysosome fluorescence in cells expressing the CellLight probe required a greater exposure time than those loaded with LysoTracker. The signal associated with CellLight did not have the same dramatic reduction in signal over time as observed with LysoTracker (Figure 17), suggesting that the CellLight probes were more resistant to photobleaching. To test the suitability of the lysosome probes for rapid recording, they were subject to 'minimised' imaging and the fastest frame rate achievable with the microscope settings. LysoTracker provided images of sufficient quality for lysosomal tracking with an exposure time of 40 ms, yielding an imaging rate of 7.4 frames/second. Whereas, CellLight, which is not as bright as LysoTracker, required an exposure time of 100 ms, thereby providing an imaging rate of 5.2 frames/second.

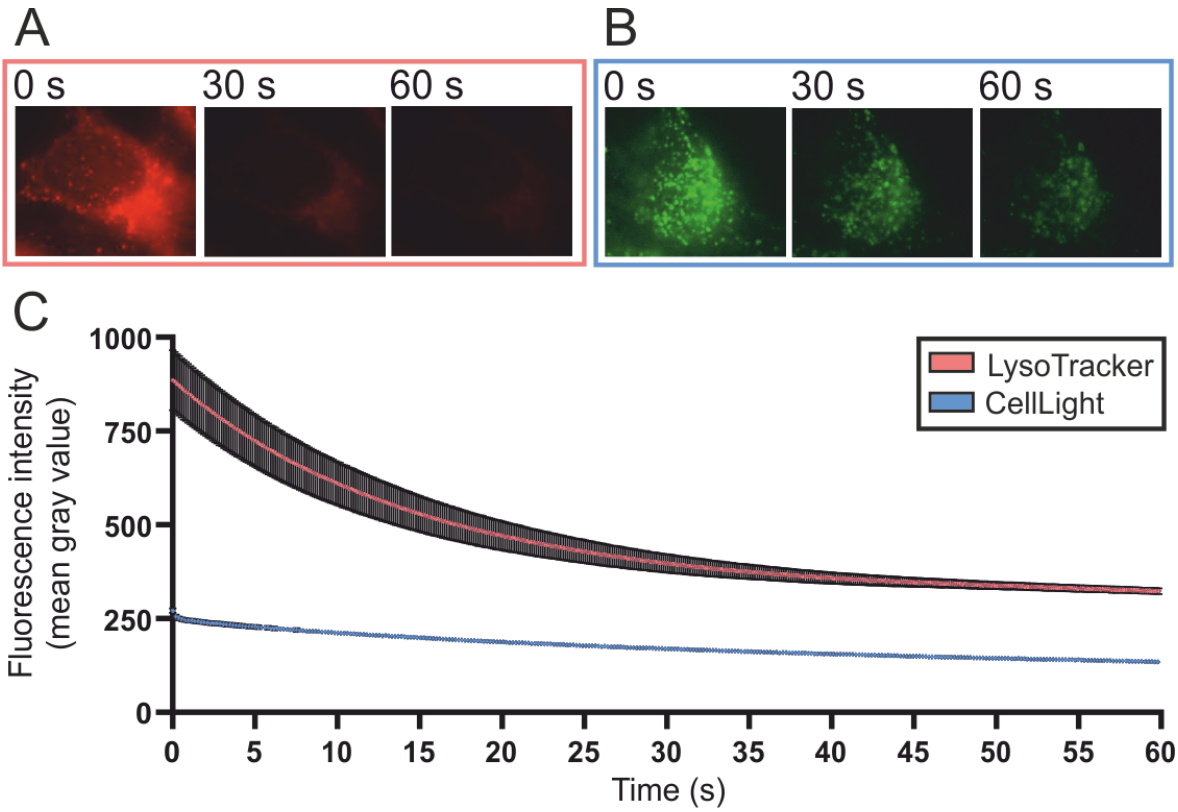


**Figure 17. Photobleaching of LysoTracker (red) and CellLight-GFP during 60 seconds of rapid imaging.** HeLa cells were imaged for 60 seconds using the minimised system settings for fastest possible recording. (A) LysoTracker fluorescence (B) CellLight fluorescence shown at 0 seconds, 30 seconds (and 60 seconds. (C) The plotted data are presented as average fluorescence intensity (mean gray value) over time, with error bars ±S.E.M. and n = 3 cells.

The data presented in Figure 11 show cell images and fluorescence intensity prior to background subtraction using the rolling ball method. Therefore, to appropriately capture the photobleaching of the probes solely localised to lysosomes, the mean fluorescence of the rolling ball-processed images was plotted in Figure 18. As expected, the signal of both probes reduced dramatically when background fluorescence was subtracted from the mean gray value. The photobleaching of LysoTracker was less pronounced in the background-subtracted images, but LysoTracker continued to have a distinct drop in fluorescence in the first 20 seconds of imaging. With the background removed, this analysis represented the fluorescence of the vesicles and confirmed that there was still an initial decrease in fluorescence associated with LysoTracker. However, the fluorescence intensity of the LysoTracker and CellLight vesicles was closer in Figure 18 than in Figure 17 in which the background fluorescence was included, consistent with the data presented in Figure 9. The significant drop in signal following the rolling ball processing indicates how necessary it is to perform background correction on fluorescence images.

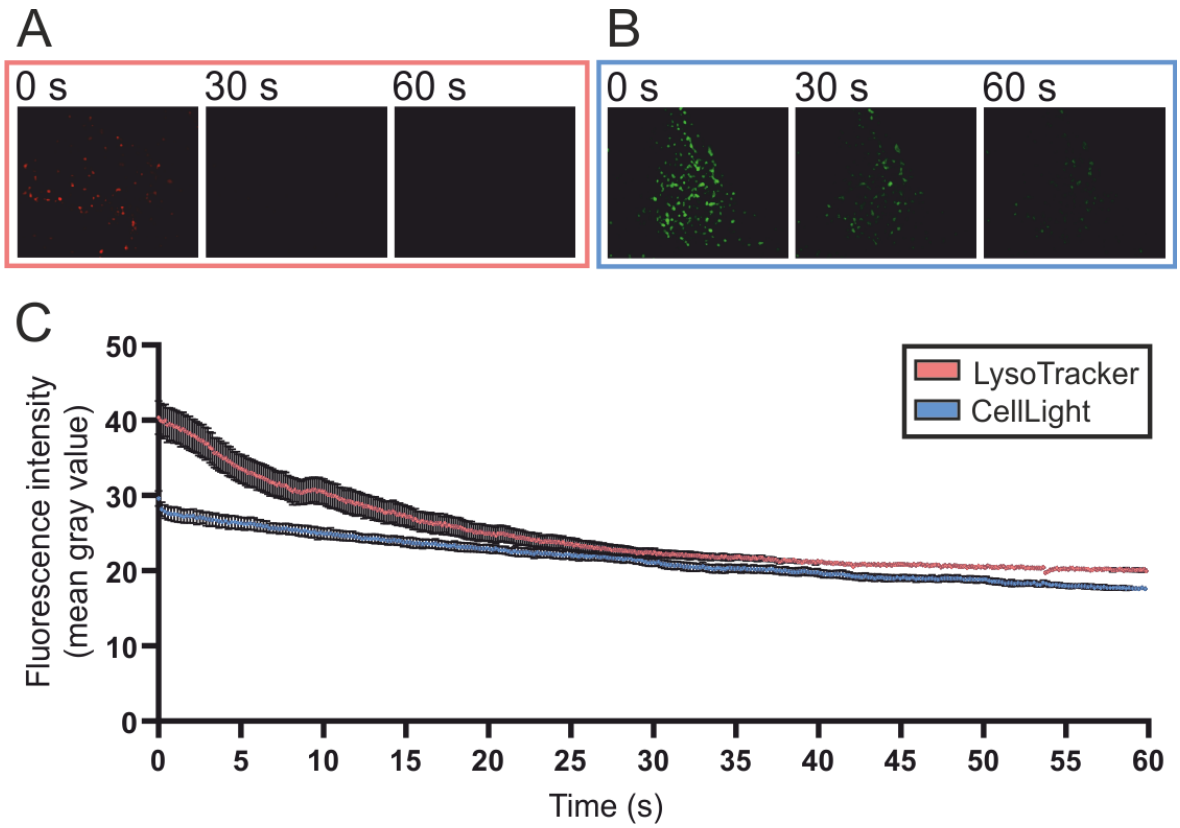


**Figure 18. Photobleaching of LysoTracker (red) and CellLight-GFP during 60 seconds of rapid imaging, calculated from background-subtracted image series.** HeLa cells were imaged for 60 seconds using the minimised system settings for fastest possible recording. Data presented as average intensity (mean gray value) error bars ±S.E.M. where n = 3 cells.

### 3.3.6 Summary of results

- LysoTracker can be used to label lysosomes as per manufacturer's instructions, but CellLight indicators require cell-specific method refinement for successful transduction (Figure 7, Table 9 and Table 10).
- Lysotracker and CellLight probes show significant cellular co-localisation with endogenous LAMP2 (Figure 11, Figure 12 and Figure 13).
- The availability of Lysotracker and CellLight probes with different excitation and emission wavelengths allow for multiplexed experiments (Figure 9, Figure 11 and Figure 12).
- The lysosomal probes show variable levels of bleed through. They were all brighter in the expected red or green imaging channel, but also show signals in the empty channel (Figure 8 and Figure 9).
- The red-shifted indicators show the highest amounts of bleed through (Figure 8, Figure 9 and Figure 13).

- There are significant levels of background signal when using any of the lysosomal probes (Figure 17 and Figure 18).
- Rolling ball subtraction can be used to minimise background (Figure 9), whilst preserving lysosome fluorescence (Figure 14, Figure 15 and Figure 18).
- Despite rolling ball background subtraction there is an uneven distribution of background pixels observed with CellLight probes compared to LysoTracker (Figure 16).
- Under the imaging conditions used in this study, the CellLight and LysoTracker probes displayed photobleaching with half-times in minutes (Figure 18).

Overall, the results showed that LysoTracker and CellLight probes were comparable to the 'gold standard' of lysosome immunostaining with the LAMP2 antibody. Therefore, it could be inferred that LysoTracker and CellLight are both specific probes for lysosomes and appropriate for use in lysosome assays. However, the differing quality of the images and challenges such as fluorescence bleed-through and photobleaching, meant that the choice of probe was best weighed up against the requirements of the imaging experiment (Table 13).

**Table 13. Summary of properties of lysosome probes.** LysoTracker Green and Red, CellLight green and red, and anti-LAMP2 antibody with red secondary antibody.

| | | LysoTracker | | CellLight | | Antibody |
|---|---|---|---|---|---|---|
| | | Green | Red | Green | Red | Red |
| **Specificity** Figure 13 | Good | ✓ | ✓ | ✓ | ✓ | ✓ |
| | Poor | | | | | |
| **Loading/imaging Figure 7** | Live | ✓ | ✓ | ✓ | ✓ | |
| | Fixed | | | ✓ | ✓ | |
| | Permeabilised | | | ✓ | ✓ | ✓ |
| **Distribution** Figure 11 | All cells | ✓ | ✓ | | | ✓ |
| | Sub-population | | | ✓ | ✓ | |
| **Signal intensity** Figure 8, Figure 9 | Good | ✓ | ✓ | ✓ | | ✓ |
| | Poor | | | | ✓ | |
| **Background signal/clarity** Figure 9 | Good | ✓ | ✓ | | | |
| | Poor | | | ✓ | ✓ | ✓ |
| **Bleed-through** Figure 8, Figure 9, Figure 13 | Good | ✓ | | ✓ | ✓ | |
| | Poor | | ✓ | | | ✓ |
| **Photostability** Figure 17, Figure 18 | Good | | | ✓ | ✓ | N/A |
| | Poor | ✓ | ✓ | | | |

## 3.4 Discussion

### 3.4.1 Lysosome probes for fluorescence microscopy

The first aim of this chapter was 'to identify a specific probe for imaging of lysosomes in living cells.' The probes were LysoTracker and CellLight, which were suitable for use in live cells (7). The third probe was the anti-LAMP2 antibody, used to immunostain for lysosomes using a fluorescently tagged secondary antibody. The immunostaining of LAMP2 is a highly specific means of labelling lysosomes and therefore this was used as a comparison to validate the localisation of the live cell indicators.

According to the manufacturer, LysoTracker accumulates within lysosomes and fluoresces at the distinctive low pH of lysosomes in cells. The LysoTracker probes are loaded into live cells and suffered a disruption to fluorescence upon fixation, followed by a loss of signal upon membrane permeabilisation. Conversely, the immunostaining of LAMP2 requires fixation and permeabilisation of cells and therefore this could not be compared directly to LysoTracker as fluorescence of the latter would be lost during the immunostaining protocol.

Live cells transduced with CellLight express Lysosome Associated Membrane Protein 1 (LAMP1) tagged with a fluorescent marker. Unlike LysoTracker which was detrimentally affected by fixation and permeabilisation, the CellLight fluorescent marker was expressed as a protein and did not disperse after permeabilisation. Therefore, CellLight was suitable for co-labelling with either LysoTracker or anti-LAMP2 antibody staining, and this presented an opportunity to compare the localisation of lysosome signal across multiple probes.

The use of LysoTracker, CellLight and the LAMP2 antibody enabled a robust comparison of three different methods of lysosome staining. However, before the co-localisation experiments were conducted, it was important to ensure that each indicator was performing correctly, and labelling vesicles as accurately and completely as could be achieved with the protocol.

#### *3.4.1.1 Optimisation of CellLight™ Lysosomes-GFP and -RFP, BacMam 2.0*

Although CellLight was a useful probe in terms of versatility, its use was not immediately straightforward. The first attempt to express CellLight resulted in no visible signal. While the second attempt (with a greater number of particles) resulted in a small cluster of extremely bright cells while the rest of the coverslip remained unaffected. Therefore, CellLight was subject to a systematic, qualitative assessment until suitable fluorescence was achieved. The four manufacturer-recommended parameters for optimisation of CellLight transduction in each cell line (concentration, seeding density, volume of medium and incubation time) were crucial. Additionally, the observed poor distribution of transduced cells on the coverslip meant that a further shaking

step was tested. The optimisation of CellLight was achieved through careful variation of each of the parameters to address the issues of poor signal and low number of cells transduced.

The poor distribution of transduced cells was observed as a cluster of cells on the coverslip were transduced, while the majority beyond this cluster had no detectable fluorescent signal. The CellLight solution was handled carefully and mixed carefully with gentle pipetting rather than a vortex mixer, to avoid damage to the particles. It was possible that the particles were therefore not well distributed if they settled in the solution which was prepared before removing the plates from the incubator. The additional steps taken to either shake or tap the plate resulted in a wider spread of fluorescent cells on the coverslip, suggesting an improvement to the distribution of particles. Gently tapping the plate for 2-3 minutes was sufficient improve distribution.

In parallel, the number of particles and incubation time were assessed within the range described in

Table 8. The number of particles was calculated (x µl per 1,000 cells) with the number of cells estimated based on the initial seeding density and appearance of confluency. By increasing the number of particles, the intensity of the signal increased but this had a cloudy appearance with poor clarity of vesicles (as shown in Figure 7). In comparison, extension of the incubation time resulted in a greater intensity of signal with a lower number of particles and most crucially an improved clarity of vesicle signal. The incubation time was comprised of two parts: (1) addition of particles in medium for uptake into the cells and, (2) incubation in fresh medium after particle addition for protein expression. Ultimately the strongest and clearest signal was achieved 48 hours from particle addition, with the particles removed after the first 16 hours.

Although the optimisation steps improved the quality of the signal and number of cells transduced, CellLight did not achieve 100% transduction (Figure 11). Consequently, there were fewer cells available for analysis compared to LysoTracker or antibody staining which was present in all cells on the coverslip. For any experiment quantifying a population of cells, the limitation of CellLight would be considerable. However, for experiments in which a single cell was analysed in detail (such as the tracking of lysosome movement, described in Chapters 4 and 5) the number of transduced cells was of less consequence for analysis.

Regardless, the selectivity of cells based on their effective transduction introduced a potential selection bias to the experimental sample. Additionally, exposure to the baculovirus particles, or LAMP1-GFP or -RFP expression within the cell may have had potentially induced unknown effects which would have added a possible confounding variable to the data. For analysis of LysoTracker images, cells were typically selected based on brightfield images to avoid any bias in choosing either a region to image or a cell to analyse. This was not possible with CellLight images, as not all cells were positive and therefore the cells had to be selected based on those which were expressing CellLight.

### 3.4.2 Lysosome probe signal and specificity for lysosomes (co-localisation)

Working with fluorescent probes, the signal is expected to be visible at distinct wavelengths depending on the fluorophore, such as GFP (488/510 nm) in the green channel and RFP (555/584 nm) in the red channel of the microscope. However, as with all fluorescence probes, there is a risk of florescence bleed through beyond the wavelengths specified into additional channels. Furthermore, some of the processing such as the immunostaining and mounting of coverslips, may have introduced additional background fluorescence. This bleed through has implications for analysis being conducted with co-loaded probes, such as the co-localisation analysis.

The co-localisation of the probes was assessed within the constraints of the loading and imaging conditions for each probe (live, fixed, or fixed and permeabilised). The comparisons were: LysoTracker/CellLight and CellLight/LAMP2 immunostaining. Imaging of the paired probes was

achieved through selection of fluorophores of distinct excitation and emission wavelengths; to be detected by the green and red channels separately. The co-localisation analysis of this paired loading could have been influenced by any signal bleed through. Therefore, it was important to confirm that the co-localisation was not a result of signal bleed through.

When the probes were imaged individually, the fluorescence of each one was far greater in the channel corresponding to their expected wavelength than in the empty channel, as shown in Figure 9. When assessing the fluorescent signal outside of the expected channel, the greatest signal was found in the green channel after immunostaining LAMP2 and a red secondary antibody. This was illustrated in Figure 8 in which a uniformly higher background cell fluorescence can be seen in the green channel; suggesting that there was background interference rather than a distinct bleed-through of the lysosome signal specifically.

The co-localisation of vesicles labelled with the LAMP2 antibody only in Figure 13 had a higher value than expected if there was no fluorescence in the green channel. However, this was still significantly lower than the co-localisation of vesicles labelled with both CellLight green and the LAMP2-antibody.

Similarly, there was an unexpected signal detected in the green channel when LysoTracker red was loaded individually (Figure 8). However, unlike the LAMP2 immunostaining, the fluorescence had a clear punctate staining which indicated bleed-through rather than a fluorescent cell background. The bleed-through was not reflected in the quantification of fluorescence intensity (Figure 9) due to the relatively low signal, however the calculation of co-localisation calculation is not based on intensity of signal, but location. Therefore, the effect of bleed-through was present in the co-localisation analysis, which showed a greater co-localisation of LysoTracker red to the green channel than expected from the individually loaded control (Figure 13). In comparison, the green version of LysoTracker and both CellLight probes had very low co-localisation to the other channels when loaded individually, which suggested minimal bleed-through and reliability in the co-localisation analysis.

In addition to acting as a control for the co-localisation, the signal bleed-through was an important finding by itself. For experiments utilising the co-loading of lysosome probes, LysoTracker red and anti-LAMP2 antibody staining would have needed to be used with utmost caution, or ideally swapped for LysoTracker green or either of the CellLight probes. However, where lysosome probes were imaged only in a single channel, the fluorescence beyond this wavelength would not influence the data.

Ultimately, these controls showed that there was some bleed through associated with LysoTracker red and a high background associated with immunostaining of LAMP2, but the resulting co-

localisation was still significantly lower than when the vesicles were co-labelled with multiple probes. Furthermore, the LysoTracker green and the CellLight probes did not have any evidence of bleed-through or other fluorescence outside of the expected channel. Therefore, it was still possible to use these probes in combination to assess the co-localisation and therefore indicate the specificity of labelling achieved with each one.

The was a high co-localisation of labelling when the composite images of co-loaded probes were quantified (Pearson's co-efficient, Figure 12), which suggested that the probes were predominantly labelling the same population of vesicles within the cells. The vesicles were expected to be lysosomes based on the similarity of staining across all methods of labelling: pH dependent loading, LAMP1 expression and particularly the LAMP2 antibody staining.

Despite the positive identification of the vesicles as lysosomes, some may be late endosomes due to the similarity of structure and protein composition of these vesicles. Hereafter, "lysosomes" refers to the vesicles positively identified by lysosome probes, with reasonable confidence that the population is representative of lysosomes but may include some late endosomes.

### 3.4.3 Characterisation of lysosome probes for live cell imaging experiments

As the probes were determined to be lysosome-specific, the next aim of this chapter was 'to characterise the specific lysosome probes for their use in live cell imaging experiments.'

The characterisation comprised of a number of parameters connected to the quality of the images obtained and their appropriateness for analysis in accordance with the requirements of the imaging experiments. The capacity for bleed-through has already been discussed in the context of co-localisation analysis. Additional parameters for the quality of LysoTracker and CellLight labelling included the extent and uniformity of background fluorescence and the photostability of the lysosome signal.

### 3.4.4 Quality of fluorescence background

Ideally, lysosome images should have a bright and clear signal localised to the lysosomes with the rest of the image displaying a minimal, uniform background in the cell and extracellular spaces. However, the use of fluorescent probes generally comes with a risk of obtaining background signal within the images. Background signal can be present for various reasons, such as autofluorescence in the cells, fluorescent interference from the buffer or accumulation of unbound indicator in the cell.

A powerful tool for the removal of background from images of cells labelled with lysosome probes is 'Subtract Background' in ImageJ, utilising the 'rolling ball radius' method of image processing. When the rolling ball radius set to 5 pixels, Subtract Background removes areas of fluorescence

larger than lysosomes (as shown in Figure 14) from the background without affecting lysosome signal.

To investigate the quality of the images of LysoTracker or CellLight labelled cells, a small study of lysosome fluorescence compared to background fluorescence (after background subtraction) was carried out with LysoTracker red and CellLight green, plotted in Figure 15. The background fluorescence was significantly lower than the indicator in both cases, as expected. Comparing the background of the images of each probe directly, there was a significantly higher fluorescence associated with CellLight, but again this was still relatively low.

As well as the overall intensity of the signal, the uniformity of any background florescence was important to consider, particularly when running automated methods of analysis. While the background may have appeared similar on the screen to the human eye, there was a possibility that images analysis tools within ImageJ may have picked up on a more subtle variation. The difference in apparently similar images was illustrated in Figure 16, which showed that increasing the contrast revealed a different variability in the background of LysoTracker and CellLight images. The plotted profile illustrated the relative difference between the background of these two indicators.

Manual image analysis carried out by a person would require vesicles to be bright enough to identify by eye, but the mean gray value across the image would not need to be viewable on screen for an algorithm to detect shapes. Therefore, there is a risk that an algorithm may segment non-lysosome regions in cases where the background is particularly noisy. This was further explored in Chapter 4, in relation to segmentation and tracking of lysosomes throughout time series imaging.

### 3.4.5 Photostability of fluorescent lysosome indicators during imaging

The photostability of the signal was the final criteria for the lysosome probes examined in this chapter, as a comparison between LysoTracker and CellLight for live cell imaging.

An analysis of photobleaching as change in fluorescence intensity (mean gray value) over time, set out in Figure 17 showed that LysoTracker had a higher initial signal which rapidly reduced within the first 10-15 seconds of continuous imaging. Conversely, the signal from CellLight was lower but remained more stable for the duration of imaging. This initial analysis took into account the images as a whole, including any background within the cells. As shown in the example images in Figure 17, many of the cells had a cloudy background which would have increased the fluorescence quantified and may have been subject to a different rate of photobleaching to the labelled lysosomes.

To accurately represent photobleaching of lysosome fluorescence rather than background, the intensity of the images was plotted after background subtraction in Figure 18. This analysis showed that the overall signal was reduced, as expected after the removal of background signal. Notably, LysoTracker was still subject to an initial drop in fluorescence but this appeared to be somewhat less pronounced and the signal from both LysoTracker and CellLight was more similar. This was most likely as when determining the exposure time on the microscope, the aim was for the lysosome fluorescence of LysoTracker and CellLight to have a reasonable clarity and intensity. The relevance of photobleaching and time series imaging was further investigated and discussed in relation to the segmentation and tracking of lysosomes in Chapter 5.

## 3.5 Conclusions

The results in this chapter provide valuable insight for the selection of an appropriate lysosome probe, based on the requirements of the experiment. Additionally, these data support the hypothesis that the lysosome probes have a high degree of overlap in labelling vesicles within a cell, which confirms that LysoTracker does specifically label lysosomes and late endosomes.

LysoTracker has the advantage of rapid loading, with no protein over-expression which could potentially influence normal cellular functions with unknown consequences. The LysoTracker signal was present in all cells, with a good clarity and uniform background which was removable with the use of Subtract Background. LysoTracker green did not have the bleed-through issue experienced with LysoTracker red, making it a useful tool for co-localisation experiments. However, the LysoTracker probes were rapidly photobleached during imaging and therefore may not be suitable for extended time series recordings. This is discussed further in Chapter 5.

CellLight was the most versatile for imaging under live or fixed and permeabilised cells. The probe was pH independent, with a good stability during imaging. Although CellLight red had a relatively weak signal compared to the other probes, CellLight green had a brighter signal and therefore could be imaged with a lower exposure time. Regardless of these benefits to CellLight, there were several limitations including the extended time of particle incubation prior to imaging (raising practical difficulties in maintaining an appropriate confluency during cell culture) and the limited number of cells expressing the labelled protein. Finally, the unknown consequence of protein overexpression in cells could influence the study of CLN3 disease in unpredictable way, particularly as the CLN3 protein is a lysosome membrane protein with its function and interactions still to be fully understood.

On the whole, LysoTracker and CellLight had distinct advantages and disadvantages, but both were specific for lysosomes and therefore could be reliably used for imaging experiments.

## 3.6 Future work

This chapter presented an assessment of lysosome probes which were selected to represent different methods of labelling lysosomes, in order to compare the specificity across the group. The natural expansion of this work would be the comparison of a greater number of probes, especially with the inclusion of any newly emerging technology which may become available.

LysoTracker was selected as a widely used live cell lysosome probe from one of the largest brands to represent the family of indicators which load by accumulation within lysosomes. Alternative products include: Cytopainter LysoOrange Indicator (ab138895) from Abcam and LysoBrite™ (22645) from AAT Bioquest. As these probes all label lysosomes through accumulation and pH gradient, they therefore had no immediately obvious advantage over the well-established LysoTracker probes. However, the subtle differences between these probes may have distinguished them in other ways and therefore may justify a further assessment in future. In particular, as observed with the different extent of bleed-through from LysoTracker green and red, the properties of the fluorophore can differ between probes.

The CellLight probe was chosen primarily for its versatility and lysosome labelling through expression of a lysosome membrane protein. Additionally, the relatively good safety profile of baculovirus makes this a more practical alternative than others such as adenovirus. Another option for lysosome staining is transfection to express a fluorescently tagged protein at the lysosome. All of these options would certainly be of interest for a more depth future analysis. However, it would be useful to determine that extent of any possible interference to normal lysosome function from transduction or transfection and this would need to be carefully considered before use in sensitive experiments.

Finally, antibodies can be used as a highly specific manner of labelling structures when immunostaining is carried out correctly. The LAMP2 antibody was selected for its specificity to Lysosome Membrane Associated Protein 2, a common marker for lysosomes alongside Lysosome Associated Membrane Protein 1 (LAMP1). An interesting future study would be the comparison of a number of antibodies targeting LAMP1 and LAMP2 from a range of sources and origins.

# 4 Development of an assay to analyse lysosomal positioning and movement

## 4.1 Introduction

Lysosomes are motile organelles that carry out numerous functions, as discussed in Chapter 1. The ability of lysosomes to move to new positions is directly linked to their function (Pu et al., 2016). The importance of analysing lysosomes in the study of CLN3 disease has already been discussed in Chapter 1. The importance of selecting an appropriate lysosome indicator for imaging experiments was discussed in Chapter 3.

The movement of lysosomes can be observed during live cell imaging, but quantification of this movement is not straightforward; especially with the aim of quantifying a large number of lysosomes with a high degree of accuracy. To achieve this aim, the quantification of lysosome movement required the following:

- **Segmentation**: identification of lysosomes within an image
- **Tracking**: plotting the location of each segmented lysosome on each frame
- **Calculation**: measuring the parameters of lysosome movement based on the location

### 4.1.1 Image Analysis and Quantification

There were several possible approaches for image analysis to obtain lysosome movement data, which were dependent upon the nature of the images and the parameters to be quantified. The images captured during the experiments discussed in this chapter included:

- **Single images** – allowing measurements such as number and size of lysosomes
- **Image sequences** (time series) – allowing tracking of lysosome movement over time

Based upon there being single images or image sequences, and the type of data to be quantified, there were a number of tools and plugins within ImageJ that presented options for the quantification. These tools allowed for manual, automated or combination approaches for analysis:

- **Manual analysis** - quantification carried out by a person (henceforth referred to as 'analyst'), such as visually identifying lysosomes in an image and counting the total number present.
- **Automated analysis** – repeatable, software-driven segmentation and measurement, in which there is minimal input from the analyst once the relevant settings were established.

For the lysosome analysis described in this chapter, even manual methods employed tools in ImageJ to improve speed and accuracy. However, these are still comparatively manual as the ultimate decision to identify, count or measure, a lysosome was determined by the analyst and not the software settings.

### 4.1.2 ImageJ plugins

The ImageJ plugin from MOSAIC, Particle Tracker 2D/3D, henceforth referred to as 'Particle Tracker' was used to track lysosome movement in an automated manner (Sbalzarini and Koumoutsakos, 2005). This was first introduced in Chapter 4, which detailed the settings and application of this plugin. The quality of the data was dependent upon good clarity of images to correctly segment lysosomes and the ability to track these segmented vesicles throughout each frame of a series.

**Aims and objectives**

**Aim 1: to quantify the number of regions of lysosomes in images of cells loaded with LysoTracker**

Objectives:

- Compare the manual (Cell Counter) and automated (Nucleus Counter) methods of lysosome counting

**Aim 2: to establish an assay to track lysosome movement in live cells**

Objectives:

- Determine whether the photobleaching of LysoTracker fluorescence affects the ability to track lysosomes over time
- Establish suitable imaging conditions for the cells, especially buffer and temperature
- Compare lysosome tracking with the Particle Tracker plugin to an alternative method to measure lysosome movement (Frame Overlay)
- Utilise the Frame Overlay method to measure movement of gross cell structures during imaging
- Assess the extent to which the cells move during imaging and how this movement might affect the measurement of lysosome movement

**Aim 3: to examine lysosome movement and quantify the plotted trajectories**

Objectives:

- Directly compare lysosomes with visually distinct 'long' and 'short' trajectories
- Quantify the lysosome movement to examine:
    - The movement frame-to-frame movement of lysosomes (sum of distance)
    - The total directional distance moved by a lysosome in the cell (maximum distance)

**Aim 4: to investigate nocodazole as a treatment to depolymerise microtubules**

Objectives:

- Confirm that nocodazole depolymerises microtubules using TubulinTracker labelling

## 4.2 Methods

### 4.2.1 Treatment and labelling of cells

This chapter details a number of experiments carried out using HeLa and fibroblast cell lines, which were cultured on glass coverslips using the methods described in Chapter 2. The buffers and solutions for imaging are detailed in and Table 14 and their formulations are given in Chapter 2.

The lysosome probes, LysoTracker and CellLight were used as previously discussed in Chapter 3. LysoTracker loading was carried out for the majority of these experiments. For the assessment of buffer temperature on lysosome movement, the cells were equilibrated at room temperature or 37°C in FluoroBrite DMEM or imaging buffer. The subsequent imaging experiments used FluoroBrite DMEM and all loading and imaging was carried out at 37°C. The maintenance of 37°C was ensured by using a cell culture incubator located close to the microscopes. The imaging chambers and solutions were warmed in the incubator prior to use to minimise any drop in temperature, and the coverslips with attached cells were incubated in the imaging chamber within the incubator during LysoTracker loading. After loading, the LysoTracker solution in the imaging chamber was exchanged with fresh warmed buffer and the imaging chamber immediately transferred from the incubator to the microscope in order to start an experiment. The microscope was already set to the approximate z-location for imaging so minimal focusing was required and imaging was completed in less than 3 minutes (30 s per region x 5 regions = 2.5 minutes).

To transduce the cells with CellLight, the particles were incorporated into the cell culture medium surrounding the cells for 8 hours. The medium was exchanged to remove the particles and the cells were incubated for a further 48 hours to ensure that expression was achieved. The coverslips on which CellLight-expressing cells were growing were subsequently removed from the plates and placed in imaging chambers with care to avoid exposure to light. Apart from the viral transduction procedure, the cells were treated in the same manner as those loaded with LysoTracker.

The methods for the loading of each indicator are briefly summarised in Table 14. Full details of the methods, including the preparation of stock solutions, are available in Chapter 2. For the cell movement experiments, the probes WGA and Hoechst were used to label cell membranes and nuclei respectively. Finally, Tubulin Tracker was used to label microtubules.

**Table 14. Methods for the labelling and treatment of cells.**

| Probe/Treatment | Conditions for cell loading or treatment |
|---|---|
| LysoTracker | 50 nM (1 in 10000 dilution) in FluoroBrite DMEM for 30 minutes |
| CellLight | 2.5 µl (1x$10^8$/ml) for 8 hours in GlutaMAX DMEM at 37°C and 48 hour incubation at 37°C in fresh GlutaMAX DMEM |
| WGA | 1 in 200 dilution for 15 minutes at room temperature |
| Hoechst | 1 in 2000 dilution for 15 minutes at room temperature |
| Tubulin Tracker | 1 in 2000 dilution for 1 hour at room temperature |
| Nocodazole | 20 µm (1/1000 dilution) solution in FluoroBrite DMEM for 30 minutes |
| DMSO vehicle control | 1/1000 DMSO in FluoroBrite DMEM for 30 minutes |

For many of the lysosome movement experiments, cells were treated with nocodazole to depolymerise the microtubules. A solution containing either 20 µm nocodazole or DMSO was prepared in FluoroBrite DMEM and added to the cells for 30 minutes. Nocodazole was dissolved in DMSO to prepare the stock solution and therefore the DMSO vehicle control solution was prepared at 1 in 1000, to match the volume of DMSO in the nocodazole solution. After incubation, the control or nocodazole solutions were exchanged for Tubulin Tracker (Figure 45), or immediately fixed with 15 minutes in 4% PFA and mounted to slides with Vector Shield containing Phalloidin (Figure 46).

The imaging experiments described in this chapter all used the Leica DMI6000 fluorescence microscope and subsequent image analysis was carried out using ImageJ. Details of the specific plugins and image analysis methods are explained in full below.

### 4.2.2 Image analysis and quantification

The methods for counting and measuring lysosomes are set out in Figure 19. The 'Cell Counter' method refers to the visual identification of each lysosome in an image by the analyst, while the 'Nucleus Counter' method refers to the software-driven segmentation of lysosomes within an image. Despite their names, these plugins were not used specifically for cells or nuclei in this study. Rather, the Nucleus Counter methods was calibrated to 5 to 100 pixels in order to segment lysosomes in cells loaded with LysoTracker. Both of the counting methods were used in this chapter but in the subsequent data presented in Chapter 5, only the Nucleus Counter method was used.

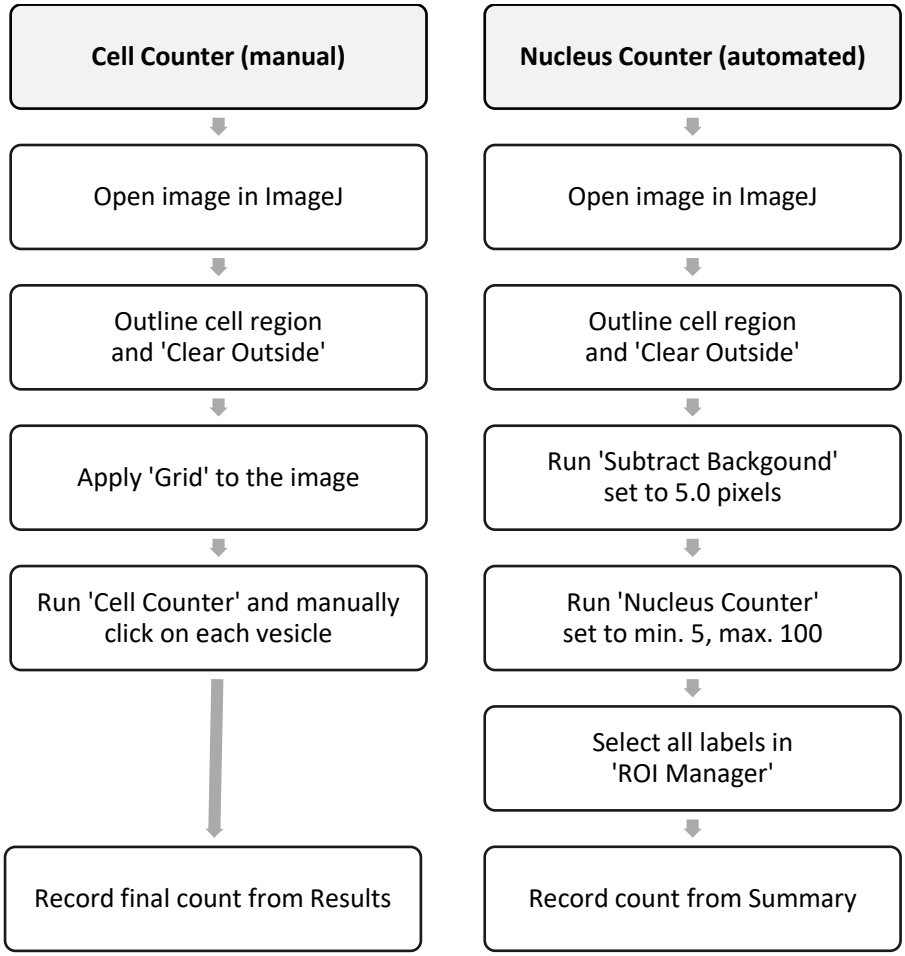


**Figure 19. The steps for manual and automated counting of vesicles using ImageJ plugins.**

### 4.2.3 Cell size (area, $\mu m^2$)

As each cell was measured on an individual basis, there was little advantage to the development of an automated analysis of cell size. Instead, the measurement of approximate cell size was carried out by drawing a line around the circumference of cells in ImageJ with the 'Freehand Selections' tool, shown as the yellow outline in Figure 20. The area ($\mu m^2$) of the outline was then measured and recorded.

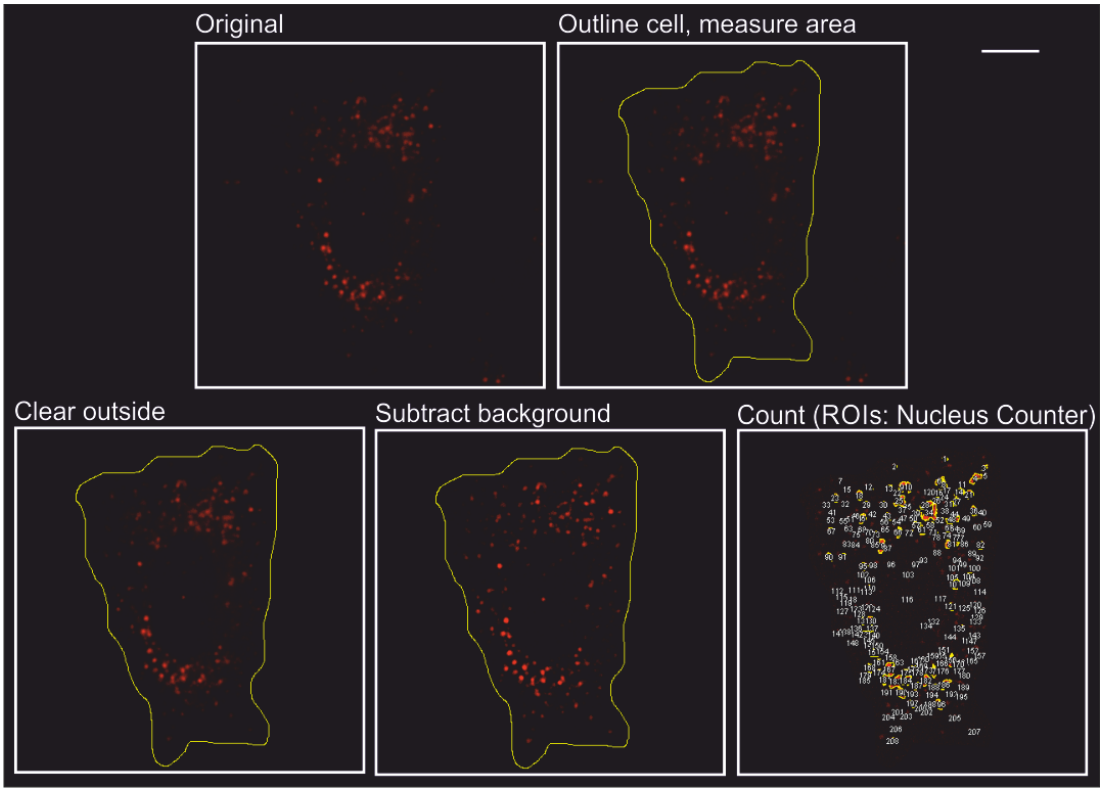


**Figure 20. Measurement of cell size, size of segmented lysosome regions and number of lysosome regions.** The cell area was measured using the 'Freehand Selections' tool (represented by the yellow outline in the images). 'Clear Outside' and 'Subtract Background' were applied to process the image before measurement with 'Nucleus Counter' with the results of segmentation shown in the Region of Interest (ROI) Manager. The scale bar is 10 µm.

### 4.2.4 Size (area, µm$^2$) and number of segmented lysosome regions

Following the measurement of cell size, the image was processed to clear the extracellular staining (particularly lysosomes in surrounding cells) and subtract the background, as shown in Figure 20. The automated measurement of size and number of segmented lysosome regions utilised the 'Nucleus Counter' method as set out in Figure 19. The ImageJ function 'Clear Outside' was used to remove staining beyond the cell outline, in surrounding cells. This limited the quantification of lysosomes to each cell individually. As described previously in Chapter 3, images were processed with 'Subtract Background' set to 5 pixels rolling ball radius in order to remove any background signal. Finally, the 'Nucleus Counter' plugin (set to 5 - 100 pixels) was used to segment the lysosomes, presenting data such as average lysosome area (µm$^2$) and number of segmented regions. Each of these steps is shown in Figure 20. The segmented regions were added to the ROI manager which could then apply labels to the image (shown in the final panel of Figure 20) which was useful to visually inspect and verify the segmentation.

### 4.2.5 Lysosome movement: Tracking

The analysis of lysosome movement was carried out by identification of lysosomes as described above, followed by tracking their frame to frame movement throughout a series of images taken at equal intervals. With the exception of Figure 24, all lysosome recordings were carried out with the most rapid achievable frame rate of 0.2 seconds per image, for 30 seconds in total. For the photobleaching experiment shown in Figure 24, the frame rates used are specified and the total imaging time was 60 seconds.

The two methods for analysis of lysosome movement are summarised in Figure 21. With the 'Frame Overlay' method, the fluorescence images at the start and end of the recording time (30 seconds) were duplicated, pseudo-coloured red and green, and merged. The contrasting red and green colours revealed two distinct borders when movement had occurred, with the distance between the two colours being measurable with the line tool in ImageJ. In contrast, the use of the Particle Tracker method allowed for lysosomes to be tracked as a continuous pathway ('trajectory') on a frame-by-frame basis throughout the recording. The stages for this method included processing the image (i.e. clear outside and subtract background) before running the Particle Tracker plugin to generate the tracking data.

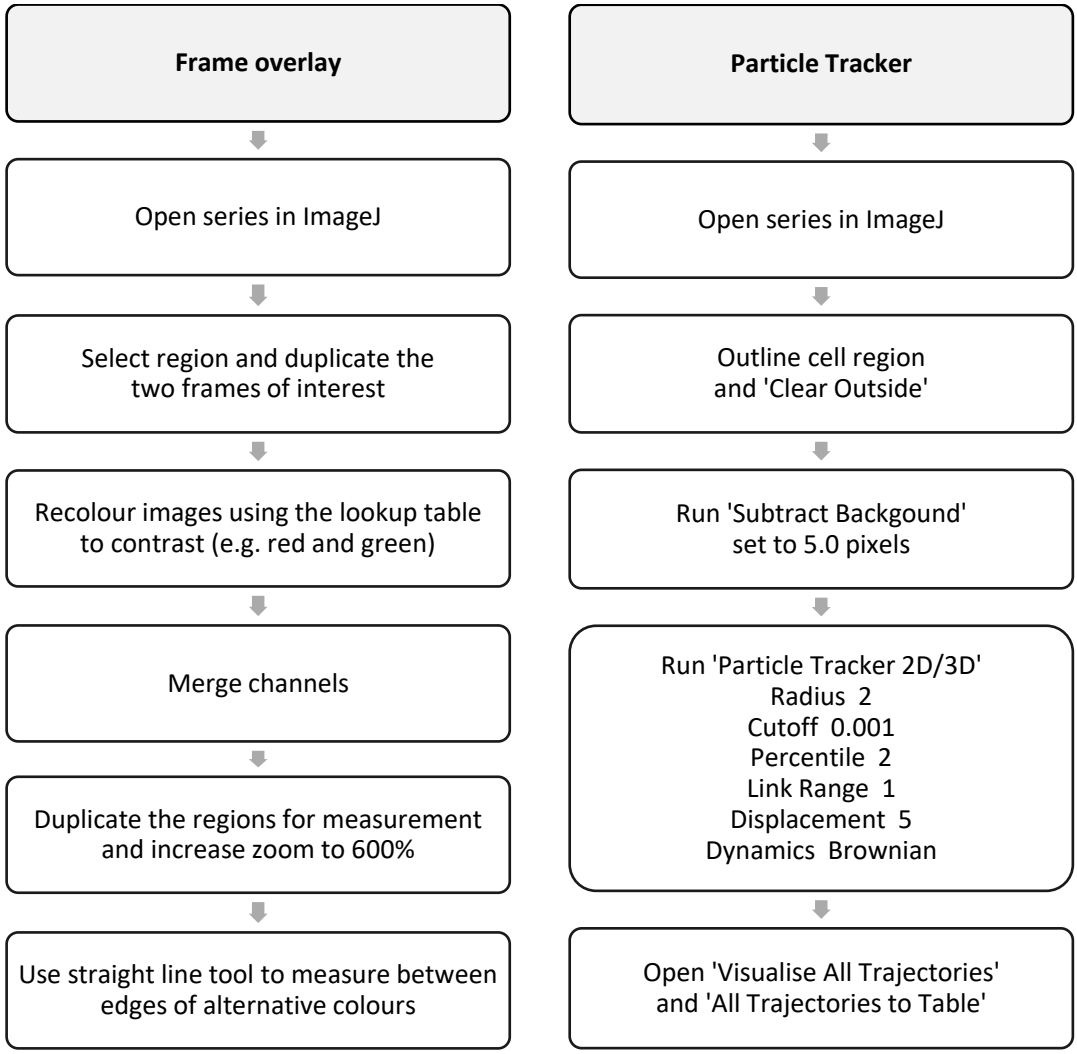


**Figure 21. 'Frame Overlay' and 'Particle Tracker' methods for lysosome tracking.**

The settings for Particle Tracker were selected using trial and error and constant cross-referencing with the 'visualise trajectories' output to ensure that lysosomes were optimally identified and tracked throughout a recording.

The lysosomes were identified in the image based on a combination of parameters:

- **Radius** - approximate size of lysosomes for detection (pixels)
- **Cutoff** - value calculated by the Particle Tracker algorithm to determine 'non-particles'
- **Percentile** - the fluorescence profile of the image was calculated as a percentile and the top 2% of brightest pixels appeared to capture lysosome fluorescence well following background subtraction

The settings related to the tracking of lysosomes through subsequent images included:

- **Link Range** - the number of frames used to identify individual lysosomes based on their relative positions
- **Displacement** - the maximum expected distance moved by a particle between frames
- **Dynamics** - lysosome trajectories do not have a straight, linear path and therefore fit the Brownian motion dynamics

The results from Particle Tracker were presented as: (1) the 'visualised trajectories' illustrating each lysosome pathway within an image series and, (2) a data table with coordinates corresponding to each identified lysosome on each frame.

## 4.3 Results

### 4.3.1 Measurement of lysosomes with Nucleus Counter

The results in this section detail some preliminary work, establishing the quantification of vesicles in live cell images. The vesicles, in this case autophagosomes, were labelled with the Cyto-ID kit and represented structures of a similar size and shape to lysosomes. The analysis was carried out using neonatal rat ventricular myocytes (NRVMs).

The quantification of number of lysosomes was carried out using ImageJ. As previously described, the Cell Counter method was based upon a manual count of lysosomes while the Nucleus Counter method utilised an automated software-driven segmentation and quantification.

To assess the manual method in detail, five images of vesicles (labelled with CytoID) were duplicated and analysed three times by two different people, as shown in Figure 22A. The comparison revealed that there was some variation in the count of the same image by the same analyst and that between analysts there was a difference in the count of Image E, but this was not significant overall. This represents the degree of human error which is associated with manual measurement. A number of factors could contribute to variation from a single analyst, such as the length of time spent on the task and the environment which could introduce variables of tiredness and distraction. Additionally, while automated analysis of images takes into account their numerical values such as pixel intensity, the display visible to an analyst was partially dependent on the screen display. This was represented in Figure 22B, in which the spread of data can be seen to vary from image to image with repeats on three different display screens. Even when the same screen was used by the same analyst, there was some variable, which may be attributed to human error as previously stated. However, another consideration may be that each individual screen could be influenced by different lighting. For example, at different times of day or dependent on weather, such as sunlight through an adjacent window, which may create glare.

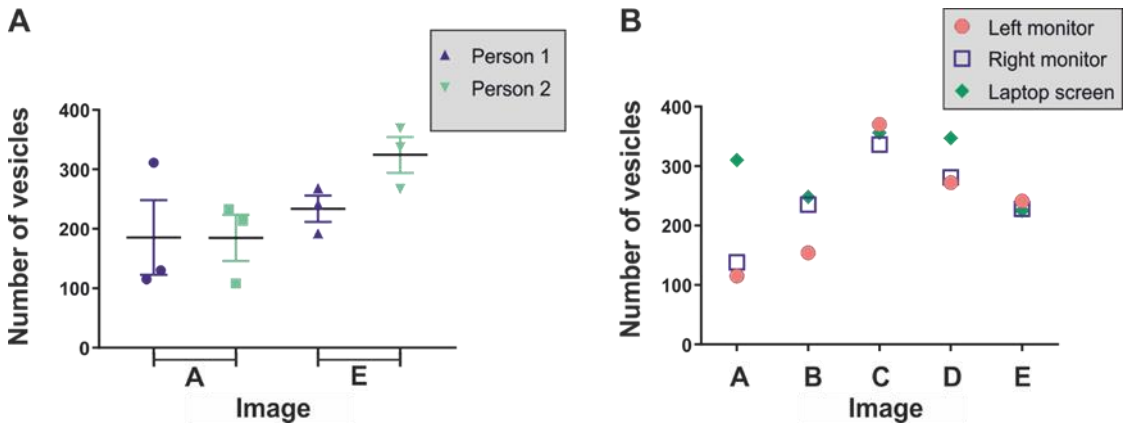


**Figure 22**. **Comparison of the results of manual vesicles counting**. Autophagosomes in NRVMs were labelled with CytoID and imaged using the fluorescence microscope. (A) The number of vesicles in two images (A and E) counted three times by two different analysts (Person 1 and Person 2). These data were analysed with an unpaired t-test and n = 3 counts per person, per image. (B) Scatter plot to show replicates of 5 images (A – E) counted 3 times on different display screens.

The manual and automated methods of vesicle counting were compared directly: the manual count was an average of three analysts and the automated count was carried out using Nucleus Counter. There was no significant difference between these methods, suggesting that on average the data from either manual or automated analysis was reliable.

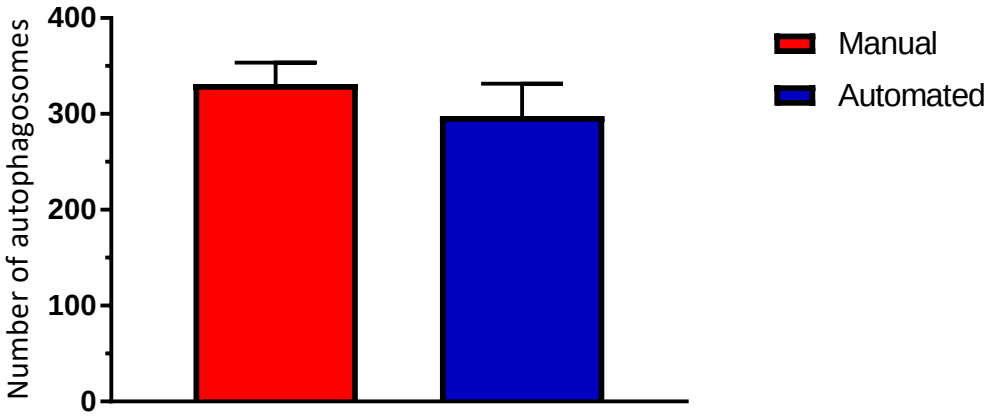


**Figure 23. Number of autophagosomes counted manually and using automated analysis in NRVMs loaded with Cyto ID.** These data are presented as a mean ±S.E.M. and show no statistically significant difference when using an unpaired t-test. n = 5 regions on 5 coverslips. The replicates of the manual counting were carried out by three separate analysts.

The analysis presented in Figure 22 and Figure 23, in which NRVMs were labelled with CytoID, was not further developed in this thesis. The NRVMs were not used as a cell model for further study, nor was CytoID used in additional experiments. However, these data present an assessment of the methods of vesicle counting which are applicable to the measurement of lysosomes in other cell types. The use of the automated Nucleus Counter method had a number of clear advantages over the manual Cell Counter method, although the result of the count was comparable between the methods indicating a reasonable level of accuracy applicable to both. Regardless, the Nucleus Counter method was more rapid and enabled a measurement of the area of each segmented region in addition to the total number. Therefore, Chapter 5 details the results of analysis carried out using the automated Nucleus Counter method.

### 4.3.2 Tracking and analysis of lysosomes with Particle Tracker

#### *4.3.2.1 Particle Tracker settings*

As set out in Chapter 3, the careful selection of lysosome probes was important in the planning of imaging experiments to ensure that high quality images could be obtained for appropriate analysis. For the experiments investigating lysosome movement, live cells loaded with a lysosome probe were imaged rapidly to create a time series. The clarity of LysoTracker signal and ability to label lysosomes without protein over-expression made it a strong candidate for use in the tracking experiments. However, the photobleaching of LysoTracker (Chapter 3) could have a detrimental effect on the tracking.

To test whether photobleaching influenced the data obtained using Particle Tracker, fibroblast cells were loaded with LysoTracker and imaged for 60 seconds. The imaging was caried out at the three frame rates set out in Table 15, which also illustrates the number of images recorded and the number of frames when reduced to half the total number in the series, which is applicable to the analysis in Figure 24C. The ‘reduced frames’ were essentially the removal of every other frame in an image sequence. This removal of frames was used as a way of seeing whether Particle Tracker could follow lysosome trajectories in situations where part of the movement profile was missing.

**Table 15. Imaging speed and number of images per 60 seconds (s) recording.**

| Frame rate (time per image; s) | Number of images recorded in 60 s | Number of frames taken from an image sequence (half) |
|---|---|---|
| 0.2 | 303 | 152 |
| 0.5 | 120 | 60 |
| 1.0 | 60 | 30 |

The most rapid recording rate achievable was 0.2 s per image, due to the limiting factors of exposure time and microscope hardware. 1.0 s represented relatively slow imaging and therefore slower photobleaching, as shown in the panels of Figure 24A. The influence of the frame rate on photobleaching is shown in Figure 24A, in which the rapid imaging of 0.2 s and 0.5 s per frame are associated with a visible loss of lysosome signal shown in the comparison of first and last frames in image sequences. However, with an rate of 1.0 s per image the lysosome signal was still evident in the images. The comparative effects of different imaging rates on photobleaching is depicted in Figure 24B, which shows a steep decline in fluorescence when imaging at 0.2 s or 0.5 s compared to 1.0 s.

To determine whether the photobleaching affected lysosome tracking, series of images recorded at each frame rate were measured using Particle Tracker. The image series were quantified by calculating the number of lysosomes identified in the first frame and the percentage of these organells that were sucessfully tracked throughout the 60 second imaging period (Figure 24C). As shown in Table 15, the imaging frame rate altered the number of images that were obtained within the 60 s imaging time. To detemine whether the number of frames in an image series had an impact on the tracking even number frames (2, 4, 6 etc.) were removed from a copy of the recordings to reduce the number of frames as described above, while retaining the photobleaching effect throughout the series. The quantificaton of lysosomes successfully tracked for each frame rate is shown in Figure 24C. Data obtained using the original image series with all frames (solid bar, 'all' frames) is plotted alongside the results seen with reduced frames (striped bar, 'half' number of frames). There was no significant difference in tracking with altered imaging speed, photobleaching or number of frames in an image series.

Therefore, the Particle Tracker was clearly able to continuously track lysosomes, even when the signal was significantly reduced by photobleaching. A large number of lysosomes were not tracked throughout all frames, but this was observed to be a result of events such as lysosomes passing in close proximity as previously discussed. The large numbers of lysosomes lost from the tracking was partially a consequence of the setup of the link range and displacement. In order to avoid incorrect

linking between neighbouring lysosomes and therefore an artificially elevated distance, the linking and displacement were set very low. The strict settings dramatically improved confidence in the measurements, but elevated the number of incompletely tracked lysosomes when the tracker was unable to link the frames in which a lysosome was temporarily lost.

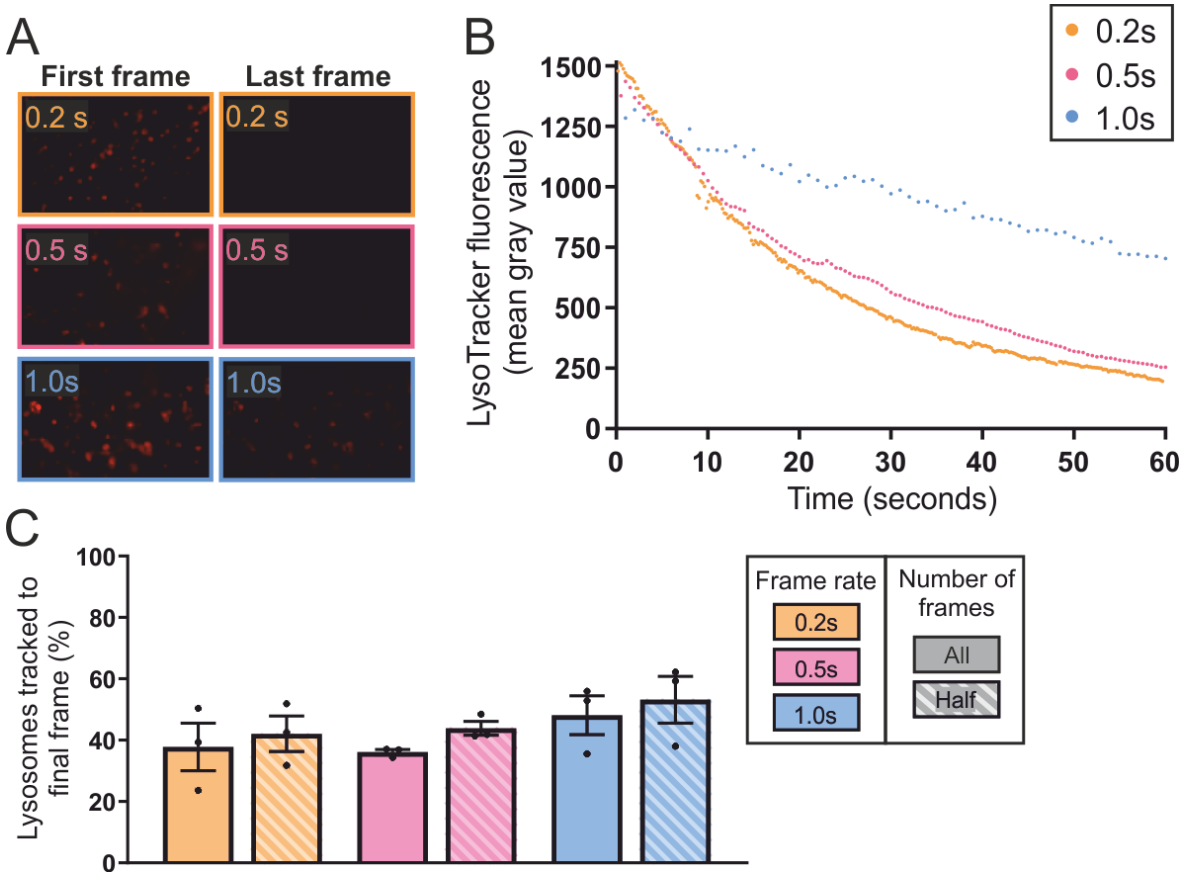


**Figure 24. Photobleaching, frame rate and particle tracking.** (A) The first and last frames of image series are shown to illustrate how imaging speed influenced photobleaching. LysoTracker images were acquired at 0.2, 0.5 and 1.0 seconds per frame over a 60-second imaging period. (B) The LysoTracker fluorescence intensity at each imaging speed was plotted over time. (C) The percentage of lysosomes tracked from first to last frame was plotted for each imaging frame rate, with tracking across all, or a reduced set, of the original frames. These data are plotted as mean ± S.E.M. and analysed with a Kruskal-Wallis test, with multiple comparisons.

The results shown in Figure 24 suggest that the photobleaching of LysoTracker did not compromise lyososme tracking in comparison to a condition with less photobleaching. Additionally, the speed of imaging and number of frames did not significantly influence the tracking outcome. Taken together, these findings indicate that LysoTracker is a suitable probe for labelling lysosomes in these experiments and that the most rapid imaging speed can be used.

As there was no apparent detriment to lysosome tracking caused by changing imaging frame rate, the photobleaching of LysoTracker was of apparently little consequence. Therefore, LysoTracker was selected for the bulk of lysosome tracking experiments in this study. Furthermore, with comparable tracking across multiple imaging speeds, the most rapid imaging rate (0.2 s/frame) was used in order to capture the maximum detail of lysosome movement. The ability of Particle Tracker to continually segment and track lysosomes despite the considerable loss of LysoTracker fluorescence meant that this plugin was well suited to the assay.

#### *4.3.2.2 Loading and imaging of lysosome movement: buffer and temperature*

The choice of lysosome probe was not the only consideration for the tracking assay setup. The use of LysoTracker meant that cells could be imaged within 30 minutes of removal from cell culture. However, even within 30 minutes it was possible that the change of environment could influence lysosome movement and affect the results of this sensitive assay, the choice of solution used for LysoTracker loading and imaging was investigated. The extracellular solutions used in this study were Imaging Buffer (IB) and FluoroBrite DMEM (FB) (each solution was formulated and supplemented as described in Chapter 2). IB was a simple pH buffered solution, while FB was a supplemented medium more comparable to the cell culture medium.

In addition to the formulation of the buffer, the effect of temperature was investigated. The optimum temperature for cell culture is 37°C, as maintained by cell culture incubators to mimic physiological body temperature. The room temperature (RT) of the laboratory was maintained at around 20°C. To assess whether there was an effect of temperature on lysosome movement, cells maintained at either RT or 37°C (as close as realistically possible) were recorded and analysed. Cells were incubated at RT, using buffer which had been equilibrated to RT, whilst others were incubated in the 37°C cell culture incubator located close to the microscopes in the imaging room. The analysis of lysosome movement in cells exposed to different conditions, i.e., combinations of buffer (IB or FB) and temperature (RT or 37°C), was plotted in Figure 25.

Initially, the distances travelled by lysosomes during imaging was plotted by percentile (i.e., plotting the distance moved by a lysosome versus its relative mobility in the whole population). Plotting lysosome movement by percentile allows visualisation of the proportions of lysosomes with different degrees of motility. As shown in Figure 25A, the majority of lysosomes moved only a small distance, which was similar between all temperature and buffer conditions below the top 25%. In the 25%, the data for lysosome movement in the different conditions began to deviate. These data were re-plotted on an expanded x-axis to illustrate the differences between the imaging conditions more clearly. The lysosome movement distance increased substantially in the top 25%, and a larger number of lysosomes moved a greater distance in the cells incubated at 37°C, compared to those

at RT. There were a greater number of lysosome movement trajectories with 'intermediate to long' distances in the cells incubated with FB, compared to cells incubated with IB in which the majority of trajectories were short with a sharp increase at around the top 5% to the longer trajectories.

The mean lysosome movement distances were plotted in a bar graph in Figure 25B, with all replicates shown as scatter points on each bar. As the vast spread of data masks the differences between the means, the bars were also plotted in Figure 25C, to show the comparison more clearly. Lysosomes in cells incubated at 37°C had a greater distance of travel in comparison to those incubated at RT. There was no significant difference in lysosome movement between the cells at 37°C when IB or FB was used. The average distance of lysosome movement was lowest in the cells in FB at RT, which was significantly lower than when IB was used at RT.

Overall, analysis of the mean lysosome movement (Figure 25C) showed a significant reduction in lysosome movement at RT compared to 37°C. While the buffer did not immediately impact the results at 37°C, there was a difference between them at RT. However, looking at the upper percentiles where the lysosome movement distances begin to deviate for each condition, it would appear that there are a greater number of lysosomes travelling further in the cells with FB at 37°C compared to IB.

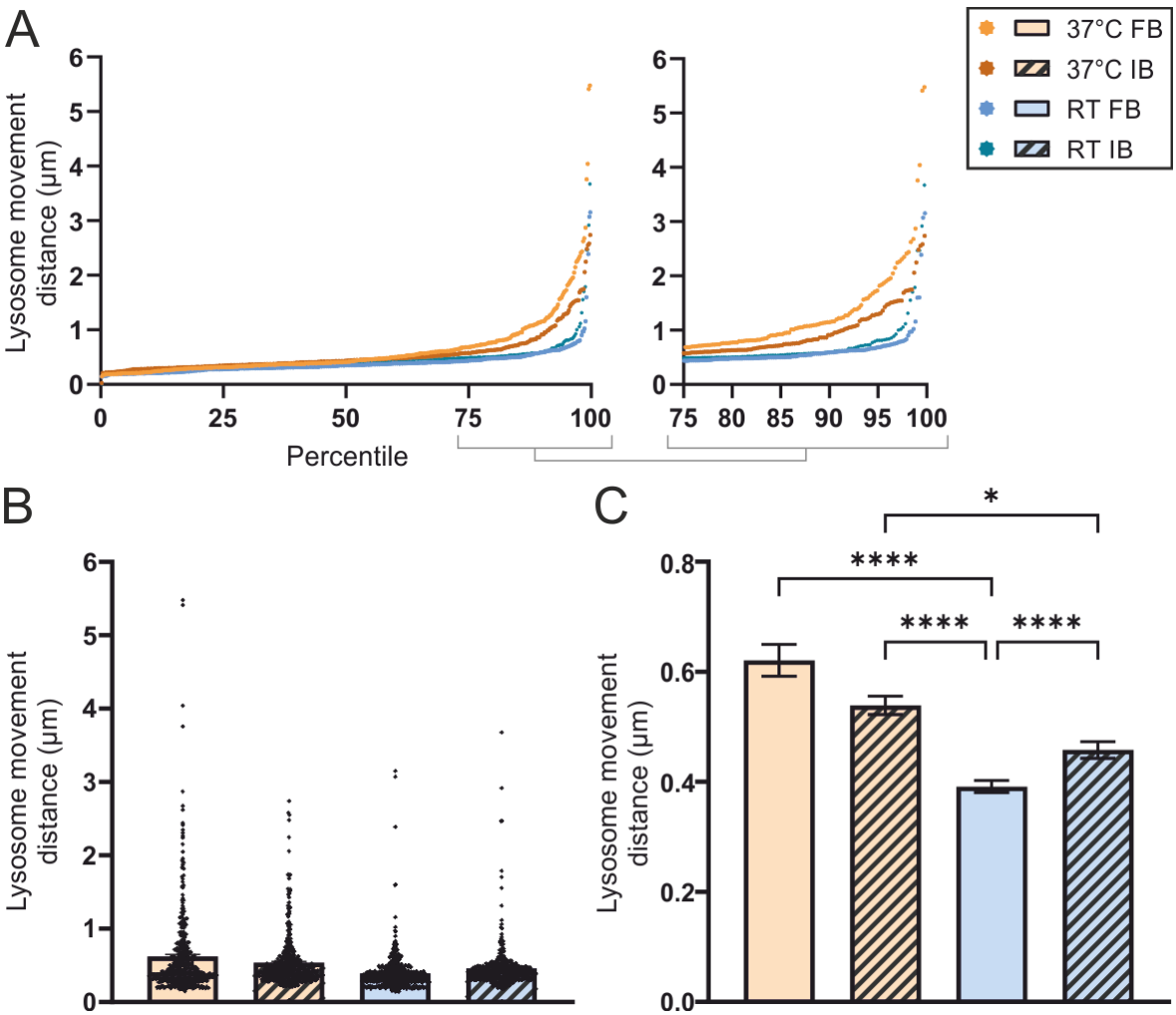


**Figure 25. Lysosome movement in fibroblasts equilibrated with different temperature and buffers.** The experimental temperature for imaging was 37°C or room temperature (RT) and buffer was either FluoroBrite DMEM (FB) or imaging buffer (IB). (A) Lysosome movement plotted by percentile of least to most distance covered. (B) All individual replicates plotted on the bars. (B) Bars without replicates to show relationship between means. All data were plotted as mean ± S.E.M. and analysed with Kruskal-Wallis test with multiple comparisons where * indicates $p \leq 0.05$, *** indicates $p \leq 0.001$ and **** indicates $p \leq 0.0001$. n = 470 ± 55 lysosomes from 5 cells per condition.

With the greatest difference in distance travelled by lysosomes occurring between the upper percentiles of the data (Figure 25A), the lysosomes falling into the top 25% of movement were analysed separately, as shown in Figure 26. The individual data points plotted in Figure 26A illustrated the spread of lysosome movement distances within the top 25% most motile lysosomes, and highlighted the pattern as seen in the percentile plots of Figure 25. As expected, analysis of these data taken from the top 25% most motile organelles of each dataset presented a more

pronounced statistical difference in lysosome movement between the imaging conditions, especially the effect of temperature. However, a surprising outcome was the loss of significance in lysosome movement between the two datasets at RT, which indicated that the difference in lysosome movement from these cells lay in the lower lysosome movement percentiles of the dataset. These analyses illustrate that lysosomes travelling a greater distance were more common in cells at 37°C, with FB as the buffer of choice for loading and imaging. For all subsequent experiments, the buffer of choice was FluoroBrite, cells were incubated at 37°C, and care was taken to ensure that imaging was carried out to avoid any effects of cooling.

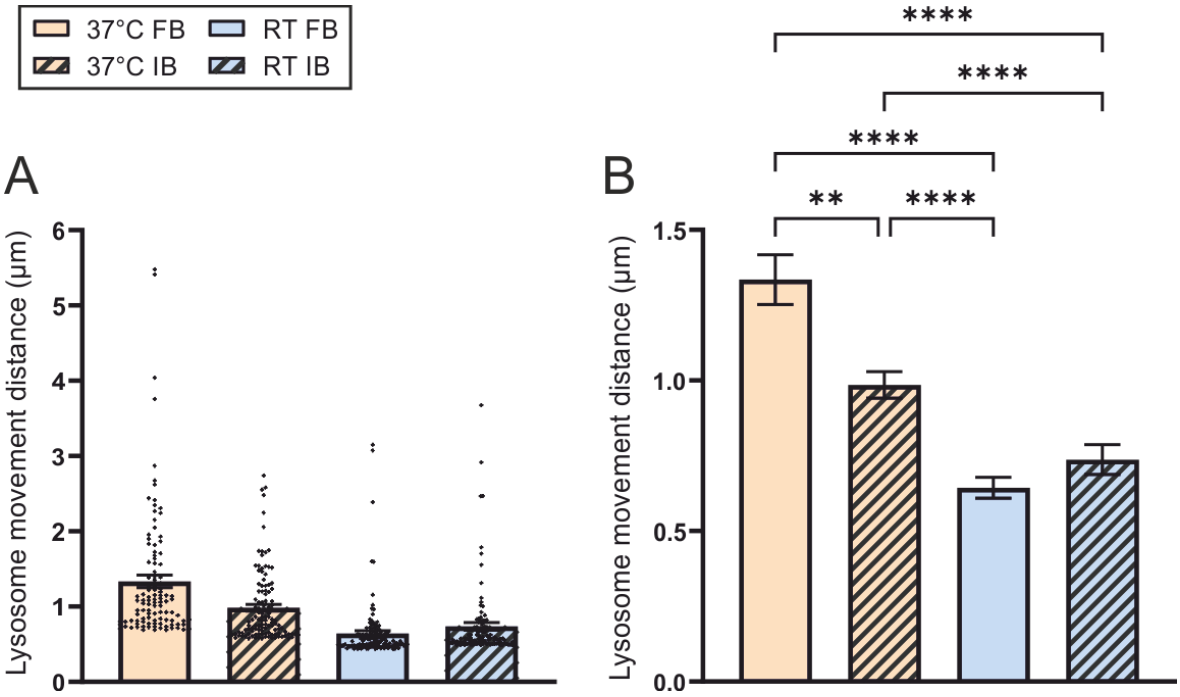


**Figure 26. Comparison of the effect of imaging conditions on the most motile lysosomes (lysosome distances of the 75-100%).** The comparative mobility of lysosomes in the top 25%. (A) All data were plotted with replicates as scatter points and, (B) as mean ± S.E.M. and analysed with a Kruskal-Wallis test with multiple comparisons where *** indicates $p \leq 0.001$ and **** indicates $p \leq 0.0001$. n = 1167 ± 14 and 47 ± 6 lysosomes representing the top 25% most motile lysosomes, respectively, from 5 cells per condition.

#### *4.3.2.3 Establishing and verifying the 'Frame Overlay' and 'Particle Tracker' measurements of movement*

Having determined which lysosome probe to use and the most appropriate imaging conditions for tracking, the next stage was to look more closely at the lysosome movement. As presented in Figure 25, the majority of lysosome movement (appearing to be at least 75%) covered relatively low

distances. These limited lysosome movements raised the possibility that the Particle Tracking assay may be sensitive to any background movement, originating from the cells or microscope stage.

To address the critical question of whether cells moved during imaging experiments and thereby influenced the tracking of lysosomes within them, movement of cells was measured. However, although Particle Tracker worked well for tracking lysosomes and similar vesicles, an alternative method was required to look at cells. This section discusses the results of the alternative method that was established for the purpose of measuring the potential movement of gross cell structures. The results obtained with this alternative method were compared to those obtained for lysosome movement with Particle Tracker.

The alternative measurement approach that was used to record movement of gross cell structures was the 'Frame Overlay' method (described in Figure 21). Cellular structures were labelled with fluorescent probes: WGA was used to label cell membranes, Hoechst for nuclei, and LysoTracker for lysosomes. Following labelling, the cells were imaged under identical conditions. Frames acquired at two time points during the imaging were duplicated and pseudo-coloured red and green to provide contrasting colours. The red and green pseudo-coloured images were then merged. If there was no movement, the cell structures would appear as uniform yellow pixels resulting from the merged red and green pseudo-colours (Figure 27, left hand panel). If there was visible movement, distinct red and green pixels would be evident with a measurable space in between (Figure 27, right hand panel). To achieve an overall measurement of movement, the labelled structures (nuclei or cell membranes) were measured on a minimum of three sides and the average measurement was taken to represent total movement. Alternatively, for lysosomes a line was drawn from the centre of these spherical organelles to mark their start and end locations within a cell.

To track movement of the cell membrane, cells were stained with WGA and recorded for 30 seconds, as shown in Figure 27. On the left-hand side panel of Figure 27, the cell had no visible movement as shown by the uniform yellow colour of the cell staining and clear border. In this particular example, a small piece of cell debris floated through the image and can be seen as distinctly red or green at its start and end locations. This debris presented a helpful contrast against the apparently static cell, for illustrative purposes. On the right-hand side of Figure 27, the example cell had clearly moved, as shown by the very distinct green and red pixels of the cell edge. The yellow line in this image is the ImageJ line tool which was used to quantitate the distance.

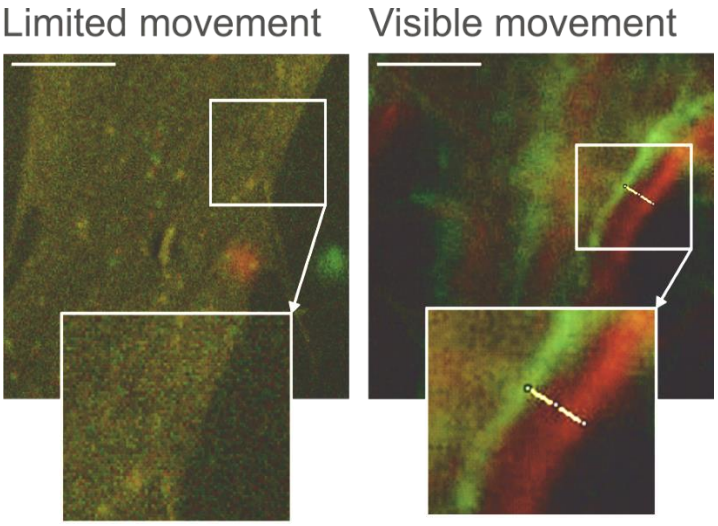


**Figure 27. Illustration of gross movement of a fibroblast cell membrane, depicted as change in WGA staining colour using the Frame Overlay method.** Example cells with no visible movement (left) and substantial movement (right). The brightness and contrast of the images was enhanced equally for clarity.

The majority of cells had limited movement as shown on the left hand side in Figure 27, while the example of visible movement is from an experiment in which the cell moved due to the imaging chamber being incorrectly seated on the microscope. Where visible movement was present, recordings would be stopped, and the chamber readjusted to ensure that there was no movement in the final image series to be analysed.

For a direct comparison of the Frame Overlay and Particle Tracker methods, the Frame Overlay method was used with a slight modification. As mentioned earlier, the lysosome movement was measured from the centre of the lysosome in each frame rather than the edge, as this is most comparable to Particle Tracker, which also measured movement from the centre of the organelles, as shown in Figure 28.

Images series with examples of lysosomes with varied trajectory lengths were selected and duplicated in ImageJ. One copy of the image series was processed according to the Frame Overlay method described above (i.e., start and end frames were pseudo-coloured red and green, and then merged). The other copy of the image series was analysed using Particle Tracker. Using these approaches, it was possible to directly compare the movement of the same lysosomes using the Frame Overlay and Particle Tracker methods. An example of this paired analysis is shown in Figure 28A. The line indicating lysosome movement that was measured using the Frame Overlay method is depicted in Figure 28A (left-hand panel). The corresponding trajectory of the same lysosome recorded using Particle Tracker is shown in Figure 28A (right-hand panel). The quantified data

presented in Figure 28B showed no significant difference in lysosome movement for the Frame Overlay and Particle Tracker measurements.

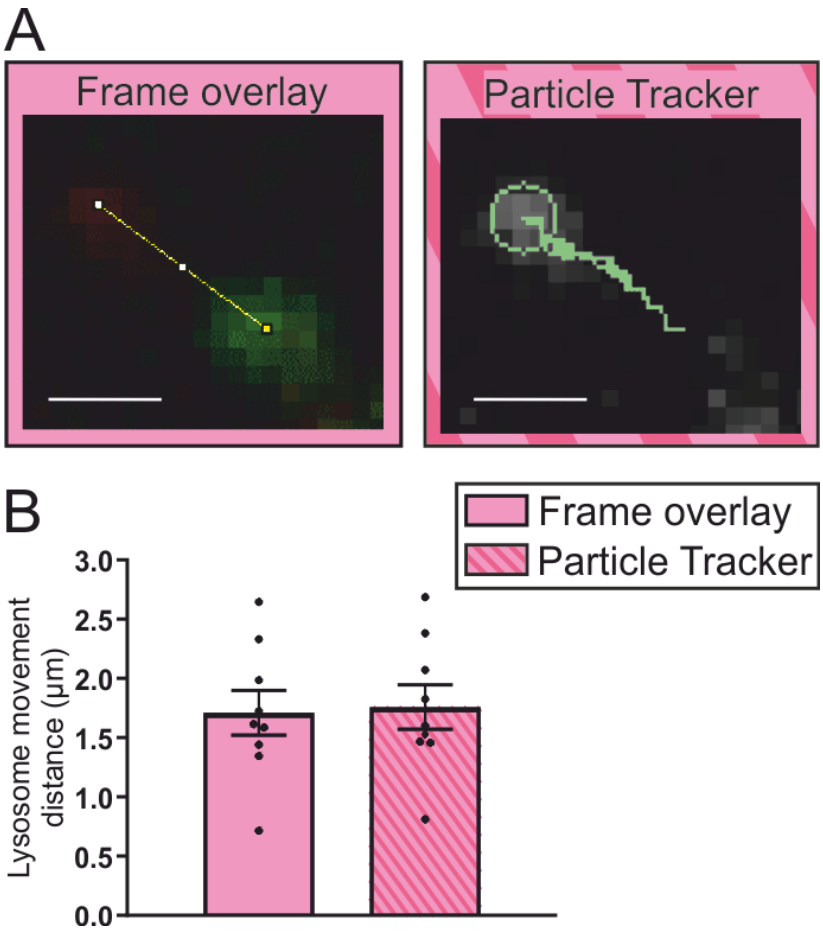


**Figure 28. Comparison of Frame Overlay and Particle Tracker measurement of lysosome movement.** These data were mean ± S.E.M. and analysed with a paired t-test, n = 9 lysosomes. The scale bar is 1 µm.

The comparison of the two methods to measure the lysosome movement over time, as shown in Figure 10, provided important corroboration of the Frame Overlay and Particle Tracking assays. For the tracking of populations of lysosomes, Frame Overlay was not a practical solution as each lysosome would need to be measured individually. Furthermore, it is evident from the lysosome movement trajectories shown in Figure 28A that the Frame Overlay could not be used to resolve subtle frame-by-frame movements. The Frame Overlay approach is only practically applicable to a single measurement of the full distance that lysosomes traverse over a period of imaging. In comparison, a large number of lysosomes could be tracked simultaneously using Particle Tracker with precise measurements even for very small frame to frame positional shifts. The advantage of

the Frame Overlay method was that it could be used to measure movement of much larger regions, such as the cell membrane.

#### *4.3.2.4 Assessment of whole cell 'background' movement and comparison to lysosome movement*

To study the extent of any background cell movement that could affect the lysosome tracking data, fixed markers were required. As many organelles of similar size to lysosomes, such as mitochondria or endoplasmic reticulum, were neither discrete particles nor static within the cell they were not suitable as fixed markers. Therefore, to determine the extent of cell movement, nuclei and cell membranes were chosen. The nuclei were labelled with Hoechst, as shown in Figure 29, and cell membranes were labelled with WGA, as previously shown in Figure 27. The Frame Overlay method described above was used to examine gross movements of these cell structures.

The nucleus illustrated in Figure 29 shows a Hoechst-labelled nucleus that was imaged for 30 seconds as a time series using the fluorescence microscope and processed using the Frame Overlay method. Four fixed points (labelled with a cross and number) are indicated around the circumference of the nucleus, each of which was examined closely under an increased magnification for the presence of red or green pixels, which would indicate movement. Enlargement of points 1 and 2 show the subtle movement that occurred (slight green and red tinge to the right-hand images in Figure 29). The distance between the red and green pixels in these regions were measured with the ImageJ line tool.

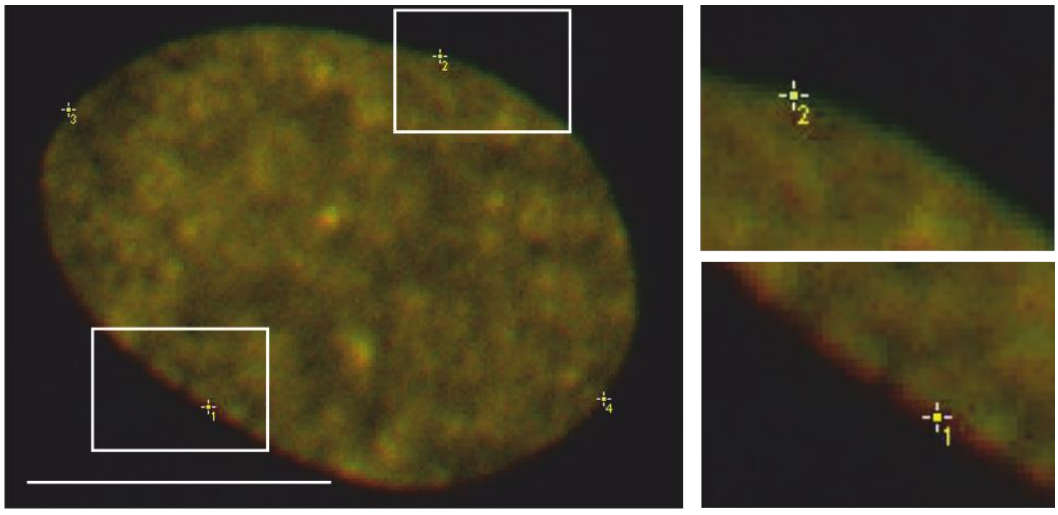

**Figure 29. Example of a nucleus (Hoechst-stained) analysed for movement using the Frame Overlay method.** A whole nucleus with four points of measurement is depicted. In brief, two images of the same nucleus were taken 30 seconds apart. One image was pseudo-coloured green, and the other was pseudo-coloured red. The two images were then overlaid, as described in the text. Where

the pixels in the red and green images overlap, the resulting merged image will appear yellow. Movement is shown by presence of non-overlapping green and red pixels at the edges of the nucleus. The scale bar is 10 µm and the enlarged images are 2x magnified.

In order to compare the background movement (represented by nuclei and membranes) to lysosomes, 9 cells were labelled with LysoTracker and recorded for 30 seconds. Lysosome movement was plotted as distance moved by the organelles (Figure 30A), organised by percentile as shown earlier. The average movement of cell membranes and nuclei are shown in Figure 30A as straight lines intersecting the lysosome data. The right-hand panel in Figure 30A shows the distance moved by the least motile 20% of the lysosomal population on an expanded scale, and indicates that the movement of the cell membranes and nuclei intersected lysosome movement at 1.4% and 1.5%, respectively.

To quantify the cell movement alongside the average lysosome movement, the mean distance moved by lysosomes, cell membranes and nuclei were plotted in Figure 30B. The movements of the cell membranes and nuclei were significantly lower than that of the lysosomes. Importantly, there was no significant difference between the movements of the cell membranes and nuclei, which would be expected for fixed reference points.

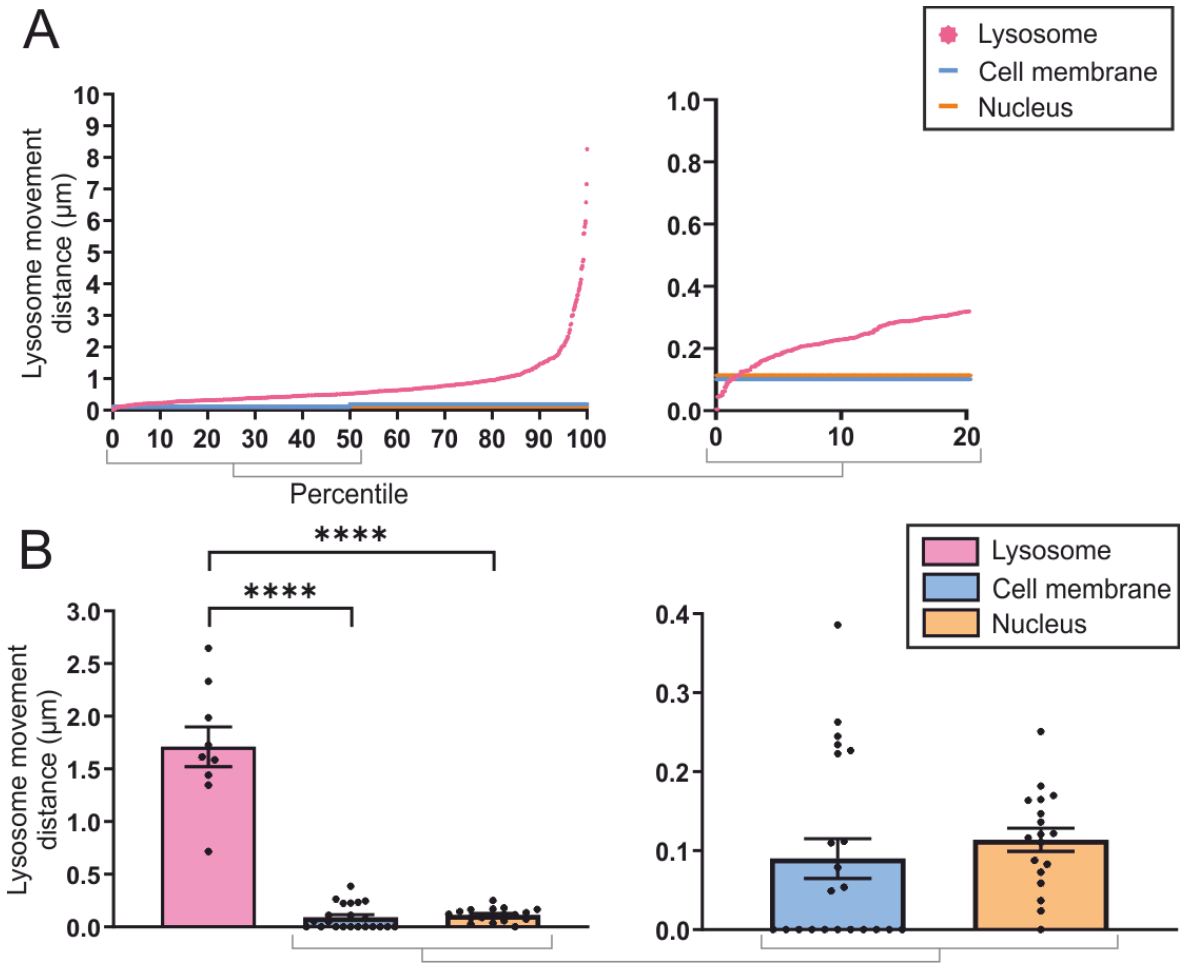


**Figure 30. Comparative analysis of the movement of lysosomes, cell membranes and nuclei during 30 seconds of recording.** (A) Example movement of lysosomes, cell membranes and nuclei, with all lysosomes plotted by percentile and lines indicating the movement of cell membranes and nuclei respectively. (B) Data are presented as ± S.E.M. and analysed with a one-way ANOVA with multiple comparisons. n = average measurements of lysosomes from 9 cells and cell membranes or nuclei from 18 cells each.

Visual inspection alone during imaging experiments is not sufficient to draw firm conclusions about potential movements of cells that may confound tracking of organelles. For this, an objective assay, such as the one using the Frame Overlay method described here, is required. The use of the cell membrane and nucleus as fixed reference points with the Frame Overlay method indicated that gross cell movement during imaging would have a negligible influence on the lysosome movement data. The results presented in Figure 30 indicate that >98% of the lysosomes within a cell moved more than the cell membrane or nucleus. Therefore, the assessment presented in Figure 30, and in particular the direct comparison of fixed cellular reference points with lysosome movement, was helpful in drawing the conclusion that there was little influence of background cellular movement on the results of this study.

### 4.3.3 Trajectory illustration

Since the measurement of lysosome movement using Particle Tracker had been verified with an alternative method (Frame Overlay; Figure 28) and the influence of potential variables, such as photobleaching (Figure 24) and background movement of the cell (Figure 30) were found to be negligible, the plotted lysosomal trajectories obtained using Particle Tracker were considered to be reliable. The key outputs from Particle Tracker consisted of 'Visualise Trajectories' (i.e. a graphic showing lysosome movement during an image series; Figure 31) and a data table in which each lysosome's trajectory was plotted as coordinates on a frame by frame basis. A unique identifier provided by Particle Tracker enabled every lysosome's visual trajectory to be matched to the relevant coordinate data in the table.

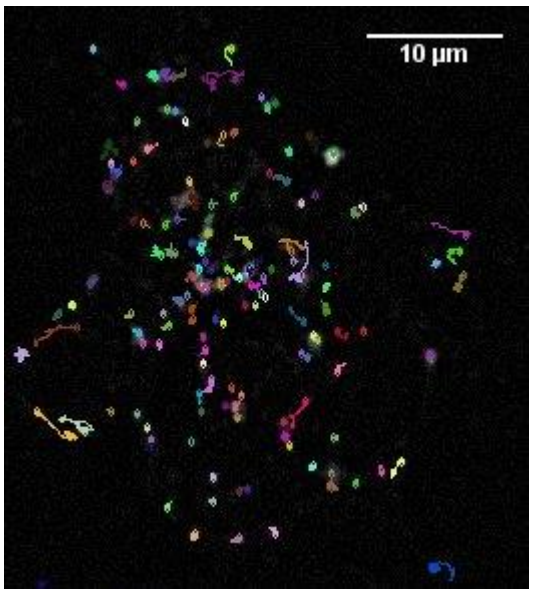


**Figure 31. Example of lysosome movements displayed in the 'Visualise Trajectories' output from Particle Tracker**. Lysosome movement was recorded during 30 seconds of imaging of a LysoTracker-loaded HeLa cell. The scale bar is 10 µm.

Some lysosome movement could be clearly observed during live cell imaging in HeLa and fibroblast cells, which was far more noticeable upon replaying the recording at a more rapid imaging speed, or, jumping between the first and last frame to see the extent of movement. Using the visual output from Particle Tracker, it was possible to observe movement in the entire population of tracked lysosomes with a greater clarity.

There were several key observations with regard to lysosome movement:

- Lysosomes continuously moved

- The majority of lysosomes hovered at a fixed point ('short' trajectories)
- Some lysosomes had an extended, directional trajectory ('long' trajectories)

Relating to those with the extended (long) trajectories:

- Lysosomes did not travel in perfectly straight lines
- The trajectories of different lysosomes did not generally move in parallel, even when the organelles were closely located
- Extended movement was often in short bursts, with organelles stopping to hover before moving again

In summary, lysosomes were shown to exhibit an array of movement patterns with the greatest distinction falling between the 'short' and 'long' trajectories. Figure 32 shows the trajectories of two lysosomes from the same recording of a single cell, highlighting the variation between the short (lysosome number 37) and long (lysosome number 306) trajectories. The total distance of the lysosome trajectory was 4.4 µm for lysosome 37 and 8.18 µm for lysosome 306. This indicates a clear difference between the movement profile of these two lysosomes. However, given that lysosome 37 did not move far across the cell, it is somewhat surprising that its frame-to-frame movements summated to over half that of lysosome 306.

The very compact trajectory of lysosome 37 showed that although the lysosome was observed to be continually moving, it was potentially tethered to another structure or otherwise anchored in place or awaiting an interaction that would enable it to reposition within the cell. Conversely, lysosome 306 appeared to be travelling within the cell in a relatively linear manner, possibly along a microtubule. Although lysosome 306 travelled in relatively straight direction, the trajectory did deviate somewhat and exhibited some drift and hovering at various points. To investigate the extent to which lysosome movement was constant in distance (and therefore velocity) between frames, the trajectories of the example lysosomes 37 and 306 were divided into either three 10-second periods, or ten 3-second periods, as illustrated in Figure 33 - Figure 36.

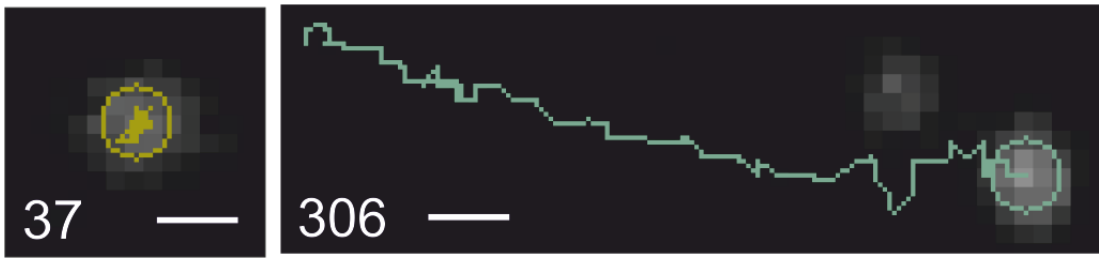


**Figure 32. Plotted trajectories of lysosomes that had a short ('37') and long ('306') travel distances in a cells during 30 seconds of imaging.** Recordings were captured during 30 seconds of rapid imaging of LysoTracker-loaded cells and the lysosome trajectories were mapped by Particle Tracker. The scale bar is 1 µm.

Beginning with the lysosome that displayed a short trajectory (lysosome 37), the frame-to-frame movement over a 30-second imaging period was calculated and plotted for 0 - 10 s, 11 - 20 s and 21 - 30s segments (Figure 33). The bars plotted in Figure 33 had variations in their height, and which indicated that lysosome 37 did not move a consistent distance throughout the three time segments. Additionally, within each bar there was a noticeable split in the data points for the frame-to-frame movements suggesting that the distance lysosome 37 moved varied from about 0.00 - 0.05 µm to 0.10 - 0.15 µm throughout the recording. However, as shown in the Figure 33, and discussed above, there was no substantial change in the location of lysosome 37 within the cell.

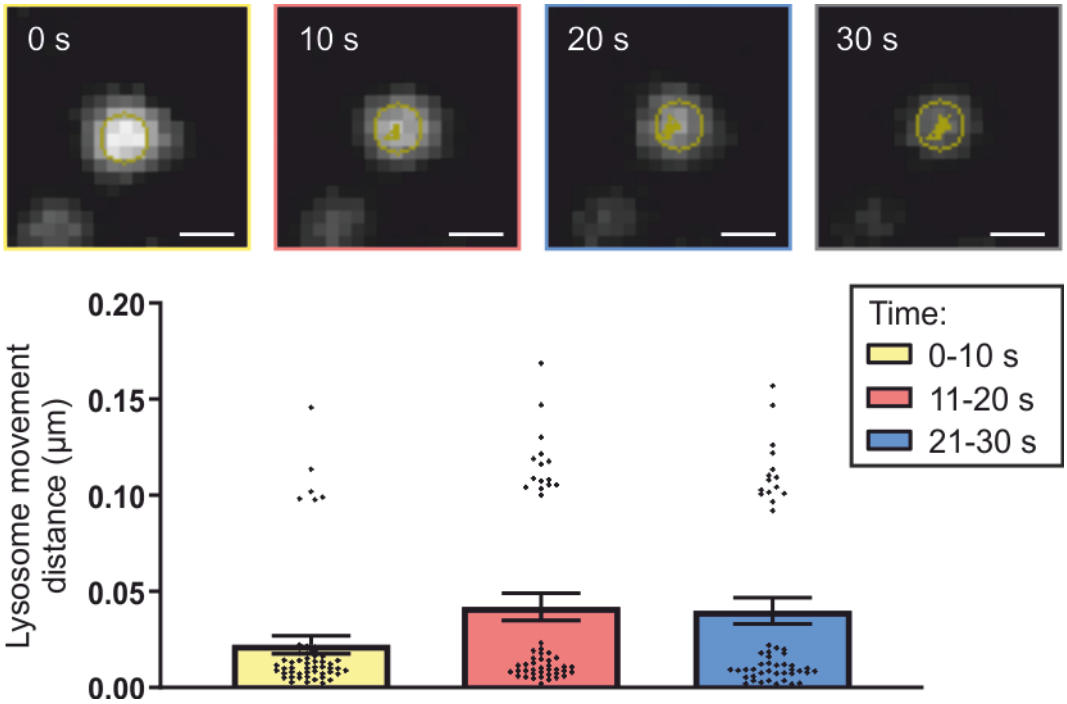


**Figure 33. Analysis of the movement of lysosome 37 in 10-second intervals over a 30-second imaging period.** The frame-to-frame movements of lysosome 37 were calculated using Particle Tracker over a 30-second imaging period. For this plot, the frame-to-frame movements were grouped into 10-second intervals and plotted as mean ± S.E.M. The individual frame-frame movements of lysosome 37 are displayed as scatter points. The scale bar represents 1 µm.

To investigate the movement of lysosome 37 in greater detail, the same data shown in Figure 33 was re-plotted using 3-second intervals, as shown in Figure 34. The deviation in the height of the bars in this Figure 16 shows a clearer picture of the changes in movement of lysosome 37, with a noticeable drop in movement between 3 - 13 seconds. Intriguingly, even separating the plot into 3-second intervals there was a noticeable grouping of shorter (0.00 - 0.05 µm) and longer (0.08 - 0.17 µm) movements. The exceptions to this variable movement were the three bars covering 3 - 13 seconds, in which the longer movements were not evident. The decrease in movement during this 3 - 13 second period was not obvious from visual inspection of the recording of lysosome 37's movement, or when using longer imaging intervals (Figure 15), emphasising the need to employ an assay that can adequately resolve rapid, sub-micrometre positional changes.

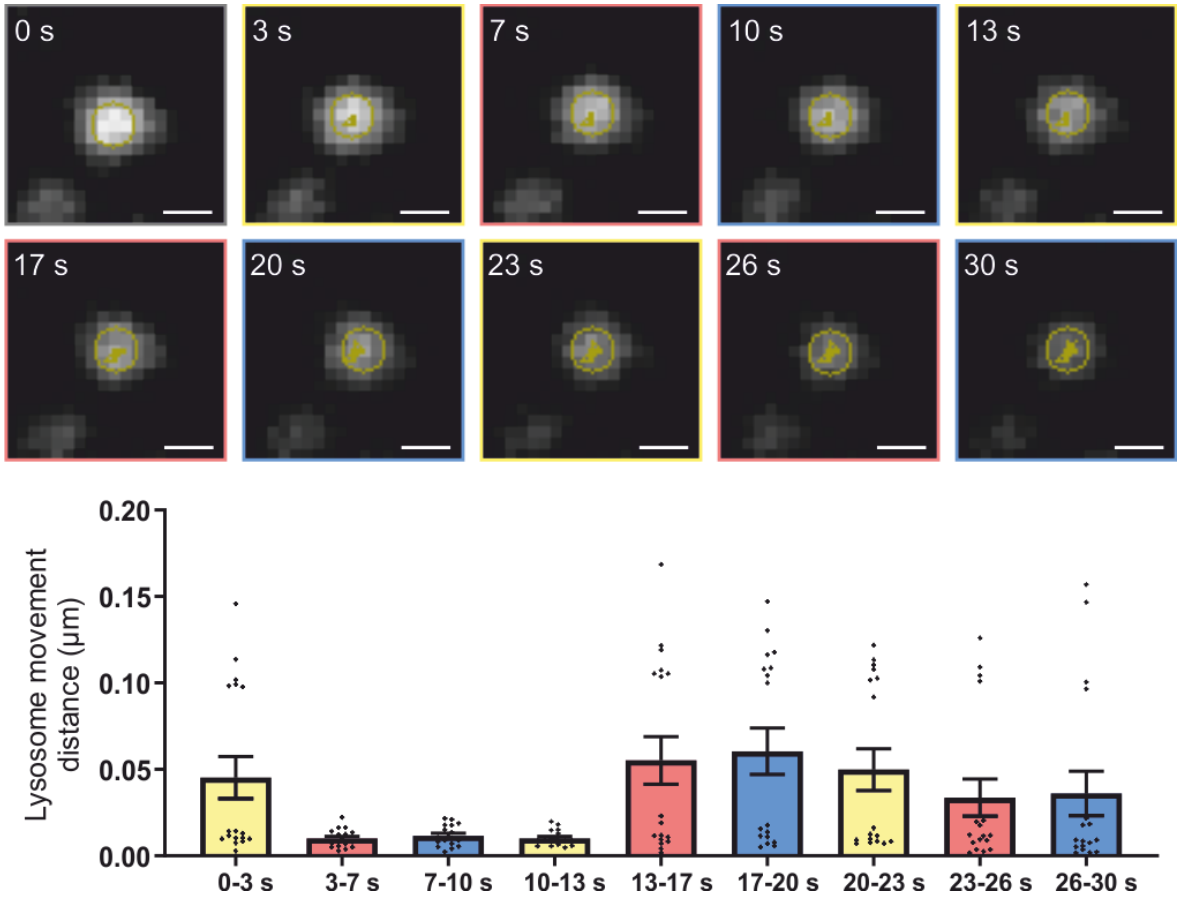


**Figure 34. Analysis of the movement of lysosome 37 in 3-second intervals over a 30-second imaging period.** The frame-to-frame movements of lysosome 37 were calculated using Particle Tracker over a 30-second imaging period. For this plot, the frame-to-frame movements were grouped into 3-second intervals and plotted as mean ± S.E.M. The individual frame-frame movements of lysosome 37 are displayed as scatter points. The scale bar represents 1 µm.

The next pattern of movement analysed was that of lysosome 306 (Figure 32), which displayed a long trajectory. Similar to the approach used with lysosome 37, the trajectory of lysosome 306 was grouped into three 10-second intervals (Figure 35). The yellow, red and blue boxes drawn over the trajectory of lysosome 306 in Figure 35 show the distance travelled by the lysosome in each of the 10 second windows. It is evident that the lysosome travelled less distance overall in the first 0 - 10 seconds compared to the following two 10-second periods. This is also reflected by the bar graph, plotted below the trajectory. As previously seen with the short trajectory of lysosome 37 (Figure 33, Figure 34), there were noticeable groupings of data points showing shorter (0.00 - 0.06 µm) and longer (0.08 - 0.24 µm) movements of lysosome 306 for each of the 10-second intervals.

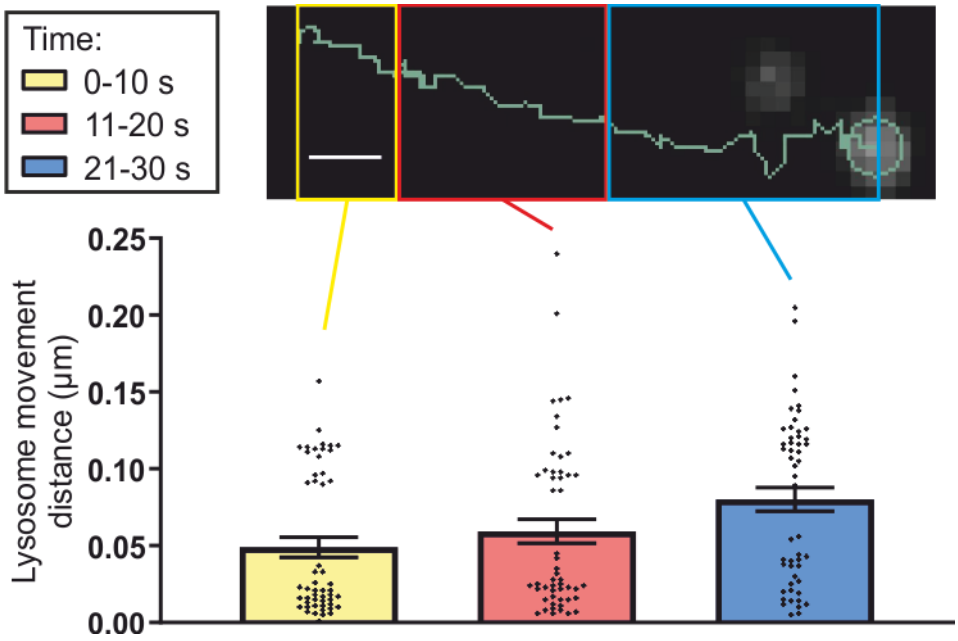


**Figure 35. Analysis of the movement of lysosome 306 in 10-second intervals over a 30-second imaging period.** The frame-to-frame movements of lysosome 37 were calculated using Particle Tracker over a 30-second imaging period. For this plot, the frame-to-frame movements were grouped into 10-second intervals and plotted as mean ± S.E.M. The individual frame-frame movements of lysosome 306 are displayed as scatter points. The scale bar represents 1 µm.

To examine the long trajectory of lysosome 306 with greater detail, the data shown in Figure 17 were re-plotted with 3-second intervals, as shown in Figure 36. It was interesting to note that there was no interval in which the frame-to-frame distances were all reduced (as shown previously with lysosome 37; Figure 34). However, there were still noticeable groupings of data points showing shorter (0.00 - 0.06 µm) and longer (0.08 - 0.24 µm) movements of lysosome 306 for each of the 3-second intervals. However, the distinction between the data points showing shorter and longer movements was less pronounced than with lysosome 37.

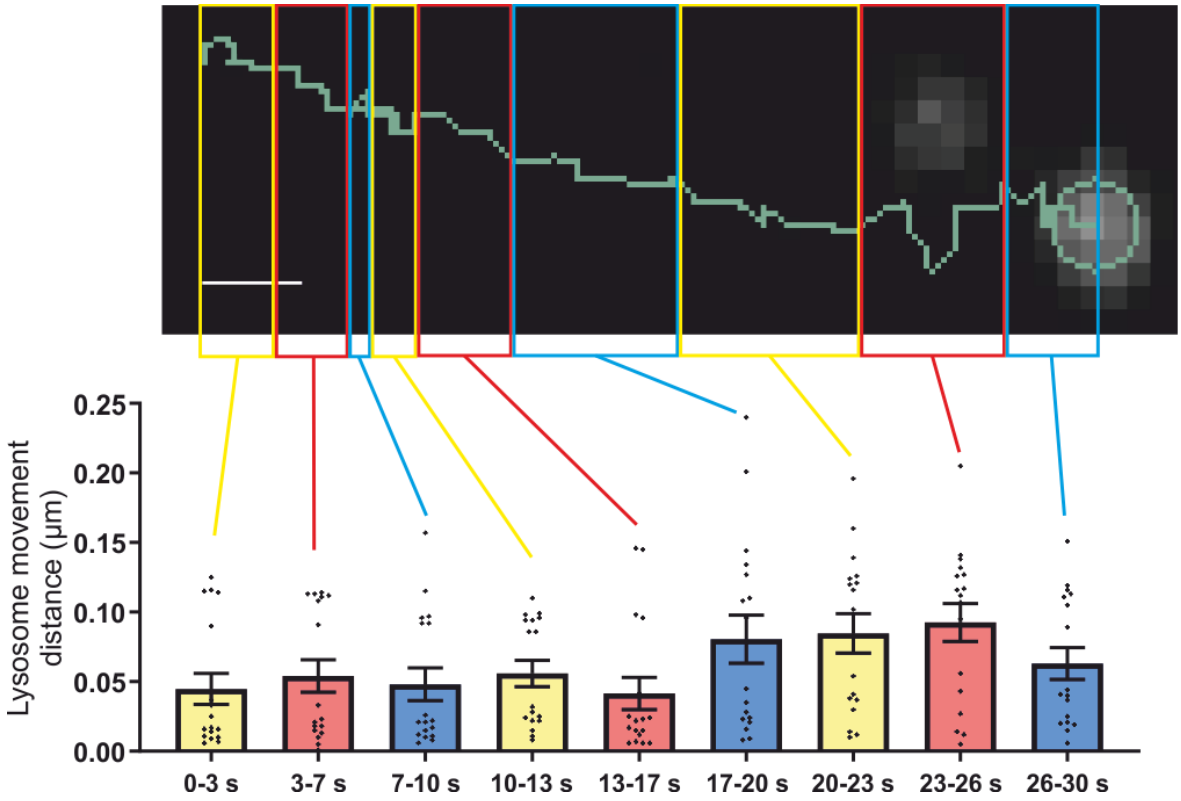


**Figure 36. Analysis of the movement of lysosome 306 in 3-second intervals over a 30-second imaging period.** The frame-to-frame movements of lysosome 306 were calculated using Particle Tracker over a 30-second imaging period. For this plot, the frame-to-frame movements were grouped into 3-second intervals and plotted as mean ± S.E.M. The individual frame-frame movements of lysosome 306 are displayed as scatter points. The scale bar represents 1 µm.

These analyses indicated that were similarities in the patterns of movement of lysosomes 37 and 306 despite the differences in overall distance moved and their linear/non-linear trajectories. In the 30-second imaging periods, the trajectories of both lysosomes showed some fluctuation in the distance moved between frames. Lysosome 37 had an approximately 10-second period in which its movement appeared to be reduced.

As the grouped data shown in Figure 33 - Figure 36 still presented some questions about the overall fluctuation in the movement of the lysosomes, the data points for the frame-to-frame movement were plotted as a simple scatter plot (Figure 37). In addition, to illustrate the movement of the lysosomes in greater detail, the frame-to-frame movements of the lysosomes in the first and last 5 seconds of the 30-second imaging period were plotted on an expanded scale.

The plot for both lysosomes in Figure 37 clearly shows the groupings of data points showing shorter and longer movements. For lysosome 37, these movements occurred approximately within two bands spanning 0.00 - 0.025 µm and 0.08 - 0.17 µm (as shown in Figure 33 and Figure 34). For

lysosome 306, the groupings of shorter and longer movements were slightly less distinct, and the plotted distances were more broadly grouped within 0.00 - 0.06 µm and 0.08 - 0.24 µm (as shown in Figure 35 and Figure 36). The dashed lines shown in the right-hand panels of Figure 19 emphasise that there appeared to be rapid reversible transitions between the shorter and longer frame-to-frame movements for both lysosomes. However, lysosome 306 displayed more of the longer frame-to-frame movements throughout the 30-second recording. The scatter plots in Figure 37 show a clear differentiation between the movements of lysosomes 37 and 306; with lysosome 306 frequently covering greater distances between frames than lysosome 37. Whilst these analyses show clear differences between movements of lysosomes 37 and 306, it is notable that this did not represent the most striking visual difference between them, which was the relative linear, directional movement of lysosome 306.

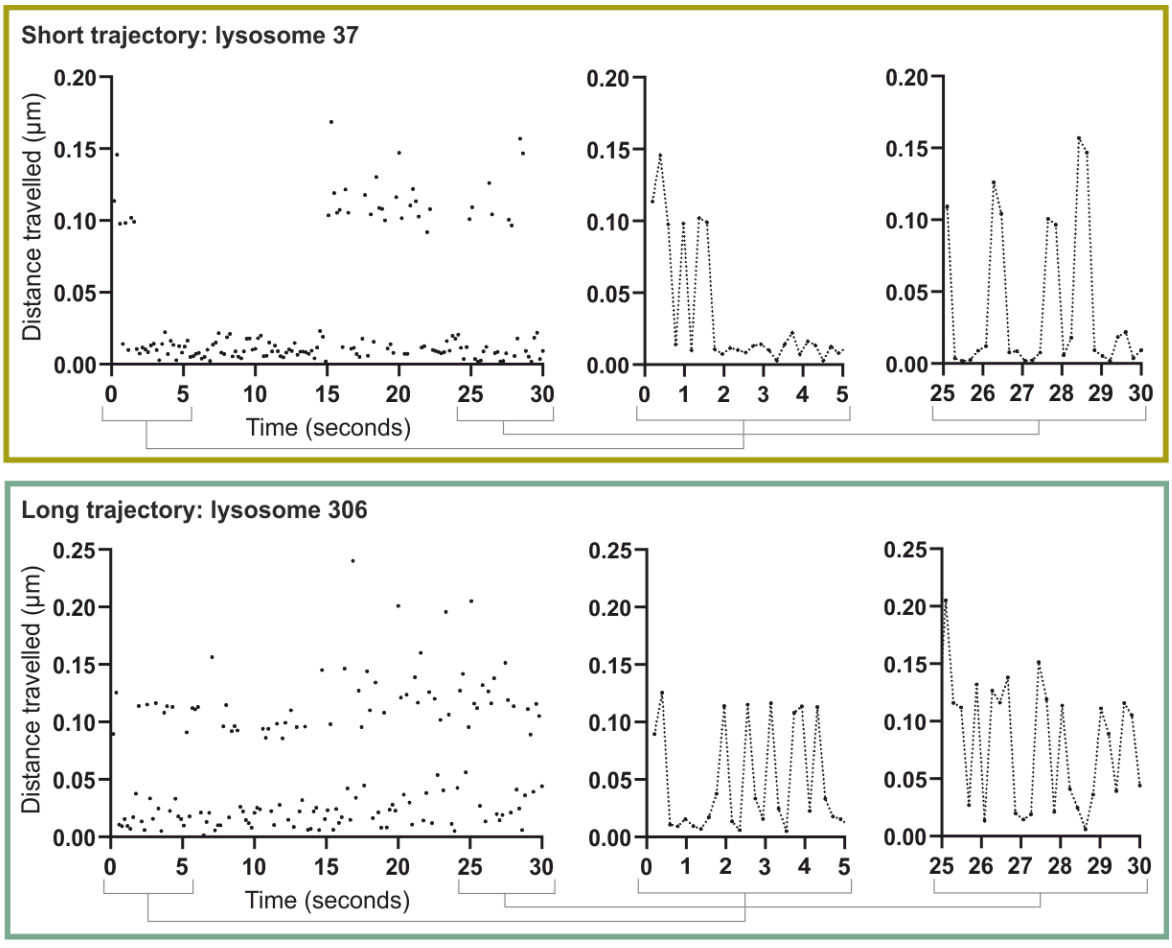


**Figure 37. Analysis of the movement of lysosomes 37 and 306 over a 30-second imaging period.** The frame-to-frame movements of lysosome 306 were calculated using Particle Tracker over a 30-second imaging period and are displayed as scatter plots. The first and last 5 seconds of the scatter plots are shown on expanded scales in the right-hand panels. The scale bar represents 1 µm.

The two examples, lysosome 37 and lysosome 306, presented an opportunity to assess the similarities and differences between two visually contrasting lysosome trajectories. Whilst the outcome from the frame-by-frame analysis indicated that there were differences in the movement of the organelles throughout the recordings, it left open the question of whether their trajectories could be differentiated by another form of analysis. Specifically, the frame-by-frame analysis of lysosomal movement indicated that lysosomes could undergo short and long movements, and that lysosome 306 that had more long movements that summated into a greater overall distance moved (8.18 µm). However, lysosome 37, which stayed in the same cellular region, completed a total movement of 4.4 µm.

### 4.3.4 Analysis and interpretation of lysosome trajectories with Particle Tracker

The analysis of frame-to-frame movement was extended by developing a method to quantitate the directionality of lysosome trajectories using Particle Tracker. A graphical summary of the method for quantification and presentation of lysosome trajectories using Particle Tracker is illustrated in Figure 38. The top panels in Figure 38represent two lysosomes (red and blue circles) tracked over three frames (Figure 38A). The panels show a frame-by-frame movement of the red and blue lysosomes. The overall trajectories of the lysosomes are shown in Figure 38B, with the corresponding co-ordinates relating to the movement listed in Figure 38C. In essence, Particle Tracker was able to provide a similar graphical representation of lysosomal movement as indicated in Figure 38B (‘Visualise Trajectories’; see Figure 31), and a table of the cellular coordinates of the lysosomes on a frame-by-frame basis, similar to that shown in Figure 38C.

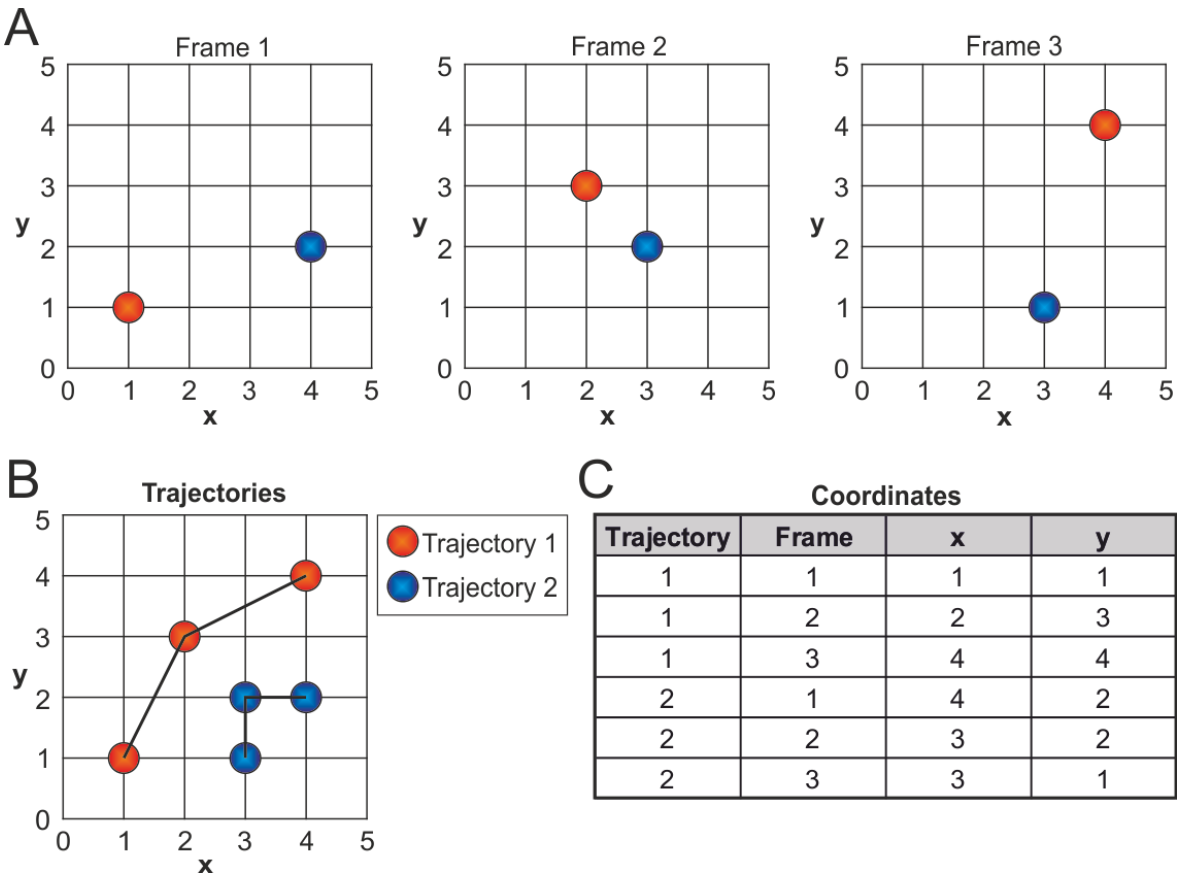


| Trajectory | Frame | x | y |
|---|---|---|---|
| 1 | 1 | 1 | 1 |
| 1 | 2 | 2 | 3 |
| 1 | 3 | 4 | 4 |
| 2 | 1 | 4 | 2 |
| 2 | 2 | 3 | 2 |
| 2 | 3 | 3 | 1 |

**Figure 38. Example representation of lysosomal trajectories and tracking.** (A) Position of trajectories 1 and 2 in three separate frames. (B) Paths illustrating trajectories and, (C) coordinates obtained as raw data output.

The coordinates obtained from Particle Tracker provided the details of location of the lysosomes in any particular image frame, but not specifically movement. To interpret these data further, additional calculations were required, and the outcomes of the analysis were planned as follows:

- **Sum**: total length of the lysosome trajectory, calculated as the cumulative frame-by-frame movement (as shown in the analysis above)
- **Maximum**: the widest span travelled by each lysosome within the cell (not necessarily the starting position to final location as lysosomes could travel back on themselves; see below)
- **Velocity**: speed of lysosome movement calculated as distance (sum) moved over time (µm/s)

The basic calculations were the 'maximum distance' (Figure 39A) and the 'sum of distance' (Figure 39B). The velocity was subsequently calculated as the sum of distance divided by time. The illustrations in Figure 39 detail the transformation of the coordinates to a measurement of the distance between them, using x and y (the given coordinates) to calculate z (the distance).

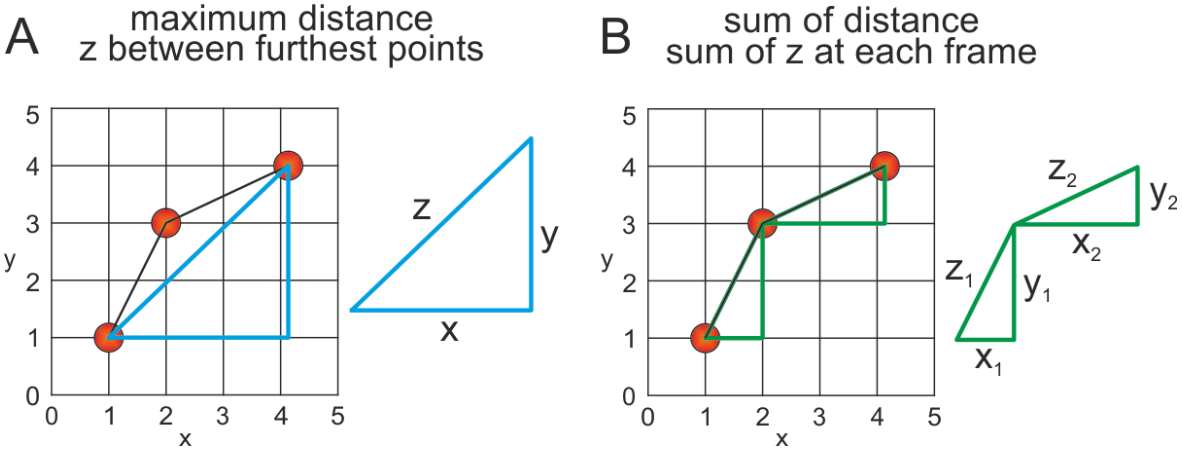


**Figure 39. Calculation of 'maximum distance' and 'sum of distance' movements based on coordinates.** (A) Maximum distance represents the travel between the two furthest points and (B) sum of distance to represents the cumulative distance of the trajectory.

The aim of 'maximum distance' was to differentiate between lysosomes that had a relatively linear and elongated cellular trajectory, and those that hovered at a fixed cellular point. Conversely, the 'sum of distance' (henceforth referred to as 'sum') is the method by which the movement between each frame is calculated and summated, in order to measure the total length of the trajectory. The sum did not take into account whether a lysosome had repositioned within a cell, but instead determined the overall movement of a lysosome (whether linear or hovering), which can also be divided by time to calculate the velocity of movement.

Since not all lysosomes are tracked over the entirety of an imaging series (Figure 24), the first step in the trajectory analysis was to remove lysosomes that had not been fully tracked from the dataset. The number of frames per trajectory was added to the dataset and those which did not match the expected total number of frames in the series were filtered out. The remaining trajectories were then quantified based on the calculations as follows:

1. Known 'x' and 'y' per lysosome, per frame.
    a. Maximum: x and y coordinates of the 'minimum' and 'maximum' values in the series
    b. Sum: x and y coordinates from all frames in the series
2. Calculation of $z = \sqrt{(x^2 + y^2)}$.
    a. Maximum: single z, distance between minimum and maximum coordinates
    b. Sum: total of each z distance between frames

Finally, the distances were transformed from pixels to microns (distance in µm = distance in pixels * 0.146).

The desired output from the maximum distance calculation was a representation of the length of the trajectory within the cell – the distance travelled, potentially coming into contact with other organelles. Therefore, the 'minimum and maximum' distance was used to locate the outer points of the area in which the lysosome travelled. An assessment of the start and end point of tracking would not necessarily capture the full extent of movement if a lysosome crossed back on its own pathway, as illustrated in Figure 40.

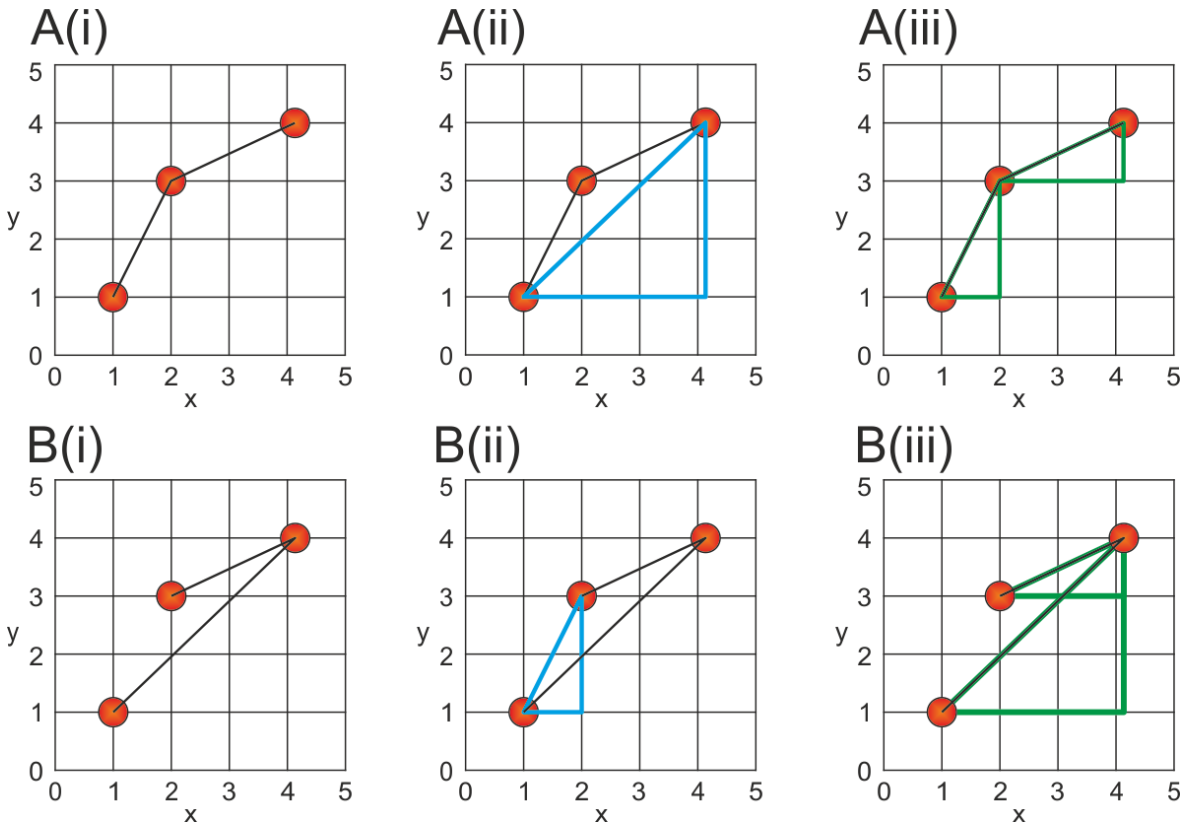


**Figure 40. Calculation of 'maximum distance' and 'sum of distance' movements based on coordinates.** (A) A lysosome with a relatively linear trajectory in which the maximum distance can be calculated from the first and last positions of the organelle. (B) A lysosome with a more complex trajectory where the maximum distance cannot be calculated from the first and last positions of the organelle.

Returning to the example movements of lysosomes 37 and 306 (Figure 41A), the results of maximum and sum distance were plotted for each lysosome. In Figure 41B, the sum was plotted as cumulative distance, indicating that lysosome 306 had a consistent and steady movement during the imaging period, ultimately travelling a greater distance in comparison to lysosome 37. The period when lysosome 37 showed only short frame-to-frame movements (Figure 34) can be seen in Figure 41 as the part of the cumulative distance line with a shallow incline. The sum and

maximum calculations for each lysosome were plotted in Figure 41C. As expected, the sum calculations (represented by the darker bars) were greater than the maximum. The difference between the two trajectories was far more pronounced when calculating the maximum distance; demonstrating the compact movement of lysosome 37 compared to the elongated travel of lysosome 306.

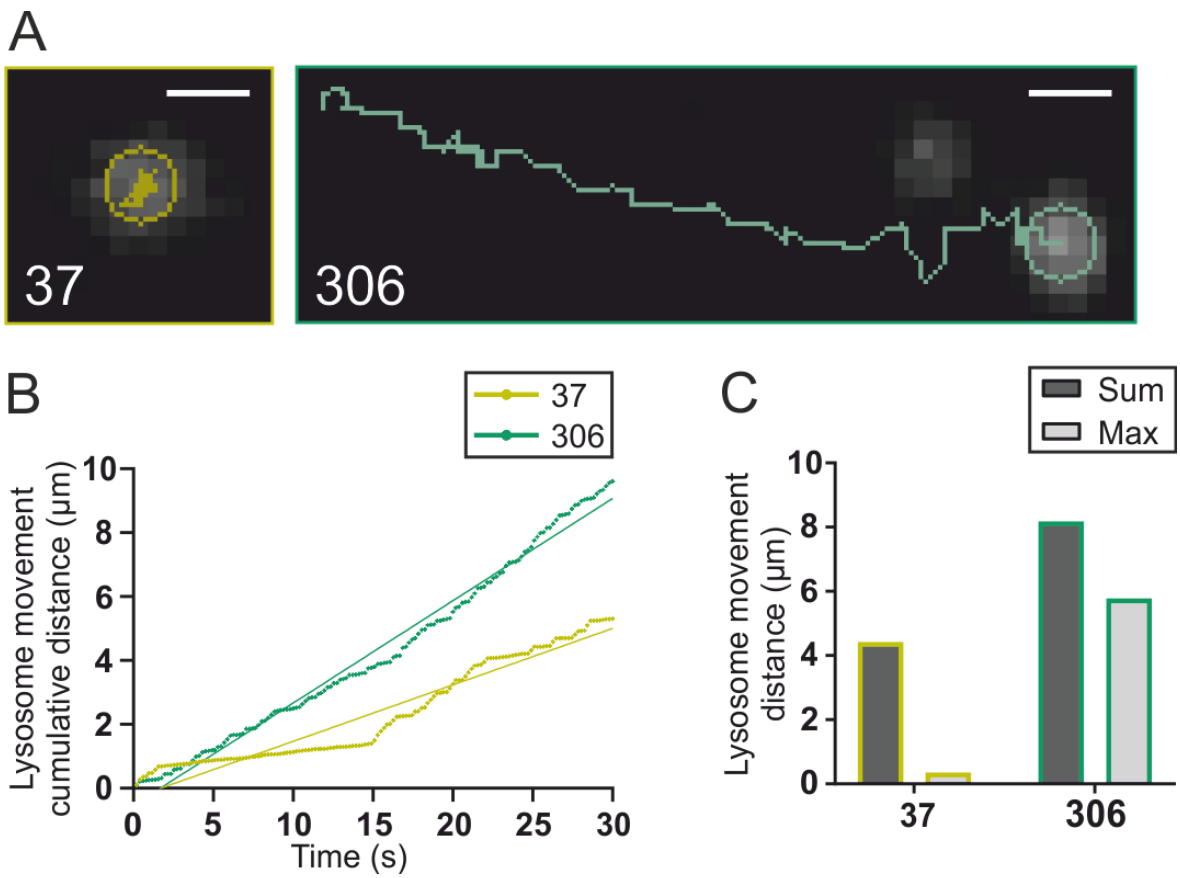


**Figure 41. Analysis of the trajectories of lysosomes 37 and 306.** (A) Illustration of lysosome trajectories for lysosomes 37 and 306. The scale bar is 1 µm. (B) The cumulative distance moved by lysosomes 306 and 37 The line of best fit (straight lines) represent the correlation coefficient ($r^2$=0.93 and $r^2$=0.99 for 37 and 306 respectively). (C) A quantitative comparison of the sum and maximum (max) distances for the two lysosomes.

Additional lysosomes, from the same cellular image, were analysed for sum and maximum movements (Figure 42). The analysis presented in Figure 42 shows 5 lysosome trajectories that were considered to be long (lysosomes 306, 261, 033, 232 and 147), and 5 lysosome trajectories that were considered to be short (lysosomes 256, 173, 252, 037 and 185).

The maximum distances presented in Figure 42B show a clear separation between the long and short lysosomal trajectories. Lysosome 232 is an example of an organelle that exhibited a great

amount of movement within the cell, which would not have been represented by the calculation based upon the first and last frame of recording. The lysosomes were organised on the graph in order of greatest to least maximum distance.

This same order was retained for the distances calculated as sum of movement (Figure 42B) and these revealed that the variation in trajectory length was not as great as expected throughout the dataset. Furthermore, lysosome 252, which appeared to be hovering, had a greater total trajectory length than lysosome 306 which had a long trajectory.

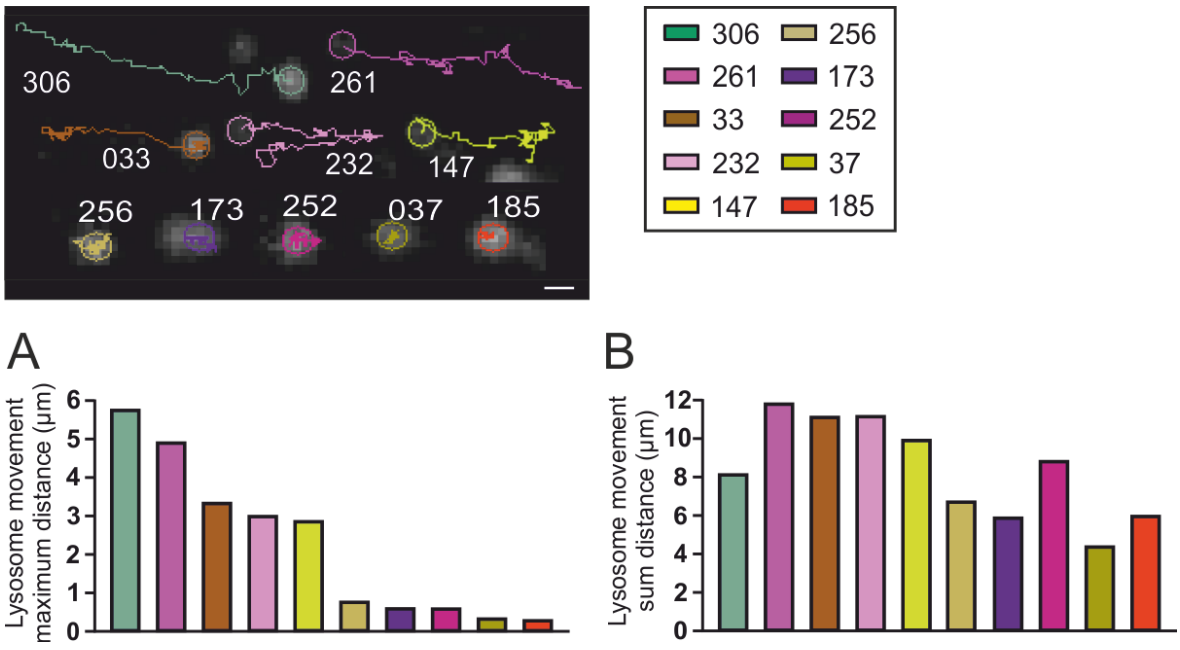


**Figure 42. A comparison of maximum and sum distances travelled by ten lysosomes within the same cell.** The example lysosomes in the top panel were all taken from a single recording of a LysoTracker loaded fibroblast cell. The scale bar is 1 µm. (A) The distances travelled by lysosomes calculated as maximum distance (µm). (B) The distances travelled by lysosomes calculated as sum distance (µm).

To further examine the relationship between the sum and maximum calculations, the distances were plotted as a scatter chart (Figure 43A). The chart indicated a weak relationship ($r^2 = 0.477$) between the points, which supported the interesting finding that a trajectory with a greater sum of movement did not necessarily travel a greater distance within the cell. The maximum and sum distances were plotted together per lysosome. The most comparable maximum and sum distances were in trajectory 306, which also had the most linear appearance of all, although it also had the shortest sum distance of all of the long trajectories.

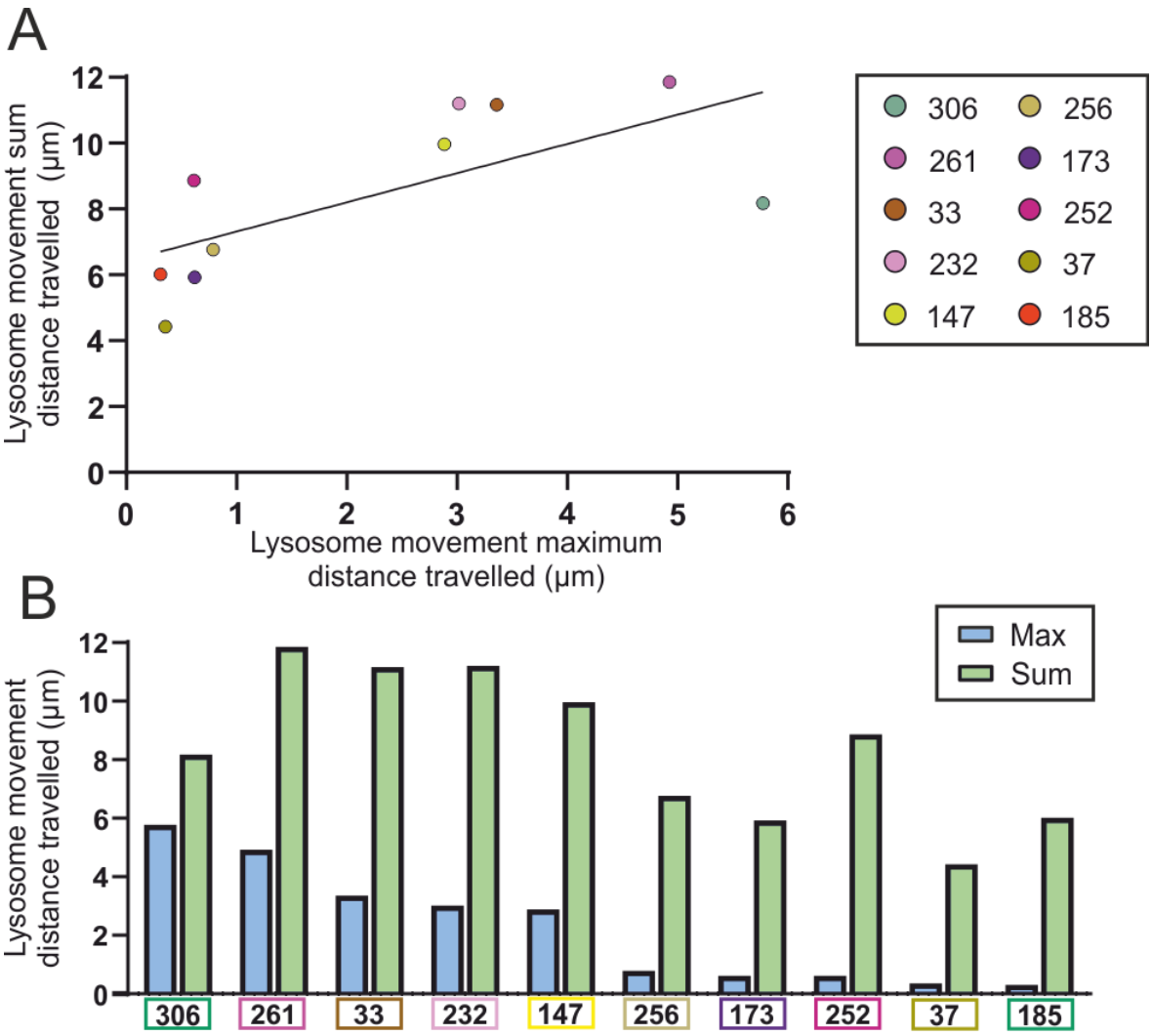


**Figure 43. A comparison of maximum and sum distances travelled by ten lysosomes.** (A) Scatter plot and, (B) bar chart, showing the maximum (max) and sum of distance measurements.

As the maximum distance appeared to differentiate between these examples, but the sum of the trajectory path was less distinctive, the examples were grouped by long and short, as shown in Figure 44A. The mean cumulative distance (Figure 44B) of the short and long trajectories (sum) showed that overall, the longer trajectories had a steeper slope and greater average distance achieved in 30 seconds of imaging. This was quantified as a comparison of the slope of these cumulative curves showed that the longer trajectories had a significantly greater slope than the shorter ones (Figure 44C).

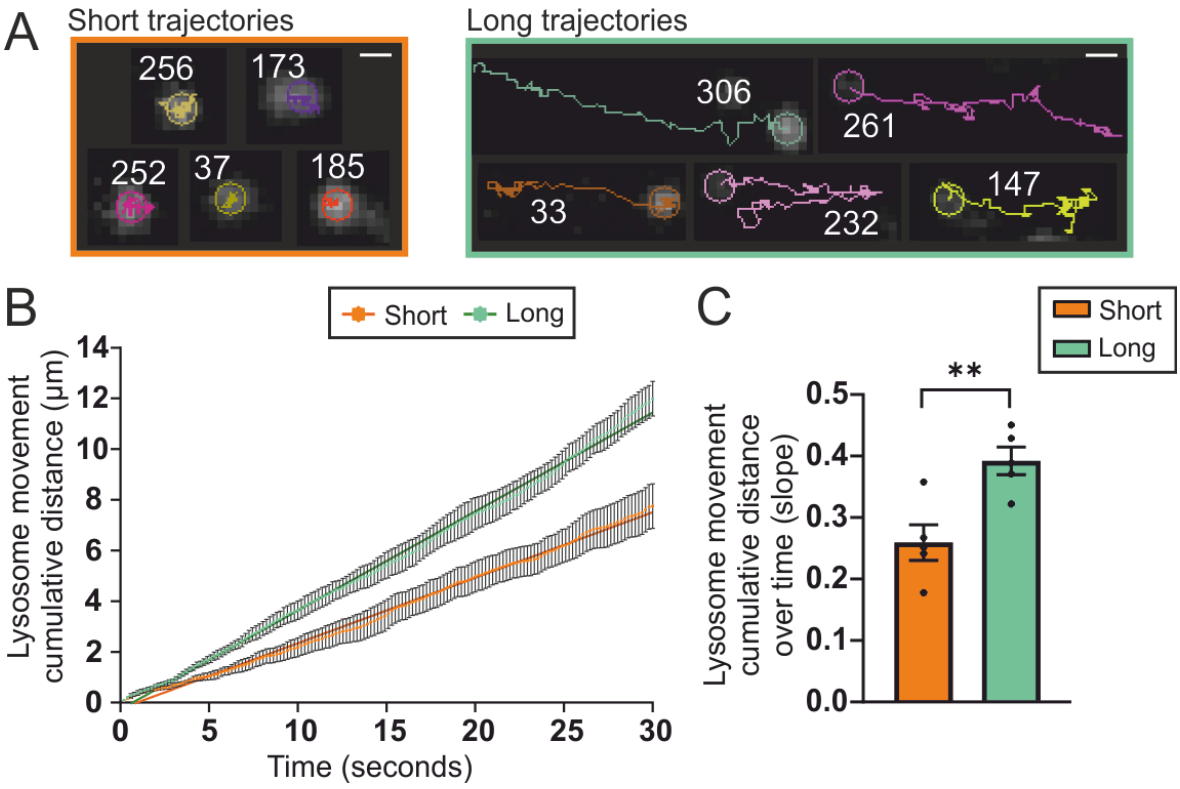


**Figure 44. Comparison of example trajectories grouped by 'short' and 'long' appearance.** The scale bar is 1 µm. (B) The mean cumulative distance of the trajectories calculated as the sum of the path. (C) The comparison of the slope of each cumulative trajectory distance. These data are plotted as mean ±S.E.M. and analysed with an unpaired t-test where ** indicates $p \leq 0.01$ and $n = 5$ lysosomes per group from 1 cell.

The maximum calculation showed a clearer distinction between the long and short movement groups and it was possible to find a significant difference. Therefore, in a much larger data set with the hundreds of lysosomes per cell accumulated into a data set, the distinction may be clearer if there was an overall change in the movement of the lysosomes. Nonetheless, there is reason to utilise both calculations in a thorough study of lysosome trajectories in order to systematically investigate both the trajectory pathway and the maximum distance of movement within a cell.

The more interesting readout from the sum of movement was the transformation to distance over time to represent the velocity of movement. Therefore, the analysis would capture distance moved within the cell (maximum distance) to establish whether a lysosome may be tethered in place or under control of a motor protein, and the velocity of the overall movement of the lysosome.

### 4.3.5 A pharmacological control treatment to induce a change in lysosome movement

The example lysosome trajectories thus far have been selected based on their appearance from a single cell, for the purposes of comparison. The next step was to determine whether lysosome movement could be influenced by a treatment to induce a phenotype in the cell, primarily to test the sensitivity of the assay and act as a control.

Lysosomes travel along microtubules in order to reposition in the cell (Pu et al., 2016). Therefore, the disruption of microtubules is a reasonable experimental approach to reduce lysosome movement. This was achieved through treatment of cells with nocodazole, the effect of which is shown on fibroblast cells in Figure 45. The microtubules were labelled with Tubulin Tracker, and there was a clear loss of fluorescence in cells treated with 20 µm nocodazole for 30 minutes. This was quantified as the fluorescent signal (mean gray value) and shows a significant reduction in the signal indicating that the Tubulin Tracker fluorescence, and therefore the microtubules, were disrupted. The fluorescence signal was not completely removed, but no longer had the distinctive appearance of microtubules as the nocodazole treatment depolymerised the structure.

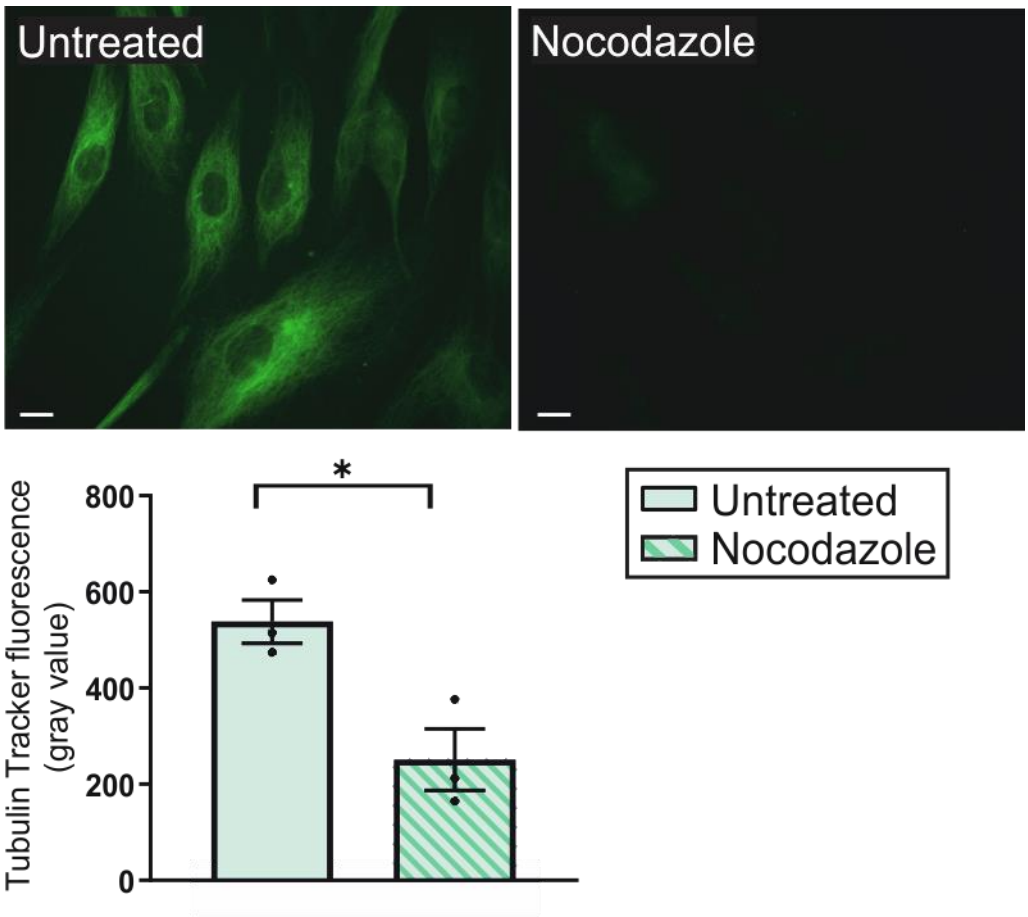


**Figure 45. Depolymerisation of microtubules with nocodazole treatment**. Microtubules were labelled with TubulinTracker and imaged after 1 hour of DMSO vehicle treatment (untreated) or 20 µm nocodazole treatment. The scale bar is 10 µm. Quantification of fluorescence of TubulinTracker

in untreated or nocodazole treated fibroblasts (mean gray value). These data are ±S.E.M. and analysed with an unpaired two tailed t-test, where * indicated $p \leq 0.05$ and n = 3 coverslips.

To determine whether the nocodazole treatment also influenced actin, fibroblast cells were treated, immediately fixed, and placed on slides in a mounting medium containing phalloidin. Three replicates were carried out and there was no difference between the labelling of untreated and nocodazole treated cells. Images of phalloidin labelled fibroblasts are shown in Figure 46 (untreated and nocodazole treated).

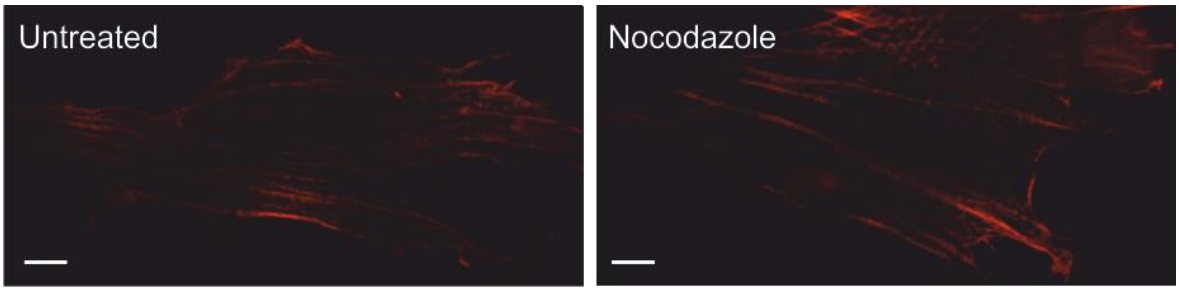


**Figure 46. Actin labelled with phalloidin in fixed fibroblast cells: untreated (left) and treated with nocodazole (right).** The scale bar is 10 µm.

The nocodazole treatment appeared to successfully depolymerise the microtubules with 20 µm nocodazole for 30 minutes. The effect of this microtubule depolymerisation on lysosome movement is shown in Chapter 5.

### 4.3.6 Summary of results

- The quantification of the number of lysosomes per cell was carried out using Cell Counter (manual method) or Nucleus Counter (automated method).
- A variation in the total number of manually counted lysosomes was found between replicates, between analysts and dependent upon the display screen. Figure 22
- Comparable results were achieved with Cell Counter and Nucleus Counter, indicating that either method was applicable. Figure 23
- The Nucleus Counter method included both the number and size of segmented regions and this is used for the analysis described in Chapter 5.

- The quantification of lysosome movement was carried out with Particle Tracker.
- The photobleaching of LysoTracker was found to have no significant impact on the ability to track lysosomes with Particle Tracker. LysoTracker was selected as the preferable probe for subsequent imaging experiments. Figure 24
- The number of frames and frequency of imaging did not detrimentally affect lysosome tracking with Particle Tracker. Therefore, lysosomes were imaged as rapidly as possible, to capture a high level of detail in their movement. Figure 24
- The movement of lysosomes was influenced by a combination of buffer and temperature. However, the difference was most pronounced in the population of lysosomes travelling the greatest distances. Figure 25 and Figure 26
- There was a larger population of lysosomes travelling greater distances (top 25%) in the cells which had been incubated at 37°C compared to room temperature. Figure 25 and Figure 26
- Lysosomes in FluoroBrite DMEM at 37°C travelled a greater distance in comparison to those in Imaging Buffer, however the reverse was true at room temperature. Figure 25 and Figure 26
- As the combination of 37°C and FluoroBrite DMEM most closely represented the physiological conditions for the cells, this condition was used for future lysosome tracking experiments.
- To analyse lysosome movement with a second method, the manual Frame Overlay method was described and compared against the automated Particle Tracker. Figure 28
- The Frame Overlay method enabled the measurement of the background cell movement, represented by the cell body and the nucleus which could be relatively static in comparison to the lysosomes. The movement of these two markers was significantly lower than that of the lysosomes, comparable to the lowest 1.5% of lysosome movement. Figure 30

- Lysosomes with characteristically different movement ‘long’ and ‘short’ pathways were compared in detail to assess the continuity of their movement. The short trajectory was found to have noticeable reduction in movement during a 10 second period out of 30 seconds. Both trajectories had the appearance of two bands of movement, with the distance changing from the high or low band between successive frames. Figure 33, Figure 34, Figure 35, Figure 36, and Figure 37
- The interpretation of lysosome movement was based upon the ‘maximum distance’ and ‘sum of distance’ (with velocity of travel being a transformation of the latter over time). Figure 39
- The relationship between ‘maximum’ and ‘sum’ distances was not linear. Figure 40, Figure 41, Figure 42 and Figure 43
- An assessment of the ‘long’ and ‘short’ trajectories showed that despite the poor correlation between sum and max, on average the population of long trajectories did have a longer trajectory (cumulative sum). This was reflected by a significantly greater slope of distance over time for the cumulative movement of the longer trajectories compared to the shorter ones. Figure 44
- Nocodazole treatment appeared to depolymerise microtubules, represented by a significant reduction in Tubulin Tracker fluorescence. However, nocodazole treatment did not have the same effect on actin, which was labelled with Phalloidin. Figure 45 and Figure 46
- The effect of microtubule depolymerisation on lysosome movement is described in Chapter 5.

## 4.4 Discussion

The experiments detailed in this chapter establish and compare methods for the analysis of lysosomes in live cells. These include the measurement of number and size of lysosomes regions, and the tracking of lysosome movement over time. Lysosomes were labelled with LysoTracker and imaged using the Leica fluorescence microscope. The methods for the quantification of these images was a key focus of this chapter.

### 4.4.1 Manual vs automated analysis

Image analysis was carried out using ImageJ, which has a number of tools available to facilitate the quantification of various parameters within the image. For simple quantification, functions such as the rectangle, straight line, or freehand selection tools can be used to measure distance, area, fluorescence intensity and amongst other readouts. More specific tools, such as the combination of Grid and Cell Counter to assist with the manual counting of lysosomes. These methods all rely on input from the analyst, such as drawing a line to measure the length, or the individual selection of each lysosome to count their total number. As the final value is determined by the analyst input, these methods are described as 'manual.' although a clearer definition may be 'semi-automated' due to the assistance of the ImageJ tools. The Nucleus Counter and Particle Tracker plugins apply a software-driven segmentation to the images based on pre-determined parameters. Therefore, there is little input from the analyst and these methods can be described as 'automated,' although it is worth considering that a degree of input was required to initially set the parameters for analysis.

Manual methods of analysis have the benefit of the enhanced decision making that a human analyst has over even complex algorithms. However, the same human decision making is open to error, subjectivity, and bias. Automated methods are highly repeatable, as a large number of images can be analysed with identical settings, reducing the variation associated with manual decision making. Furthermore, automated image analysis is carried out using the numerical data comprising the image, and therefore bypasses any influences such as the clarity of the display on screen. Finally, the use of automated methods allows for a far greater number of replicates to be analysed compared to more time consuming manual approaches.

### 4.4.2 Quantification of lysosome labelling: number and size of segmented regions of lysosomes

Measurement of the number of lysosomes was carried out with both manual and automated analysis. However, only the automated segmentation using Nucleus Counter allowed for a measurement of the size of the lysosome regions. Therefore, the comparison of these methods was

based upon the number of lysosomes, or segmented regions of lysosome staining, which were counted. The basic findings suggested that while considerable error was introduced in manual counting by different analysts and using different screens, the average count was comparable to that of the automated method. This served two purposes: to verify that the methods were comparable and to suggest that the variation in the manual count did not make a significant difference to the average when compared to the automated counting. Both methods appear to be comparable, and the benefits of the automated counting include its rapid application, high repeatability, and the measurement of size.

The measurement of the size of segmented regions is of interest to analyse their potential clustering, which is discussed further in Chapter 5. Ideally, lysosomes would be counted and measured individually to represent the absolute number and size per cell. However, there are three major challenges with this: Firstly, the segmentation of individual lysosomes in a population where many lysosomes were closely grouped. Secondly, the diffusion of the fluorescence signal. Finally, the three dimensional structure of the cell and which could result in lysosomes offset from the plane of imaging. Each of these factors could influence the measured size of the lysosomes.

The measurement of lysosomes based on segmentation is influenced by the number of clusters of lysosomes. If cells had a greater clustering of lysosomes, the number of segmented regions may be reduced, with the size of these increased. Therefore, while this analysis is not necessarily a reliable measurement of the absolute number and size of lysosomes, it presents an opportunity to assess regions of lysosome staining and determine the extent of lysosome clustering based upon the size of the regions. This was applied to the study of lysosome clustering, which is discussed in Chapter 5.

The diffusion of the signal associated with fluorescence imaging means that fluorescently-labelled structures such as lysosomes can lack a sharp boarder and may appear larger than their true size. If this was equally true of all lysosomes in all images, the relative size would still be useful for comparison purposes. However, as illustrated in Figure 47, lysosomes do not necessarily all align with the plane of imaging. The example lysosomes A, B and C are offset from the plane of imaging to different degrees and their appearance in the image is represented below.

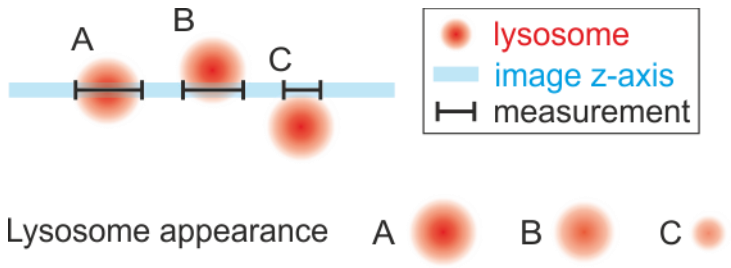


**Figure 47. Cartoon to illustrate lysosome measurements**. The blue line represents the plane of imaging (z-location), while the red structures are representative of lysosomes and the black lines denote measurement of these from the two dimensional image.

### 4.4.3 The optimal conditions for imaging lysosome movement

After lysosome counting and measurement, the second and more complex analysis of lysosomes relates to aims 2, 3 and 4: the tracking of lysosome movement. To establish this assay, the conditions first had to be optimal for imaging lysosome movement in live cells. This included the choice of lysosome probe to achieve high quality images that would be suitable for segmentation and tracking.

As LysoTracker was the preferred probe and this was associated with a high rate of photobleaching, it was important to test whether the loss of signal caused a loss of lysosome tracking during analysis. To determine the influence of the photobleaching on the tracking, the number of lysosomes tracked to final frame was plotted in, comparing 0.2 s, 0.5 s and 1.0 s. The process of tracking lysosomes involves the identification and labelling of each lysosome per frame by the Particle Tracker plugin.

Segmentation was driven by a number of factors. The most significant of these for photobleaching is the ‘percentile’ which relates to the percentile of the fluorescence profile which is considered to be a labelled structure, in this case LysoTracker fluorescece. Tracking lysosomes using the Particle Tracking plugin meant that lysosomes had to be identified in each frame of the series in order to plot their location throughout. If the plugin was unable to identify lysosomes due to a loss of fluorescence over time caused by photobleaching, this would be unsuitable. However, the results of Figure 24 clearly show that photobleaching did not deterimentally affect the tracking of the lysosomes. This may be because the photobleaching effect was constant and universal across the image, so the top percentile remained relative.

Lysosomes trajectories were not always complete, but for the purposes of analysis, the trajectories of interest are those plotted from the first to the final frame. The data was filtered after tracking to remove any incomplete trajectories and therefore all data was comparable for the full 30 second imaging period.

### 4.4.4 Buffer and temperature

The next stage of the assay setup was to detemine the optimal conditions for imaging, to ensure that the tracked lysosome movement was representative of cells in physiological conditions. The influence of conditions such as starvation on processes related to lysosome movement meant that all loading and imaging was carried out in conditions as close to cell culture as possible. For many experiments, live cell indicators are loaded at room temperature, in a simple imaging buffer (IB). For lysosome tracking, loading was carried out in the 37°C incubator and FluoroBrite DMEM (FB) was used in place of imaging buffer. The medium was selected for its lack of phenol red to minimise background fluorescence and supplemented with GlutaMAX. The medium was partially complete, as no serum was added to minimise the background fluorescence and avoid interference during loading and imaging. The lack of serum raises the possibility that the cells were subject to starvation, but this is likely to be minimal within the rapid 30 minute loading and 3 minutes of imaging. Furthermore, all cells were incubated in the same formulation, so this was not introduced as a variable.

Amongst the different combinations of buffer and temperature, it was temperature that appeared to have the most significant impact on lysosome movement. The greatest distances were travelled by lysosomes in the cells incubated in FB at 37°C, followed by those incubated in IB at 37°C. Conversely, between the two conditions at RT, lysosomes travelled a greater distance in the cells in IB compared to FB. It is possible that the formulation of FB did not perform correctly at RT, as this is a cell culture medium designed for use within an incubator. However, the FB was pH adjusted and stabilised with HEPES to regulate pH independently of the $C0_2$ incubator and the pH of the medium was stable upon checking after completion of experiments, so it is unlikely that this was responsible. Although the mean distance travelled by lysosomes was significantly different overall (Figure 24) the percentile plots showed that the greatest effect of temperature and buffer appeared to be in the lysosomes travelling the furthest (Figure 25). Analysing the top percentile of movement from lysosomes in the cells strengthened the significant differences between the conditions (Figure 26).

### 4.4.5 Background movement of lysosomes

The Frame Overlay method was used to measure distance between structures within images taken at a set time apart. This was useful for: (1) the verification of Particle Tracker measurements and, (2) the tracking of background cell movement, which could not be analysed using Particle Tracker.

Background movement from the cell was not expected to be the underlying cause of the measured lysosome movement, as the lysosome trajectories plotted by Particle Tracker clearly travelled in multiple dimensions. If the cell had drifted, it might be expected that all lysosomes would be

measured as travelling in a single direction. Regardless, any cell movement could still be enough to interfere with the very sensitive and detailed frame by frame measurements of lysosome movement.

### 4.4.6 Characteristics of lysosome movement

#### *4.4.6.1 Trajectory illustrations*

The observed trajectory illustrations revealed two distinct movement patterns: 'short' trajectories which hovered at a fixed point and 'long' trajectories which travelled within the cell. The majority of lysosomes appear to have short trajectories and the difference between the movement patters is of interest due to its potential biological importance. As lysosomes are motile organelles, the ability to reposition within the cell, transport material and closely interact with other organelles (such as fusion with autophagosomes) is a critical part of their function. Therefore, analysing the maximum distance of travel is useful to examine the total trajectory length.

The other readout for lysosome movement was the sum distance (length of trajectory, regardless of the directional, linear distance travelled within the cell) which was also transformed to velocity (distance over time). These indicated the length and speed of the trajectory overall, without specifically differentiating between those travelling over a distance or moving around a fixed point. The combination of the study of maximum distance, sum of trajectory path and velocity of movement all provide opportunities for the assessment of lysosome dynamics in cells healthy and CLN3 disease model cells, which was carried out in Chapter 5.

The movement of lysosomes in the cell may be driven by motor proteins, or subject to diffusion and passive transport within the cell (Bandyopadhyay et al., 2014, Cabukusta and Neefjes, 2018). This may include Brownian motion occurring due to the fluid plasma membrane (Saxton and Jacobson, 1997). Although the movement of the cell and nucleus were found to be relatively low compared to the lysosome, the size of lysosomes compared to the nucleus suggests that these may be more suspectable to forces of passive movement such as diffusion which is discussed further in Chapter 5.

The analysis of example lysosomes with long and short trajectories (306 and 37) showed that movement was somewhat continuous, although the short trajectory had a period in which movement was almost negligible. It was possible that the low level fluctuating movement was a result of some instability of the microscope stage which was not picked up by the analysis of total background movement (Figure 30). However, as both lysosomes 37 and 306 were from the same example, it might be expected that any influence on the cell would be observed in both trajectories equally. The reduction in movement of lysosome 37 at around 5 to 15 seconds is not mirrored in the same period of time on the plotted distances of lysosome 306.

The extremely rapid imaging of these lysosomes means that movement are tracked in a very precise and sensitive manner. This is excellent for the study of lysosome trajectories in great detail but also leaves the assay vulnerable to over-interpretation or perhaps minor changes from external influences. On the other hand, a slower recording would lose much detail of the trajectories and given the small size of lysosomes, even a small movement can represent a significant distance within the cell and perhaps an exertion of energy in response to stimulation.

One of the possible influences on the sensitive tracking assay, especially given the extremely small distances being measured, is the plane of imaging. This was previously discussed in relation to lysosome location and therefore their apparent number and especially their size. However, with tracking, a slight misalignment with the plane of imaging could influence the measurements to a considerable degree.

As illustrated in Figure 48, lysosome movement may not be parallel to the frame of imaging. The arrows (A, B and C) show differently angled trajectories; if each lysosome moved an equal distance in each of those directions, only lysosome B would have an accurate measurement due to being parallel to the axis of imaging. Conversely, A and C would appear to have shorter trajectories due to their travel on the z-axis.

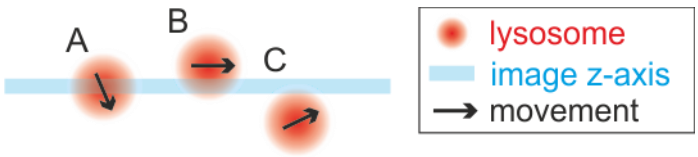


**Figure 48. Cartoon to illustrate lysosome movement.** The blue line represents the plane of imaging (z-location), while the red structures are representative of lysosomes and the black arrows represent directional movement.

Two visual clues suggested that the lysosome movement was more likely to be parallel to the plane of imaging than perpendicular. Firstly, the appearance of the lysosomes themselves did not show an increase in fluorescence which would indicate that lysosomes were travelling towards the plane of imaging from another region. The change in LysoTracker fluorescence over time was the universal steady decline caused by photobleaching with no rapid drop in individual lysosome fluorescence to suggest a lysosome travelling away from the plane of imaging. Secondly, the Tubulin Tracker staining indicates that microtubules are arranged in a linear manner along the plane of imaging, as illustrated in Figure 49. This cell was grown on a glass coverslip and imaged using the fluorescence microscope, the same conditions as used for imaging lysosome movement.

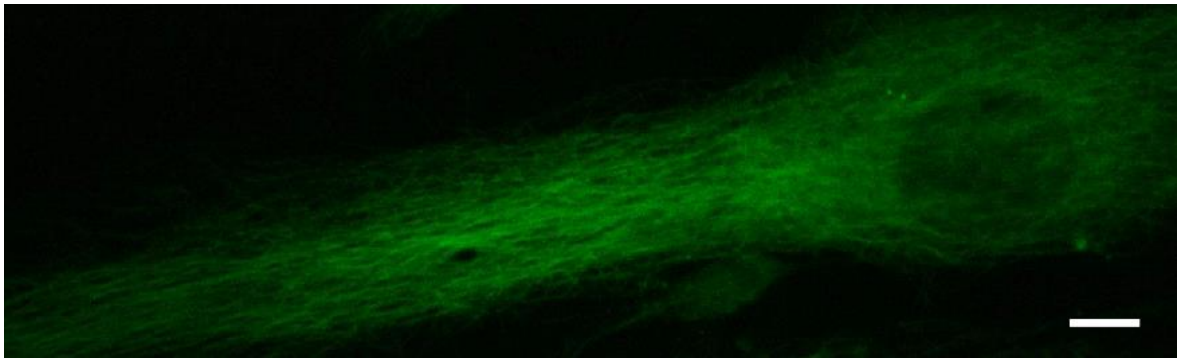

**Figure 49. Microtubules in a Tubulin Tracker loaded fibroblast cell.** The microtubules have an organised and elongated appearance which suggests a degree of parallel with the plane of imaging. The scale bar is 10 µm.

On the whole, it was very unlikely that the majority of lysosomes exhibiting their hovering movement were travelling up and down, perpendicular to the x-axis. Nonetheless, it was certainly possible that the trajectories were not all strictly parallel. The results were strengthened by the large number of lysosomes tracked per cell, the number of replicates (multiple cells, from multiple coverslips across multiple days) and the precise replication of the imaging conditions and analysis methods. The assay was carefully carried out to ensure that it was sensitive and robust despite the challenges associated with the three dimensional nature of the cells and the limitation of fluorescence imaging.

As explained previously, the 'link range' which facilitated tracking of lysosomes over a greater distance was harshly reduced to avoid aberrant linkage. Briefly, this was due to the proximity of lysosomes in the cell and the high risk of linking separate lysosomes using this alogrithm. As a result, a large number of lysosomes were not tracked throughout each frame and this was often where lysosomes had come ino very close proximity (likely crossing paths above or below another, with the appearance of close contact due to the single z-plane of imaging). The harsh reduction of link range reduced the available data, but improved the accuracy of the tracking that was sucessfully completed. In addition to loss of segmented lysosomes from the first frame, new lysosome labels were added, often in place of a trajectory which had been briefly disrupted. The data was cleaned for broken trajectories to represent the full trajectory plotted across 30 seconds.

The continuity of movement was illustrated through plotting the average distances in 3 or 10 second intervals within the total 30 second imaging time (Figure 33, Figure 34, Figure 35 and Figure 36). The plots showed that even by splitting up the frames to sections of 10% of the total imaging time (3 seconds) there was distinctive variation represented by the size of the S.E.M. and the distribution of the scatter plots representing the distance between each frame.

## 4.5 Future work

### 4.5.1 The effect of temperature on lysosome movement

The finding that temperature had a measurable influence on lysosome movement was an interesting result in its own right which could warrant some further investigation.

This would be best carried out with a microscope with a chamber which would allow for the precise control of temperature to determine the full extent to which lysosome movement is sensitive to temperature. Additionally, it would be interesting to introduce some more extreme temperatures, such as raising the temperature of the cells above 37°C.

### 4.5.2 The effect of buffer/nutrients on lysosome movement

The formulation of Imaging Buffer was essentially a pH 7.4 balanced salt solution with minimal supplementation such as glucose. As such, Imaging Buffer missed some of the key components of cell culture medium such as amino acids and serum. The FluoroBrite DMEM was purchased as a clear alternative to cell culture medium. The FluoroBrite DMEM was additionally supplemented with GlutaMAX, in order to closely match the formulation of the GlutaMAX DMEM which was used in cell culture.

### 4.5.3 Imaging experiments

As an assay for lysosome movement, the tracking method has a lot of potential and this is applied in Chapter 5 to the study of CLN3 disease. However, in order to learn more about the specific dynamics of lysosome movement under normal conditions, it would be interesting to expand the imaging to incorporate colocalisation as a means to

- **Cellular structures**: microtubules and the nucleus. If the movement of lysosomes is indeed along microtubules it would be valuable to plot the trajectories along these tracks in confirmation of the microtubule-dependent nature of this movement. The accumulation of lysosomes at the nucleus is associated with lysosome function and a response to conditions such as starvation (Pu et al., 2016). Therefore, the proximity of lysosomes to the nucleus may be an interesting clue to the purpose of their movement.
- **Other organelles**: autophagosomes, endoplasmic reticulum and mitochondria. The observation that lysosomes often stopped and started their movement at set points makes it extremely interesting to determine whether another organelle was present at these locations.

Naturally, the challenge with both multiplexed imaging and z-stacks is that these dramatically reduce the available imaging speed and increase exposure which would photobleach the fluorescent probes.

Finally, in combination with lysosome labelling, it would be interesting to express markers of early and late endosomes in order to compare these populations with LysoTracker-labelled vesicles. The extent to which lysosomes overlap with late endosomes was previously discussed in Chapter 4 and it would be interesting to determine whether the lysosomes with greatest movement were in fact late endosomes, or more structurally similar to these. As endosomes are responsible for endocytosis and therefore these are certainly expected to move throughout the cell (Pu et al., 2016).

Furthermore, an ideal use for the assay may be in combination with autophagosome labelling and the induction or inhibition of autophagy through pharmacological treatment of live cells. Any cell model with a defect in autophagy may reveal an alteration in the movement of lysosomes if their ability to correctly reposition to undergo autophagy is affected.

Ultimately, the ability to track lysosomes in large numbers and a high level of detail has great potential for: (1) the examination of lysosome dynamics and a greater understanding of their movement within the cell, and (2) application to cell models of disease to inspect lysosome movement.

# 5 Examining putative effects of CLN3 knockout on lysosomal positioning and movement

## 5.1 Introduction

Chapters 3 and 4 outlined the empirical steps that determined the choice of lysosomal probe used in this study, and the careful setup for assays to analyse the numbers, clustering, and movement of lysosomes in live cells. Whilst the previous chapters established the essential methodology, the work described in this chapter depicts how the toolkit was applied to study the behaviour of lysosomes in cells with and without mutations in their *CLN3* gene.

Chapter 4 also established that depolymerisation of microtubules significantly inhibited lysosomal movement. The movement of lysosomes within cells is known to be dependent upon microtubules (Pu et al., 2016). Nocodazole is a well-known effector of microtubule depolymerisation in live cells. Numerous studies have verified the effect of nocodazole at various doses and incubation times: 10 µM for 5 hours (Matteoni and Kreis, 1987), 20 µM for 30 minutes (Baravalle et al., 2005) and 20 µM and 50 µM for 30 minutes (Jahreiss et al., 2008). In Chapter 4, depolymerisation of microtubules was demonstrated by a reduction in Tubulin Tracker staining after a treatment of 20 µM nocodazole for 30 minutes. Therefore, the treatment conditions were used as a positive control in this chapter in the study of lysosome movement in CLN3 cell models.

**Aims and objectives**

**Aim 1: to measure lysosome clustering in CLN3 cell models**

Objectives:

- Measure the size (area in $\mu m^2$) of HeLa and fibroblast cells, to compare the WT and the CLN3 disease model cell lines.
- Establish whether there is a relationship between cell size and the number of segmented lysosome regions.
- Measure the size of the lysosome regions segmented by Nucleus Counter (described in Chapter 4) to determine whether the lysosome clustering effect of nocodazole treatment in HeLa cells could be quantified.
- Measure the size of segmented lysosome regions to determine whether the CLN3 mutation in HeLa and fibroblast cells causes clustering of lysosomes.

**Aim 2: to measure lysosome movement in CLN3 cell models**

Objectives:

- Track and quantify lysosome movement in HeLa and fibroblast CLN3 cell models using Particle Tracker (described in Chapter 4)
    - Maximum distance of lysosome movement (distance between furthest points)
    - Velocity of lysosome movement (sum of distance over time)
- Determine whether any changes to the distances moved by lysosomes occur for all lysosomes, or solely those travelling in the top 25% of moving lysosomes
- Compare the movement of lysosomes in WT HeLa and fibroblast cells

## 5.2 Methods

The methods for cell culture and imaging are described in Chapter 2. The methodologies used for lysosome counting and tracking are described in Chapter 3. The 'Nucleus Counter' method was used for segmenting, counting, and measuring the size of areas of lysosome fluorescence. The 'Particle Tracker' method was used for the tracking of lysosomes, with subsequent calculations carried out to determine; (1) maximum distance, representative of the distance travelled by lysosomes within the cell and, (2) velocity of movement, as the sum of the lysosome trajectory in a defined period of time to represent the overall speed of travel.

The control cells and cell models of CLN3 disease studied in this chapter are:

1. HeLa cell lines
    a. WT
    b. CLN3 KO
2. Fibroblast cell lines
    a. Healthy donor (WT)
    b. CLN3 patient with the Δex7/8 mutation
    c. CLN3 patient with the D416G mutation

The cells were untreated (DMSO vehicle control) or treated with 20 µM nocodazole for 30 minutes to depolymerise microtubules. To image lysosomes, the cells were loaded with LysoTracker and imaged using the fluorescence microscope as described in Chapter 2.

## 5.3 Results

### 5.3.1 Accuracy in the identification of individual lysosomes vs. groups of clustered lysosomes

As discussed in Chapter 4, LysoTracker staining could be quantified using the Nucleus Counter plugin. Images were segmented by Nucleus Counter, which recorded the total number and average size of these regions (area in $\mu m^2$), henceforth called segmented lysosomes. Initially, this statistic was considered to be useful as a quantification of the approximate number of lysosomes (based on regions of LysoTracker staining) and their relative size. However, an observation emanating from the use of nocodazole-treated cells led to an additional question: does the segmentation and quantification achieved using Nucleus Counter accurately reflect an increase in the size of individual lysosomes, or may it report an increase in size because lysosomes cluster together so that individual lysosomes can no longer be resolved and distinguished by the segmentation?

Cells loaded with LysoTracker were treated with nocodazole for the purpose of depolymerising microtubules, as first described in Chapter 4. The LysoTracker staining in untreated cells showed lysosomes of a similar size, shape, and intensity, distributed throughout the cells (Figure 50A). Conversely, the LysoTracker staining in the nocodazole treated cells showed some larger regions with an elliptical shape and brighter staining (Figure 50B). To determine whether this effect was a true representation of the lysosomes, or an effect on the LysoTracker probe, the treatment was repeated in cells expressing CellLight to label lysosomes. As described in Chapter 3, CellLight is a pH-independent probe that labels lysosomes through expression of a GFP-tagged lysosomal membrane protein rather than via accumulation within the lysosomes. The appearance of larger, brighter regions following nocodazole treatment was replicated in cells expressing CellLight, as shown in Figure 50.

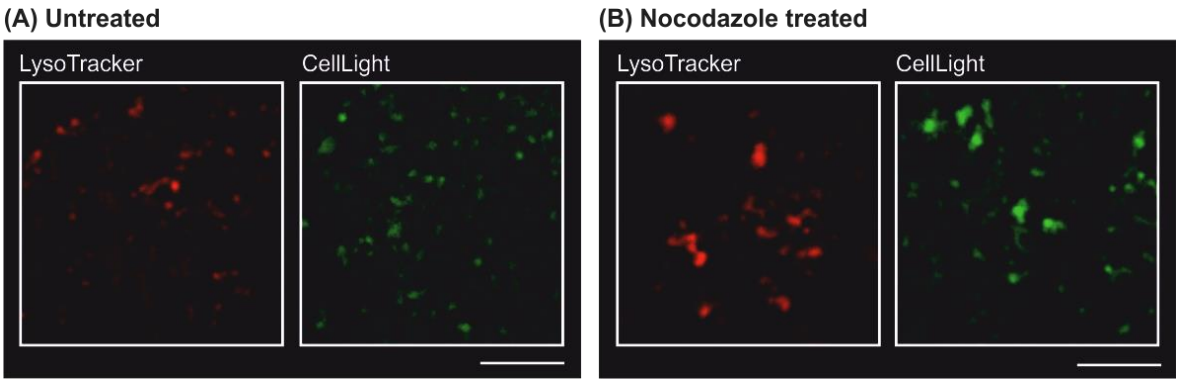


**Figure 50. The appearance of lysosomes in untreated and nocodazole treated cells.** The panels show the appearance of LysoTracker and CellLight probes in: (A) untreated HeLa cells and (B) cells after 30 minutes 20 µM nocodazole treatment. The scale bars are 10 µm.

To confirm whether the appearance of the larger, brighter, and unusually shaped regions of lysosome staining was caused by enlargement of individual lysosomes, or by clustering of several lysosomes that could not be separated using the segmentation, the fluorescence profile of several examples was examined (Figure 51).

Figure 51 shows the fluorescence profiles of two distinct and separate lysosomes (Figure 51A) and two other lysosomes that were close in proximity but were still clearly resolved as discrete entities (Figure 51B). The traces shown in Figure 51 indicate the fluorescence intensities measured along a lines drawn through the lysosomes (yellow line in the images) in Figures 2A and B. Where the lysosomes were separate (Figure 51A), each lysosome had a distinct peak in the fluorescence trace. The lysosomes in closer proximity (Figure 51B) had two peaks which were almost merged, as the fluorescence intensity profile did not return to baseline in between the peaks. These data illustrate that lysosome fluorescence profiles may be joined, but each individual lysosome should show a peak towards its centre where the signal is strongest.

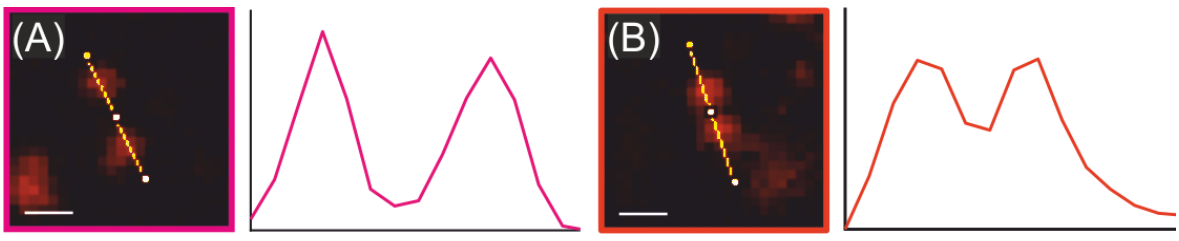


**Figure 51. Resolving adjacent lysosomes.** (A) Two clearly distinct peaks associated with lysosomes that are not touching. (B) Two lysosomes in closer proximity. The fluorescence signal intensity (gray value) along the yellow line drawn through the image was plotted in the line traces. The scale bar is 1 µm.

Examples of both LysoTracker- and CellLight-labelled lysosomes in cells with and without nocodazole treatment were examined. In the untreated cells, the majority of lysosomes had a clear single peak as shown in Figure 52(A). In cells treated with nocodazole, the distribution of lysosomes was less uniform, and cells showed regions with large areas of fluorescence. A profile plotted through these larger areas of lysosome staining generally showed multiple peaks signifying that these were several individual lysosomes clustering in close proximity Figure 52(B).

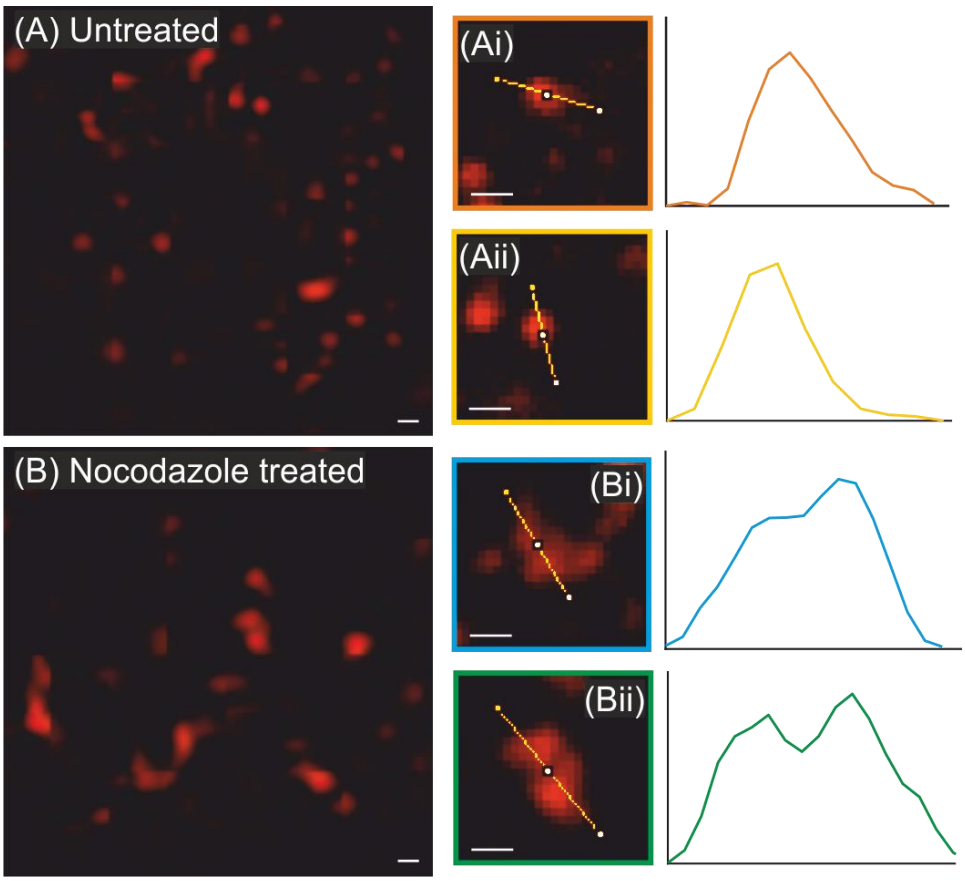


**Figure 52. Comparison of lysosome distribution in untreated and nocodazole-treated cells.** LysoTracker-loaded HeLa cells: (A) Untreated and (B) nocodazole treated. The plotted fluorescence profile (gray value plotted on the y-axis) illustrates the LysoTracker signal along the yellow lines. (A) In the top panels, single lysosomes from the image of an untreated cell can be identified in the images and by their single peak. (B) In the bottom panels, from the image of a nocodazole treated cell, the plotted profiles have a less smooth appearance with two peaks, indicating that two lysosomes were in close proximity. The scale bar is 1 µm in all images.

The treatment of cells with nocodazole induced a phenotype of lysosome clustering. The segmentation attainable with the Nucleus Counter plugin was not able to segment the individual lysosomes following nocodazole treatment, but it allowed the clustering phenotype to be investigated by measuring an increased area for the segmented regions, as discussed below. To indicate that the measured numbers and areas are not necessarily those of individual lysosomes, they are henceforth called 'segmented lysosome regions.'

### 5.3.2 Cell size, number of lysosomes and clustering of lysosomes in HeLa cells

To study if knockdown of CLN3 caused changes in the number of lysosomes or induced a clustering phenotype, untreated and nocodazole-treated WT and CLN3 KO HeLa cells, were analysed using the Nucleus Counter method. The number of lysosomes in a cell could be affected by the area of the cell, with a larger cell potentially having more lysosomes. Therefore, in a first step, cell area and number of lysosomes were analysed to establish if there is a relationship between cell area and the number of lysosomes.

There was no significant difference between the average cell area of the WT HeLa and the CLN3 KO HeLa cell lines as shown in Figure 53A. Figure 53B and C show a weak relationship between cell area and the number of lysosomes for both cell lines. Therefore, the number of segmented lysosomes could be compared directly, and did not have to be normalised to cell area.

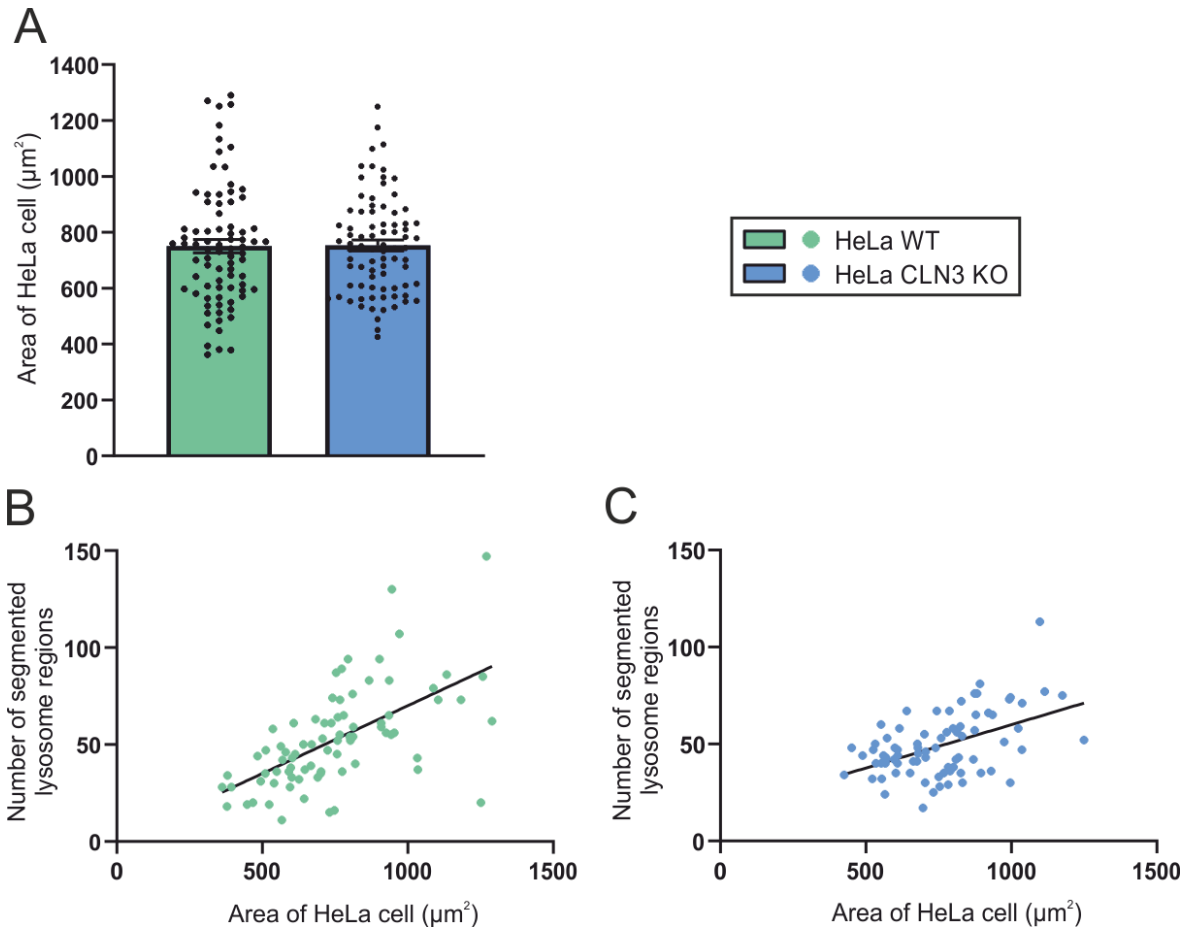


**Figure 53. Area of HeLa cell and the relationship with number of lysosomes.** (A) Area of HeLa cells plotted as mean ± S.E.M. with scatter points representing individual cell area. These data were analysed with an unpaired t-test and n = 81 cells from 9 images (from 3 coverslips on 3 days). (B) The number of lysosomes per cell plotted against the size of each WT cell. (C) The number of lysosomes per cell plotted against the size of each CLN3 KO cell. The lines show the results of a linear regression calculation for both data sets and indicates a weak correlation (WT, $r^2 = 0.36$ and CLN3 KO, $r^2 = 0.24$).

To test whether the clustering of lysosomes in the nocodazole treated cells caused a significant difference in the area of the segmented lysosomes, and if this area was affected by the genotype, the area of segmented lysosomes was quantified (Figure 54). There was a significant increase in the size of the segmented lysosomes in the nocodazole treated cells. The increased area is interpreted as a larger number of clustered lysosomes being present in the cells. The size of the segmented regions does not differ between the WT and CLN3 KO cell lines, suggesting no effect of the CLN3 mutation on clustering of lysosomes.

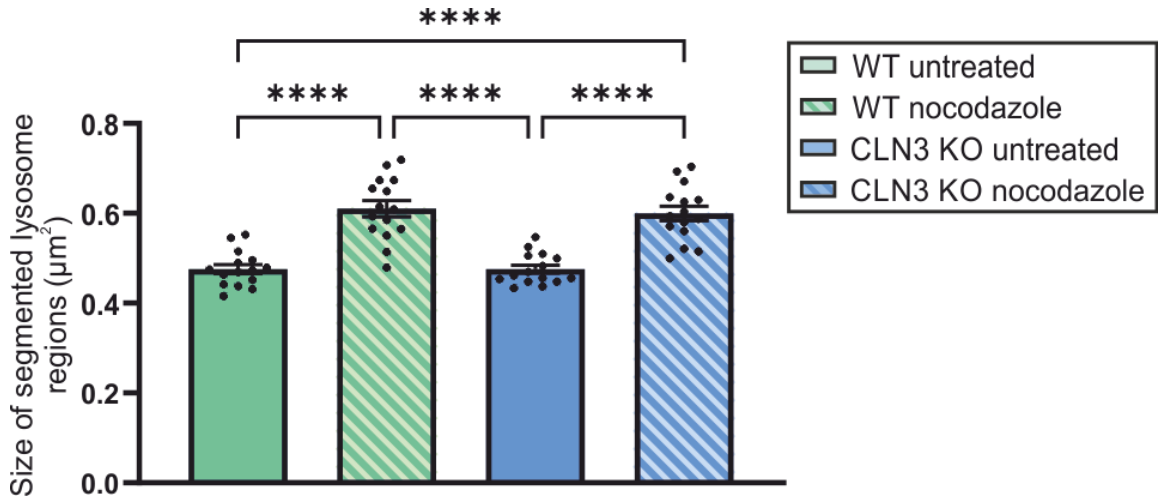


**Figure 54. Lysosome clustering in HeLa cells.** These data were analysed with an Ordinary one-way ANOVA with Tukey's multiple comparisons test and n = 81 cells from 9 images (from 3 coverslips on 3 days).

### 5.3.3 Cell area, number of lysosomes and clustering of lysosomes in fibroblasts

Cell size, number of segmented lysosomes and their area were also analysed for the WT, Δex7/8 and D416G fibroblast cell lines. First, it was established whether the number of segmented lysosomes correlated to cell area (Figure 55). No differences were found for the cell area (Figure 55A), and, like the results in HeLa cells, only a weak correlation of cell area and number of segmented lysosomes was found (Figure 55B).

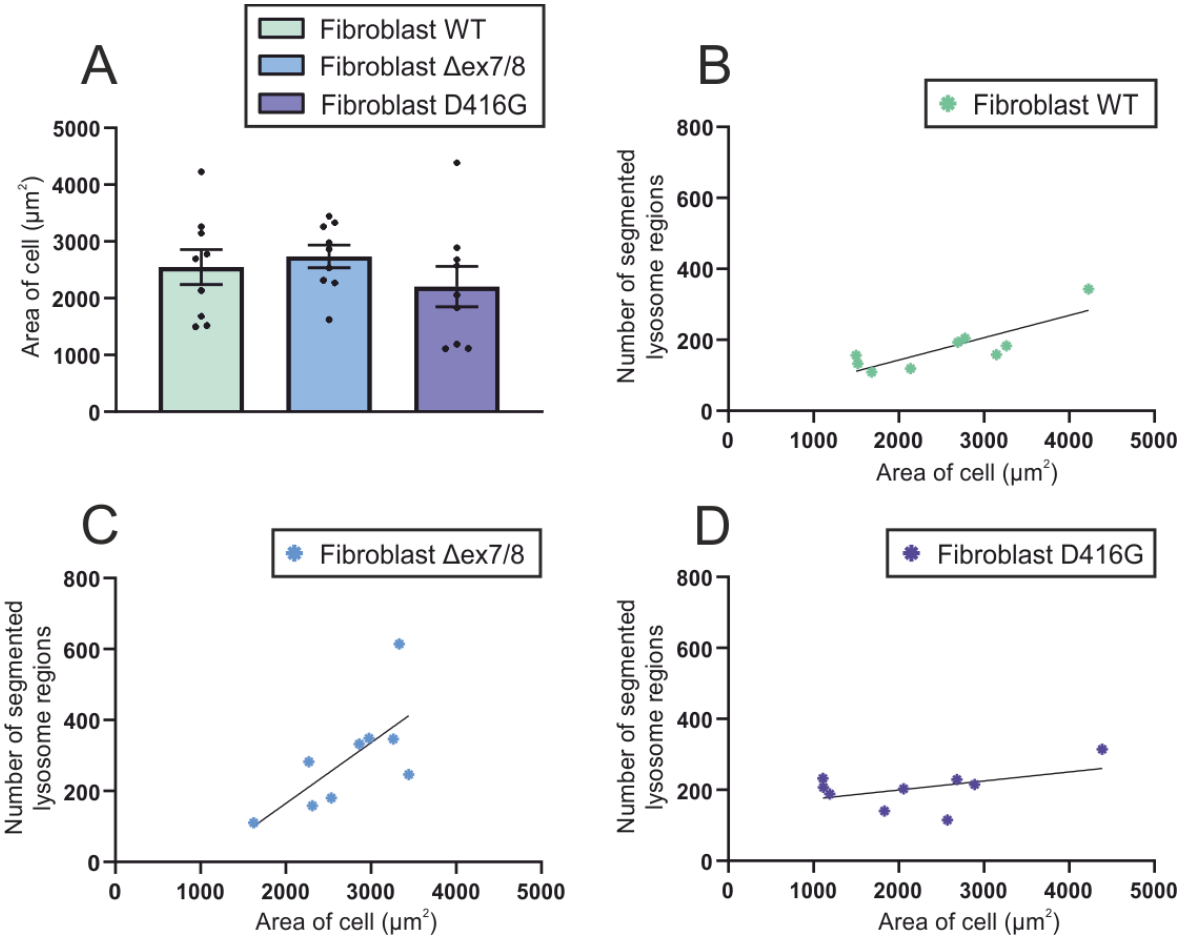


**Figure 55. Fibroblast cell area and number of segmented lysosome regions**. These data were analysed with an Ordinary one-way ANOVA with Tukey's multiple comparisons test for n = 9 cells (from 3 coverslips, on 3 days). The lines show the results of a linear regression calculation for each data set and indicate a weak correlation (WT, $r^2 = 0.31$, Δex7/8, $r^2 = 0.10$ and D416G, $r^2 = 0.20$).

The comparison of the WT, Δex7/8 and D416G fibroblast cell lines in Figure 56 revealed no significant difference between the size of the segmented lysosome regions. This suggests that there is no quantifiable clustering of lysosomes within any of the fibroblast cell lines.

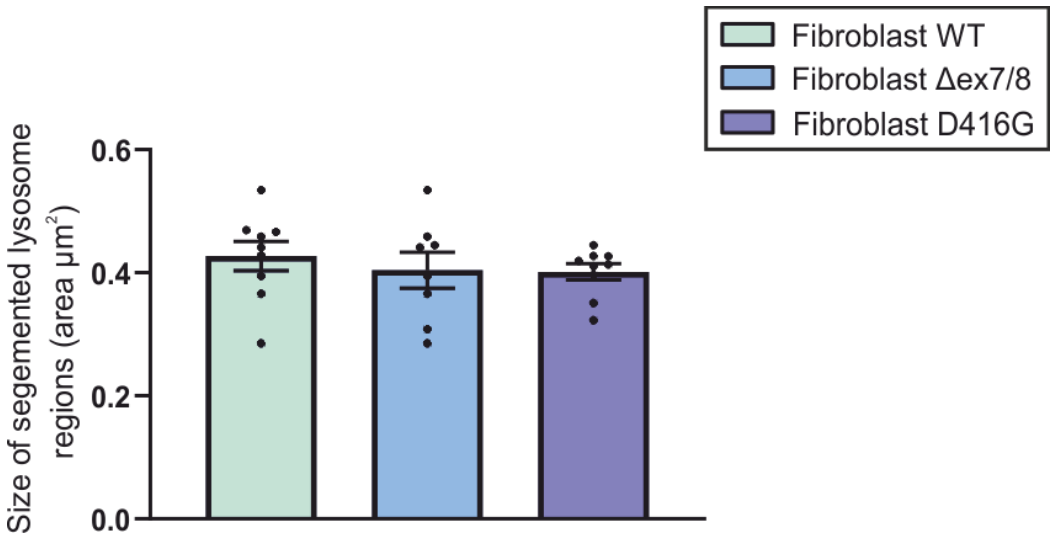


**Figure 56. Lysosome clustering in fibroblast cells.** These data were analysed with an Ordinary one-way ANOVA with Tukey's multiple comparisons test and n = 9 cells (3 coverslips on 3 days).

### 5.3.4 Tracking lysosome movement in live cell models of CLN3 disease

The assay to track and analyse lysosome movement was explained in Chapter 4. The experiments described in this section detail the application of the lysosome tracking assay to the CLN3 cell models.

To induce a phenotype of reduced lysosome movement in the cells, the microtubules were depolymerised with nocodazole treatment. DMSO was used as a vehicle control. Following these treatments, the cells were loaded with LysoTracker and imaged as set out in Chapter 2. The analysis and interpretation of the data was carried out according to the methods described in Chapter 4.

Lysosomal movement was analysed in two ways:

**1) Maximum distance** – the widest span travelled by each lysosome within the cell.

**2) Velocity** – a transformation of the sum distance (total frame-by-frame movement) over time

### 5.3.5 Tracking Lysosome movement in HeLa cells

WT and CLN3 KO HeLa cells were used to investigate whether there was a change to lysosome movement in this cell model of CLN3 disease. The movement analysed here is the maximum distance, which gives an idea if a lysosome moved over a long distance in a cell.

The movement of lysosomes for individual cells of each cell line (untreated or treated with nocodazole) was measured and plotted in Figure 57 to give an idea about the variability of the cells within each dataset. The bars represent the mean distance moved by lysosomes per cell, with the

scatter points showing the measured distance moved by each individual lysosome. There is some variation in the height of the bars which is most pronounced in the CLN3 KO cell lines and indicates that the mean of lysosome movement distance was not entirely consistent across the replicates (cells) per dataset.

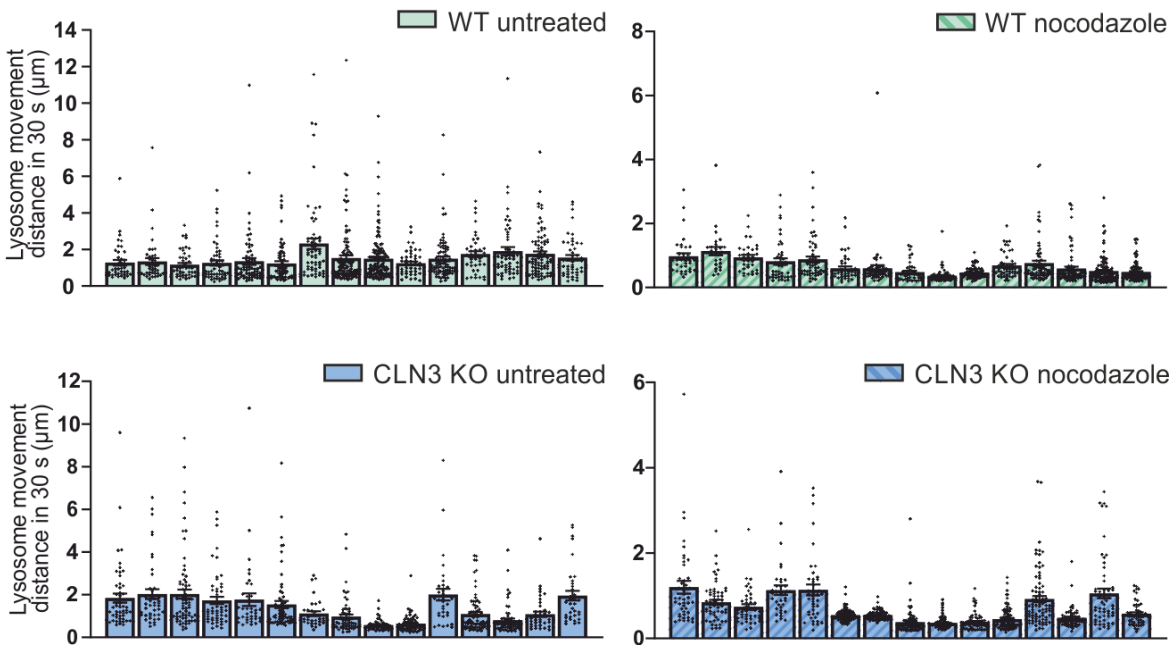


**Figure 57. The maximum distance travelled by lysosomes in HeLa cells.** HeLa cell lines were either untreated or nocodazole treated, loaded with LysoTracker and movement of lysosomes was recorded for 30 seconds. These data are mean ± S.E.M. per cell, with scatter points representing individual lysosome movement within each cell. The y-axis scale is adjusted to clearly present the spread of data points relative to the height of the bars for each data set.

To summarise the data, the average distance of lysosome movement was plotted for each condition shown in Figure 58. For both the WT and CLN3 KO cell lines, nocodazole significantly reduced the distance travelled by lysosomes within the 30 second imaging period. There was no significant difference between the WT and CLN3 KO cells, which were comparable in both the untreated and nocodazole treated conditions. However, there was a noticeable increase in the S.E.M. of the distances travelled by lysosomes in CLN3 KO cell line, particularly in the untreated cells (Table 16). The S.E.M. of the data from the untreated cells was lower than the nocodazole treated cells, as the treated cells lacked the population of lysosomes travelling greater distances.

**Table 16. The S.E.M. of maximum distance travelled by lysosomes in the HeLa cells.**

| WT untreated | WT nocodazole | CLN3 KO untreated | CLN3 KO nocodazole |
|---|---|---|---|
| 0.08 | 0.06 | 0.14 | 0.08 |

While nocodazole did still significantly reduce movement in lysosomes in the CLN3 KO cells, the significance of this difference was weaker due to the larger S.E.M. of the untreated cells.

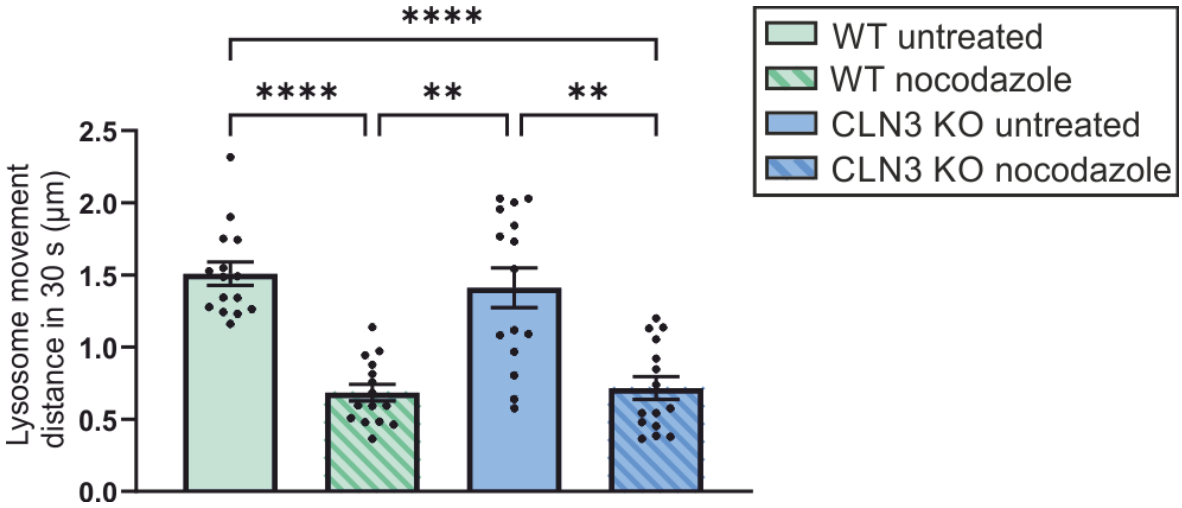


**Figure 58. The mean maximum distance travelled by lysosomes in HeLa cells.** HeLa cell lines were either untreated or nocodazole treated, loaded with LysoTracker and recorded for 30 seconds. These data are mean ± S.E.M. per cell, with scatter points representing mean lysosome movement per cell. These data were analysed with Kruskal-Wallis with Dunn's multiple comparisons where ** indicates $P \leq 0.01$, **** indicates $P \leq 0.0001$ and n = mean distance of lysosomes in 9 cells (from 3 coverslips on 3 days).

The distances travelled by lysosomes were plotted by the percentile in Figure 59. There was a clear distinction between the profile of lysosome movement in untreated cells compared to nocodazole treated cells: a far greater number of lysosomes travelled further in the untreated cells which is represented by the increase of the distances as early as 50% and a very clear increase throughout the top 25%. Conversely, the majority of lysosomes in nocodazole-treated cells travelled very little and the small increase seen in the top percentiles remained far lower than that of the untreated cells, indicating that the directed movement over longer distances was inhibited by nocodazole.

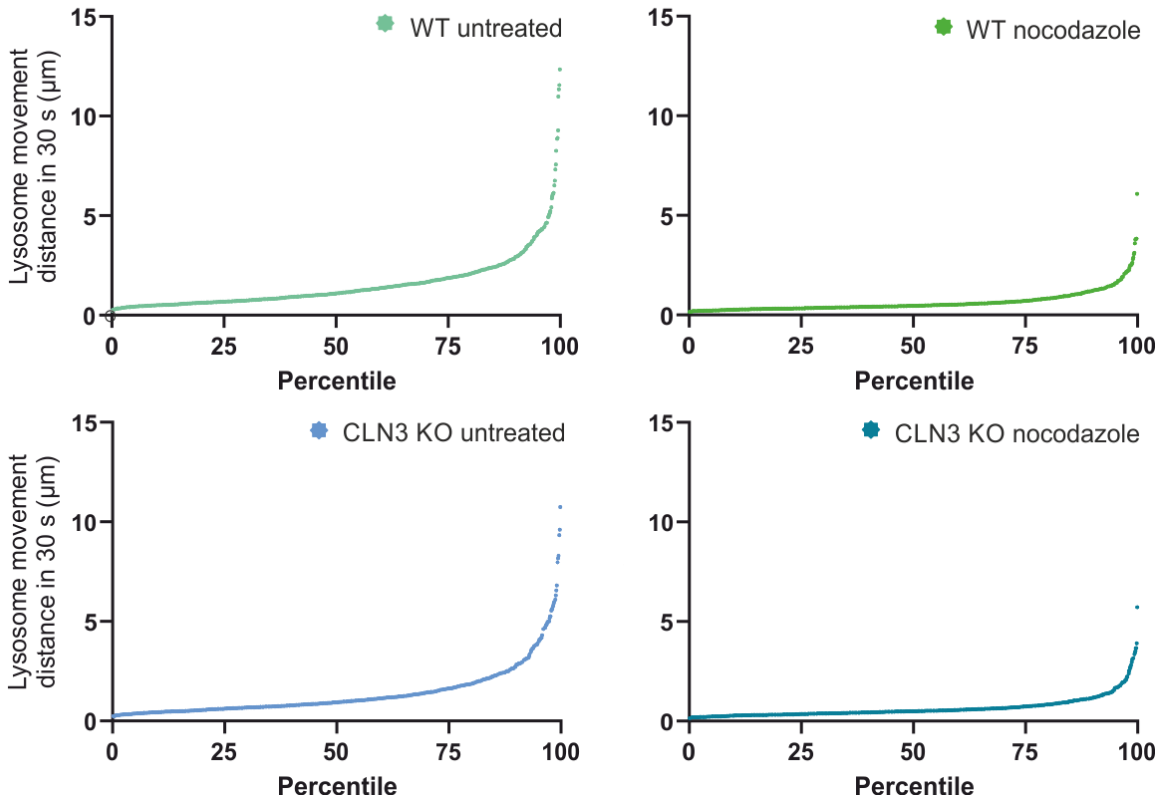


**Figure 59. The maximum distance travelled by each lysosome in 9 cells per condition, plotted by percentile.** These data are plotted as distance organised by percentile of approximately 900 ± 100 lysosomes from 9 cells (from 3 coverslips on 3 days).

To directly compare the different conditions, the percentile plots were combined as shown in Figure 60. Traces for the WT and CLN3 KO cells showed a high degree of overlap in both conditions. The majority of lysosomes do not move appreciably, and only lysosomes in the highest percentiles move a longer distance. To test if this 'directed movement' over a longer distance is affected in the CLN3 KO cells, the same analysis was repeated for the top 25% (Figure 60B). However, traces for both cell lines still showed a great overlap in each condition.

Therefore, while Figure 58 showed that the mean movement was comparable, Figure 60 illustrates the comparison of lysosome movement in greater detail. The proportion of lysosomes travelling different distances was very similar between the cell lines, with microtubule depolymerisation inducing the same reduction in lysosome movement.

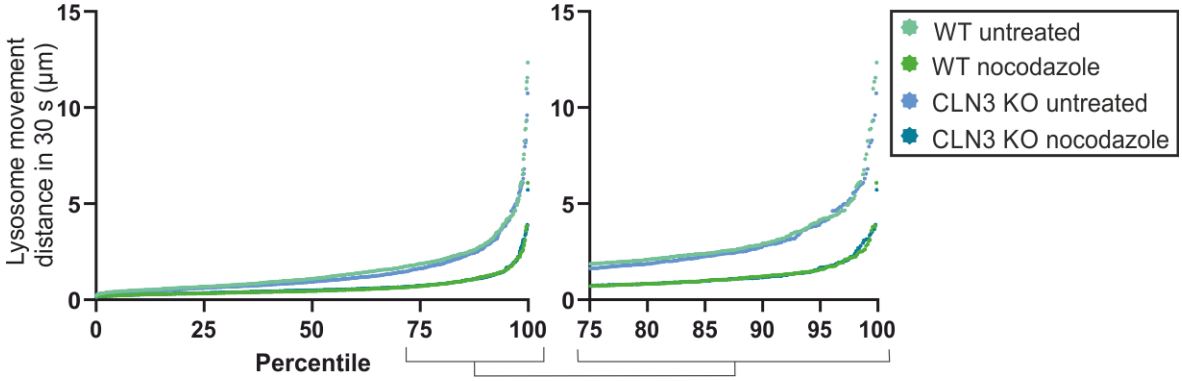


**Figure 60. A comparison of the distance travelled by each lysosome in 9 cells per condition, plotted by percentile.** These data are plotted as distance organised by percentile of approximately 900 ± 100 lysosomes from 9 cells, per condition.

To analyse the movement of the lysosomes with longest trajectories from each data set in more detail, those falling within the top 25% were plotted in Figure 61. The difference in the distance moved between the untreated and nocodazole treated cells was more pronounced, but there was no significant difference between the WT and CLN3 KO HeLa cell lines.

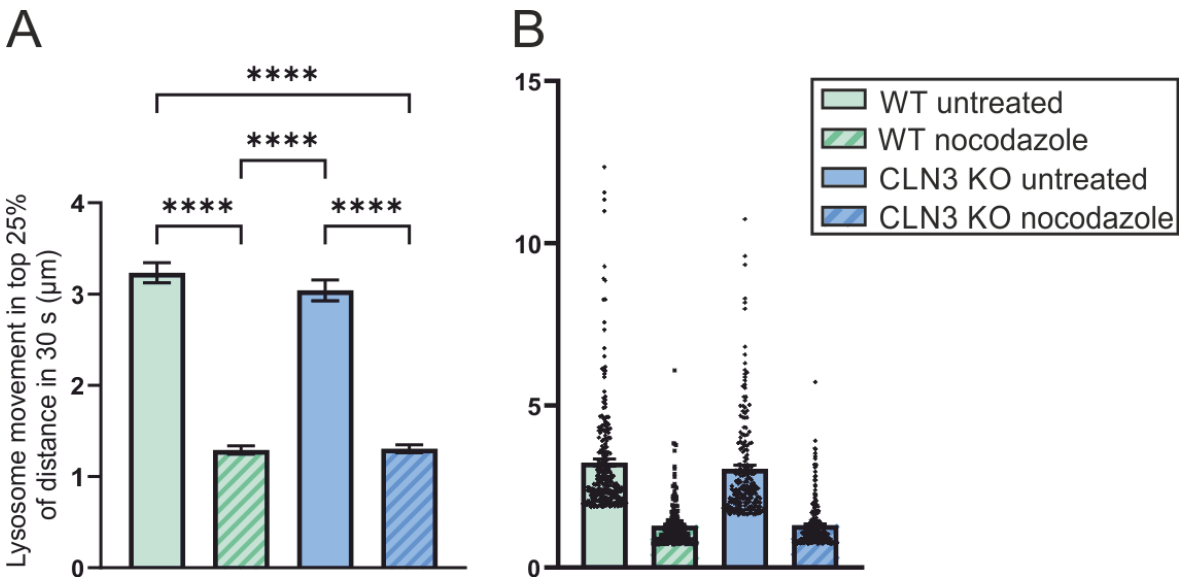


**Figure 61. The mean maximum distance travelled by lysosomes in HeLa cells: top 25%.** (A) WT and CLN3 KO HeLa cell lines were either untreated or nocodazole treated, loaded with LysoTracker and recorded for 30 seconds. These data are mean ± S.E.M. per cell and were analysed with Kruskal-Wallis with Dunn's multiple comparisons where **** indicates P ≤ 0.0001 and n = mean distance of lysosomes in 9 cells (from 3 coverslips on 3 days). (B) The right-hand side figure shows the mean values as a bar with distance per lysosome as scatter points on the bars.

The velocity of lysosome movement was calculated based on the sum of the distance over time, as described in Chapter 4. The sum of the distance reports the cumulative movement, which is a different value to the maximum distance that was presented in Figure 57 - Figure 61. The lysosomes moved throughout the whole recording, so the sum of the distance moved by the lysosomes divided by the duration of imaging yields the average velocity. While the measurement of distance presents information on the ability of lysosomes to travel within the cell, the velocity calculation could reveal a different phenotype. For example, if lysosomes could travel on microtubules but there was a phenotype affecting efficiency, this may be reflected in the velocity of travel.

To provide an insight into the variability of the velocity between the different cell lines and conditions, the mean velocity of lysosomes per cell was plotted in a separate bar, with the velocity of each individual lysosome plotted as a scatter point (Figure 62). The distribution of individual lysosome velocities illustrates a spread of data, although the mean represented by the bars did not appear to be greatly variable. Unlike the measurement of distance plotted in Figure 58, the variability of the velocities plotted for the same cells in Figure 62 is less pronounced as all data points appear closer to the mean.

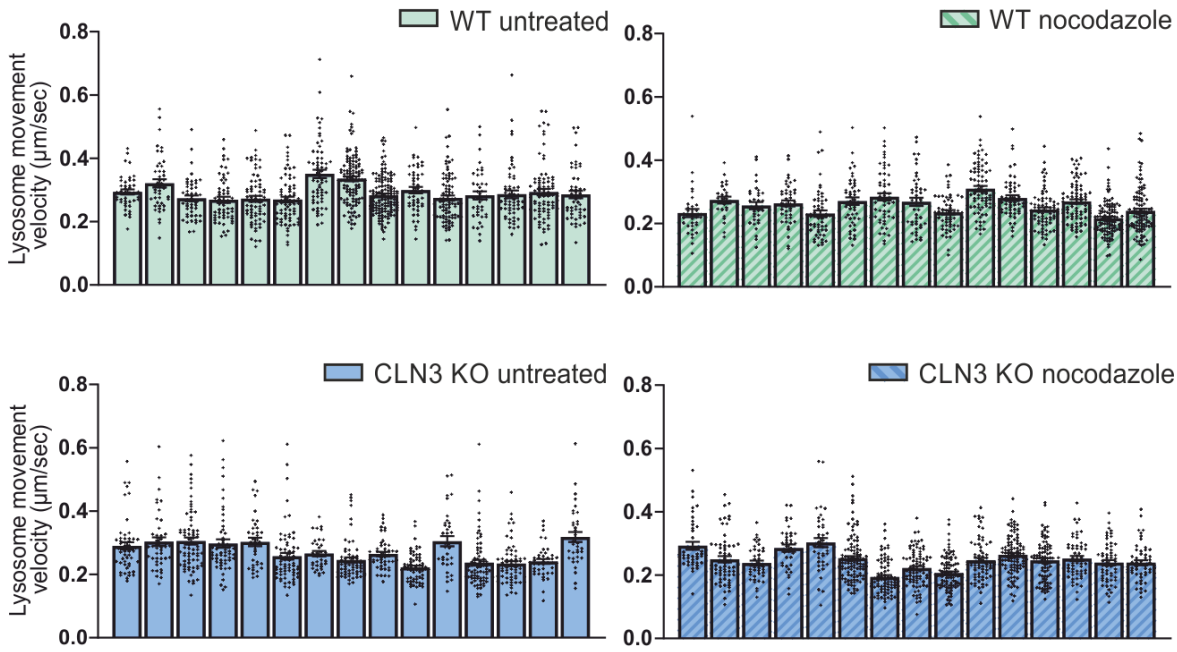


**Figure 62. The velocity of lysosomes in HeLa cells**. HeLa cell lines were either untreated or nocodazole treated, loaded with LysoTracker and movement of lysosomes was recorded for 30 seconds. These data are mean ± S.E.M. per cell, with scatter points representing individual lysosome movement within each cell.

To summarise the data, the average lysosome velocity was plotted for each condition, with the scatter points representing the mean distance per cell (Figure 63). This revealed a reduction in the movement of lysosomes in nocodazole treated CLN3 KO HeLa cells compared to the untreated WT HeLa cells.

Nocodazole treatment was earlier shown to significantly reduce the maximum distance that lysosomes travelled in both, WT and CLN3 KO cells (Figure 58). The fact that the velocity within cells from the same genotype was not reduced is important to note and indicates that the sum of distance (or cumulative distance) that lysosomes move is not affected strongly by nocodazole.

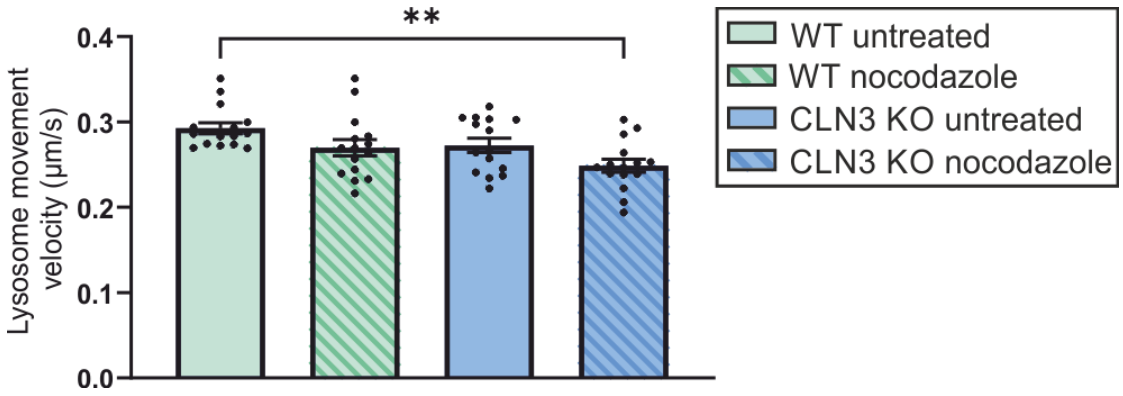


**Figure 63. The mean velocity of lysosomes in HeLa cells.** HeLa cell lines were either untreated or nocodazole treated, loaded with LysoTracker and recorded for 30 seconds. These data are mean ± S.E.M. per cell, with scatter points representing mean velocity of the lysosome movement per cell. These data were analysed with Kruskal-Wallis with Dunn's multiple comparisons where ** indicates $P \leq 0.01$, and n = mean distance of lysosomes in 9 cells (from 3 coverslips on 3 days).

### 5.3.6 Tracking lysosome movement in fibroblast cells

WT fibroblast cell lines were compared to two CLN3 patient cell lines carrying the Δex7/8 and D416G mutations, respectively. These cell lines were treated, imaged, and analysed in the same manner as the HeLa cells, with a comparison between untreated and nocodazole treated cells.

To provide an overview of the variability of lysosomal movement in different cells, the replicates in Figure 64 show the distance of lysosome movement in each of the conditions, with the scatter points showing the distance travelled by individual lysosomes. On first inspection, the profile of movement within the untreated WT fibroblasts looks different to that of the CLN3 cell lines and the nocodazole treated fibroblasts. The untreated WT fibroblasts show lysosomes moving a far greater distance compared to both cell lines with mutations in *CLN3* (note the difference in the y-axis

scales). The maximum distance lysosomes travel within the untreated CLN3 cell lines is more comparable to the reduction seen in the nocodazole treated cells.

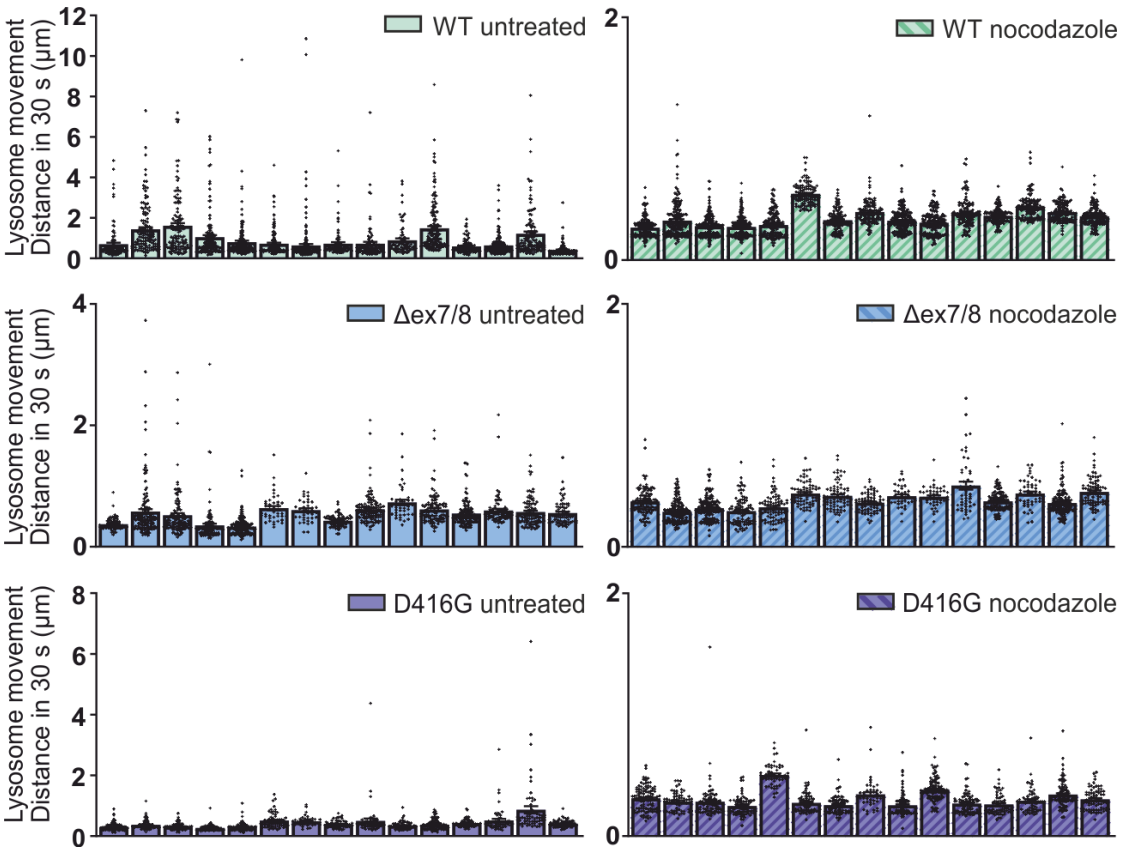


**Figure 64. The maximum distance travelled by lysosomes in fibroblasts.** Fibroblast cell lines were either untreated or nocodazole treated, loaded with LysoTracker and lysosome movement was recorded for 30 seconds. These data are mean ± S.E.M. per cell, with scatter points representing individual lysosome movement within each cell.

To summarise these data, the average maximum distance of lysosome movement was plotted for each condition, with the scatter points representing the mean distance of lysosome movement per cell (Figure 65). As previously demonstrated in HeLa cells (Figure 58), nocodazole treatment was able to significantly reduce the distances travelled by lysosomes in the WT fibroblasts. However, this is not true of the two CLN3 patient cell lines (Δex7/8 and D416G) in which there was no significant reduction of movement with nocodazole treatment of these cell lines compared to their untreated counterparts.

The data shown in Figure 65 has a greater S.E.M. in the untreated WT cell than any other, which indicates that the spread of data was greatest amongst these replicates (Table 17). This reflects more variation in the distances travelled by lysosomes in different cells, while all lysosome

movement was relatively comparable amongst the nocodazole treated WT cells and in the untreated and nocodazole treated CLN3 patient cell lines.

**Table 17. The S.E.M. of maximum distance travelled by lysosomes in the HeLa cells.**

| WT untreated | WT nocodazole | Δex7/8 untreated | Δex7/8 nocodazole | D416G untreated | D416G nocodazole |
|---|---|---|---|---|---|
| 0.09 | 0.02 | 0.03 | 0.02 | 0.04 | 0.02 |

The untreated and nocodazole treated Δex7/8 and D416G cells are more comparable to the WT fibroblasts which had been treated with nocodazole. There is a significant reduction in lysosome movement in the Δex7/8 nocodazole-treated cells and D416G untreated and nocodazole-treated cells. While lysosome movement in the untreated Δex7/8 is lower than the untreated WT fibroblasts, this is not significant.

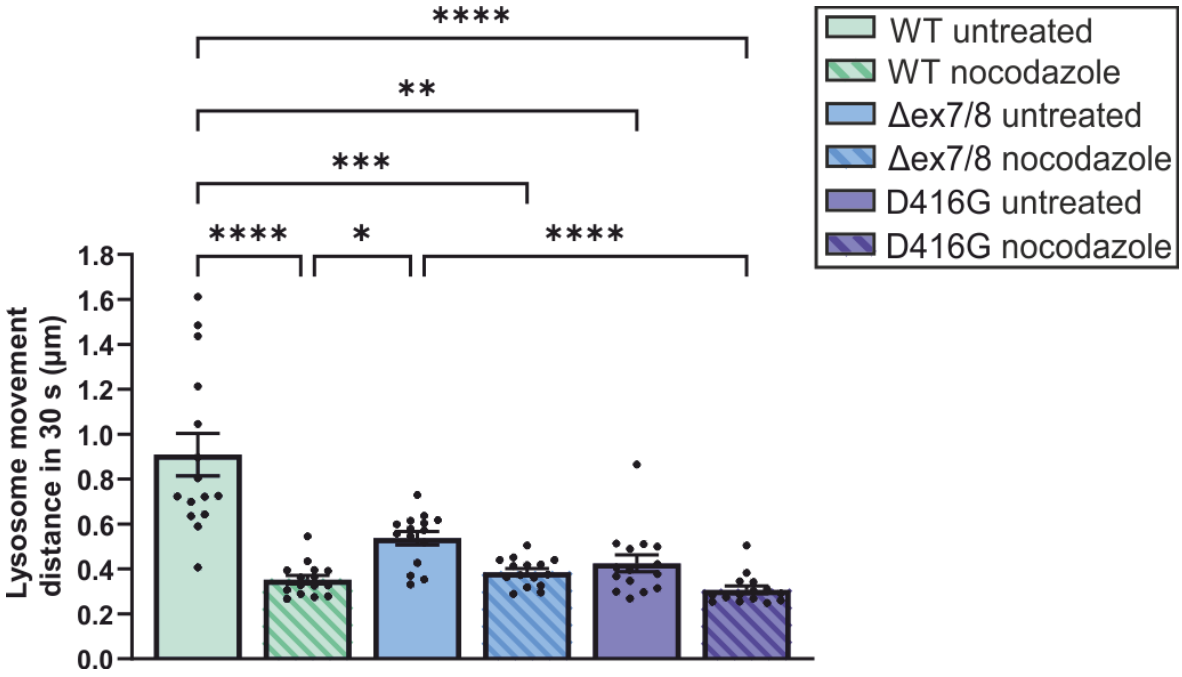


**Figure 65. The maximum distance travelled by lysosomes in fibroblasts.** Fibroblast cell lines were either untreated or nocodazole treated, loaded with LysoTracker and recorded for 30 seconds. These data are mean ± S.E.M. per cell, with scatter points representing mean maximum distance of the lysosome movement per cell. These data were analysed with Kruskal-Wallis with Dunn's multiple comparisons where * indicates $P \leq 0.05$, ** indicates $P \leq 0.01$, *** indicates $P \leq 0.001$ and **** indicates $P \leq 0.0001$ and n = mean distance of lysosomes in 9 cells (one each from 3 coverslips on 3 days).

The maximum distance of each lysosome's movement was plotted by percentile in Figure 66, to examine the distribution of distances in each condition. There is an immediate difference between the untreated WT fibroblasts compared to all other cells and conditions, which exhibits the pattern of an increasing number of lysosomes travelling greater distances towards the top percentiles. Conversely, the nocodazole treated cells all have relatively flat distribution with the majority of lysosomes travelling low distances and very little increase in the top percentiles, indicating that lysosomes did not move over a long distance within the cells.

The lysosome movement in the untreated Δex7/8 and D416G is greater than in the nocodazole treated cells and shows a moderate increase in distance of lysosomes in the top percentiles. However, there are far fewer lysosomes in the upper percentiles travelling longer distances and these do not travel as far as in the untreated WT cells.

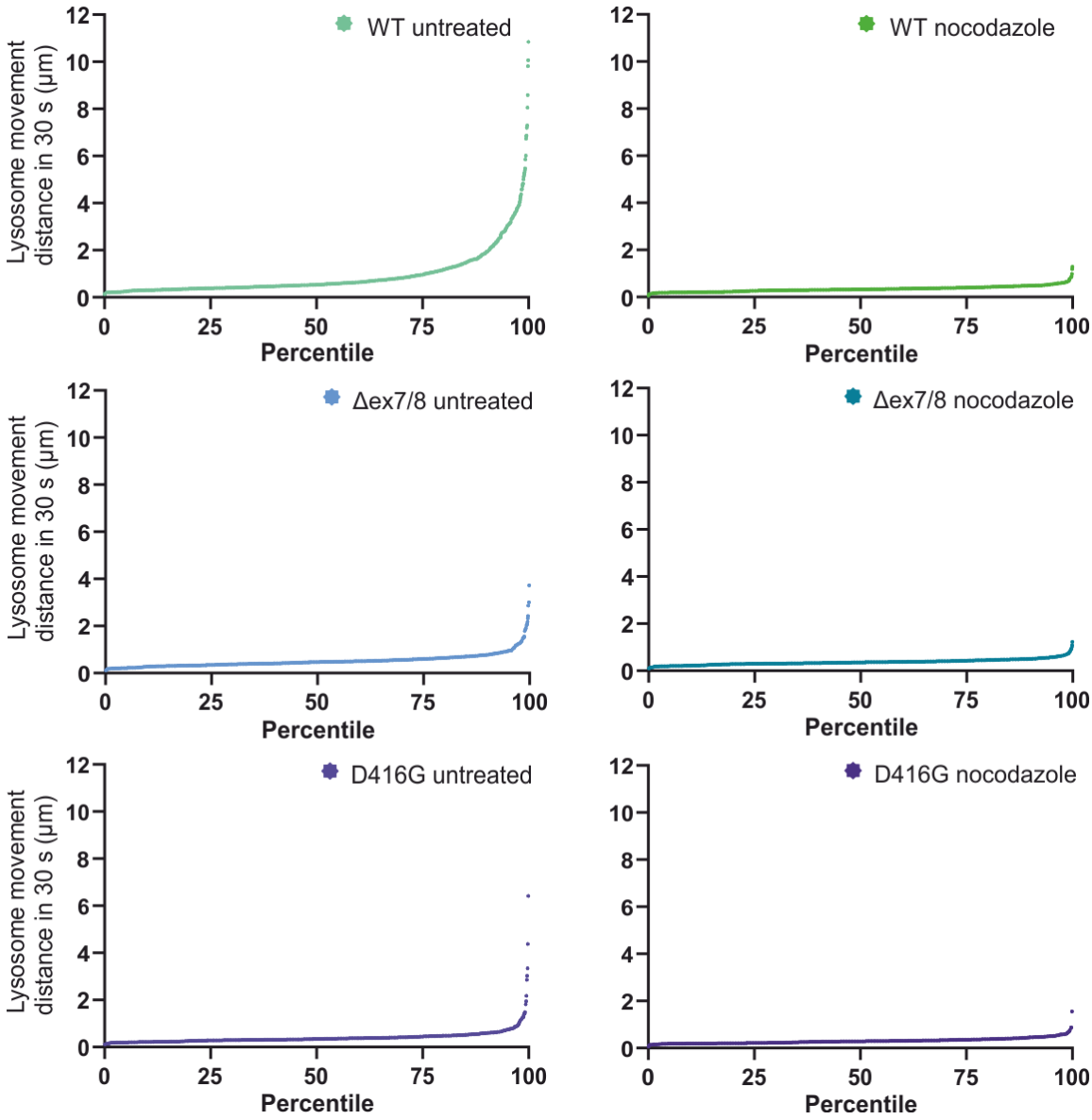


**Figure 66. The maximum distance travelled by each lysosome in 9 cells per condition, plotted by percentile.** These data are plotted as distance organised by percentile of approximately 1800 ± 600 lysosomes from 9 cells, per condition.

To better compare the movement between the different genotypes and conditions, the respective percentile plots were combined (Figure 67), illustrating that movement of lysosomes in untreated WT cells differed greatly to those in the nocodazole treated WT, and both the untreated and nocodazole treated Δex7/8 and D416G cells. In WT cells, more cells show movement of lysosomes, starting before the 75%, and they travel a greater maximum distance (Figure 67). Plotting only the top 25% of value, more lysosomes travel a greater distance in the CLN3 patient fibroblasts without nocodazole treatment, compared to all cell lines that were treated with nocodazole.

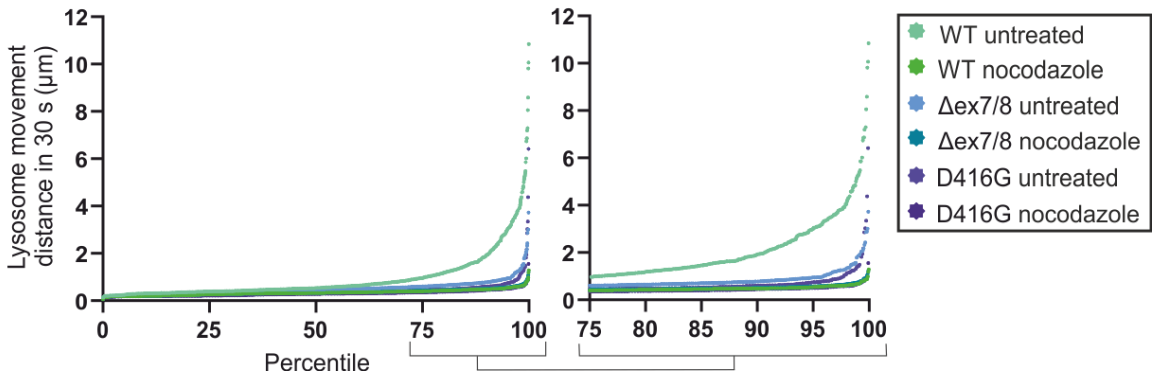


**Figure 67. A comparison of the distance travelled by each lysosome in 9 cells per condition, plotted by percentile.** These data are plotted as distance organised by percentile of approximately 1800 ± 600 lysosomes from 9 cells, per condition.

To compare lysosomes travelling the greatest distances in each condition, the top 25% were shown in Figure 68. Earlier it was shown that nocodazole did not reduce the maximum distance travelled for the two CLN3 patient cell lines (Figure 65). However, when plotting only the top 25%, there was a clear significant difference between all conditions. Nocodazole significantly reduced the maximum distance lysosomes travelled in all cell lines, WT, Δex7/8 and D416G.

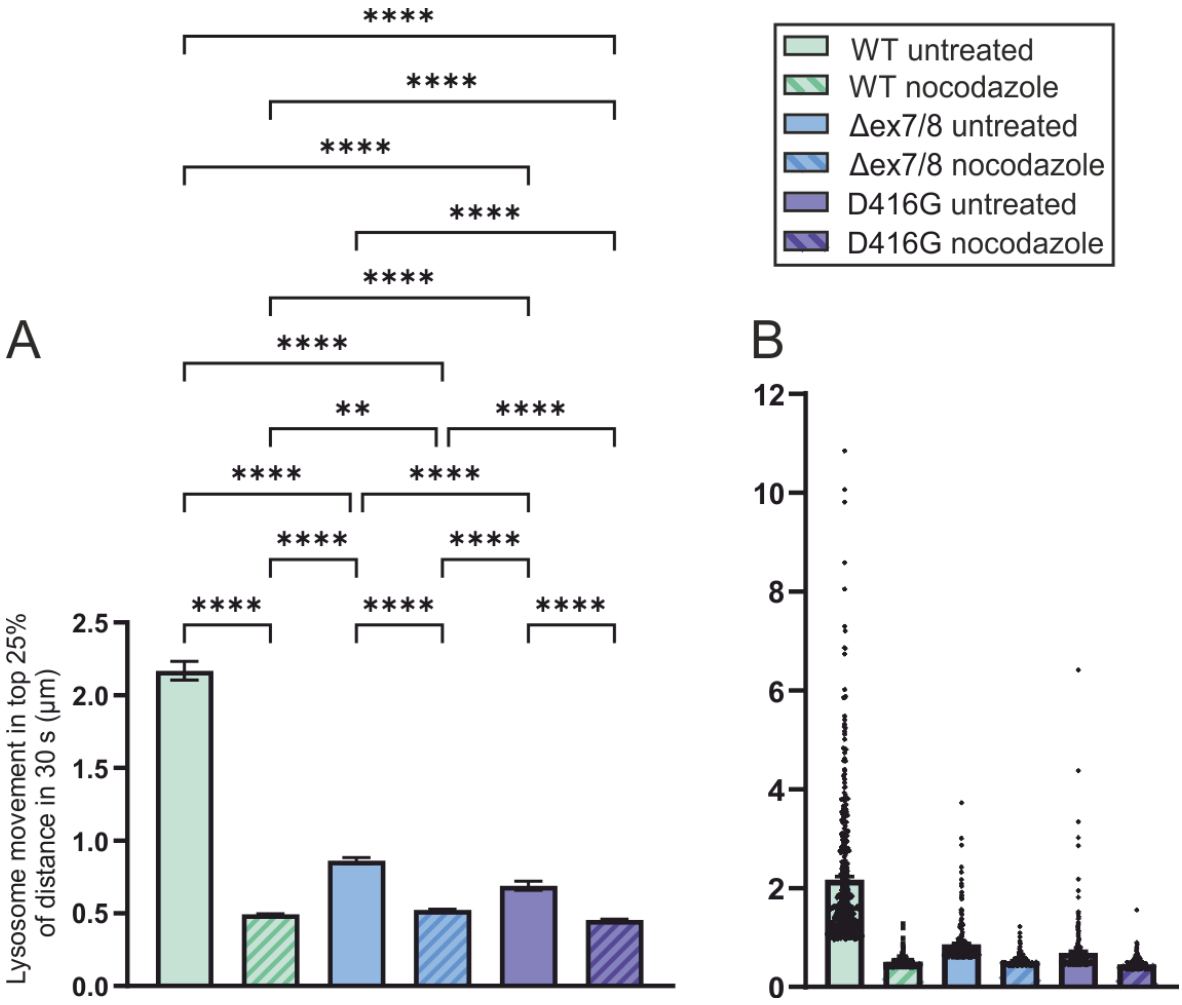


**Figure 68. The mean maximum distance travelled by lysosomes in fibroblast cells for the top 25%.** Fibroblast cell lines were either untreated or nocodazole treated, loaded with LysoTracker and recorded for 30 seconds. (A) These data are mean ± S.E.M. per cell and were analysed with Kruskal-Wallis with Dunn's multiple comparisons where ** indicates P ≤ 0.01 and **** indicates P ≤ 0.0001 and n = mean distance of lysosomes in 9 cells (one cell each from 3 coverslips on 3 days). (B) The right hand side figure shows the mean value for the maximum distance as bar, with the distance per lysosome as scatter points.

As for HeLa cells, after analysing the maximum distance moved, additional analysis sought to investigate whether the velocity of the movement changed in fibroblasts of the different genotypes, or with nocodazole treatment. To get an impression on the variability of the data, the mean velocity of lysosome movement per cell was plotted in bars, with the velocities of individual lysosomes displayed as scatter points (Figure 69). The plotted velocities have a smaller ± S.E.M. compared to the plotted distances previously shown in Figure 64. There is some variation between the cells, which is most noticeable in the Δex7/8 cells, both untreated and nocodazole-treated.

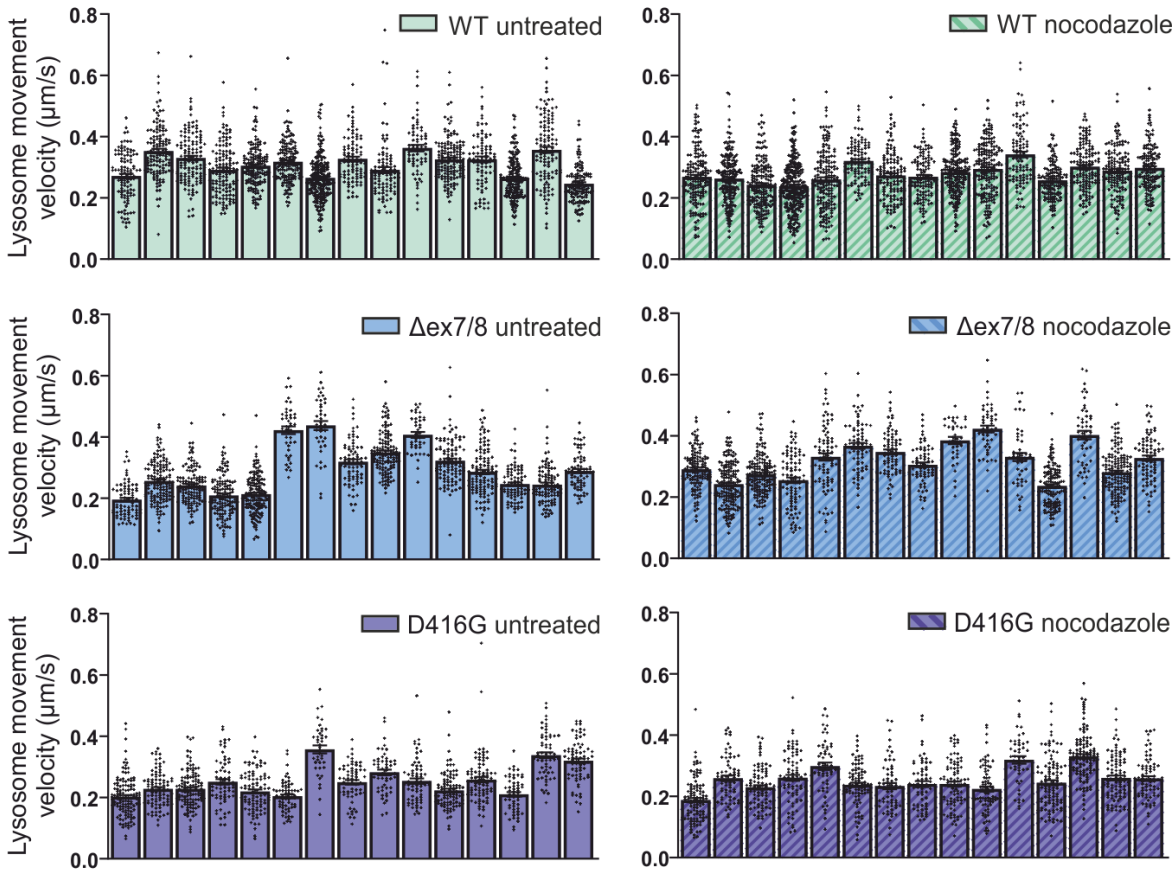


**Figure 69. The velocity of lysosome movement in fibroblast cells.** Fibroblast cell lines were either untreated or nocodazole treated, loaded with LysoTracker and recorded for 30 seconds. These data are mean ± S.E.M. per cell, with scatter points representing individual lysosome movement within each cell.

To summarise the data, the mean lysosome velocities per cell were plotted (Figure 70). There was no significant difference between the velocity of lysosomes in any of the untreated or nocodazole treated pairings per cell line. However, the lysosomes in D416G cell line trended towards slower overall lysosome movement compared to WT and the nocodazole-treated Δex7/8 cells. The Δex7/8 and D416G mutations did not appear to impact lysosome velocity to the same extent as their maximum distance (Figure 65).

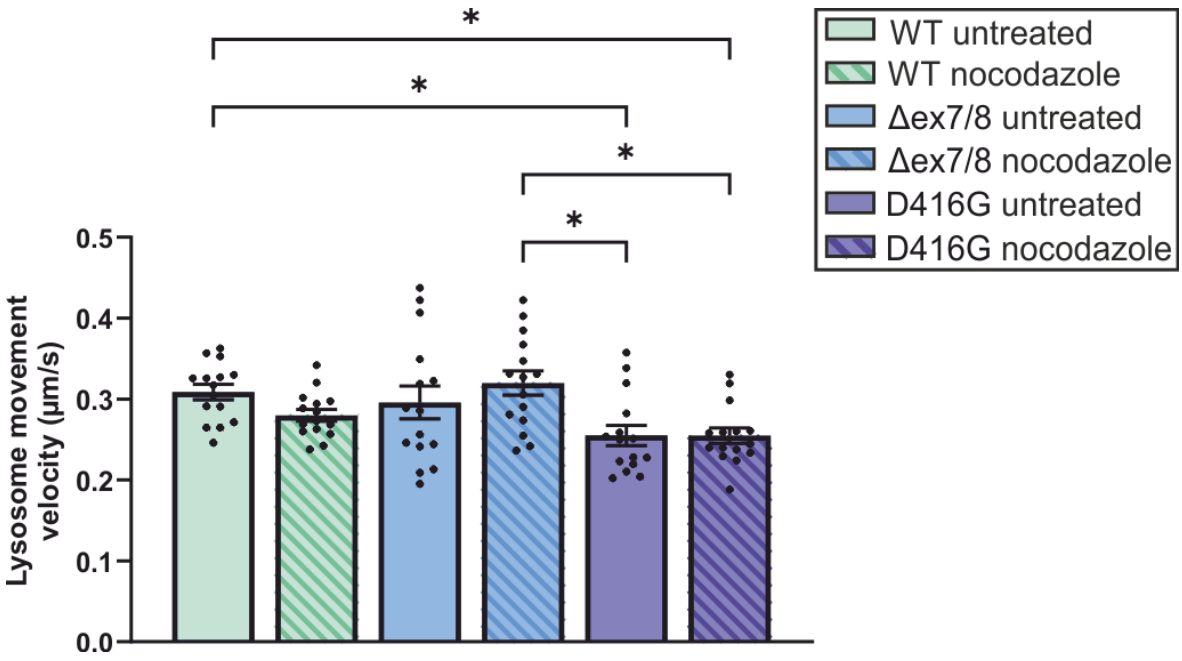


**Figure 70. The mean velocity of lysosomes in fibroblast cells.** Fibroblast cell lines were either untreated or nocodazole treated, loaded with LysoTracker and recorded for 30 seconds. These data are mean ± S.E.M. per cell, with scatter points representing mean lysosome movement per cell. These data were analysed with Kruskal-Wallis with Dunn's multiple comparisons where * indicates $P \leq 0.05$, and n = mean distance of lysosomes in 9 cells (one cell each from 3 coverslips on 3 days).

### 5.3.7 Variation in tracking results by cell type

In HeLa cells, nocodazole treatment significantly reduced the maximum distance but not the velocity of lysosome movement. There was no significant difference between the WT and CLN3 KO cell lines in the measurement of either distance or velocity (neither when analysing all cells, nor when only analysing the top 25%). Conversely, when analysing all cells, nocodazole treatment was only able to induce a significant reduction in the WT fibroblasts, while the Δex7/8 and D416G cell lines did not show a significant difference between the untreated and nocodazole treated cells for each. One explanation for this could be a reduced maximum distance that lysosomes travelled in fibroblasts compared to HeLa cells which was observed when comparing the results of lysosome tracking in the two different cell types (Figure 71).

In the absence of a comparable CLN3 mutation (KO, Δex7/8 or D416G) between cell lines, only the WT are compared. The spread of data in Figure 71A showed a very similar distribution of the maximum distance lysosomes moved in the HeLa cells compared to the fibroblasts: the majority of distances fell within a group at the bottom, with a tapered top representing a small population of lysosomes travelling many times greater than the mean. The mean ± S.E.M. plotted Figure 71B showed that lysosomes in HeLa cells travelled significantly further overall than in fibroblast cells.

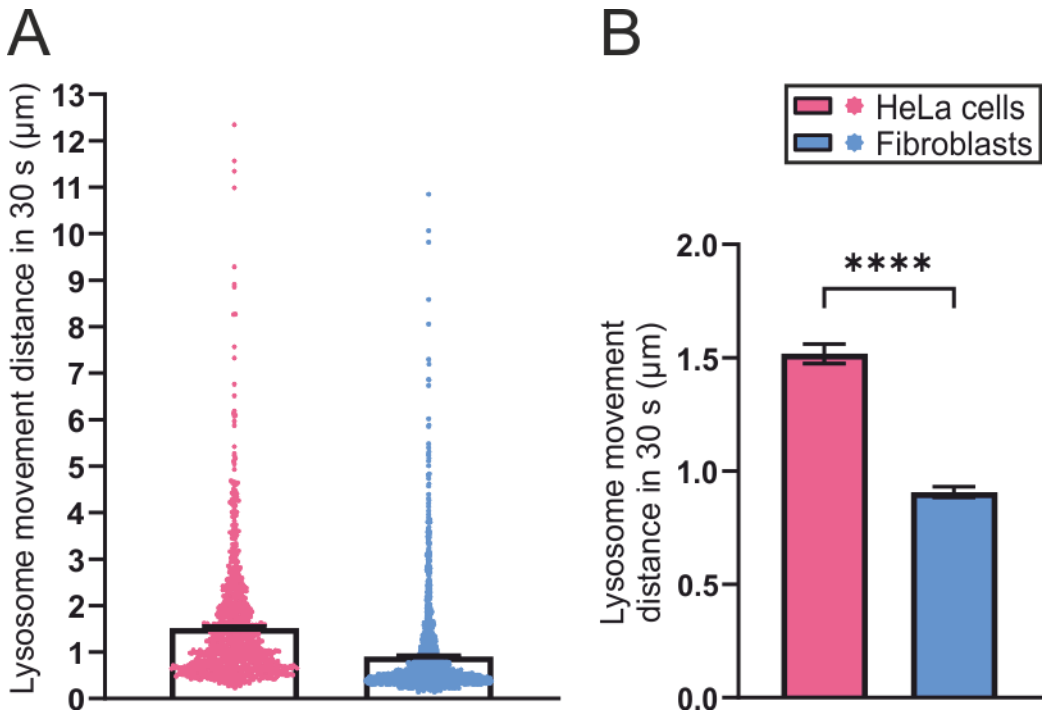


**Figure 71. A comparison of the distance travelled by lysosomes in WT HeLa and WT fibroblast cells.** (A) The left hand figure includes the individual replicates of the distance travelled by each lysosome. (B) These data are mean ± S.E.M. per cell and were analysed with two-tailed Mann Whitney test, where **** indicates $P \leq 0.0001$ and n = mean distance of lysosomes in 9 cells (from 3 coverslips on 3 days) per cell type.

The percentile plot of the distances, shown in Figure 72, also illustrated the spread of data and shows the greater distances travelled by lysosomes in HeLa cells. Unlike previous figures showing a suppressed movement which was most prominent in the top percentiles (nocodazole treatment of cells, Figure 60 and Figure 67) this is not the cause of the lower mean distance recorded in fibroblasts. When plotted by percentile, HeLa and fibroblast cells have a similar shape of the curve in the top 25% but the distances of lysosome travel are far greater in the HeLa cells from a much earlier percentile.

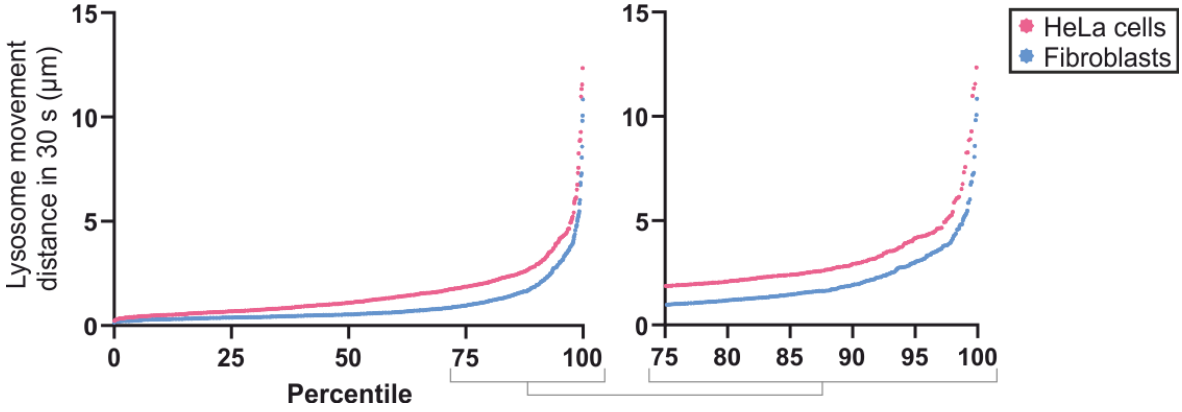


**Figure 72. A comparison of distance travelled by lysosomes in HeLa and fibroblast cells: percentile.** These data are plotted as distance organised by percentile of 1009 and 1950 lysosomes from 9 HeLa and 9 fibroblast cells respectively.

In order to compare the velocity of lysosome movement in HeLa and fibroblast cells, the values found in WT cells were plotted in Figure 73, showing no significant difference between the cell types. Therefore, lysosomes in fibroblasts travelling a shorter maximum distance within the cells, they were no slower than in the HeLa cells.

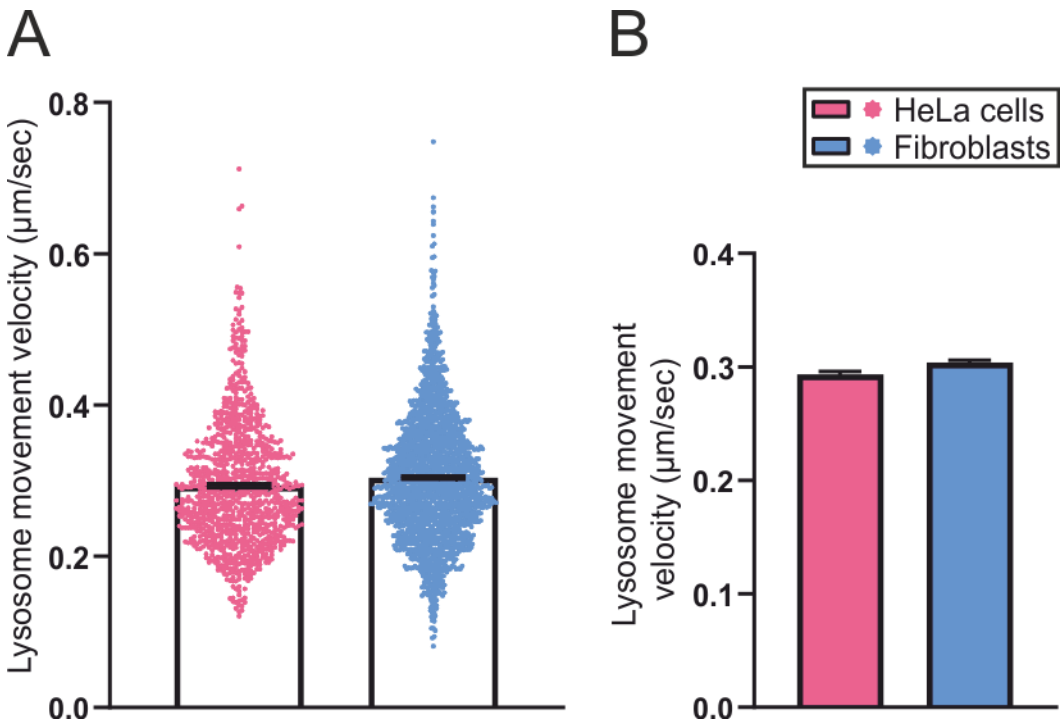


**Figure 73. A comparison of the velocity of lysosomes in HeLa and fibroblast cells.** (A) The left hand figure includes the individual replicates of the distance travelled by each lysosome. (B) These data are mean ± S.E.M. per cell and were analysed with two-tailed Mann Whitney test. n = mean distance of lysosomes in 9 cells (from 3 coverslips on 3 days) per cell type.

Summary of results:

- Counting and measurement of lysosomes were analysed using the assay described in Chapter 4.
- Enlarged or clustered lysosomes were observed in nocodazole-treated cells, which was consistent when lysosomes were labelled with LysoTracker or CellLight. The fluorescence profile of the large regions of lysosome signal had multiple peaks, indicating that these regions were indeed clusters of lysosomes. Figure 50, Figure 52
- There was no difference in cell size between HeLa WT and CLN3 KO, or fibroblast cell lines WT, Δex7/8 or D416G. The correlation between cell size and number of lysosomes per cell was found to be weak. Therefore, the quantification of segmented lysosome regions was not normalised to the size of the cell. Figure 53, Figure 55
- The effect of clustering after nocodazole treatment was assessed in HeLa cells by segmentation and measurement of number and size of segmented regions of LysoTracker staining. In both cell lines, nocodazole treatment increased the sizes of the segmented regions. There was no difference between the WT and CLN3 KO cell lines. Figure 54
- The fibroblast cell lines (WT, Δex7/8 and D416G) had no significant difference in the number and size of segmented lysosome regions, suggesting that lysosomes were not clustering within any of the fibroblast cell lines. Figure 56
- Lysosome movement was analysed using the tracking assay which was described in Chapter 4.
- The maximum distance of lysosome movement in HeLa cells was reduced by nocodazole in both WT and CLN3 KO cells, and there was no difference between the WT and CLN3 cells. Figure 57, Figure 58
- The reduction in movement was more pronounced when looking at the top 25% of distances travelled by lysosomes in the HeLa cells. Figure 61
- There was no significant difference to velocity of lysosome movement with nocodazole treatment in the HeLa cells, although there was a slight reduction in velocity of lysosomes in the CLN3 KO cells which resulted in a significant reduction in the nocodazole treated CLN3 KO cells compared to the untreated WT cells. Figure 62, Figure 63
- The maximum distance of lysosome movement in fibroblast cells was reduced by nocodazole only in the WT cell line. Conversely, the Δex7/8 and D416G cells already had a reduced lysosome movement and nocodazole was not able to further reduce this. Figure 64, Figure 65
- When analysing only the top 25% of cells showing the longest lysosome movement, nocodazole significantly reduced the maximum distance moved in both CLN3 patient cell lines. Figure 68
- This analysis also showed a reduced maximum distance for lysosomal movement in the untreated Δex7/8 and D416G cells compared to the WT fibroblasts.

- There was a significant reduction in lysosome velocity in the D416G fibroblasts, compared to the WT fibroblasts. This reduction in velocity was not true of the Δex7/8 fibroblasts. Figure 70
- A comparison of WT HeLa and WT fibroblast cells revealed that lysosomes travelled greater maximum distances in HeLa cells but not with greater velocity. Figure 71

## 5.4 Discussion

The directional movement of lysosomes over longer distances is not a continuous movement, but could be described as saltatory, with phases of fast movement, after which the lysosome is static (Matteoni and Kreis, 1987). Examples for such movement, and of lysosomes returning to the place where they originated were shown in Chapter 4. It was found that this directional movement depends on microtubules and could be inhibited by nocodazole treatment. A small percentage of lysosomes in nocodazole-treated cells (4%) still showed movement over shorter distances, consistent with Brownian motion (Matteoni and Kreis, 1987).

The contribution of actin filaments to lysosome movement is less clear. Whilst one study found no effect of depolymerising actin filaments or the intermediate filaments on lysosome movement (Matteoni and Kreis, 1987), other studies find that lysosomes also move along actin filaments, mostly at the cells periphery (Cordonnier et al., 2001).

The treatment of HeLa cells with nocodazole resulted in a visual and measurable clustering of lysosomes Figure 54. The nocodazole treatment was responsible for depolymerisation of the microtubules within the cell, therefore impacting the lysosome movement over longer distances. It only affected movement over shorter distances to a lesser effect, as shown by the fact that nocodazole did not inhibit the maximum distance that lysosomes travelled in WT fibroblasts.

The clustering of lysosomes is described as a result of movement towards the microtubule organising centre (MTOC), where lysosomes interact with a number of other vesicles (Matteoni and Kreis, 1987). This manner of lysosome clustering is an expected function in cells, and is proposed to be related to the interaction of lysosomes with other organelles, such as endosomes (Ba et al., 2018).

However, normal lysosome clustering appears to be different to the clustering observed in Figure 50 of this chapter. Firstly, clustering described in literature predominantly occurs at the MTOC (close to the nucleus), while the lysosome clustering seen within the nocodazole treated cells of this chapter was showing regions distributed throughout the cell where lysosomes were too close together to be segmented with the techniques used. Secondly, based on literature it may be expected that the depolymerisation of microtubules would decrease the clustering and increase

the distribution of lysosomes throughout the cell (Matteoni and Kreis, 1987). This was not the case, and again suggests that the clustering observed in the nocodazole treated HeLa cells was different from the clustering of lysosomes at the MTOC.

To determine whether there was any clustering of lysosomes in the cell models of CLN3 disease, the size of segmented lysosome regions were quantified for both HeLa (WT and CLN3 KO) and fibroblast cells (WT, Δex7/8 and D416G) in Figure 54 and Figure 56 respectively. There was no clustering of the lysosomes in either of the CLN3 disease cell models to suggest a phenotype comparable to the inducible clustering observed in response to microtubule depolymerisation with nocodazole treatment.

The disruption of microtubules has been shown with super-resolution microscopy to increase the number of pauses in lysosome movement, while decreasing the distances travelled (Mohan et al., 2018). This published work presents a detailed assessment of a small number of lysosomes and regions with microtubule staining.

The methodology established for a lysosome tracking assay explained in Chapter 4 was here implemented in the study of CLN3 disease. This presented an analysis of a large number of lysosomes per cell rather than relying on the qualitative assessment of single trajectories, as had been done before. In the WT and CLN3 KO HeLa cells, the maximum distance of lysosome travel was significantly reduced by depolymerisation of the microtubules with nocodazole.

However, there was no difference between lysosome movement in the WT and CLN3 KO cells Figure 58. Conversely, the mean velocity of lysosome movement was not affected by nocodazole treatment, although some effect was seen on the treated CLN3 KO HeLa cells in comparison to the untreated WT HeLa cells Figure 62. At best, there was a subtle reduction in velocity, but this effect was certainly not as pronounced as the measurable impact of maximum distances travelled by lysosomes. This apparent discrepancy can be explained by the fact that the velocity was calculated based on the sum of the distance lysosomes moved, not the maximum distance.

In fibroblast cell lines, the WT fibroblasts exhibited a significant reduction in maximum distance of lysosome movement after nocodazole treatment Figure 65. However, the CLN3 patient cell lines (Δex7/8 and D416G) did not have a significant reduction in maximum distance of lysosome travel in the nocodazole treated cells due to an already reduced distance in the untreated cells, that was similar to that in nocodazole-treated WT fibroblasts Figure 65. Consequently, when only analysing the 25% of fibroblasts in which lysosomes move over the longest distance (Figure 68), nocodazole was found to inhibit the lysosomal movement in all fibroblast cell lines. This analysis also showed significantly reduced movement in fibroblasts from CLN3 patients compared to the WT. This suggests that the patient cell lines have a reduced lysosome movement phenotype.

As previously shown in HeLa cells, nocodazole did not influence the velocity of movement in the fibroblast cell lines. While the maximum distance of lysosome movement was significantly affected in the CLN3 patient cell lines, this was not mirrored to the same extent in the measurement of velocity (Figure 70). However, there was some reduction in the lysosome velocity, which was significant in the D416G patient cell lines but not in the Δex7/8 cell lines.

The relationship between maximum distance moved and the velocity was discussed in Chapter 4 and found to only have a weak correlation. Therefore, the fact that changes were found to distance and not velocity in; (1) nocodazole treated cells and, (2) the CLN3 patient fibroblast cell lines, further confirms the poor relationship between maximum distance and velocity. It is important to note that the velocity calculation here was based on the sum of the distance, which includes the movement over short distances with less clear direction. It might be suggested that this type of velocity of lysosomes is less dependent on microtubules and their associated motor proteins and that the speed of movement is dependent upon other factors. Lysosomes may be subject to diffusion by Brownian motion within the cell, which could go some way to explaining the baseline 'hovering' movement of lysosomes lacking the elongated, directional manner of travel (Robson et al., 2013, Bandyopadhyay et al., 2014).

As the reduced lysosome movement phenotype in CLN3 patient fibroblasts was comparable to the nocodazole induced microtubule depolymerisation in WT cells, this could suggest that the phenotype is microtubule dependent. However, there was no appearance of lysosome clustering within any of the CLN3 cell models, which might also be a microtubule dependent process based on the observation and quantification in Figure 50 and Figure 54 respectively.

Finally, the use of both HeLa and fibroblast cells in this chapter revealed that the results in the fibroblast patient cells were not directly comparable to the CLN3 KO HeLa cells. A comparison of the WT of each cell line showed that HeLa cells had a significantly greater maximum distance of lysosome movement overall compared to the fibroblast cells Figure 71. The change in mean lysosome distance was previously shown (with nocodazole treatment, or in the case of fibroblasts, the CLN3 mutations) to be predominantly a reduction in the top percentile of lysosome distance. However, when looking at the percentile plot of lysosome movement HeLa and fibroblast cells, (Figure 72) it was clear that rather than a loss of lysosome travelling the furthest, there were simply fewer of them in the fibroblast cell lines.

As CLN3 disease is known to predominantly affect sensitive cells with less proliferation (as described in Chapter 1) it is possible that the HeLa cells were a less suitable model for assessing the effects with the sensitive lysosome movement assay than fibroblasts. Further investigation with a greater number of cell types, especially neuronal and cardiac, would be highly valuable.

## 5.5 Future work

In addition to the straightforward application of the lysosome tracking assay to a far greater range of CLN3 cell models, or other LSD models, there are a number of more immediate opportunities for future work based upon this chapter.

As the clustering of lysosomes observed in nocodazole treated cells was different from the expected clustering of lysosomes associated with the MTOC, a further study may be warranted to determine the effect of clustering under different conditions. For example, would the lysosomes in nocodazole treated cells reposition differently after starvation, compared to those in untreated cells.

The results in this chapter describe a phenotype of reduced lysosome movement which was observed in the fibroblasts from CLN3 patients but not in the CLN3 KO HeLa cell model. To further interrogate the phenotype discovered in the fibroblast cell lines, the rescue or induction of the phenotype through manipulation of the CLN3 protein would strengthen these findings. This may be achieved with transfection of the *CLN3* gene to express either the WT or a mutant copy of the CLN3 protein, raising two key questions:

- Can the reduced lysosome movement phenotype in CLN3 patient fibroblasts be rescued with the transfection of the WT *CLN3* gene?
- Can the reduced lysosome movement phenotype be replicated in WT fibroblasts with the transfection of a mutation carrying *CLN3* gene?

The difference between the results of the HeLa and fibroblast cell models suggests a fundamental consequence of either the CLN3 KO compared to patient mutations, or possible an effect of cell type.

It is unlikely that the CLN3 KO was unable to replicate the effects of the disease, as this cell line represents a more complete disruption to CLN3 than the patient mutations. On the other hand, if some function of the CLN3 protein is conserved in the partial deletion or point mutation, it may be that the complete knock out allowed the cell to compensate for the mutation compared to the less severe impact of the Δex7/8 and D416G mutations. To compare this directly, a CLN3 KO fibroblast model would be ideal, or HeLa cells with the Δex7/8 deletion or D416G point mutation.

An interesting point of future work would be to determine whether the reduced movement phenotype was induceable in HeLa CLN3 KO cells compared to HeLa WT. This may be achieved through manipulation of cell culture to induce stress, or otherwise influence the characteristics of the cells.

As one major difference between HeLa and fibroblast cell lines is the rapid proliferation of the HeLa cells, it may be possible to observe a phenotype if cells were inactivated. The mitotic inactivation of cells is described in Chapter 8 in relation to Mouse Embryonic Fibroblasts and this treatment could be applied to the HeLa cells. The rationale for these experiments is that the phenotype may be masked by the rapid proliferation of the cells in culture and mitotic inactivation would allow for the cells to be maintained in culture for longer and possibly in time to develop a phenotype.

Finally, as previously discussed, there appeared to be a difference between the lysosomes which were moving by diffusion and those with directed motion. A method of analysis to differentiate particle movement based on these effects is Mean Square Displacement (MSD), which has been previously described in literature (Burlakov et al., 2010, Qian et al., 1991). This method would allow for lysosomes with movement that correlated to the longer trajectories, to be mathematically identified as directed movement rather than diffusion. As shown in this chapter, the differences between lysosome movement, arising from nocodazole treatment or CLN3 patient mutations, appeared to be found in the longest trajectories when these were plotted by percentile, rather than those which were likely to be diffusing. Therefore, implementation of MSD could be a great asset to the analysis of lysosome movement in these experiments.

# 6 Examining putative effects of CLN3 knockout on mitochondrial membrane potential, ROS production and mitochondrial calcium uptake

## 6.1 Introduction

Mitochondria are important components of the calcium signalling toolkit. It has been widely demonstrated that mitochondria sequester calcium from the bulk cytosol at a relatively slow rate, and at a significantly faster rate when calcium channels on organelles proximal to mitochondria are activated (Collins et al., 2001). The sequestration of calcium by mitochondria buffers cytosolic calcium rises and can prevent the spreading of intracellular calcium waves (Mackenzie et al., 2004, Tinel et al., 1999). In addition, increases in calcium concentration within the mitochondrial matrix are linked to the stimulation of mitochondrial respiration via the activation of calcium-sensitive dehydrogenases within the citric acid cycle (Jouaville et al., 1999). Moreover, calcium uptake by mitochondria underlies the induction of apoptosis (Pinton et al., 2008, Harr and Distelhorst, 2010), and reduction of mitochondrial calcium uptake is one mechanism that cancer cells employ to escape cell death and gain a survival advantage (Distelhorst and Bootman, 2019).

Dysfunctional mitochondria are common aspects of the pathology of neurodegenerative diseases including Parkinson's and Alzheimer's (Osellame and Duchen, 2013, Demers-Lamarche et al., 2016). The impairment of mitochondria in neurodegenerative diseases has also been linked to some lysosomal storage disorders, such as Gaucher disease (Osellame and Duchen, 2013). Complex dysfunctions in mitochondrial form and function have also been described in cell models of CLN3 disease. These observations include alteration in mitochondrial membrane polarisation and $Ca^{2+}$ storage in a CLN3 cell model carrying the Δex7/8 mutation (Chandrachud et al., 2015), and abnormal elongation of mitochondria and a decrease in cellular ATP (Fossale et al., 2004).

Mitochondria and lysosomes are both dynamic and important organelles that are known to interact, especially through $Ca^{2+}$ signalling (Peng et al., 2020). A link between mitochondrial dysfunction and lysosomes has been described in neurodegenerative disease, with the generation of reactive oxygen species (ROS) as the proposed cause of lysosome impairment (Demers-Lamarche et al., 2016). Cells routinely produce ROS as a by-product of the oxidation of metabolites (Murphy, 2009). In most cell types, mitochondria are the principal producers of ROS, with superoxide ($O_2^-$) being the most common product. Since this oxygen radical is highly reactive and can damage cellular proteins and lipids, it is typically rapidly reduced to hydrogen peroxide by superoxide dismutase. However, hydrogen peroxide, and other oxidative species, can still be harmful inside cells. Note: generally, ROS refers to both radical (e.g., superoxide and hydroxyl) and non-radical (e.g., hydrogen peroxide) oxidising species (Zorov et al., 2014). Whilst some ROS production is

physiological, a persistent accumulation of ROS likely to tip the balance toward pathological outcomes. Moreover, ROS production can lead to an autocatalytic effect, known as ROS-induced ROS release that can spiral out of control and cause cell death. A lack of mitophagy, preventing the removal of ROS-producing dysfunctional mitochondria has been linked to many of the phenotypic alterations that characterise Parkinson's disease (Park et al., 2018). In addition to increased ROS production causing cellular damage, a decrease in the mechanisms by which cells buffer ROS production, such as production of the tripeptide glutathione, have been shown to lead to increased oxidative stress (Jahoor et al., 2019). With CLN3 disease, ROS production was found to be slightly increased (and to a greater extent, it is increased in CLN2 disease) (Vidal-Donet et al., 2013). In *Drosophila*, loss of CLN3 function sensitised the cells to ROS, suggesting a link between the role of the CLN3 protein and the response to ROS (Tuxworth et al., 2011).

**Aim 1: to characterise mitochondrial function**

Objectives:

- Compare the mitochondrial membrane potential in wild type and CLN3 mutant cells

**Aim 2: to characterise ROS levels in the CLN3 HeLa cell model**

Objectives:

- Characterise ROS levels in wild type and CLN3 mutant cells
- Measure basal ROS levels and responses to challenge with ROS donors in wild type and CLN3 mutant cells

**Aim 3: to characterise the calcium release from the endoplasmic reticulum (ER)**

Objectives:

- Analyse $Ca^{2+}$ release from the ER in response to agonist stimulation in wild type and CLN3 mutant cells

Compare mitochondrial $Ca^{2+}$ uptake following agonist stimulation of cells in wild type and CLN3 mutant cells

## 6.2 Methods

The methods for cell culture, details of fluorescence imaging, and the preparation of chambers for fluorescence imaging of live cells are described in Chapter 2. These experiments were carried out using the Leica fluorescence microscope. WT and CLN3 KO HeLa cells grown on glass coverslips in 12-well plates were transferred to imaging chambers just prior to use in an experiment. The loading and imaging buffer used in the TMRE and ROS Brite experiments was FluoroBrite DMEM (FB), supplemented with GlutaMAX and adjusted to pH 7.3 with HEPES to stabilise. The loading and imaging buffer used in the CaI-520/Rhod-2 experiments was HBSS, adjusted to pH 7.3.

### 6.2.1 TMRE

Tetramethylrhodamine ethyl ester (TMRE) was used to measure mitochondrial membrane potential (ΔΨm) in live cells. WT and CLN3 KO HeLa cells were loaded with 2 µm TMRE in FluoroBrite DMEM (FB) for 15 minutes. The loading solution was exchanged for fresh FB containing 0.1 µM TMRE immediately before imaging. The cells were imaged for 180 seconds, and at 60 seconds the solution was exchanged by superfusion of the cells with FB supplemented with either DMSO or FCCP.

**Table 18. The solutions used in the TMRE experiments.**

| Compound | Concentration | Diluent | Application |
|---|---|---|---|
| TMRE | 2 µM | FluoroBrite DMEM | Indicator |
| DMSO | 1 in 1000 dilution | FluoroBrite DMEM with 0.1 µM TMRE | Negative (vehicle) control |
| FCCP | 20 µM | | Positive control |

### 6.2.2 ROS Brite

WT and CLN3 KO HeLa cells were incubated in a solution of FB containing either tBHP (150 µM), $H_2O_2$ (150 µM), or DMSO (1 in 500 dilution) for 1.5 hours. The cells were loaded with 5 µM ROS Brite 570 in FB for 15 minutes and the loading solution was exchanged for fresh FB immediately before imaging. The cells were imaged for 180 seconds to record a time series.

**Table 19. The solutions used in the ROS Brite experiments.**

| Compound | Concentration | Diluent | Application |
|---|---|---|---|
| ROSBrite | 5 µM | FluoroBrite DMEM | Indicator |
| DMSO | 1 in 500 dilution | | Negative (vehicle) control |
| tBHP | 150 µM | | Positive control |
| $H_2O_2$ | 1 mM | | |

### 6.2.3 Mito calcium – Cal-520/Rhod-2

WT and CLN3 KO HeLa cells were loaded with of 1 µM Cal-520 and 1 µM Rhod-2 in HBSS for 30 minutes, followed by 30 minutes of de-esterification in HBSS. Once placed on the microscope stage, the cells were superfused with HBSS as a wash before imaging and to confirm that there was no calcium response during the exchange of imaging medium. The cells were subsequently imaged for 210 seconds, with the addition of 100 µM ATP in HBSS by superfusion at 30 seconds.

**Table 20. The solutions used in the Cal-520/Rhod-2 experiments.**

| Compound | Concentration | Diluent | Application |
|---|---|---|---|
| Cal-520 | 1 µM | HBSS with Rhod-2 | Indicator loading |
| Rhod-2 | 1 µM | HBSS with Cal-520 | |
| N/A | N/A | HBSS | Indicator de-esterification |
| ATP | 100 µM | HBSS | Agonist |

The recordings were quantified in ImageJ through the placement of an ROI on every cell and use of the Time Series Analyser V2 to record fluorescence signal over time.

## 6.3 Results

### 6.3.1 Assessing mitochondrial polarity using TMRE

The cationic cell-permeant fluorescent indicator TMRE was used to assess mitochondrial membrane in wild type and cells bearing a CLN3 mutation. Due to its cationic characteristic, TMRE partitions across cell membranes in proportion to the voltage across the membrane (i.e., in a Nernstian manner) (Perry et al., 2011). Since TMRE can traverse cell membranes rapidly, any change in membrane potential will lead to a re-equilibration of the TMRE concentration across the membrane that can be monitored using fluorescence imaging. The mitochondrial matrix is highly negative with respect to the outside of the cell ($\Delta\psi_m$ ~150 mV), TMRE accumulates significantly within active, polarised mitochondria and measures the potential across the inner mitochondrial membrane. TMRE has therefore been used in many studies to assess mitochondrial polarity and energetics.

In this study, TMRE was loaded into cells grown on glass coverslips, as described in Chapter 2. Example images, illustrating the accumulation of TMRE within cells are shown in Figures 1Ai and Aiii. The TMRE fluorescence was relatively stable within the cells for a period of 3 minutes of recording. There was a gradual decline of the TMRE fluorescence that was likely due to TMRE leaving the cells or photobleaching. Superfusing the cells with extracellular solution (FB) caused an acute decrease in the cellular TMRE fluorescence (c.f. Figure 74Ai and Figure 74Aii; note that the timings for image capture and solution additions are indicated in Figure 74B). This drop in fluorescence was expected since TMRE partitions in a Nernstian manner across the plasma membrane and washing away the extracellular TMRE component would cause re-equilibration of the TMRE within the cell. Superfusion of cells with extracellular solution containing the mitochondrial uncoupler FCCP caused a significant drop in the TMRE fluorescence in both wild type and CLN3 KO cells (cf. Figure 74Aiii and Figure 74Aiv). The time course of changes in the TMRE signal is depicted in Figure 74C and D.

Quantitation of the absolute change in TMRE fluorescence caused by superfusion with either extracellular solution or extracellular solution + FCCP is shown in Figure 2A. These data indicate that superfusion with extracellular solution alone evoked a ~10% decline in TMRE fluorescence, whilst the application of FCCP provoked a ~40% reduction in TMRE fluorescence. The extent of the decline in TMRE fluorescence caused by either extracellular solution or FCCP was not different between the wild type or CLN3 KO cells (Figure 75A).

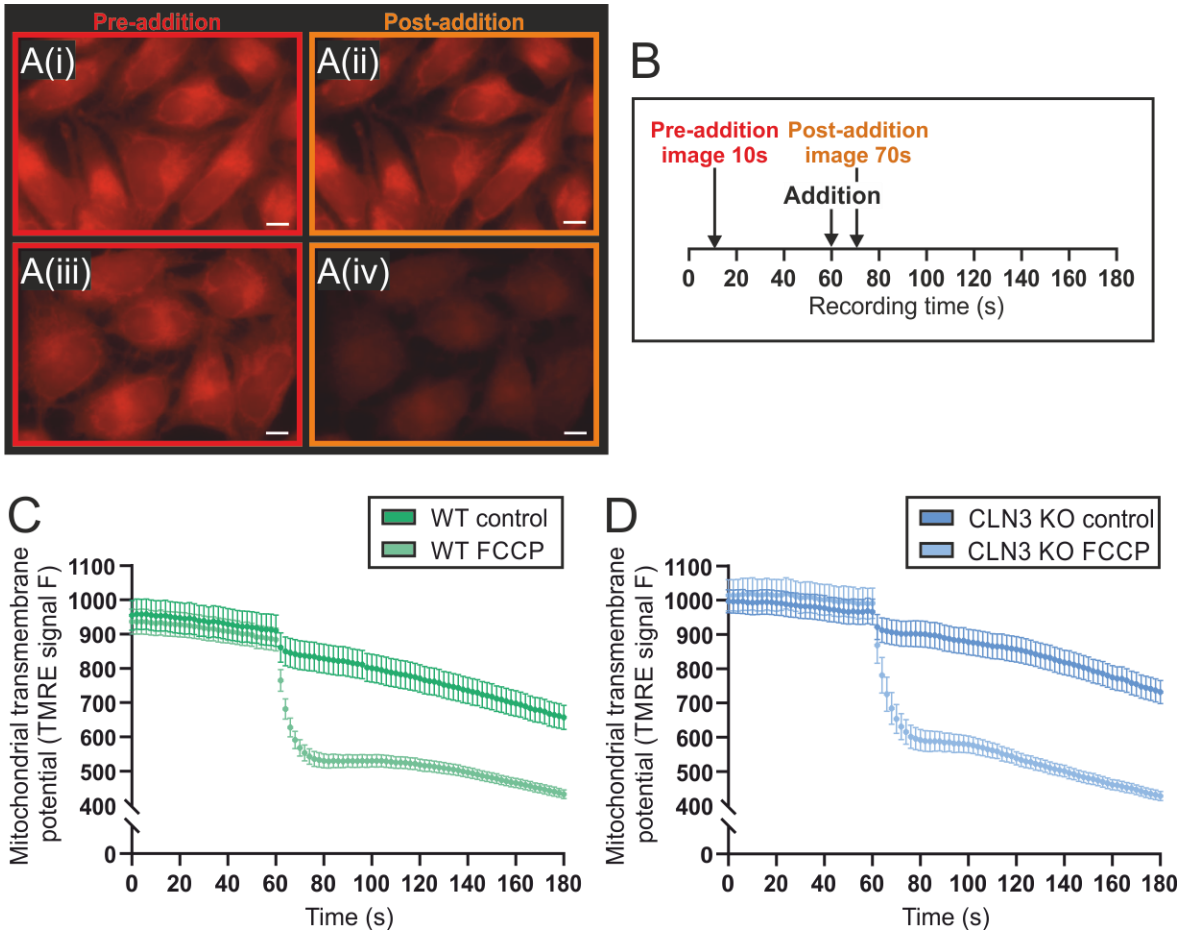


**Figure 74. TMRE fluorescence in wild type and CLN3 KO cells.** HeLa cells loaded with TMRE were imaged for 60 seconds prior to the addition of either a control solution or a solution containing 20 µM FCCP. (A) Images of TMRE loaded HeLa cells before and after the treatments indicated. The scale bar indicates 10 µm. (B) Timeline of imaging experiment and solution addition at 60 seconds. Images used for analysis were taken from frames at 10 s and 70 s, pre- and post- addition. (C) TMRE signal in WT HeLa cells, plotted over time. (D) TMRE signal in CLN3 KO HeLa cells, plotted over time. n = 27 cells (from 3 coverslips on 3 days).

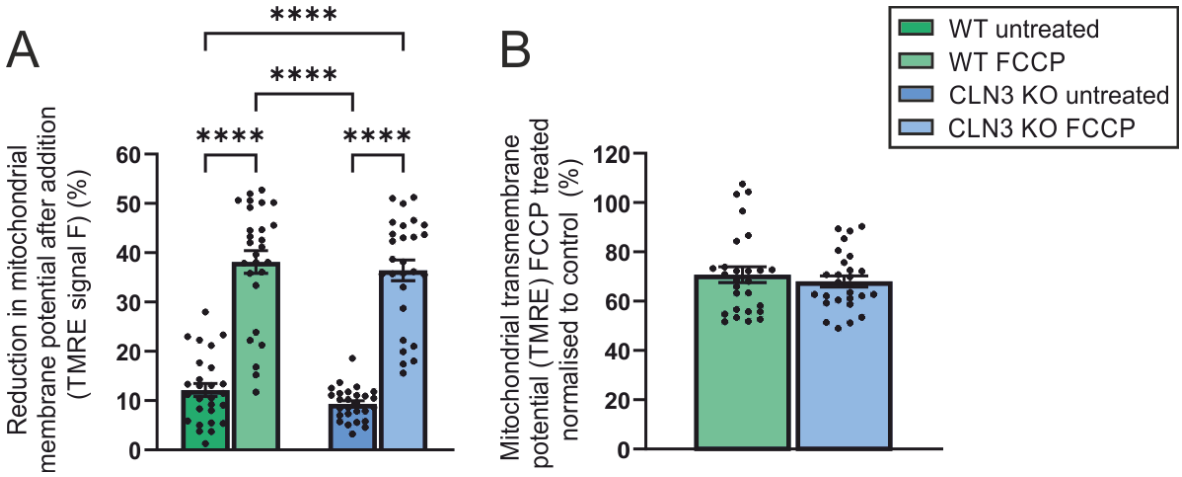


**Figure 75. Quantitation of TMRE fluorescence in wild type and CLN3 KO cells.** HeLa cells were untreated or treated with positive control (20 µM FCCP) to induce mitochondrial depolarisation. (A) shows absolute TMRE fluorescence levels in untreated and FCCP-treated cells. (B) depicts the normalised post-FCCP TMRE fluorescence. The bars indicate that the FCCP diminished TMRE fluorescence by a similar proportion in both WT and CLN3 KO cells. These data were analysed with an Ordinary one-way ANOVA with Tukey's multiple comparisons test where **** indicates $P \leq 0.0001$. These data are mean ± S.E.M. per cell, with scatter points representing individual lysosome movement within each cell and n = 27 cells (from 3 coverslips on 3 days).

### 6.3.2 Assessing ROS production using ROS Brite

Cells produce a variety of chemically reactive molecules that are collectively termed reactive oxygen species (usually abbreviated to ROS) that can lead to cell damage, for example via lipid peroxidation. ROS molecules include superoxide, hydroxyl radicals and peroxides, which can originate from cellular metabolism, and in particular via mitochondrial electron transport (Connolly et al., 2018). The production of ROS occurs in physiological conditions but can accelerate in pathological situations such as with mitochondrial dysfunction.

In this study, the ROS indicator ROS Brite was loaded into cells grown on glass coverslips, as described in Chapter 2. ROS Brite is weakly fluorescent until it is oxidised. The rate of increase in ROS bright fluorescent emission is directly proportional to ROS production within cells (until the ROS Brite concentration becomes limiting). Example images, illustrating the progressive increase of ROS Brite within control cells are shown in Figure *75*A. In addition to measuring increased ROS Brite fluorescence due to basal ROS production with the wild type and CLN3 KO cells, the effects of treating the cells with the compounds tBHP and peroxide, known to cause oxidative stress, were also measured. The rationale for using the oxidative stress reagents was that any small differences in ROS production or buffering between wild type and CLN3 KO cells might be exaggerated. As

illustrated in Figure 75B, there was a progressive increase in ROS Brite fluorescence over time, and both of the oxidative stress reagents enhanced the increase in ROS Brite fluorescence.

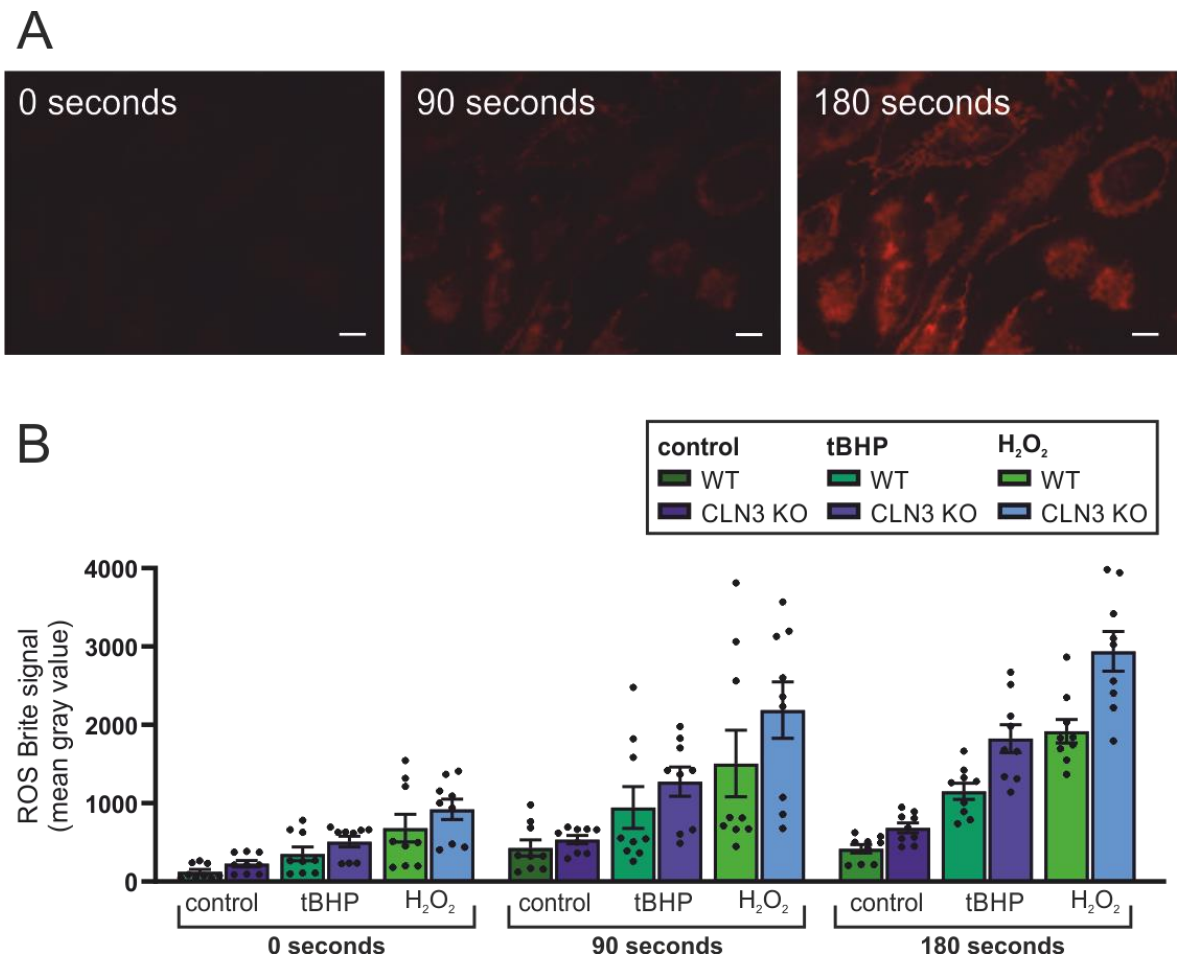


**Figure 76. ROS Brite fluorescence in wild type and CLN3 KO cells.** HeLa cells were untreated (negative control - DMSO) or treated to induce oxidative stress (positive controls - tBHP or $H_2O_2$). (A) Example images of TMRE-loaded WT HeLa cells at 0, 90 and 180 seconds of the imaging series. The scale bar indicates 10 µm. (B) Mean gray value of ROS Brite plotted to indicate oxidative stress at 0, 90 and 180 seconds. These data are mean ± S.E.M. per cell, with scatter points representing individual lysosome movement within each cell and n = 9 cells (from 3 coverslips on 3 days).

The time course of ROS Brite fluorescence increases is depicted in Figure 77A – C for each of the conditions monitored. There was a roughly linear increase in ROS Brite fluorescence over the imaging period. Calculating the slope of the ROS Brite fluorescence data depicted in Figure 77A – C produced the same overall outcome as measuring the absolute change in ROS Brite fluorescence (cf. Figure 76B and Figure 77D): there was a progressive increase in ROS Brite fluorescence over

time, and both of the oxidative stress reagents enhanced the increase in ROS Brite fluorescence. Although the data from the wild type and CLN3 KO cells were not significantly different (when comparing data at the same time timepoint and with the same treatment), there was a tendency for the CLN3 KO cells to display higher ROS Brite fluorescence.

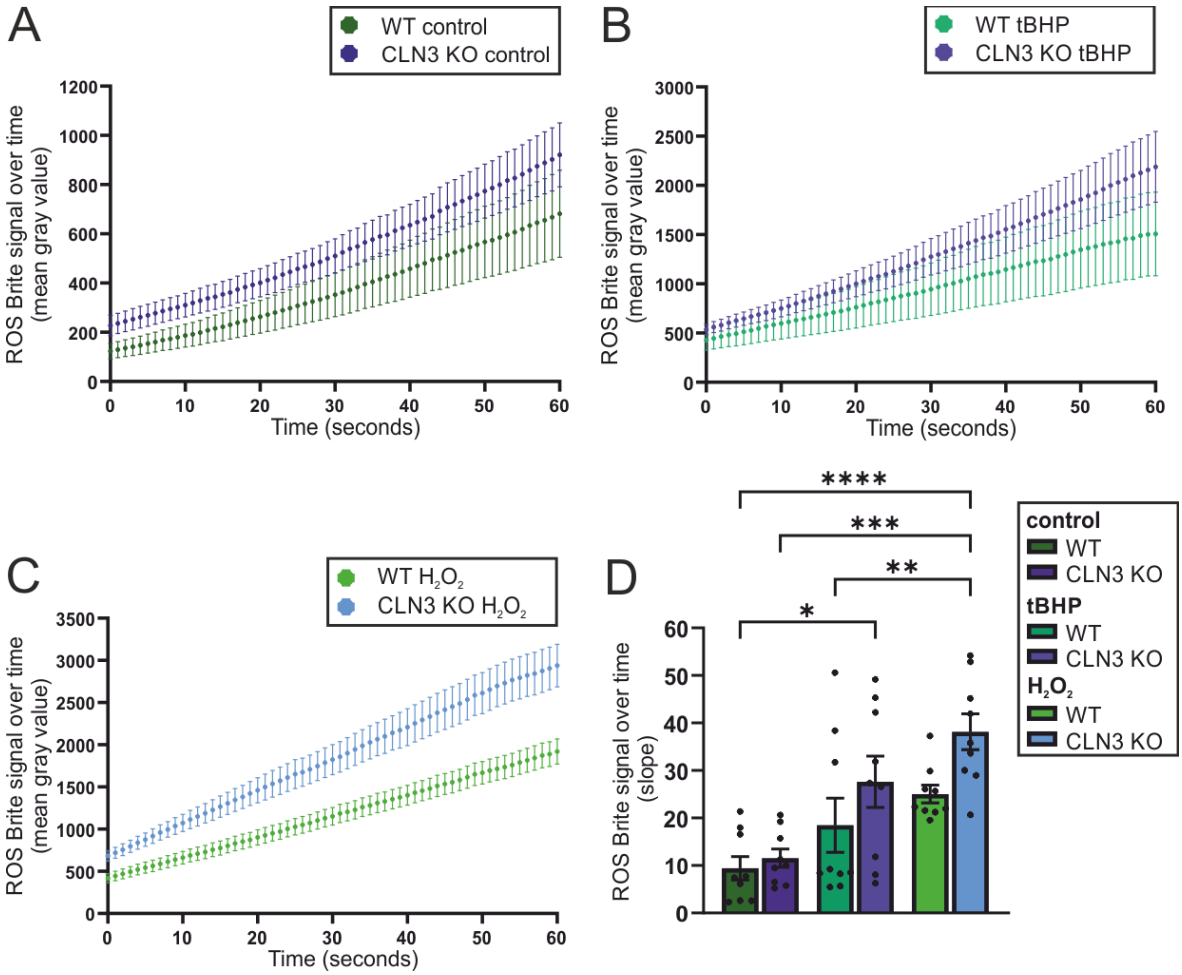


**Figure 77. Time course of ROS Brite fluorescence in wild type and CLN3 KO cells.** HeLa cells were untreated (control) or treated with positive controls (tBHP or $H_2O_2$) to induce oxidative stress. These data were analysed with an Ordinary one-way ANOVA with Tukey's multiple comparisons test where * indicates P ≤ 0.05, ** indicates P ≤ 0.01, *** indicates P ≤ 0.001 and **** indicates P ≤ 0.0001. These data are mean ± S.E.M. per cell, with scatter points representing individual lysosome movement within each cell and n = 9 cells (from 3 coverslips on 3 days).

### 6.3.3 Assessing relative mitochondrial calcium uptake using Cal-520 and Rhod-2

To assess mitochondrial calcium uptake, cells were co-loaded with the cytosolic calcium indicator Cal-520 and the mitochondrial calcium indicator Rhod-2. As with TMRE, Rhod-2 possesses a net positive charge. Hence, Rhod-2 accumulates within the mitochondrial matrix, where it can report changes in calcium concentration. Unlike TMRE, however, Rhod-2 is loaded into cells in an esterified form, and once the indicator is de-esterified it is trapped in situ. By co-loading cells with cytosolic and mitochondrial calcium indicators it is possible to assess relative calcium signals in both compartments simultaneously.

In this study, Cal-520 and Rhod-2 were loaded into cells grown on glass coverslips, as described in Chapter 2. Example images, illustrating ATP-induced calcium signals in Cal-520- and Rhod-2-loaded cells are shown in Figure 6. It is evident that there was a substantial and rapid increase in Cal-520 fluorescence upon superfusion of the cells with ATP (applied at the 30-second time point). The Rhod-2 fluorescence increased more slowly than the Cal-520 signal but persisted for considerably longer. The temporal displacement of the Cal-520 and Rhod-2 responses indicates that there was not significant bleed through between the green and red imaging channels.

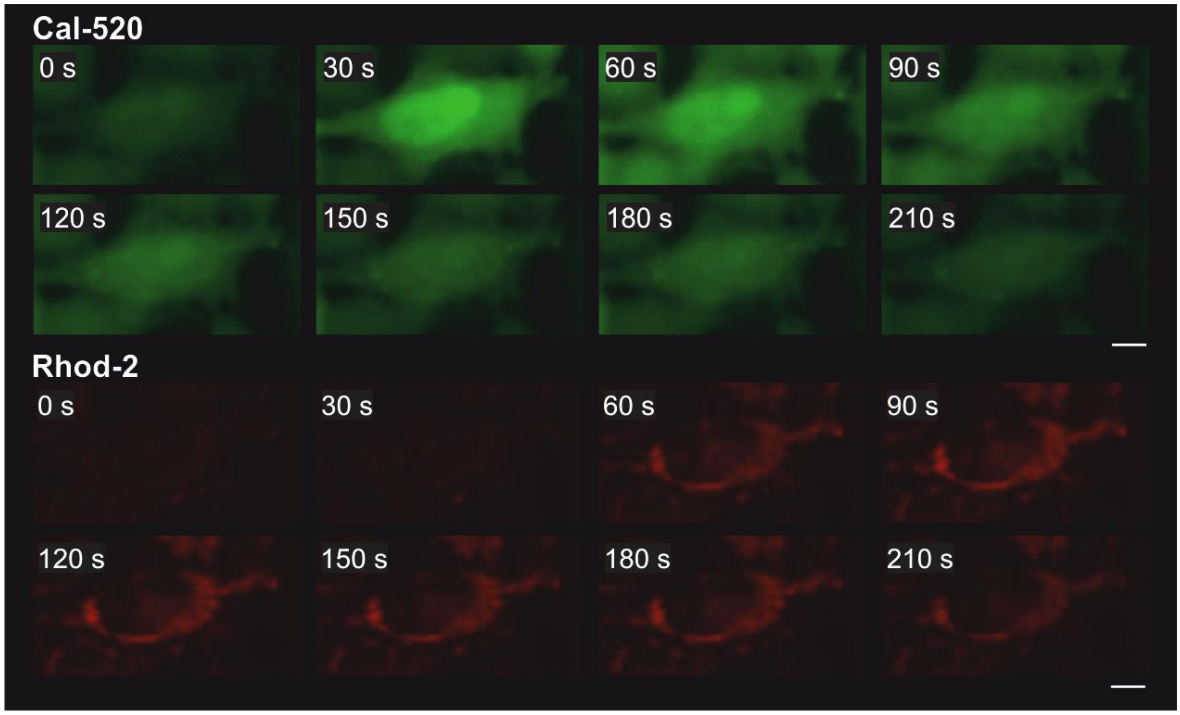


**Figure 78. Cal-520 and Rhod-2 signals in a HeLa cell stimulated with ATP.** The ATP was applied at 30 seconds. The scale bar indicates 10 µm.

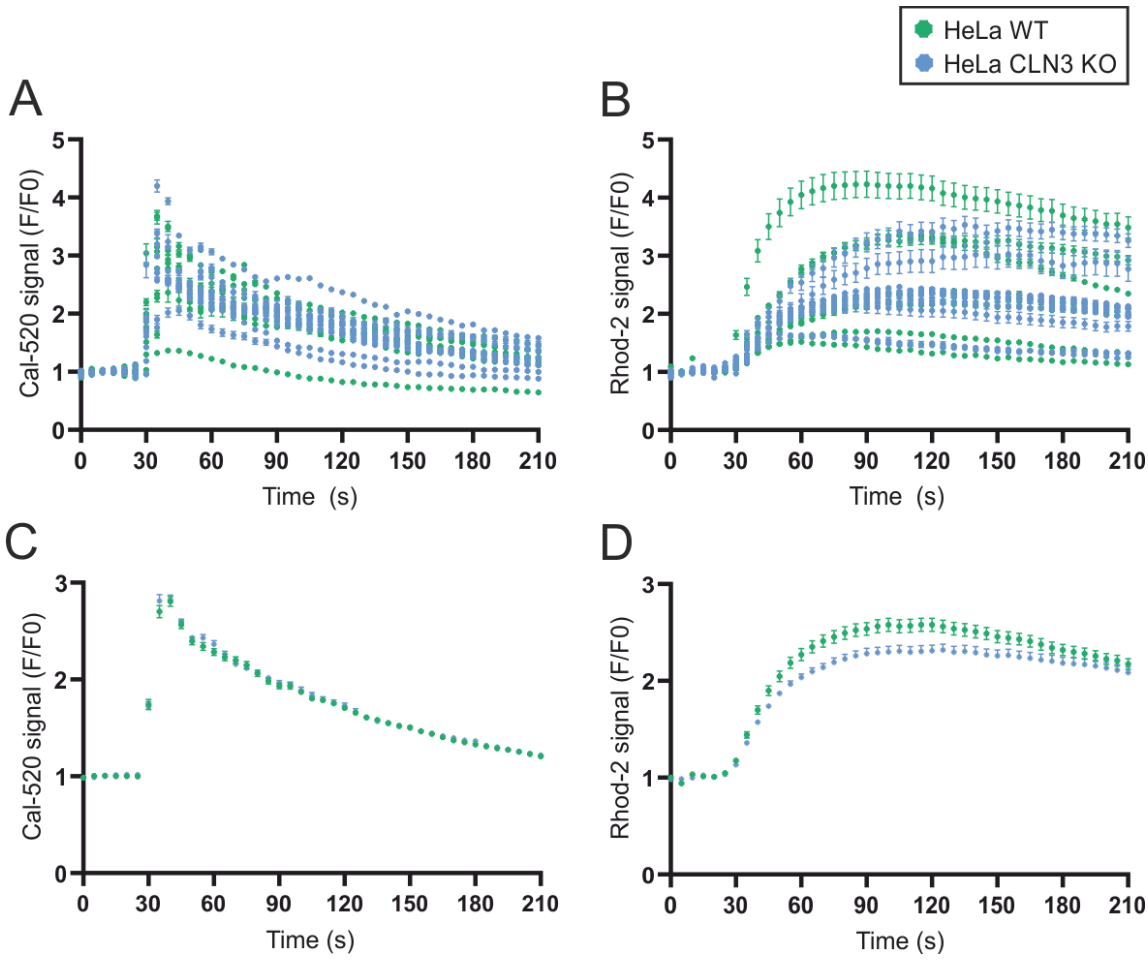


**Figure 79. Cal-520 and Rhod-2 responses in ATP-stimulated wild type and CLN3 KO HeLa cells.** (A and C) cytosolic calcium measured with Cal-520. (B and D) mitochondrial calcium measured with Rhod-2. (C) and (D) show the mean of all replicates. Data are presented as mean ± S.E.M. n = 180 (20 ± 7 cells per coverslip from 3 coverslips per condition, on 3 days).

The traces shown in Figure 79A and B illustrate Cal-520 fluorescence (Figure 79A; cytosolic responses to ATP) and Rhod-2 fluorescence (Figure 79B; mitochondrial responses to ATP) over the time course of an experiment. Consistent with the images shown in Figure 78, the Cal-520 response rapidly rose to a peak that then declined back to baseline over a couple of minutes (Figure 79A). Moreover, similar to the relatively slower change in Rhod-2 fluorescence shown in Figure 79, the Rhod-2 signal developed with a latency and lesser rate of rise but was sustained for longer (Figure 79). Averaging the traces from individual cells indicated that the time course of the Cal-520 and Rhod-2 responses were similar for the wild type and CLN3 KNO cells (Figure 79C and D). Quantification of the Cal-520 and Rhod-2 responses by calculating the peak ATP-induced fluorescence change and the area under the curve indicated that there was no significant difference for the wild type and CLN3 KNO cells (Figure 80). Moreover, neither the rate of rise nor the recovery

of the ATP-induced Rhod-2 responses were significantly different between the wild type and CLN3 KNO cells (Figure 81).

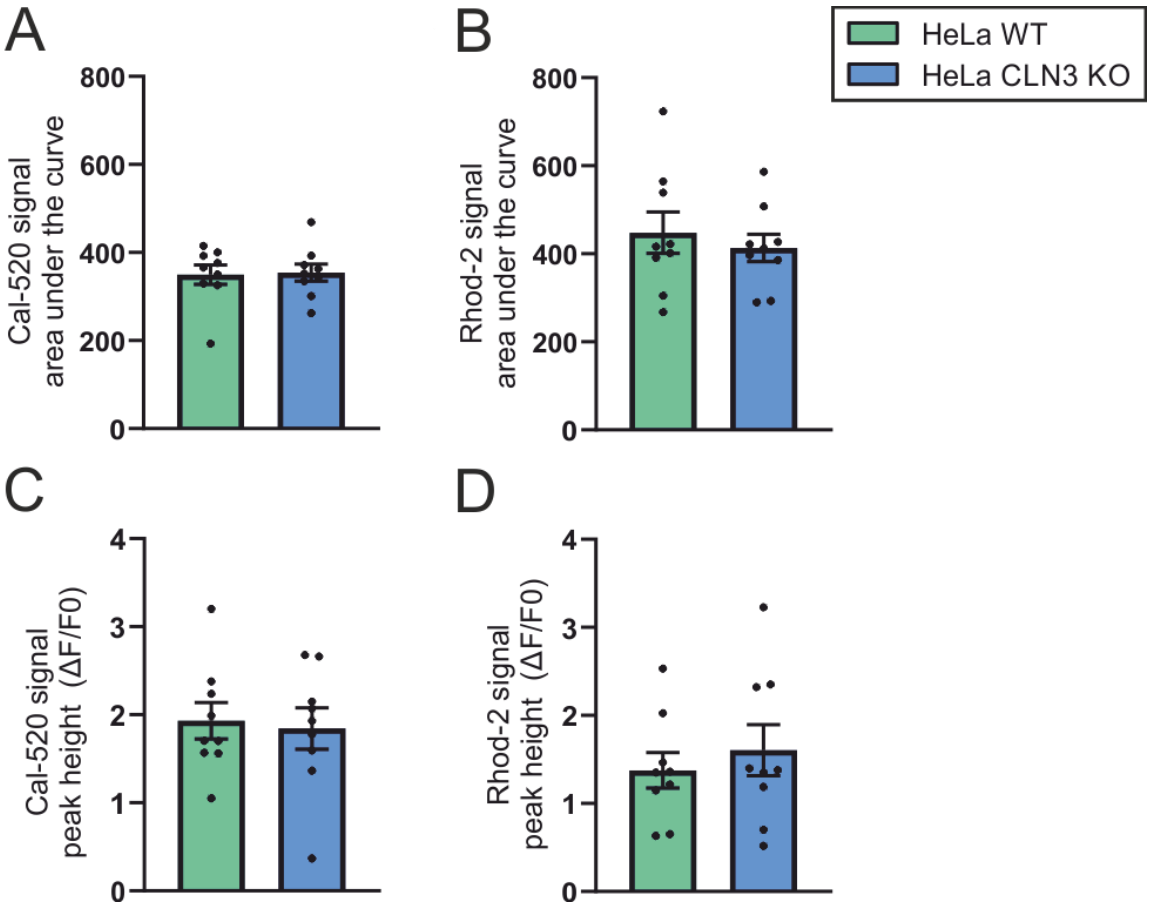


**Figure 80. Quantification of Cal-520 and Rhod-2 responses in ATP-stimulated wild type and CLN3 KO HeLa cells**. The data are presented as mean ± S.E.M were analysed with a two-tailed unpaired t-test, with n = 180 (20 ± 7 cells per coverslip from 3 coverslips per condition, on 3 days).

In addition to the quantification in Figure 80, it was interesting to look at the kinetics of the response to, and recovery from, stimulation with ATP, as measured with Rhod-2. The relevant timepoints for increase and recovery were plotted in Figure 81A and B, and the slopes quantified in Figure 81C and D for response and recovery respectively. There was no significant difference between the WT or CLN3 HeLa cells.

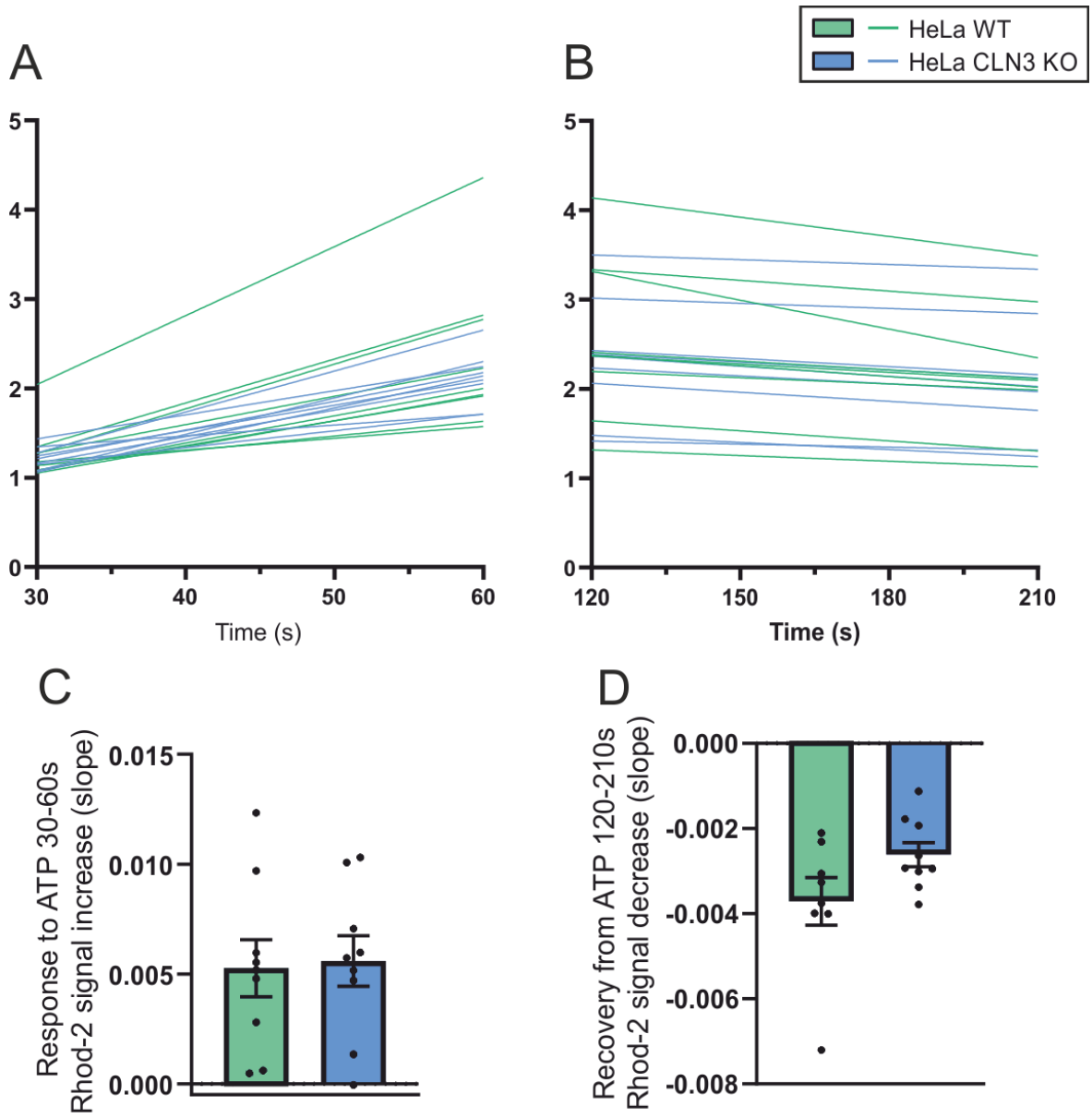


**Figure 81. Mitochondrial calcium response to ATP (increase) and recovery (decrease).** (A) shows the slope of the rise of the Rhod-2 signal from the point of ATP application to the fluorescence value 30 seconds later (i.e., a straight line drawn between the value of the Rhod-2 fluorescence at time = 30 seconds and t = 60 seconds). (A) shows the slope of the decline of the Rhod-2 signal (i.e., a straight line drawn between the value of the Rhod-2 fluorescence at time = 120 seconds and t = 210 seconds). The data are presented as mean ± S.E.M were analysed with a two-tailed unpaired t-test, with n = 180 (20 ± 7 cells per coverslip from 3 coverslips per condition, on 3 days).

Summary of results

- Under the same standard loading conditions, TMRE accumulated within the wild type and CLN3 KNO cells to the same level (Figure 74).
- Superfusion of the wild type and CLN3 KNO cells with extracellular solution containing FCCP caused a drop in TMRE fluorescence consistent with rapidly depolarisation of the cells' mitochondria (Figure 74).
- The magnitude of the FCCP-evoked decline in TMRE fluorescence was not significantly different between the wild type and CLN3 KNO cells (Figure 74, Figure 75).
- ROS Brite indicated the progressive production of oxidising species with the wild type and CLN3 KNO cells (Figure 76).
- The rate of increase in ROS Brite fluorescence could be accelerated by application of tBHP and peroxide, consistent with the known actions of the oxidising agents (Figures 3 and 4).
- The extent and rate of ROS Brite fluorescence increase was not different between the wild type and CLN3 KNO cells (Figure 76, Figure 77).
- The tendency of CLN3 cells to show higher ROS Brite levels could indicate a reduced ability to ameliorate the effects of increased ROS production in cells, making an increase in ROS levels more harmful.
- Co-loading of Cal-520 and Rhod-2 allowed ATP-evoked calcium signals to be simultaneously monitored in the cytosolic and mitochondrial compartments (Figure 79).
- There was no difference in the peak or cumulative Cal-520 and Rhod-2 signals in cells stimulated with ATP when comparing the wild type and CLN3 KNO cells (Figure 80, Figure 81).
- There was no difference in the rates of increase or recovery of the Rhod-2 signals in cells stimulated with ATP when comparing the wild type and CLN3 KNO cells (Figure 81).

## 6.4 Discussion

The link between mitochondria dysfunction and neurodegenerative disease has been well established (Deus et al., 2020). Cell models of CLN3 disease have revealed some changes to mitochondrial function (Fossale et al., 2004, Chandrachud et al., 2015). The experiments in this chapter aimed to further investigate the role of mitochondria in CLN3 disease using the CLN3 KO HeLa cell model. These assays covered critical mitochondria functions such as the membrane potential (TMRE assay), the ROS production within the cells (ROS Brite assay), and as mitochondria and lysosomes are linked by their function as calcium stores, the cellular calcium response to ATP (Cal-520/Rhod-2 assay). Within this comprehensive assessment of a number of parameters, there was no statistical difference that could be established between the WT and CLN3 KO HeLa cells. Therefore, either the assays were not sensitive enough to measure modest differences between WT and CLN3 KO cells, or the use of the HeLa cell model did not represent the changes found in more sensitive cells that are typically affected by CLN3 disease. This could be further investigated with a combination of additional assays and cell types.

## 6.5 Future work

Since the principle cellular defect(s) caused by CLN3 mutation are not known, using a plethora of assays remains a viable approach to understanding what may have changed within cells.

The measurements were collected from multiple cells across three coverslips and the n number reflected the number of cells. The robustness of the statistical analysis could be improved in future experiments by introducing a greater number of coverslips and using each coverslip as an n of 1, to improve the independence of the sampling.

To follow on from the ROS Brite experiments, a more specific ROS indicator may be useful. For example, MitoSOX could reveal whether there were any changes specifically to mitochondrial superoxide production as a result of the CLN3 mutation.

The assays described in this chapter could be applied to additional CLN3 cell models to investigate cell types which may be more sensitive. Additionally, the manipulation of the HeLa cells lines such as starvation or prolonged culture may reveal a phenotype if the CLN3 KO cells are less capable of handling stress. It would also be interesting to compare the assays used in this study with responses from cell models of neurodegenerative diseases in which clear phenotypic and function lysosomal and mitochondrial changes have been found. In addition to the calcium assays using Cal-520 and Rhod-2, it would be extremely interesting to measure lysosomal calcium in these cells. A similar experimental setup with the co-loading of Cal-520 or Rhod-2 with an indicator for lysosomal calcium would facilitate the direct comparison of calcium traces, as shown for Cal-520 and Rhod-2 in Figure 79.

# 7 Ultrastructural changes in cardiac myocytes from CLN3 and WT control mice

## 7.1 Introduction

As discussed in Chapter 1, there have been a handful of papers documenting CLN3 disease patients developing a cardiac pathology towards the end of life (Reske-Nielsen E, 1981, Michielsen et al., 1984, Tomiyasu et al., 2000, Dilaveris P, 2014, Ostergaard JR, 2011). In addition, changes to the heart were identified in some animal models of CLN3 disease. For example, in the *CLN3*$^{\Delta ex7/8}$ mouse model, the heart had an increased average weight compared to that in WT control mice at 20 weeks, but this was not reflected in any measurable functional change (Staropoli et al., 2012). The heart of the zebrafish model of CLN3 disease was enlarged and abnormally shaped, but no further investigation into functional changes of this phenotype was carried out (Wager et al., 2016). Accumulation of storage material has been described in heart tissue of humans and dogs in both, cardiac myocytes and the conduction system (Armstrong et al., 1986, Fidziańska et al., 2013). In fact, before genetic diagnosis was possible, storage material in skeletal muscle was used as a marker for the diagnosis of NCLs (Goebel, 1975). On the whole, there has been little focused study of the pathology of CLN3 disease in the heart. Recent reviews have summarised the available literature of both humans and animal models, and highlighted the anecdotal clinical observations of those working with CLN3 disease patients; highlighting the need for more in-depth studies of structural and functional changes that underpin the cardiac pathology in CLN3 disease (Ostergaard, 2016, Rietdorf et al., 2019).

As described in Chapter 1, the correct and efficient function of the heart is reliant upon the highly organised tissue arrangement. Changes in heart tissue, such as from disorganisation of structure and/or organelle dysfunction, could affect heart function and therefore provoke a progressive cardiac pathology in patients. Mitochondria are important in heart tissue, where they provide energy for contraction of cardiac myocytes. The link between mitochondrial dysfunction and conditions leading to heart failure has been well documented (Li et al., 2020, Rosca et al., 2013). The findings included changes to mitochondria in various stages of disease and ageing. For example, an increase of mitochondrial DNA damage, an increase in ROS production, increase in fission and a decrease in density of mitochondria in heart failure (Li et al., 2020). It was reported that increased demands of hypertrophy could be matched by an increase in the number and size of mitochondria, but rapidly declined when this condition progressed to heart failure (Rosca et al., 2013). In CLN3 patients, hypertrophy (particularly of the left ventricle) was the most commonly reported condition in the heart (Rietdorf et al., 2019).

Ageing has been widely accepted as a risk factor for heart failure, and exercise has been linked to amelioration of the pathological changes related to cardiac ageing, such as an increase in cardiac myocyte size (Li et al., 2020). Both number and volume of mitochondria measured in the left

ventricle of hearts from mice allowed to voluntarily exercise were greater than in matched control mice; this was despite no significant change in the number or volume of cardiac myocytes in the heart, or overall heart weight (Eisele et al., 2008). It is interesting that the study set out to study the influence of exercise on heart mass, but it revealed that significant changes were in fact seen in the mitochondria within the tissue, rather than the cardiac myocytes or overall tissue mass.

Throughout their lifespan, mitochondria undergo fission to divide and fusion to merge; processes that have been implicated in ageing as a risk factor for heart failure (Liu et al., 2020). Fission and fusion events impact the mitochondria availability and activity, potentially altering the energy output in the form of ATP (Kowald and Kirkwood, 2011, Liu et al., 2020). The number of mitochondria per cell affects the expression of mitochondrial DNA (mtDNA) and processes such as ATP or ROS production (Cole, 2016). The number of mitochondria present in a cell is also influenced by mitophagy, a process for removal of dysfunctional mitochondria. Mitophagy also declines with age and therefore may allow accumulation of dysfunctional mitochondria over time (Liu et al., 2020).

In addition to mitochondrial number, the size of mitochondria may be affected by disease and ageing (Hoppel et al., 2009). For example, extremely large mitochondria, termed 'megamitochondria', were found in a patient with cardiomyopathy (Tandler et al., 2002). Mitochondria inside cells can have different shapes and vary in their functional aspects (e.g., their membrane potential or ability to take up $Ca^{2+}$). Often, a higher density of mitochondria is found near the nucleus than in a cell's periphery. The shape of mitochondria may be rounded, or more elongated in appearance, which might be relevant to their individual or syncytial function (Collins et al., 2002). The localisation of mitochondria and their movement inside a cell is affected by the cytoskeleton (Anesti and Scorrano, 2006). Mitochondria that are found in the tightly packed continuous groups in cells were described as 'power-transmitting cables' to describe how these may be functionally more efficient for example in the equilibration of electrochemical signals (Skulachev, 2001). Studies have found that when energy demand increases, mitochondria formed clusters, rather than having the appearance of individual entities during periods of low energy demand (Skulachev, 2001).

Cardiac myocytes are characterised by a high energy demand, and a highly organised arrangement of myofibres. There are three types of mitochondria within cardiac myocytes: perinuclear, sub-sarcolemmal, and interfibrillar mitochondria. Mitochondria from these three groups differ in their typical shape, morphology of their cristae and their function. Sub-sarcolemmal mitochondria are found under the sarcolemma. They vary in shape and provide the energy for transport processes involving the sarcolemma. Perinuclear mitochondria are found near the nucleus. They are thought to provide energy for processes taking place inside the nuclei and are spherical in shape and

typically smaller than the interfibrillar mitochondria that are found between the myofibres. The interfibrillar mitochondria are typically elongated in shape, larger than perinuclear mitochondria, and provide energy for the myocyte contraction (Hollander et al., 2014, Ong et al., 2017). In this chapter, the subpopulation of interest is the interfibrillar mitochondria.

As mentioned before, no systematic study has yet investigated changes in the heart of patients or animal models of CLN3 disease. However, studies in other cell types indicate how mitochondrial structure and function can be affected in CLN3 disease. The accumulation of subunit C of the ATP synthase in the lipofuscin storage materials in cells affected by CLN3 disease has long been established (Kominami et al., 1992). Studies in cells from individuals with CLN3 disease have shown various abnormalities in the mitochondrial function, including lower ATP levels, reduced overall function, altered $Ca^{2+}$ homeostasis and changes in shape (Luiro et al., 2006, Fossale et al., 2004, Chandrachud et al., 2015).

In this chapter, a detailed characterisation of the ultrastructure of cardiac myocytes from the hearts from the *CLN3*$^{\Delta ex7/8}$ mouse model will be presented. Because changes in mitochondrial structure and function have been described in other cell types, a detailed analysis of mitochondrial changes was performed. TEM imaging of the fixed hearts from the *CLN3*$^{\Delta ex7/8}$ mouse model and matched WT control mice was performed and images were analysed as described in Chapter 2.

**Aims and objectives**

The work presented in this chapter compared the number, size, shape, and distribution of interfibrillar mitochondria within ventricular cardiac myocytes, observed by transmission electron microscopy (TEM) of WT and *CLN3*$^{\Delta ex7/8}$ mice at the ages of 6, 12 and 18 months of age.

The specific aims were:

1) To quantify any observed changes to mitochondria relating to:
    a) Number
    b) Size
    c) Shape

2) To quantify the distribution (clustering) of mitochondria in tissue
3) To describe storage material found in cardiac myocytes

## 7.2 Methods

Hearts from the mouse model of CLN3 disease carrying the *CLN3*$^{\Delta ex7/8}$ mutation (henceforth referred to as 'CLN3 mouse' or 'CLN3 mice'), with matched control mice carrying the wild type (WT) *CLN3*$^{+/+}$ gene (henceforth referred to as 'WT mouse' or 'WT mice'), were available from Professor Jonathan Cooper at Washington University School of Medicine in St. Louis. When these animals were sacrificed at 6, 12 and 18 months, the hearts were preserved by PFA fixation and transferred to The Open University where they were stored frozen. Prior to imaging, 1mm$^3$ sections were cut from the ventricles and subsequent sample preparation and contrast staining was carried out by staff at the Electron Microscopy (EM) Suite at The Open University. The samples were randomised and coded by the EM Suite staff to ensure that imaging and analysis were carried out blinded. Images were taken using the JEM1400 transmission electron microscope (TEM) as described in Chapter 2.

To ensure that only comparable areas were included in the analysis, regions for imaging and analysis were selected based on the presence of uncontracted myofibers. These were identified as having evenly spaced Z-lines with I-bands visible in light grey in-between the Z-lines and the myofibres (or A-bands) (Figure 82). This selection was made to avoid comparing regions in different states of contraction (as can happen in cardiomyocyte sample preparation) and therefore ensure that measurements could be compared from region to region and across multiple samples.

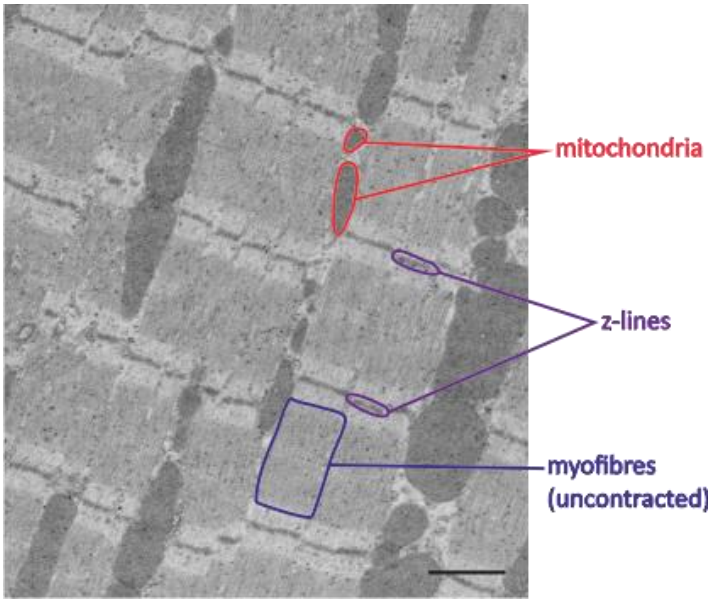


**Figure 82. TEM image of mouse cardiac myocytes, illustrating mitochondria (red), Z-lines (purple) and myofibres (blue).** Regions of uncontracted tissue were identifiable by the light and dark areas of the myofibres between z-lines. In uncontracted muscle, the light grey I-bands are visible between the A-bands.

### 7.2.1 Number of mitochondria

All images were taken at a magnification of 2000x. To ensure consistency during the analysis, this magnification was performed on images maximised to the screen size, resulting in a view scaled at 31.8% of the original image. In ImageJ, a grid of 0.5 inches$^2$ as shown in Figure 83 was applied with the Grid plugin to aid counting. Mitochondria were counted using the Cell Counter plugin. Where mitochondria were touching the top and left boarders of the image they were included in the count, while those on the bottom and right were excluded. If boundaries between mitochondria were not completely clear (as in the case of tightly packed mitochondria), the number of mitochondria were estimated by careful inspection of the shape of the outer membrane, which typically dipped inwards between mitochondria. Where these dips were visible within a cluster, a separate mitochondrion was counted. All images were saved with the count overlay to check for any error in counting.

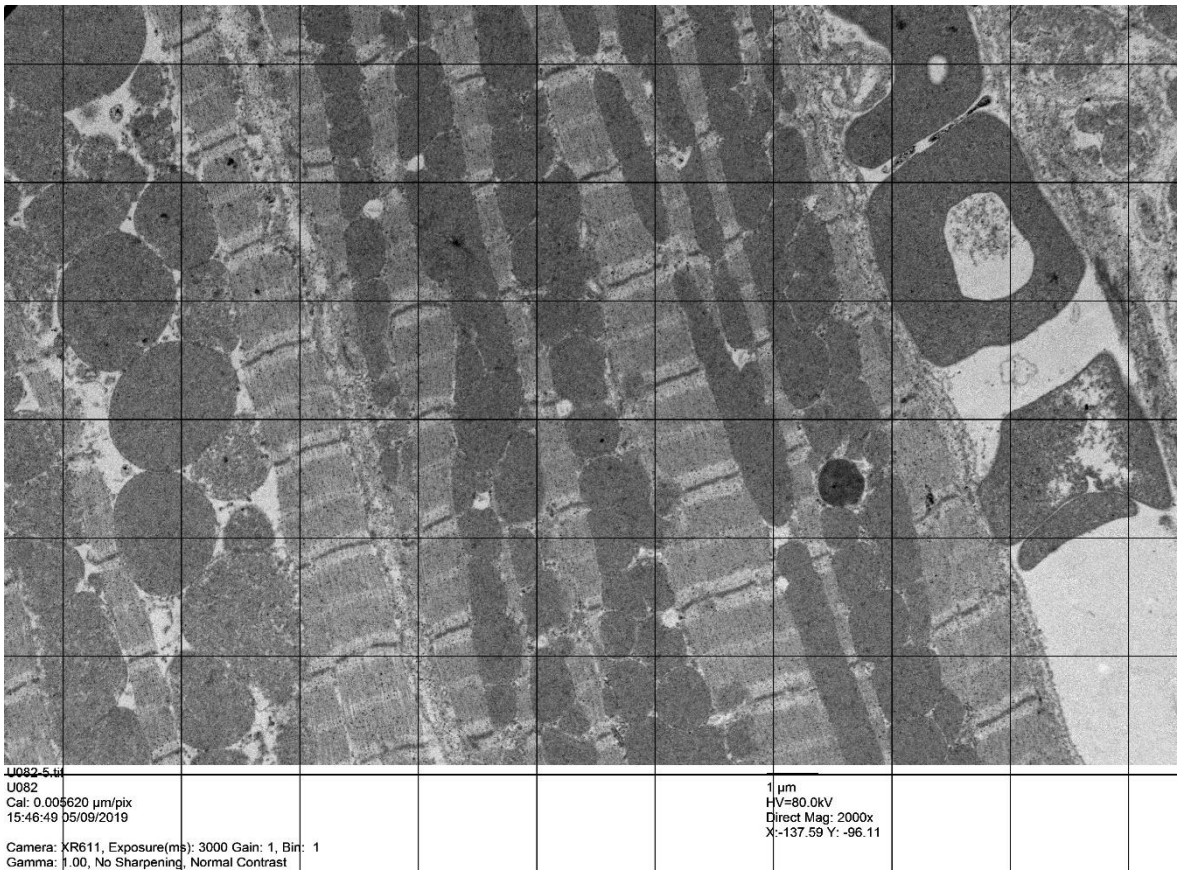


**Figure 83. Example of the 0.5 inches$^2$ grid applied to images in ImageJ.** This was used to aid counting of mitochondria or clusters of mitochondria across the entire image and for the selection of mitochondria for measurement, starting from the first mitochondria in the first complete grid square in the upper left corner. Alternate squares were used for counting to reduce the area that had to be counted whilst ensuring that an area spanning the whole image was counted in an unbiased manner.

### 7.2.2 Shape and size

To measure the shape and size of mitochondria, 10 mitochondria were measured from each of 10 images, resulting in 100 measured mitochondria per heart. To remove bias in attempting to randomly select mitochondria to measure, they were selected based on the grid, shown in Figure 83, measuring the top left mitochondria from alternating grid squares across the image until 10 were reached.

To estimate the size and shape of mitochondria, their diameter was measured across the centre, as illustrated in Figure 84. The first measurement, called d1 (Figure 84a-c), was taken across the mitochondria at the widest point, noted as 'length', and a second measurement, called d2, was taken perpendicular to the first (Figure 84a-c), noted as 'width'.

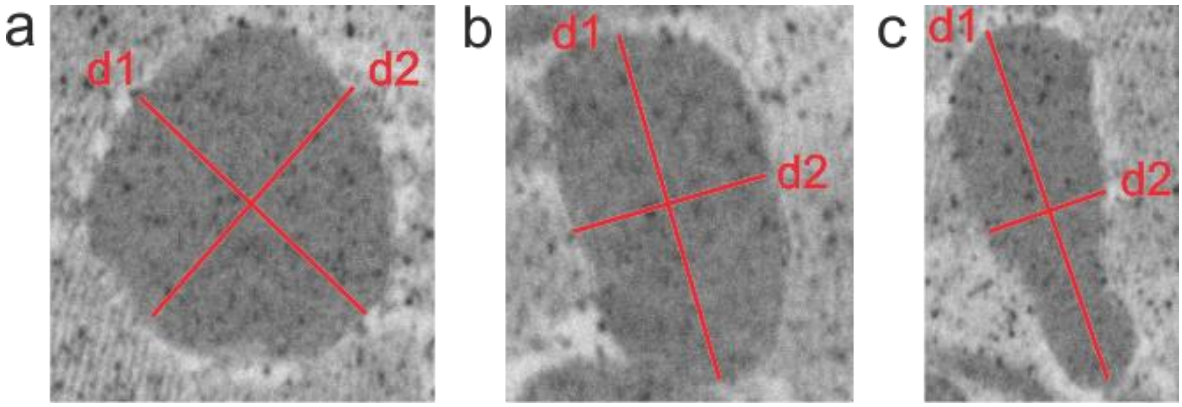


**Figure 84. Example measurements of three representative mitochondria (a-c), to calculate size and shape.** Measurement of the diameter at the furthest points (line d1) to indicate length and measurement of the perpendicular line as diameter (line d2) to indicate width.

From these length (d1) and width (d2) measurements of diameter as described in Figure 84, the size and shape of mitochondria were calculated. Size was calculated as the approximate area of mitochondria, illustrated in Figure 85, using the assumption that mitochondria were generally close to being either circular or elliptical in shape. The measured diameters of length (d1) and width (d2) were divided by 2 to calculate each radius. The radius of length (r1) and radius of width (r2) were then used in the equation $\pi*r1*r2$ to determine the area. This method did not provide an absolute size, as some error will be introduced by the assumption of elliptical shape but allowed a rapid quantification for comparison of mitochondria size in different samples.

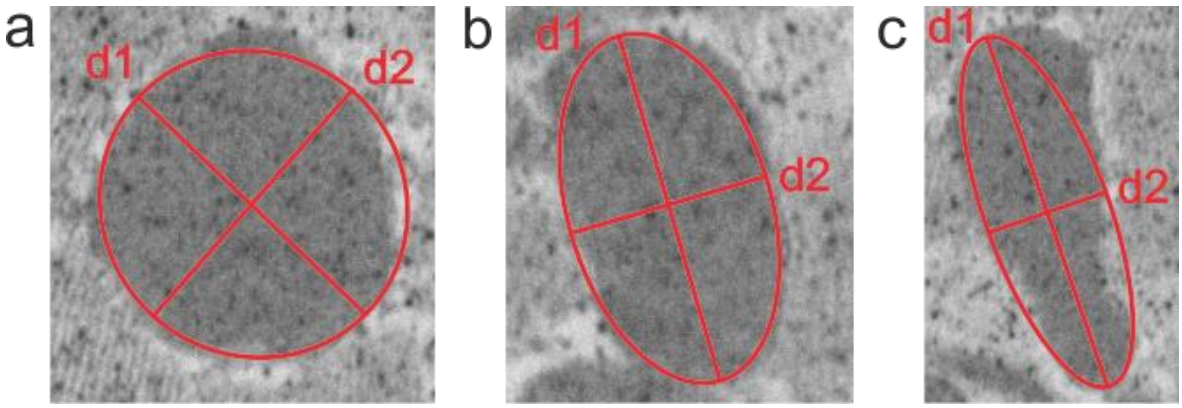


**Figure 85. Example measurements of representative area for three example mitochondria (a-c)**. The calculated area is illustrated by the red circle or ellipse, where area = π*(d1/2) *(d2/2).

To test if mitochondria were indeed spherical or elliptical shape, their shape was determined by the length divided by width. A ratio of 1 would indicate a circular mitochondrion, while the higher the ratio the greater the deviation from circular and more elongated the shape.

### 7.2.3 Distribution of mitochondria within the tissue and clustering

Typically, the interfibrillar mitochondria in cardiac myocytes form long clusters that are in close contact Figure 86a). However, in some images the mitochondria appeared to be scattered between and within the myofibres, either individually or in very small clusters (illustrated in Figure 86b). Clusters were defined as a group of mitochondria (i.e., two or more mitochondria) formed by contiguous, directly-contacting organelles that ended when a gap was visible. A mitochondrion that was not touching another was counted as one. The number of clusters was quantified to determine whether the distribution of mitochondria was altered with the *CLN3* mutation, compared to WT and with age of both WT and CLN3 mice. The results were normalised to an area of 100 $\mu m^2$.

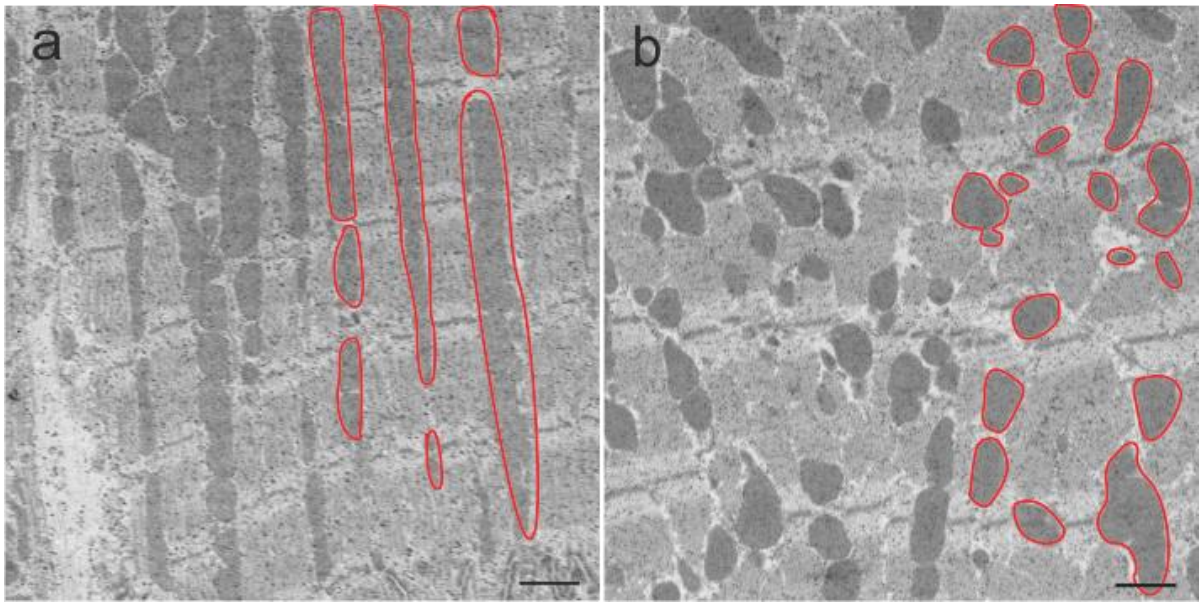


**Figure 86. EM images showing distribution of mitochondria in cardiac myocytes.** Panel a illustrates a region in which mitochondria are forming long clusters (groups of mitochondria in continuous contact with each other). Panel b illustrates a region in which most mitochondria are isolated, and only a few small clusters are visible, such as the group in the bottom right corner of the image. Mitochondria are closer packed in panel a and therefore counted as fewer clusters, whereas distribution of mitochondria in panel b demonstrates many mitochondria in small clusters or individually. The scale bar is 1 µm.

The quantification of the mitochondria was carried out blinded and each sample was analysed prior to decoding. The results were plotted with the average of 10 images per sample represented as a column on a bar graph and each image represented as one scatter point on the bar. Once decoded, the bars were grouped by type (genotype and age). To compare the effects of age and genotype, the image replicates for each sample were combined.

## 7.3 Results

The heart tissue that was analysed came from WT control and CLN3 mice that were sacrificed at 6 months (6m), 12 months (12m) and 18 months (18m) of age.

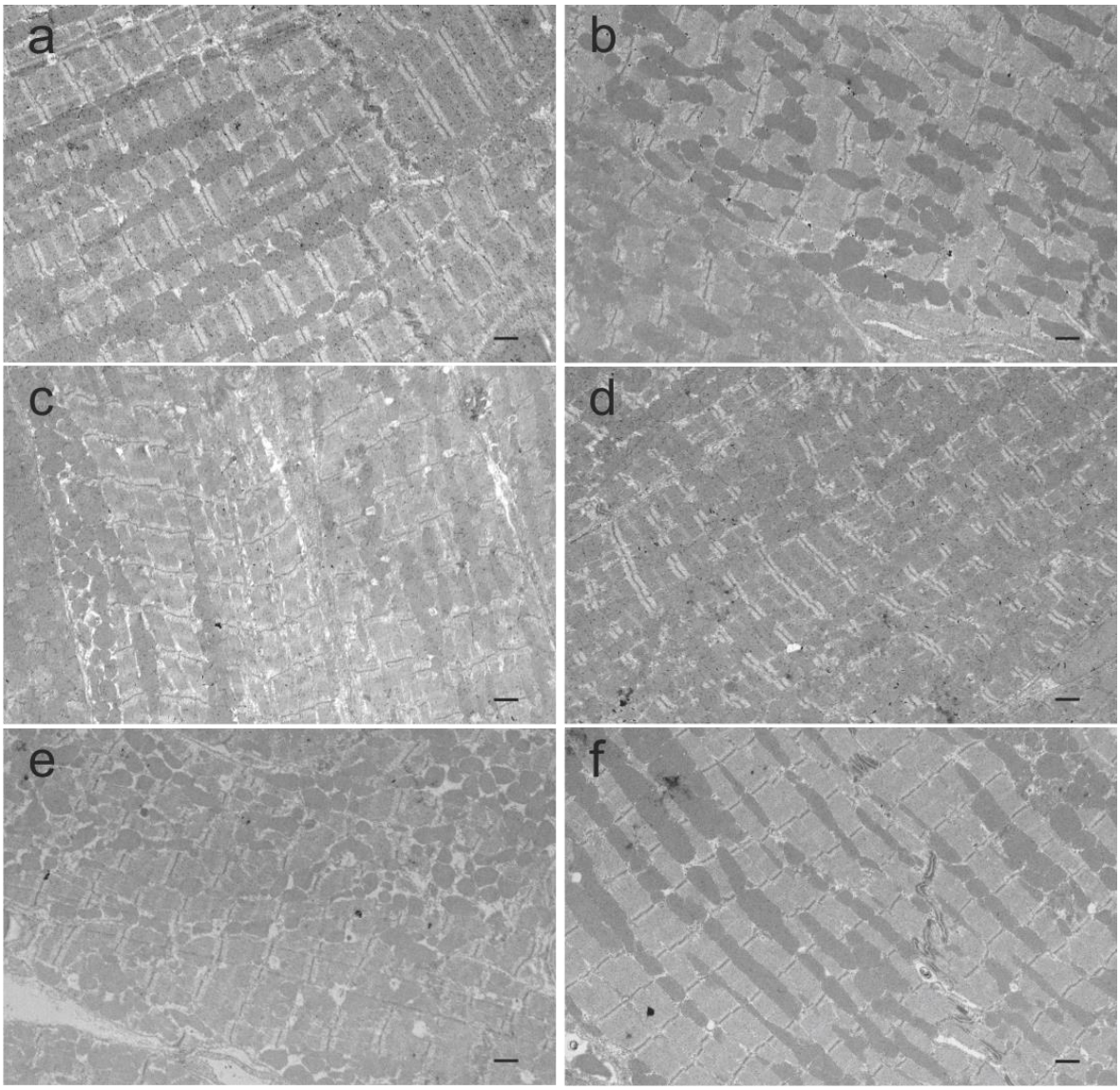


**Figure 87. Representative TEM images of cardiac myocytes.** Images of heart tissue from; (a) WT mouse at 6 months, (b) CLN3 mouse at 6 months, (c) WT mouse at 12 months, (d) CLN3 mouse at 12 months, (e) WT mouse at 18 months and (f) CLN3 mouse at 18 months. The scale bar is 1 µm in all images.

### 7.3.1 Number of mitochondria per 100 µm$^2$

To understand the variability in the number of mitochondria between animals of the same age and genotype, the average number of mitochondria for each image is shown as scatter point in Figure 88. Each bar represents the measurements taken from one animal of the specified age and genotype. Especially for the 18 months-old animals, a considerable variation in the number of mitochondria can be seen. Whilst the majority of these cardiac myocytes showed the largest number of mitochondria seen, one of the hearts from a CLN3 mouse showed a very low number of mitochondria. Summarised, there was a considerable variation in the number of mitochondria in the cardiac myocytes of the different animals.

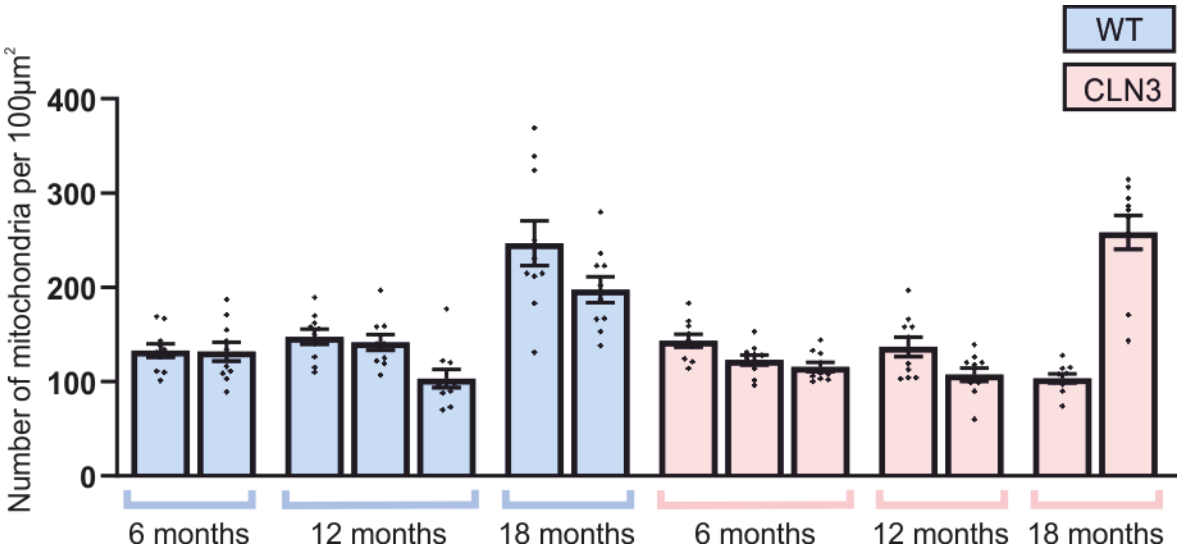


**Figure 88. Number of mitochondria per heart.** The data are presented as the number of mitochondria per 100 µm$^2$ (mean ±S.E.M.). Each point on the columns represents the average measurement from 10 cardiac myocytes images for each heart.

The numbers of mitochondria per heart, as shown in Figure 88, were grouped by age and genotype, and are presented in Figure 89. The average number of mitochondria was greater in the images of cardiac myocytes from the WT mice at 18 months, compared to all other animals. In contrast, mitochondria did not appear in greater numbers with age in CLN3 hearts. In 18-month animals, cells from WT mice contained significantly more mitochondria than those of CLN3 mice. However, the data points in Figure 88 indicate that the variation between the two 18-month CLN3 mice was greater than in any other group.

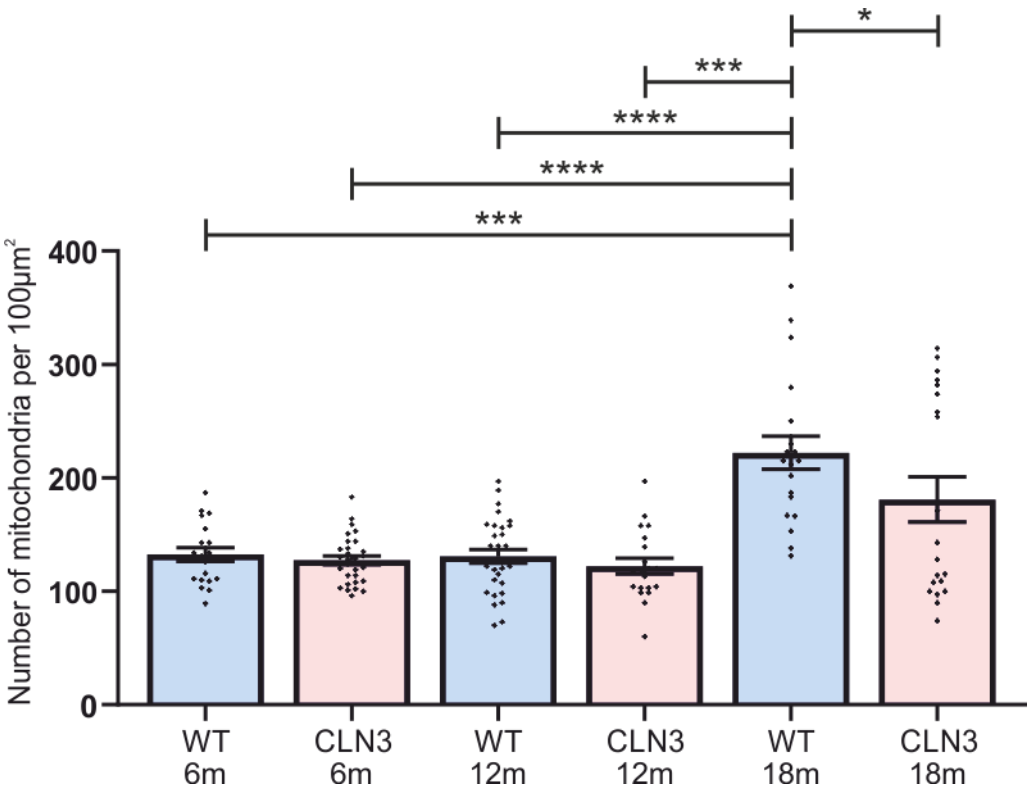


**Figure 89. Number of mitochondria.** This bar graph was obtained by combining the data shown in Figure 7 for each of the CLN3 and WT cardiac myocytes at the specified ages. The data were analysed using a Kruskal-Wallis test with Dunn's post-hoc comparison. * indicates $p<0.05$, *** indicates $p<0.001$ and **** indicates $p<0.0001$. n = 20 - 30 images per condition (2 or 3 hearts each with 10 cardiac myocytes images per heart, as depicted in Figure 7). The data are presented as mean ± S.E.M.

### 7.3.2 Average size of mitochondria

To investigate if the average size of mitochondria also showed a variability between the cardiac myocytes of hearts of animals from the same age and genotype, the data obtained from the different animals were plotted separately and are shown in Figure 90. Whilst the number of mitochondria was a total for each image, normalised to 100 $\mu m^2$, the size of mitochondria was the average measurement taken from only 10 mitochondria per image. The average size of mitochondria for each heart as plotted in Figure 90 varied from between 0.322 $\mu m^2$ and 0.700 $\mu m^2$ with the largest being approximately twice the size of the smallest. However, there was no identifiable pattern or grouping of these values for the different conditions. The largest inter-group variation was between cardiac myocytes in the pair of 18-month WT hearts (average 0.322 - 0.636 $\mu m^2$).

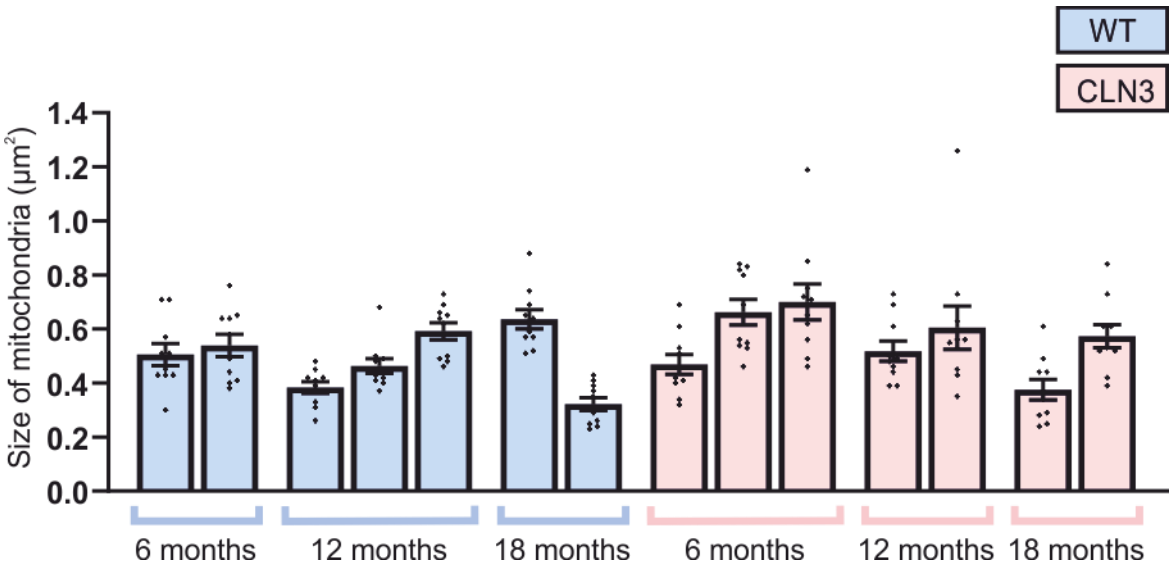


**Figure 90. Size of mitochondria (µm$^2$).** Data are presented as mean size of mitochondria per heart ± S.E.M. The average size of mitochondria was calculated from 10 mitochondria per image each plotted as scatter point on the bar. Per heart, a total of 100 mitochondria was analysed; 10 mitochondria measured per image from 10 images each).

To analyse if age or genotype affected the size of mitochondria, the data from different animals of the same age and genotype were grouped and plotted (Figure 91). As shown in Figure 91, there was no significant difference in the average size of mitochondria across any of the ages or genotypes. Therefore, size did not change with age of the mice and did not significantly vary between the WT or CLN3 disease model mice.

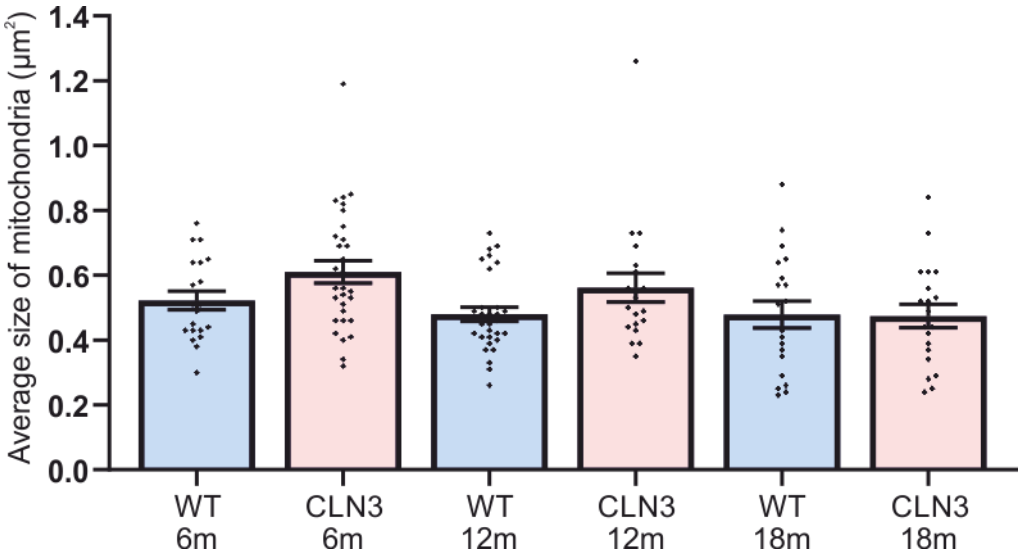


**Figure 91. Average size of mitochondria (µm$^2$).** This bar graph was obtained by combining the data shown in Figure 9 for each of the CLN3 and WT hearts at the specified ages. The data were analysed

using a Kruskal-Wallis test with Dunn's post-hoc comparison. n = 20 - 30 images per condition (2 or 3 hearts each with 10 images per heart, as depicted in Figure 90). The data are presented as mean ± S.E.M.

### 7.3.3 Roundness of mitochondria

The roundness of mitochondria was assessed with a ratio of length to width measurements, where a value of 1 is a circle and the greater the value, the more elongated the mitochondria. To investigate variability of the roundness within the different ages and genotypes, the data obtained from the different animals were plotted in separate bars, shown in Figure 92. No mitochondria were found to be perfectly round, as a mathematically determined circle, although some were close. There was no clear pattern in roundness between the ages and genotypes, although on the whole the mitochondria in the cardiac myocytes of CLN3 mice appeared to be rounder than in the WT tissue. There was considerable variation in the shape within each image and in each group.

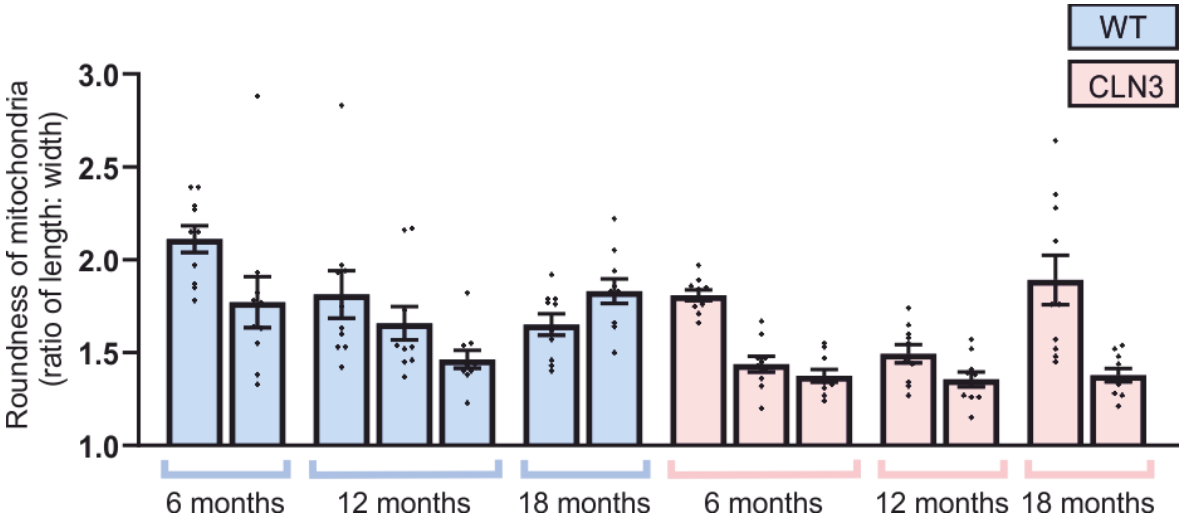


**Figure 92. Roundness of mitochondria (ratio of length to width).** A value of 1 indicates a perfect circle and the greater the increase the more elongated the shape of the mitochondria. Data are presented as mean roundness for each heart ± S.E.M. with average calculated ratio from 100 mitochondria, across 10 images (10 mitochondria per image, average size from each image plotted on each bar).

To analyse if age or genotype affected the roundness of mitochondria, the data from different animals of the same age and genotype were grouped and plotted in Figure 93. Mitochondria were significantly more elongated in cardiac myocytes of WT mice at 6 months, compared to CLN3 mice of all ages, but not to WT mice at 12 or 18 months. The roundest mitochondria were in the cardiac myocytes of the CLN3 mice at 12 months; these were significantly rounder than in the cardiac

myocytes of WT mice at 6 and 18 months. Although there were no significant differences between the roundness of mitochondria in WT mouse cardiac myocytes at any age, it is notable that only the mitochondria in the WT mouse cardiac myocytes at 12 months were not significantly more elongated than the mitochondria in the CLN3 mouse hearts at 12 months. As shown in the Figure 93, the mitochondria in the cardiac myocytes of CLN3 mice on the whole had a tendency to be rounder than in the WT mice of similar age, although this difference was not significant.

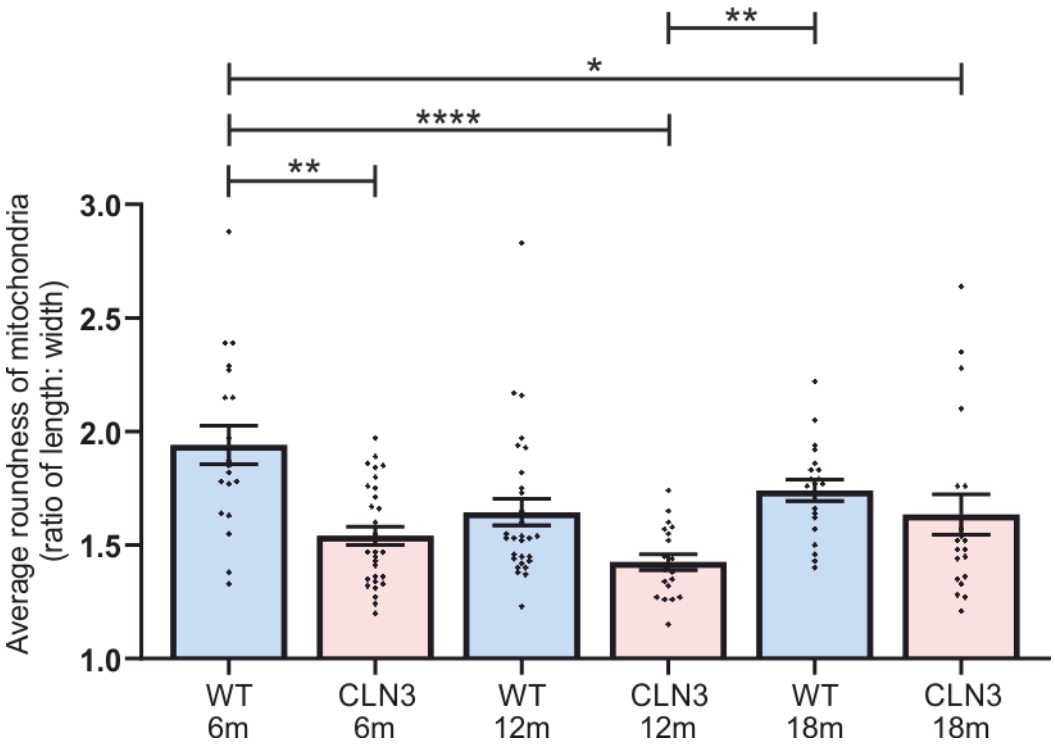


**Figure 93. Roundness of mitochondria (ratio of length: width).** This bar graph was obtained by combining the data shown in Figure 92 for each of the CLN3 and WT hearts at the specified ages. The data were analysed using a Kruskal-Wallis test with Dunn's post-hoc comparison. * indicates $p<0.05$, ** indicates $p<0.01$ and **** indicates $p<0.0001$. Data are presented as mean ± S.E.M., of 2-3 hearts, with n = 20-30 (average roundness of mitochondria calculated from 10 mitochondria, in 10 images (scatter points on each bar) for each heart).

### 7.3.4 Distribution of mitochondria within tissue

Typically, the mitochondria in cardiac myocytes form long clusters of interfibrillar mitochondria that are in close contact. To quantify any changes or fragmentation of the mitochondria, these clusters were counted as described in the methods above. A small number of clusters indicates that these are likely to contain several mitochondria, forming a string in-between the myofilaments. However, this analysis did not actually count how many mitochondria are present in each cluster.

The average number of clusters per cardiac myocytes, as plotted in Figure 94, varied dramatically, with numbers ranging between 9 and 65 clusters per 100 µm$^2$. No pattern in the variation was evident, and it was noticeable within groups, and especially obvious for example in the cardiac myocytes of the CLN3 mice at 6 and 18 months.

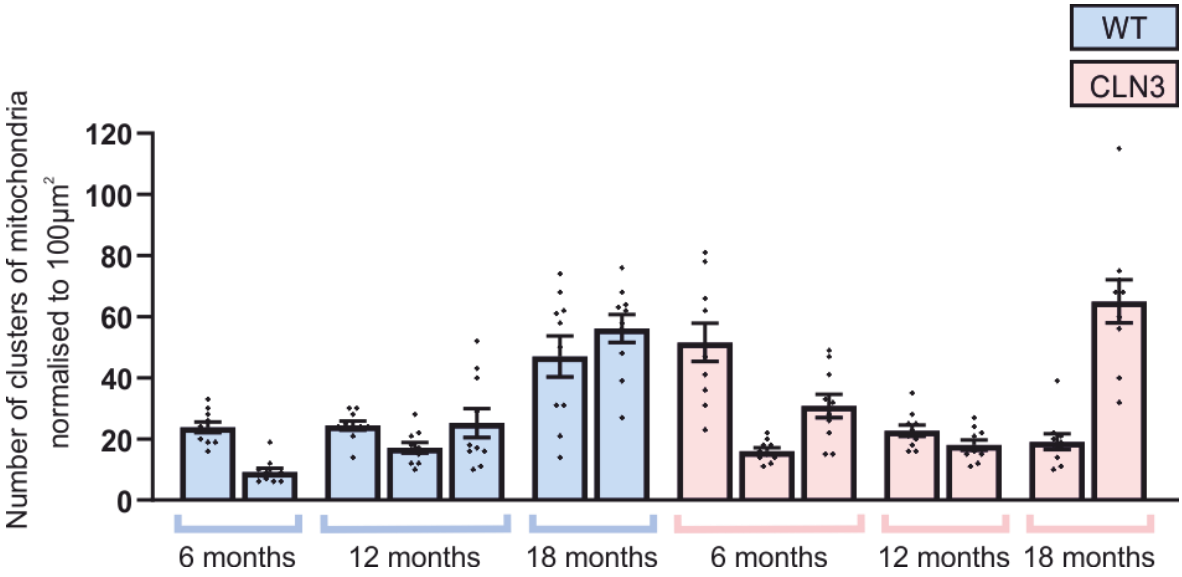


**Figure 94. Number of clusters of mitochondria per 100 µm$^2$.** Data are presented as mean number of clusters per 100µm$^2$ per heart ± S.E.M., each scatter point indicated the average number of clusters from 10 images (plotted on each bar) per heart.

To analyse if age or genotype affected the number of clusters per image, the data from different animals of the same age and genotype were grouped and plotted in Figure 95. The cardiac myocytes with the smallest number of clusters were from the WT animals at 6 months. The number of clusters was significantly lower compared to cardiac myocytes from CLN3 mice of the same age, and to cardiac myocytes of 18 months-old animals from both genotypes.

In contrast, the greatest number of clusters was found in the cardiac myocytes of WT mice at 18 months. This was significantly greater than in cardiac myocytes of both younger ages of WT mice and of hearts from 12 months-old CLN3 mice. Overall, there was a trend for an increase in the number of clusters in WT mouse cardiac myocytes with age. However, this change with age was not obvious in cardiac myocytes from CLN3 mice.

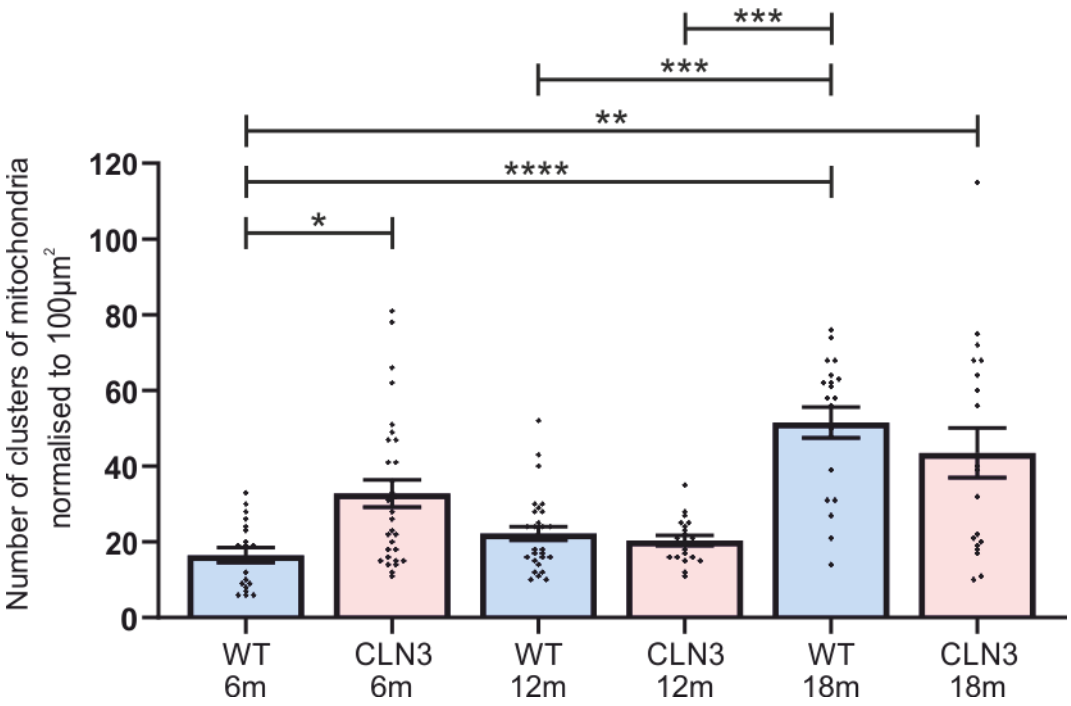


**Figure 95. Number of clusters of mitochondria per 100 µm².** This bar graph was obtained by combining the data shown in Figure 94 for each of the CLN3 and WT hearts at the specified ages. The data were analysed using a Kruskal-Wallis test with Dunn's post-hoc comparison. * indicates $p < 0.05$, ** indicates $p < 0.01$, *** indicates $p < 0.001$ and **** indicates $p < 0.0001$. n = 20 - 30 images per condition (2 or 3 hearts each with 10 images per heart, average of these 10 images is presented as a scatter point on the bars). The data are presented as mean ± S.E.M.

An alternative way of looking at the data was to relate the number of clusters to the total number of mitochondria in an image, thereby providing a more accurate understanding of average number of mitochondria per cluster (I.e., number of mitochondria / number of clusters). As before, the data are first presented on a per animal basis to understand the variability between mice of the same age and genotype (Figure 96). For most animals, the clusters only contained a relatively small number of mitochondria, between 3-9 mitochondria per cluster. Only one heart of a WT mouse of 6 months of age showed a far higher average of 16 mitochondria.

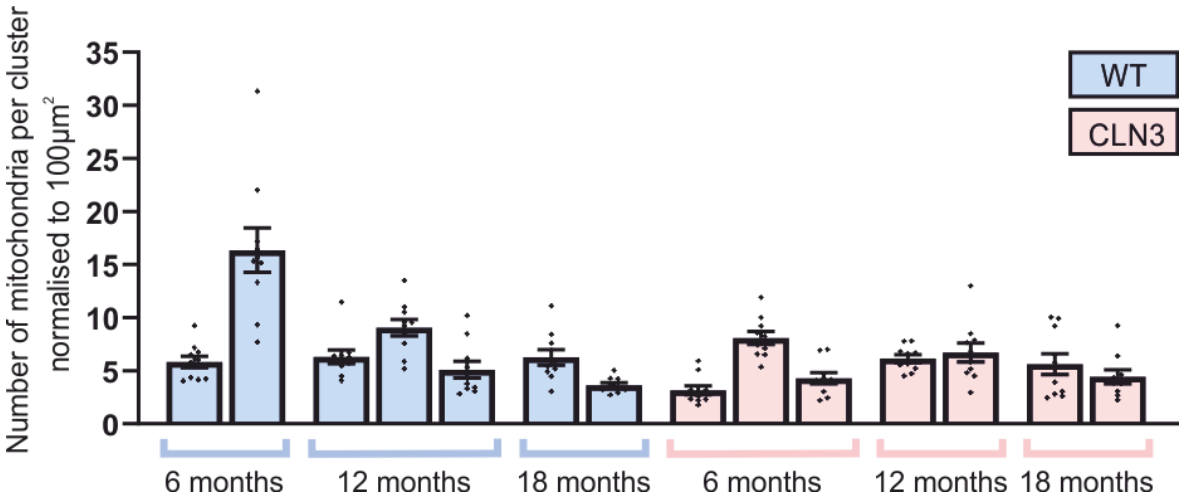


**Figure 96. Estimated number of mitochondria per cluster.** Both, the number of mitochondria and the number of clusters were normalised to the value per 100 µm$^2$. The cluster size was calculated by dividing the number of mitochondria by the number of clusters and is presented as mean ± S.E.M. n = average number from 10 images (plotted as scatter points on each bar) per heart.

To analyse whether age or genotype affected the number of mitochondria per cluster, the data from different animals of the same age and genotype were grouped and plotted in Figure 97. It showed a significantly higher number of mitochondria per cluster in cardiac myocytes from 6 months-old WT mice compared to CLN3 mice of the same age, and to mice of both genotypes at 18 months of age.

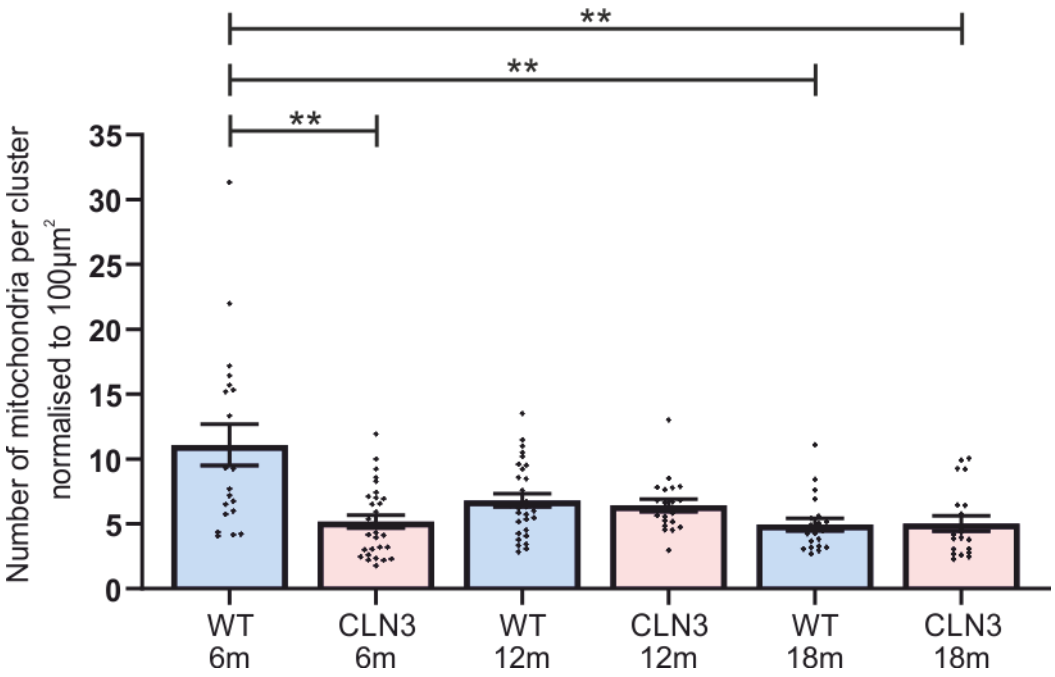


**Figure 97. Estimated number of mitochondria per cluster.** This bar graph was obtained by combining the data shown in Figure 96 for each of the CLN3 and WT hearts at the specified ages. The data were analysed using a Kruskal-Wallis test with Dunn's post-hoc comparison. ** indicates $p < 0.01$. n = 20 - 30 images per condition (2 or 3 hearts each with 10 images per heart). The data are presented as mean ± S.E.M.

### 7.3.5 Storage Material in cardiac myocytes

This aspect of the study aimed to investigate the accumulation of storage material in cardiac myocytes of WT and CLN3 mice of the different ages. No storage material was found in tissue from WT mice. It was possible to find areas containing storage materials in tissue from CLN3 mice. However, these were very rare, not allowing for a quantification in randomly chosen regions. When present, storage material could be seen between myofibres Figure 98 (top panels), but was often present at the periphery of the cell Figure 98 (bottom panels).

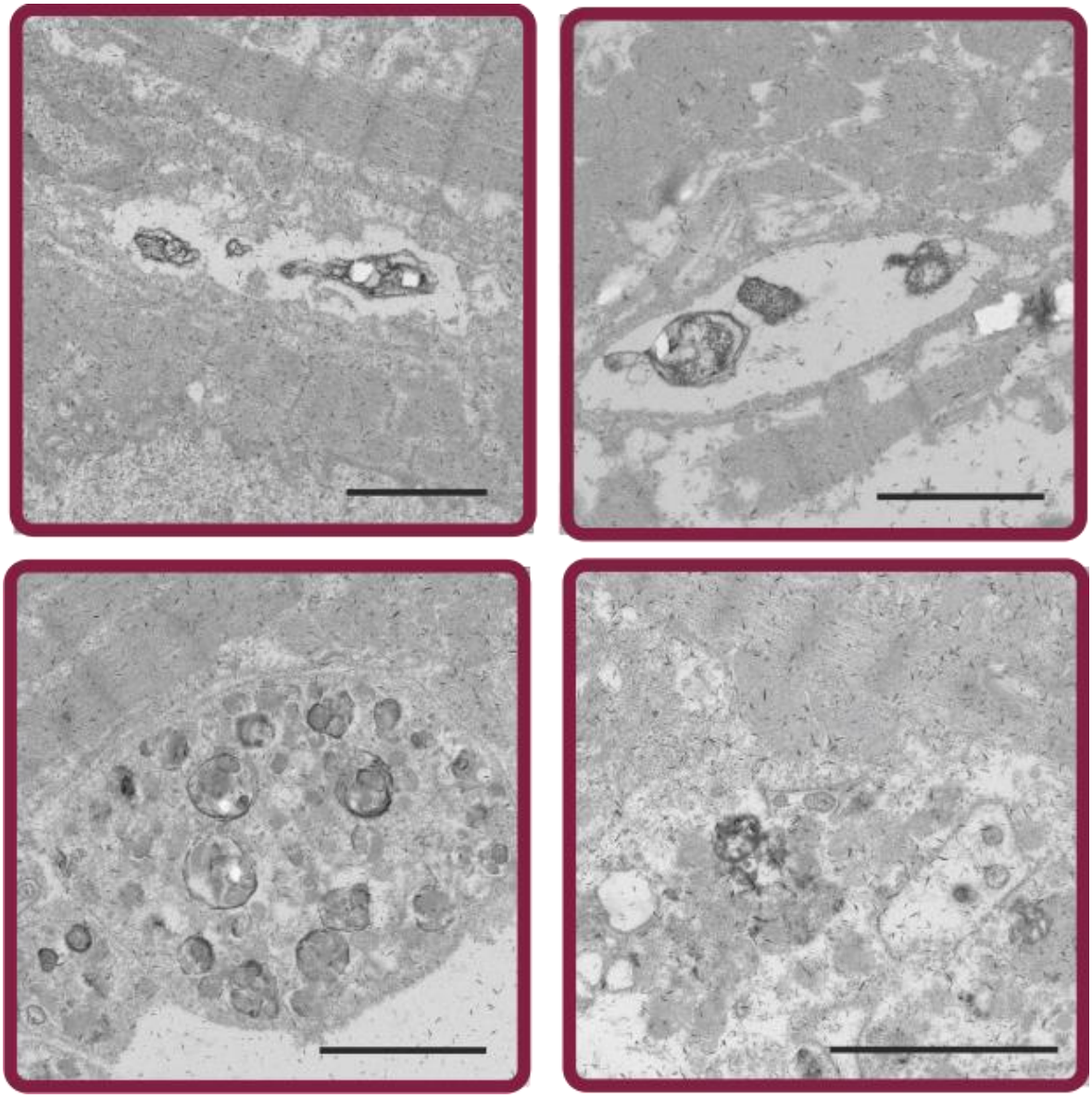

**Figure 98. Examples of storage material found in heart tissue from 18 months-old CLN3 mice.** The panels show examples of storage material between myofibres (top panels), storage material in the cell's periphery (bottom panels). The scale bar is 2 µm.

**Summary of the results**

So far, the results have been presented one-by-one. However, to make it easier to see a bigger picture of potential mitochondrial changes with age or genotype, the same data are presented as a summary (Figure 99). As shown in the previous figures, there were a limited number of hearts available and considerable variation within the groups which should be taken into account when looking at the averages.

- The largest number of mitochondria (Figure 99a) was found in cardiac myocytes from 18 month-old WT mice, but this was primarily due to one replicate. It was higher than that in cardiac myocytes from both groups of younger WT mice and that in cardiac myocytes from 18 month-old CLN3 mice. There was a trend for a larger number of mitochondria in the old CLN3 mice, but the difference was not statistically significant.
- There was no difference in the size of mitochondria between cardiac myocytes of different ages and genotypes within the samples available (Figure 99b).
- Cardiac myocytes from the 6 month-old WT mice had less rounded mitochondria than CLN3 mice of all ages. Mitochondrial roundness did not change with age in the WT or in CLN3 mice sampled (Figure 99c).
- Cardiac myocytes from 6 month-old WT mice contained fewer clusters of mitochondria than those of age-matched CLN3 mice and than those of 18 month-old animals of both genotypes. There is a trend for an increased number of clusters with age in cardiac myocytes of WT mice, which is not obvious in CLN3 mice (Figure 99d).
- In contrast, cardiac myocytes from 6 month-old WT mice contained more mitochondria per cluster than those of age-matched CLN3 mice or than 18 month-old animals of both genotypes (Figure 99e), despite the cardiac myocytes of the old animals containing more mitochondria overall than those of younger animals (Figure 99a).

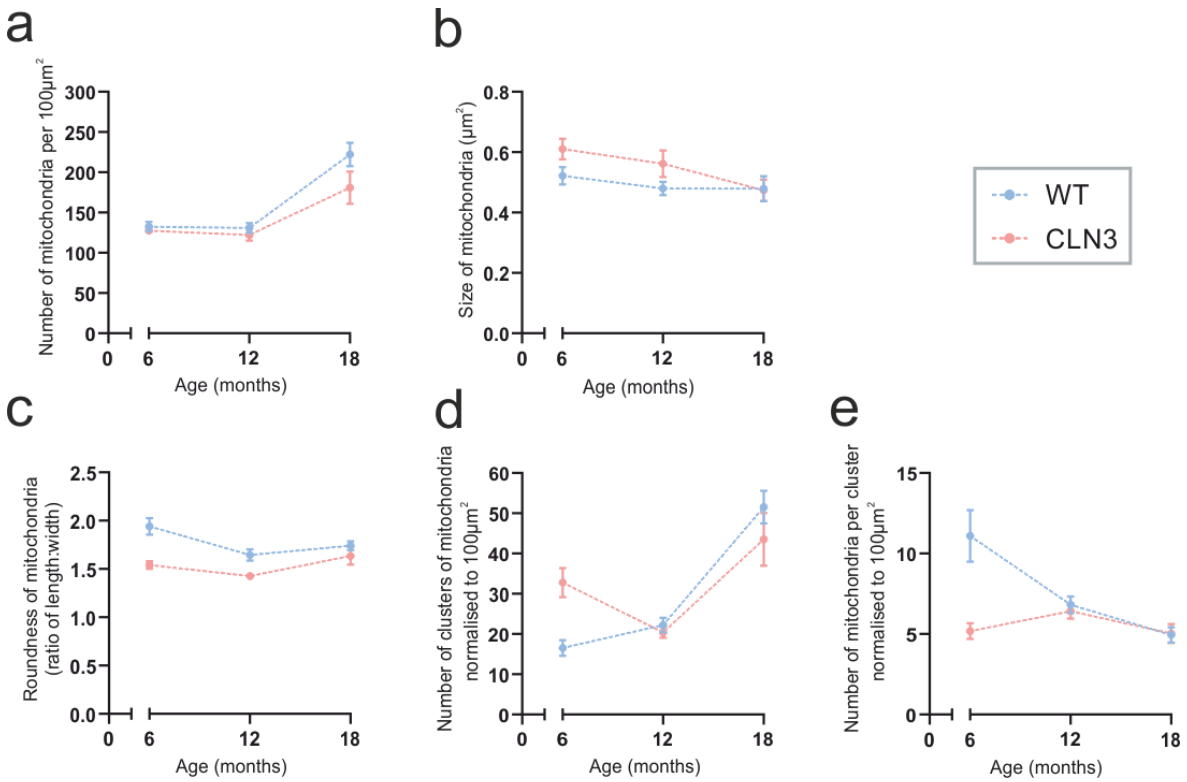


**Figure 99. Summary plots to illustrate interaction of genotype (WT and CLN3) with age (6, 12, 18-months**). Plotting mitochondria quantified by; (a) number, (b) size, (c) roundness and clustering by (d) number of clusters and (e) number of mitochondria per cluster. Data are presented as mean ±S.E.M., of 20-30 images (10 images per heart, from 2-3 hearts) per condition. No additional statistical analysis was performed, and results of the previous analysis is not shown here, but can be found in Figure 89, Figure 91, Figure 93, Figure 95 and Figure 97.

## 7.4 Discussion

A progressive deterioration of cardiac function is observed in individuals with CLN3 disease. Whilst first differences in ECG traces can be observed early in the disease (unpublished, personal communication), it is only in later stages that more profound changes, as described in Chapter 1, manifest themselves. This part of the study aimed to examine whether structural changes were present in hearts from *CLN3*$^{\Delta ex7/8}$ mice, and if these changed with age. The relative ageing of mice comapred to humans is not entirely linear (Dutta and Sengupta, 2016, Hagan, 2017); therefore the x-axis for the data in this chapter was plotted relative to time, but not necessarily accurate to the age represented in equivalent human years. However, the hearts from the mice at 6 and 12 months would have been equivalent to adults in a reproductive stage, while the heart at 18 months equivalent to adults in a post-reproductive age, just prior to old age (Dutta and Sengupta, 2016). The analysis focussed on changes in the mitochondria, as these organelles are critical to provide energy for the regular contractions of the heart, and because changes in mitochondria have been described in other cell types with mutations in the *CLN3* gene.

This study found an increased number of mitochondria in cells from 18 months-old mice of both genotypes which was higher in the WT mice than in CLN3 mice. However, it is important to note that there was a considerable variability in the number of mitochondria found in the cardiac myocytes of different 18 months-old animals of the same genotype. Variable results have also been reported in the literature: one study found a reduction in the number (and increase in size) of mitochondria in 14 months-old mice (Corsetti et al., 2008), whilst another study found no changes in the number of mitochondria in ventricular myocytes from 24 months-old mice (Masoud, 2018).

The apparently increased number of mitochondria found here could be explained as an adaptation for the decline of the efficiency in energy production that has been described to happen with age (Boengler et al., 2017). Another explanation would be a reduction in the level of mitophagy, the process by which defect mitochondria are degraded. This decreased clearance of mitochondria has been described in ageing cardiac myocytes (Leon and Gustafsson Å, 2016).

Reduced mitophagy can lead to an increase in the average size of mitochondria (Corsetti et al., 2008). However, this study found no effect of age or genotype on the size of mitochondria in the samples that were available (Figure 91).

Earlier studies described mitochondria in cardiac myocytes become more rounded with age (Cheng et al., 2013), without reporting the number of mitochondria. However, this study found no progressive change in the shape of mitochondria in the WT control animals from the different ages (Figure 93). Whilst mitochondria of the youngest WT animals seemed most elongated (or least rounded), this difference was not statistically significant when compared to that of the 12- or 18

months-old WT mice. It is possible that the change in roundness would be influenced by other factors such as the count, which here increased dramatically at 18 months. Therefore, the changing shape may not be a single process, but a combination of factors, for example mitochondria may become rounder with age but if an increased number has to be packed into the tissue, they might become elongated, potentially explaining the lack of a change in shape.

When studying the effect of the genotype on mitochondrial shape, mitochondria from 6 months-old WT animals were significantly less rounded than those of CLN3 mice from all ages (Figure 93). This contradicted results from a previous study, in which mitochondria cells with the same mutation in the *CLN3* gene were found to be more elognated than those in WT cells (Fossale et al., 2004). However, it is important to note that this earlier study was performed in iPSC-derived neuronal precursor cells. These cells typically have shorter mitochondria, and the elongation was seen as abnormality related to CLN3 disease. In contrast, an elongated shape is normal in interfibrillar mitochondria of cardiac myocytes. Considering the different starting points, a shape change caused by the mutation in the CLN3 gene could have a different outcome in cardiac myocytes than in iPSC-derived neuronal precursor cells.

The count of number of clusters (Figure 95) and the number of mitochondria per cluster (Figure 97) showed a lower number of clusters in cardiac myocytes from WT mice overall, which each contained more mitochondria. Large clusters of interfibrillar mitochondria is the pattern expected to be present in cardiac myocytes from young WT animals. In contrast, CLN3 mice contained significantly more clusters, each with significantly fewer mitochondria. Note that the absolute number of mitochondria in these two groups was the same. This indicates that the mitochondrial clusters were more fragmented in CLN3 mice, potentially affecting their function of efficient energy supply to the contracting myofibres. For WT animals, a progressive increase in the number of clusters, and decrease in the number of mitochondria they contain was seen with age (significant at 6 vs. 18 months of age). Interestingly, the increased number of mitochondria found in 18 months-old animals (Figure 89) did not prevent the clusters becoming smaller. This change to a higher number of smaller clusters again potentially indicates a less efficient energy delivery to the myofibres. The numbers for 12- and 18 months-old CLN3 mice are similar to those in WT control mice. However, different to the WT control mice, there is no progressive change with age.

Structural changes occuring with age were expected to occurr progressively, rather than returning the to values seen at an earlier age. However, the change in roundness of mitochondria and number of clusters for CLN3 mice both have their lowest values in 12 months-old animals (Figure 98),which could be seen as a shift in the direction of change. But it is important to remember that there were no significant differences for these values between the ages of the CLN3 mice, and these data cannot be over-interpreted. Here, it was mostly found in tissue from 18 months-old CLN3 mice

(Figure 98), either between myofibres or at the cell periphery. Storage material can be classified based on the shape (Anderson et al., 2013) and differs between the NCLs. Curvilinear storage material and fingerprint bodies are most prominent in the hearts from humans (Gilbert-Barness, 2004, Fidziańska et al., 2013) and in skeletal muscle biopsies (Goebel, 1975). The material found here does not have the characteristic shapes described in human hearts.

Based on the progression of CLN3 disease, it may have been reasonable to expect that the disease would mirror any phenotype observed with age in a more severe manner, and/or occurring at a younger age. As previously mentioned, the mice were sacrificed at 6, 12 and 18 months of age and the hearts were fixed and stored to allow simultaneous comparison of the hearts. If the relative ages of mice to humans is taken to be linear across the life span, the mice at 6 months represent 20 human years, 12 months represent 40 human years and 18 months represent 65 human years approximately. This was based on the calculation of 40.6 human days to 1 mouse days, as reported by (Dutta and Sengupta, 2016). However, whilst this comparison might be useful, the authors warned that the relative ageing of mice varies by stage of life. Mice at 6 and 12 months would have been equivalent to adults in a reproductive stage, while the heart at 18 months equivalent to adults in a post-reproductive age, just prior to old age (Dutta and Sengupta, 2016, Hagan, 2017). Relative to CLN3 patients, the mouse *CLN3*$^{\Delta ex7/8}$ model outlived the typical lifespan of human patients by extending beyond early adulthood. The *CLN3*$^{\Delta ex7/8}$ animal model was discussed in more detail in Chapter 1. So far, no systematic study has investigated changes in the heart function in the CLN3 mice used in this study. It is therefore unclear whether the *CLN3*$^{\Delta ex7/8}$ mice accurately reflect the cardiac symptoms experienced by many CLN3 patients. The cardiac phenotype in patients emerges later than other symptoms, so changes in the heart may accumulate over a longer time than in organs such as the brain and eyes, which present with symptoms earlier in disease progression.

Surprisingly, the overall effect of the genotype (based on a significant difference within the same age) was more frequently found for the young, 6 months-old animals (in roundness, number of clusters and number of mitochondria per cluster), than for the older animals (no difference for 12 months-old animals and only the number of mitochondia was different for 18 months-old animals). Therefore, the assumption that the tissue from CLN3 mice may deteriorate with age to a larger extent than that from the WT mice, in the manner expected from such a progressive disease, was not found to be true within the scope of this study.

Several reasons might explain the lack of differences found here between cardiac myocytes from WT control and CLN3 mice, for example the variability found between animals or the region of the heart that was analysed. All images only represented an extremely small section of heart as is the nature of TEM imaging. Assessing a larger number of samples could help to understand the reasons for the variability found in images of hearts from animals of the same age and genotype (most

extreme in the 18 months-old CLN3 animals). It is unknown which cell type, or which region of the heart contributes to the cardiac phenotype seen in individuals with CLN3. Here, only ventricular myocytes were analysed. There may have been considerably more changes in other regions of the heart, e.g. the atria, the SA- or the AV-node, that were not captured in the analysis.

Ideally, an analysis of the mitochondrial size, or area, should be performed on a 3D reconstruction. Within an TEM image, not all mitochondria will be cut in the same plane, or at the same angle, adding variability to a size-analysis based on 2D images. Instead of the estimation of the mitochondrial size used here, calculating the mitochondrial volume based on a 3D reconstruction would provide more accurate results. Such a 3D reconstruction is planned for WT and CLN3 KO HeLa cells in the future. Performing it for cardiac myocytes would be of great interest to strengthen the results. However, we are confident that the methodological and blinded manner of the analysis allowed the collection of reliable data.

## 7.5 Future work

This chapter detailed an exciting and much needed area of research for CLN3 disease. There were some limitations on sample availability and there is scope to follow on from this project. Improvements can be grouped into three areas: sample preparation, relevance of species, and collection of additional data.

The samples analysed here were obtained from animals using a protocol that was not optimised for cardiac samples. For example, no glutaraldehyde was included in the fixative, and no contraction inhibitor was given to the animal, to ensure that the cardiac myocytes were not contracted. The long-term storage of the hearts at -20°C may have caused some degradation of sample quality. Hearts from patients with CLN3 disease have shown changes in the cristae and inclusions in mitochondria (Fidziańska et al., 2013). These could lead to a reduced ability of the mitochondria to produce ATP. However, the quality of the fixation performed here did not preserve the cristae structure well enough to analyse it. Finding out if there are structural changes that could cause mitochondrial dysfunction would be a valuable result for an extension of this study.

The samples analysed here were obtained from mice. Mice hearts differ from human hearts in several points, for example their higher beating frequency (Janssen et al., 2002). The usefulness of mice as model for heart changes in humans is debated, and large animal models are seen as superior (Camacho et al., 2016). The use of hearts from large animal models of CLN3 which may be more comparable to humans, for example the pig (Johnson et al., 2019), may provide a more faithful imitation of cardiac changes in patients than mice did. A full study in which animals could

have ECG data collected while alive, prior to collection and imaging of the hearts, would give a fuller picture of the way the heart is affected from symptoms through to ultrastructure. Additionally, collecting data such as heart weight prior to fixation, could be valuable in understanding differences between mice of the same age and genotype.

Obtaining access to human samples would also be hugely beneficial, but also brings the pitfall of a non-optimal fixation (considerable amount of time passing between death and taking the sample) and the possible lack of well-matched control samples. Therefore, similar imaging and quantification as documented in this chapter, with a wider range of tissue from different CLN3 disease models, in combination with a study of heart function in the animals would be an interesting aspect of future work. This would also allow to understand the contribution of the cardiac conduction system; to understand whether initiation of contraction is affected, and to support the assessment of structural changes as a potential cause of contraction abnormalities in patients.

Finally, in addition to the analysis detailed in this chapter, it would be interesting to expand the measurement to quantification of additional structures such as t-tubules. As t-tubules are important structural features of cardiac tissue with a role in function (such as calcium signalling), locating and measuring these could be highly beneficial. Additionally, the proximity of the measured mitochondria to the t-tubules could provide an interesting context for the measurements if any variation was found.

# 8 Methodology and troubleshooting iPSC culture and differentiation to cardiac myocytes

## 8.1 Introduction

In recent years, there has been a call for research to study the cardiac phenotype of CLN3 disease, as reported by clinicians and a small number of papers (Rietdorf et al., 2019, Ostergaard, 2016). The existing research and the importance of further investigation were discussed in Chapter 1. Chapter 7of this thesis described findings from the analysis of hearts from the CLN3 Δex7/8 disease mouse model compared to hearts from matched wild type mice, using electron microscopy. The imaging and analysis of heart tissue with electron microscopy was a valuable approach to investigate ultrastructural changes. However, to extend the research into studying functional changes in cardiac myocytes, it was beneficial to consider additional models for experimental investigation of the *CLN3* mutation within cardiac cells. A comparison on the different models of CLN3 disease, including animal and cell models, was discussed in Chapter 1.

The momentous publication of a method to induce pluripotency in fibroblasts presented a significant opportunity for research (Takahashi and Yamanaka, 2006). The use of induced pluripotent stem cells (iPSCs) allowed propagation of the iPSC cell lines in culture, and, when needed, the transformation of fibroblasts from patients into cell types which are otherwise difficult to obtain and culture, such as neurons and cardiac myocytes. These differentiated cells can then be used for experiments. In the CLN3 disease research community, iPSC cell lines have been generated and utilised in study of the disease. iPSCs carrying a *CLN3* mutation were generated from patients with CLN3 disease (Lojewski et al., 2014) and an isogenic pairing of wild type (WT) control and CLN3 disease model cell lines was generated by insertion of a *CLN3* mutant gene into the WT iPSC line (Gomez-Giro et al., 2019). Cell types studied as a result of the differentiation of *CLN3* mutation carrying iPSCs include retinal neurons (Wiley et al., 2016) and cerebral brain organoids (Gomez-Giro et al., 2019). However, at the time of writing, there were no research groups known to be using cardiac myocytes generated from iPSCs in the study of CLN3 disease.

There are a number of limitations to the use of iPSC derived cell models of lysosomal storage disorders, such as CLN3 disease (Borger et al., 2017). Broadly, these include considerations such as the unknown impact of the disease-causing mutation on the reprogramming of the cells, as well as selection of control cells with a suitable genetic background (Borger et al., 2017). Established iPSC lines that are known to reliably differentiate into cardiac myocytes might not be a good age or gender match for the iPSCs generated from CLN3 patients. To identify changes caused by mutations in CLN3 it was not only important to compare their function to those of cardiac myocytes derived from iPSCs (from here onwards referred to as iPSC-CMs) from healthy donors, but also to compare their function to that of primary cardiac myocytes, as outlined below.

iPSC-CMs have been described as structurally and functionally immature compared to adult cardiac myocytes, resembling foetal cardiac myocytes more closely (Ronaldson-Bouchard et al., 2018). When planning to use iPSC-CMs to study CLN3 disease, the lack of maturity was considered as risk of masking any phenotype of CLN3 disease that may present only in adult cardiac myocytes. In CLN3 disease patients, any cardiac symptoms are reported in adulthood, whereas the visual and neurological symptoms arise in childhood. However, patients have been reported to show abnormalities on ECG prior to the complaint of symptoms and the cellular phenotype leading to this may have developed earlier still. For the planned study, we wanted to use cardiac myocytes with as mature a phenotype as possible, using previously established maturity markers.

In order to judge the maturity of iPSC-CMs, a number of studies have tracked characteristics in iPSC-CMs using a wide range of markers (Karbassi et al., 2020). Expression of these markers differs significantly between foetal and adult cardiac myocytes, as described below.

Troponin is a protein in skeletal and cardiac muscle cells which regulates contraction. Different isoforms of cardiac troponin are being expressed during development: expression of ssTnI has been predominantly found in neonatal or foetal cardiac myocytes, whilst cTnI is expressed in adult cardiac myocytes (Bedada et al., 2016, Zuppinger et al., 2017).

Transverse tubules (T-tubules) are cell membrane invaginations found in adult striated muscle. They bring the cell membrane receptors in close contact with the sarcoplasmic reticulum (SR). Foetal cardiac myocytes have little to no T-tubules. The absence of t-tubules and the troponin isoform expressed in newly differentiated iPSC-CMs were comparable to foetal cardiac myocytes, indicating a lack of maturity (Cadet and Kamp, 2017).

Structure and function of cardiac myocytes are very closely linked, as was explained in Chapter 1. Calcium signalling is providing one such link between structure and function (Koivumäki et al., 2018). In mature cardiac myocytes, following the depolarisation of the cell membrane a strong calcium releases happens from the SR. However, in newly differentiated iPSCs this does not happen, and around 15-21 days of iPSC-CM culture to establish (Hwang et al., 2015). After this time, the SR functions like that of a mature cardiac myocyte.

Cardiac myocytes have a high energy demand. Mature cardiac myocytes contain a large number of mitochondria, as was shown in Chapter 7. Newly differentiated iPSC-CMs contain fewer mitochondria. Under closer inspection, these also differed in their function: they expressed different enzymes, showed a lower respiratory activity and had a lower membrane potential in comparison to iPSC-CMs which had matured during extended time in culture. These are characteristics of immature cardiac myocytes. However, after culturing the cells for 100 days, a 2.8 x greater number of mitochondria was found, and these functionally resembled mature cardiac

myocytes more closely (Dai et al., 2017). As explored in Chapter 6, mitochondria are an organelle of interest in CLN3 disease and they are of significance as a readout to examine any influence of the *CLN3* mutation in cardiac myocytes. A final consideration for the use of iPSC-CMs to study CLN3 disease was that unlike cardiac myocytes from the hearts of animal models of CLN3 disease, or CLN3 patients, these cells had no history in the heart as an organ, receiving input from the conduction system, or been contact with other cell types. Therefore, any aberrant systemic changes, such abnormalities arising from initiation or conduction of electrical signals, would not be identified with the iPSC-CM model. While this presented a limitation of the model, it also allows for the study of phenotype that may arise within cardiac myocytes independent of any potential changes resulting from aberrant signalling from the conduction system or further afield throughout other cell types. Consequently, there would be great value in comparison between cardiac myocytes derived from iPSCs and the hearts of animal models.

This chapter describes the establishment of methods to differentiate cardiac myocytes from iPSCs. These should be used in the next chapter to assess the structure and function of iPSC-CMs at various time points, spanning 100 days post-differentiation to allow cells to reach a mature state. Patient-derived iPSCs carrying the Δex7/8 mutation and an iPSC-line with a CRISPR generated point mutation at Q352X were available for the study.

**Aims and objectives**

The aims of the work in this chapter were:

1. Learning two techniques of iPSC culture
    a. a feeder-free culture
    b. a feeder-dependent culture
2. Learning the differentiation of iPSCs into cardiac myocytes
3. Setup a quality control method to check the success of the differentiation
4. Establishing these techniques at The Open University

## 8.2 Methods

Two main techniques for culturing iPSCs exist: they can grow feeder-free on coated surfaces or grow on a layer of feeder-cells. iPSCs carrying a CRISPR-generated mutation in the CLN3 gene and iPSCs from Nottingham were grown feeder-free, whilst those derived from CLN3 patients, carrying the Δex7/8 deletion were grown on feeder cells (Table 21). To avoid the interfering with the conditions for growth, each iPSC line was cultured according to the protocol used in the laboratory of origin, meaning that both techniques had to be established at The Open University.

The cell culture was carried out in sterile cell culture conditions, as explained in Chapter 2. All cell lines were carefully monitored for signs of infection. Flasks were visually inspected for changes such as discoloured or cloudy medium, or any appearance of foreign bodies visible under the microscope. No infection was observed in any cultures and all mycoplasma testing (upon receipt of the cells and every 3 months afterwards) was negative for all iPSC lines.

### 8.2.1 Culture of iPSCs

The iPSCs that were received from collaborators are detailed in Table 21. Due to the sensitivity of iPSCs and high risk of irreversible spontaneous differentiation, special care was taken to retain consistency in culture conditions for iPSCs. The major difference between the feeder-free and feeder-dependent methods from the different laboratories was the matrix: iPSCs were either cultured feeder-free on Matrigel plate coating, or in a feeder-dependent manner with inactivated mouse embryonic fibroblasts (MEFs) on a gelatin coating.

**Table 21. iPSC cell lines: genotype and cell culture method used in the originating laboratory.** iPSC cell lines kindly supplied by: [1]Prof Chris Denning at The University of Nottingham, [2]Prof Jens Schwamborn at The University of Luxembourg, [3]Prof Tristan McKay at Manchester Metropolitan University.

| Cell line | Genotype | Culture method |
|---|---|---|
| Rebl-PAT[1] | WT, healthy donor | Feeder-free (Matrigel) |
| CLN3 Q352X[2] | CLN3 Crispr-Cas9 generated Q352X mutant | |
| A13777 WT[2] | WT, healthy donor | |
| PA 338[3] | CLN3 patient cell line (p.Val142LeufsX39 and Δex7/8) | Feeder-dependent (iMEF) |
| 417 PB[3] | CLN3 patient cell line (D416G) | |
| CTRL NHDF[3] | WT, neonatal human dermal fibroblasts | |

#### *8.2.1.1 Feeder-free method*

The feeder-free method for the culture of iPSCs on Matrigel, was taught by Professor Chris Denning's laboratory at The University of Nottingham. It was used for the iPSCs used in training at The University of Nottingham (ReBL-PAT) and the isogenic *CLN3* mutation-carrying cell line with matched control iPSCs from Prof Jens Schwamborn (CLN3 Q352X and A13777 WT respectively).

Matrigel is a matrix containing extracellular membrane proteins and growth factors widely used for culturing iPSCs. Matrigel was handled carefully due to the risk of polymerisation in solution even at low temperature, which would prevent Matrigel from forming an even coating.

To prepare Matrigel aliquots, the stock bottle was defrosted slowly overnight on ice, in a 2-8°C refrigerator. The stock bottle was removed from the fridge before the ice had fully melted and pipetted into pre-labelled 1ml Eppendorf tubes in 0.5 ml aliquots. All pipettes and tubes were chilled in the -20°C freezer prior to use and pipetting was carried out rapidly to minimise any risk of polymerisation occurring. The aliquots were transferred immediately stored in a -80°C freezer.

To prepare Matrigel coated flasks, 50 ml of DMEM (without supplements) was filtered into a 50 ml falcon tube using a 0.2 µm syringe filter. The falcon tube was then chilled in the freezer alongside all pipettes and tips but removed before the DMEM began to freeze. Flasks were labelled and stacked in the cell culture hood and a tray of ice was placed next to the hood for intermediate storage of the tube of DMEM and tips, which were all wiped and sprayed with 70% IMS prior to transfer into the hood. Finally, the Matrigel aliquot was mixed into the ice cold DMEM by pipetting DMEM onto the frozen Matrigel and mixing up and down before transferring the DMEM back to the falcon tube. This process was repeated until the Matrigel was completely thawed and transferred in to the DMEM. A chilled 25 ml pipette was used to mix the solution by slowly pipetting up and down, and to transfer the solution to flasks and plates as required (5 ml/T25, 10 ml/T75 and 2 ml per well/6-well plate). The coated plasticware was gently rocked to ensure an even coverage of the surface and either left in the in the hood for 45 minutes at room temperature, or transferred to the fridge overnight, for the Matrigel to polymerise and form a matrix. If flasks were prepared in advance and refrigerated, these were stored for a maximum of 1 week and allowed to warm to room temperature before use. DMEM was kept in the coated flasks to prevent Matrigel from drying out and this was exchanged for the appropriate fresh medium prior to use. Before use, all Matrigel coated plasticware was inspected under the cell culture microscope for any disruption to the matrix, indicated by clumps of coating which would suggest a premature polymerisation of the Matrigel in the coating solution.

#### *8.2.1.2 Feeder-free method: Culture of iPSCs*

##### 8.2.1.2.1 Recovery from storage

To thaw iPSCs, the vial was transferred from the freezer to 37°C water bath where it was rapidly defrosted until only a small block of ice was left in the middle. This was transferred to a 15 ml falcon tube containing 9 ml of medium to make 10 ml, defrosting the last of the frozen cell suspension by rinsing the tube with medium. The falcon tube was then spun at 160 g for 4 minutes, before the supernatant was aspirated and the pellet gently resuspended in E8 medium supplemented with 10 µm Y-27632. The Rho Kinase (ROCK) inhibitor, Y-27632, was added to medium whenever iPSCs were in suspension to protect against apoptosis (Watanabe et al., 2007). The medium was exchanged for fresh, warmed E8 medium to remove the Y-27632 after 24 hours. The iPSCs were cultured for 3-5 days, until they reached approximately 80% confluency, during which time the medium exchanged for fresh E8 medium every 24 hours. At 80% confluency, the iPSCs were either passaged for maintenance of the culture, to set up iPSCs for differentiation or to freeze.

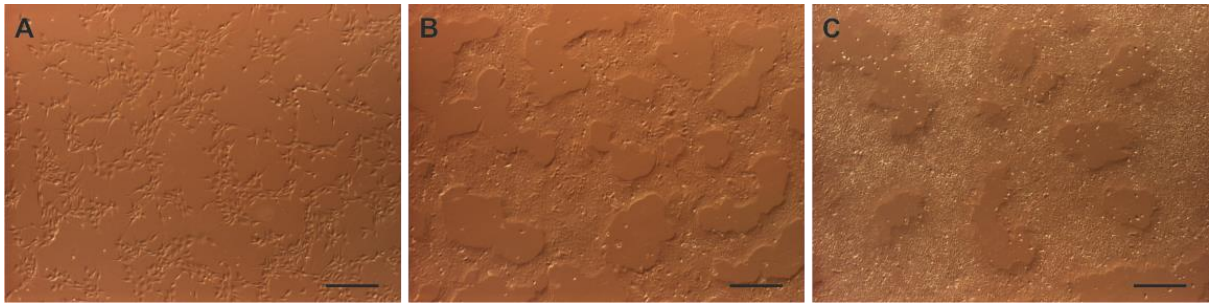


**Figure 100. Expansion of ReBl-PAT iPSCs over 3 days in culture.** The iPSCs were cultured in Matrigel coated T25 flasks. As passage, the cell suspension was diluted 1 in 6 for seeding which was estimated at around 0.6-0.8 million iPSCs transferred to the new flask. The images taken were at (A) 24 hours, (B) 48 hours and (C) 72 hours, post-passage. At 72 hours, the flask required passaging to avoid becoming over confluent. The scale bar is 0.25 mm.

##### 8.2.1.2.2 Passaging and cell dissociation

Prior to passaging the iPSCs, the storage medium was aspirated from a Matrigel coated flask, gently washed once with PBS and replaced with fresh E8 medium supplemented with 10 µm Y-27632. The flask was placed in the hood to equilibrate to room temperature. To passage the iPSCs, the medium was aspirated, and the flask was washed with PBS warmed to room temperature. After aspirating the PBS, 1 ml of 0.5 µM EDTA solution was added. The flask was then returned to the incubator for 4 minutes. After this time, the flask was carefully removed to avoid disrupting the iPSCs and observed under the microscope to confirm that iPSCs had become rounded. If the iPSCs were not rounded, they were returned to the incubator for a further 30 seconds and observed again. When the cells were rounded, the EDTA was very carefully aspirated to avoid losing any iPSCs. The flask was then tapped to release the iPSCs from the coated surface and 1 ml of fresh medium was

pipetted into the flask from the neck and across the cell surface, to rinse any iPSCs which remained attached. The 1 ml of cell suspension was then removed from the flask and divided amongst the new flasks. To passage to a flask of the same size, a 1:6 ratio was typically used. To passage a T25, 166 µl of the cell suspension was pipetted into the fresh flask containing 5 ml supplemented E8 medium and placed in the incubator for 24 hours, before repeating the iPSC culture steps as described above. The protocol was scaled accordingly, for example, up to 500 µl was transferred to a T75, for the purpose of expanding and freezing the culture. The EDTA passage method was used to dissociate iPSCs in clumps for regular passaging to limit the damage to iPSCs when exposed to a harsher dissociation method.

The EDTA dissociation method was unsuitable for obtaining a cell count, as the large number of clumps hindered an accurate count. Therefore, when dissociating with EDTA for expansion or maintenance of the iPSC culture, a ratio was used to dilute the iPSCs for seeding in a new flask. Where an accurate cell count was required, such as freezing or preparing a flask for differentiation, the alternative Accutase enzyme dissociation method was used. To passage iPSCs in a T75 with Accutase: the medium was aspirated, the flask washed with 10 ml of warmed PBS and 1.5 ml of Accutase solution was added to the flask. The flask was returned to the cell culture incubator for 3 minutes. On removal, the flask was tapped several times until the majority of iPSCs were detached and suspended in the Accutase solution. If some iPSCs remained after 4-5 taps, these were left attached as retrieving all iPSCs was of less importance than avoiding damage to the iPSCs through additional tapping and expose to Accutase. By pipetting from the neck across the cell surface, 13.5 ml of E8 medium was added to the flask, to dilute the Accutase and rinse any iPSCs which may have remained loosely attached. A sample of the iPSC suspension was taken and counted while the remainder was transferred to a 50 ml falcon tube and centrifuged at 160 g for 4 minutes.

#### 8.2.1.2.3 Passage for differentiation

To passage iPSCs for differentiation, they were dissociated with the Accutase method, counted and centrifuged. The iPSC pellet was resuspended in E8 medium with 10 µm Y-27632, at the appropriate volume to dilute and seed the required number of iPSCs for differentiation. The iPSCs were then cultured for 2 days following the feeder-free iPSC culture before beginning differentiation at Day 0, as described in section 8.2.2, below.

#### 8.2.1.2.4 Generation of frozen stocks

To generate frozen stocks, iPSCs were cultured in T75 flasks to a maximum of 80% confluency. Cryovials were labelled and aliquots of FBS and FBS with 20% DMSO were both thawed and placed in the hood. The cryovials were then filled with 0.5 ml of FBS with 20% DMSO and the caps loosely

replaced. The iPSCs were then dissociated with Accutase, counted and centrifuged, as described above. The resulting pellet was re-suspended in FBS at a volume calculated to achieve 2 million iPSCs per ml. The suspension was divided amongst the pre-prepared cryovials, adding 0.5 ml to each so that the result was 1 million iPSCs per vial in FBS with 10% DMSO. The caps were secured, and the vials rapidly transferred to a freezing chamber which was placed in a -80°C freezer before transfer of the vials to liquid nitrogen storage the following day.

#### *8.2.1.3 Feeder-dependent method:*

The feeder-dependent method for the culture of iPSCs using mouse embryonic fibroblasts (MEFs), was taught by Professor Tristan McKay's laboratory at Manchester Metropolitan University (MMU). It was used for culturing two CLN3 patient cell lines and a control cell line which he provided (PA 338, 417 PB and CTRL NHDF). The feeder cells were MEFs, which had been mitotically inactivated (referred to as iMEFs, post-inactivation) on a gelatin coated plate. This method required culturing two different cell types: iPSCs and MEFs. Procedures for the culturing of both are described below.

##### 8.2.1.3.1 Culture and inactivation of Mouse Embryonic Fibroblasts (MEFs)

Instead of a matrix mimicking the extracellular matrix, like Matrigel, iPSCs can be grown on a layer of feeder cells. Inactivated MEFs, which do not divide any longer, are commonly used for this purpose. To prepare the coating substrate for feeder cells, a 0.1% gelatin solution was prepared by dissolving gelatin in distilled water and autoclaving the solution, which was then stored in the 2-8°C refrigerator for up to 2 weeks. To coat plasticware, the gelatin solution was warmed to room temperature and pipetted onto the base of the flask or plate. This was then gently rocked to allow the solution to cover the surface and incubated in the cell culture hood for 20 minutes at room temperature. The solution was aspirated, and the flasks or plates were immediately used.

##### 8.2.1.3.2 MEF culture, freezing and recovery

Mitotically active MEFs were purchased from Cambridge Bioscience and cultured in DMEM supplemented with 10% FBS, 4mM L-Glutamine and 1x Pen-Strep. Frozen stocks of the active MEFs were prepared between passage 1 and 3 as described for the thawing of iPSCs in 8.2.1.2.

To create a large number of iMEFs stocks for later use, the active MEFs were expanded until passage 4, where they were cultured to approximately 90% confluency prior to mitotic inactivation by addition of 2 µg/ml Mitomycin C to the cell culture medium. After 3 hours of keeping the cells in the cell culture incubator, the medium was replaced with fresh culture medium without Mitomycin C.

These iMEFs were dissociated and frozen for later use, according to the protocol described in 8.2.1.2., but with the modification of TrypLE Express used in place of Accutase. For use in iPSC culture, iMEFs were rapidly thawed and plated as per thawing protocol described in 8.2.1.2, modified by resuspending in DMEM and placing iMEFs in a gelatin coated plate. The plate was placed in the incubator at 37°C for a minimum of 7 hours to allow iMEFS to settle before the addition of iPSCs. For use with iPSCs, the iMEFs were plated in the wells of a 6-well plate so that iPSC colonies could be accessed for picking

### 8.2.2 Feeder-dependent method: Culture of iPSCs

Feeder-dependent iPSCs were grown in FD medium, consisting of DMEM/F12 supplemented with manufacturer recommended concentrations of non-essential amino acids, Knockout Serum Replacement, Pen-Strep and 10 ng/ml basic fibroblast growth factor (bFGF).

The iPSCs were thawed according to the protocol described in 8.2.1.2 and resuspended in warm FD medium , to be consistent with the conditions in which the iPSCs were previously cultured in Professor Tristan McKay's laboratory. The iPSC suspension was gently pipetted into wells of a 6-well plate, pre-prepared with iMEFs and equilibrated to room temperature. For the first 24 hours post-thaw or passage, the FD medium was additionally supplemented with 10 μM Y-27632. The FD medium was changed every 24 hours and colonies were closely observed for morphological changes indicating spontaneous differentiation, as illustrated in Figure 101. If iPSC colonies began to look flatter, darker and less uniform they were removed, as they were considered to be spontaneously differentiating and at risk of triggering differentiation in surrounding colonies. The removal of colonies was carried out using a small, sterile pipette tip to gently scratch the colony in order to detach it from the surrounding iMEFs. Once the colony or colonies for removal were detached and in suspension, the medium was changed for fresh FD medium. After removing colonies that were spontaneously differentiating, the remaining colonies were detached to passage the cultures. Passage was required when colonies became too large, or the iMEFs appeared to have deteriorated in condition, most commonly observed as a contraction of iMEFS indicating that they were no longer suitable to support iPSC growth. When colonies were detached for passage, they were transferred to a new 6-well plate prepared with iMEFs, in a 10 ml serological pipette and gently pipetted up and down to break up the colonies to smaller clusters. The FD medium was supplemented with 10 μM Y-27632 for 24 hours, before exchange to fresh FD medium.

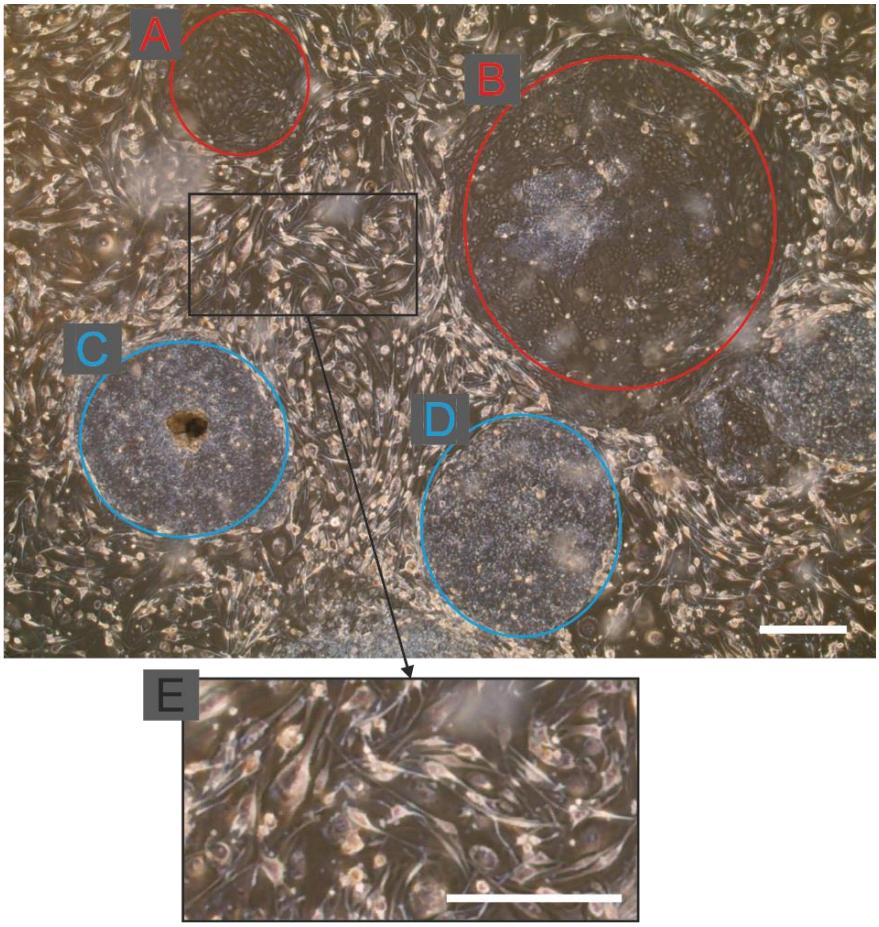


**Figure 101. iPSC colonies growing with iMEF feeder cells**. The cells in colonies A and B appeared darker and less dense, with irregular morphology of the iPSCs of the colony. The cells in colonies C and D had the brighter, more regular appearance of undifferentiated iPSCs. Panel E highlights the iMEFs surrounding the iPSC colonies. The scale bars are 250 µm.

#### *8.2.2.1 Conditioning of feeder-dependent iPSCs prior to differentiation*

The differentiation protocol starts with iPSCs grown in a feeder-free culture. Consequently, feeder-dependent iPSC cultures required reconditioning to the feeder-free protocol prior to differentiation. To achieve this, 80% confluent iPSCs were gently washed with PBS and briefly incubated in TrypLE Express to dissociate the colonies. The iPSCs, along with any iMEFs, were then transferred to a Matrigel coated flask with mTeSR medium supplemented with 10 µm Y-27632 for 24 hours. The subsequent medium change to fresh mTeSR removed any suspended iMEFs which had not attached after the transfer.

#### *8.2.2.2 Differentiation of iPSCs to cardiac myocytes*

The differentiation of iPSCs to cardiac myocytes (iPSC-CMs) was carried out using the method taught by Professor Chris Denning's laboratory at The University of Nottingham. The differentiation process is initiated by adding a large number of signalling molecules and other compounds in a specific order to the iPSCs. Prior to establishing it at The Open University, aliquots all of these compounds had to be prepared. On the day of use, the aliquots were diluted according to the working concentration (Working conc.) set out in Table 22, in the pre-warmed medium specified in 'Diluent,' Table 22. All aliquots were prepared in sterile conditions and stored frozen. The signalling molecules for differentiation were: Activin A (growth factor), BMP4 (bone morphogenetic protein 4) and the small molecules KY02111 and XAV939 (WNT inhibitors). To generate stocks, Matrigel was thawed as described in section 8.2.1.1 and divided into single use aliquots. Activin A was reconstituted with 4 mM hydrochloric acid (HCl) with 0.1% human serum albumin (HSA) and BMP4 was reconstituted with 4 mM HCl and 0.1% bovine serum albumin (BSA). The dissociation solution was formulated from: Collagenase II enzyme, N-benzyl-p-toluene sulphonamide (BTS) to inhibit beating while in suspension and therefore protect the cytoskeleton and HEPES pH buffer. DNase II was used in a blocking solution during dissociation. KY02111, XAV939 and BTS were reconstituted in dimethyl sulfoxide (DMSO). Collagenase II was reconstituted in calcium ($Ca^{2+}$)-free Hank's Balanced Salt Solution (HBSS), HEPES was dissolved in deionised water and DNase II was reconstituted in phosphate buffered saline (PBS).

**Table 22. Preparation of aliquots for the culture, differentiation and dissociation of iPSC-CMs.** Aliquots were prepared in advance at a high concentration and diluted to the working concentration as required. Small aliquots, especially those in DMSO, were vortexed and centrifuged prior to use.

| | Component | Stock conc. | Stock diluent | Working conc. | Diluent |
|---|---|---|---|---|---|
| **Differentiation** | Matrigel | 8-10 mg/ml | None | 80-100 µg/ml | RPMI medium |
| | Activin A | 5 µg/ml | 4mM HCL 0.1% HSA | 8 ng/ml | RPMI medium |
| | BMP4 | 10 µg/ml | 4mM HCl 0.1% BSA | 1 or 10 ng/ml | RPMI medium |
| | KY02111 | 10 mM | DMSO | 10 µM | RPMI medium |
| | XAV939 | 10 mM | DMSO | 10 µM | RPMI medium |
| **Dissociation** | Collagenase II | 200 U/ml | HBSS (- $Ca^{2+}$) | 200 U/ml | N/A |
| | HEPES | 1 M | $dH_2O$ | 1 mM | Collagenase II |
| | BTS | 30 mM | DMSO | 30 µM | Collagenase II |
| | DNase II | 12 mg/ml | PBS | 12 µg/ml | Blocking solution |

*8.2.2.3 Differentiation process*

The differentiation of iPSCs to cardiac myocytes, as summarised in Table 22, was carried out using the ReBl-PAT iPSC line under the instruction of Professor Chris Denning's group. These iPSCs were cultured with the feeder-free (Matrigel) method. For iPSCs originally grown with feeder-dependent culture methods, these would have been transferred to Matrigel prior to differentiation and passaged in E8 medium 2-3 times to condition the cells to this medium. Each stage of the differentiation was carried out according to precise timing, so that no incubation time was reduced or extended.

**Table 23. Summary of the timeline for feeder-free culture of iPSCs and differentiation to cardiac myocytes (CMs).** The time frame was based on ReBl-PAT iPSCs, but growth varied between cell lines. Steps marked with → indicate repeat until appropriate confluency/maturity is reached for next stage. *Estimated day of dissociation based on ReBl-PAT. All incubations were in a humidified cell culture incubator at 37°C and 5% $CO_2$ unless otherwise stated.

| Protocol | Day | Incubation | Details |
|---|---|---|---|
| **iPSC culture (feeder-free)** | Day 1 | 1 hour (RT) | Matrigel coating of flasks/plates |
| | | 24 hours | iPSC plated in E8 + Y-27632 on Matrigel |
| | Day 2 → | 24 hours | Change to E8 medium |
| | 80% confluency: passage or proceed to differentiation Day 0 | | |
| **Cardiac myocyte differentiation, maintenance and dissociation** | Day 0 | 12 hours | StemPro-34 + BMP4 + Matrigel (pre-condition) |
| | | 36 hours | StemPro-34 + BMP4 + Activin A |
| | Day 2 | 48 hours | RPMI/B27 without insulin. + KY02111 + XAV939 |
| | Day 4 | 48 hours | RPMI/B27 + KY02111 + XAV939 |
| | Day 6 → | 48 hours | Change to RPMI/B27 medium |
| | Beating cells observed in tight colonies: proceed to dissociation | | |
| **Cardiac myocyte maintenance** | Day 12* | 24 hours | Dissociation: plating in RPMI/B27 + Y-27632 |
| | Day 13* → | 72 hours | Change to RPMI/B27 (maintenance) |

During training, the differentiation was carried out at a range of densities (25k/cm$^2$, 40k/cm$^2$, 50k/cm$^2$ and 65k/cm$^2$) in a 6-well plate, to determine appropriate seeding density for the ReBl-PAT iPSCs. The optimal seeding density for high percentage of iPSC-CMs post-differentiation was analysed for each new cell line, or for re-optimisation in the case of poor differentiation outcome. In T25 flasks, 0.6-1 million ReBl-PAT iPSCs were seeded 48 hours before commencing differentiation at Day 0.

The protocol for differentiation of iPSCs to cardiac myocytes began on the morning of 'Day 0' with a pre-conditioning step. Pre-conditioning was achieved with the exchange of complete E8 medium for StemPro-34, containing 1 ng/ml BMP4 and 1/100 Matrigel. Matrigel was added to the medium with the intention to forming a second Matrigel layer on top of the cells, practically sandwiching the differentiating iPSCs between the two layers. The iPSCs were incubated at 37°C for 6-10 hours, before the media was changed for StemPro-34 containing 10 ng/ml BMP4 and 8 ng/ml Activin A to stimulate WNT signalling pathway. The cells were then incubated for 36 hours, until the morning of Day 2, when the media was replaced with fresh RPMI medium supplemented with B27 (without

insulin), and with 10 µM KY02111 and 10 µM XAV939. From pre-conditioning Day 0 to Day 2, the appearance of the culture changed from branching colonies to a dense monolayer as shown in Figure 102 and retained the monolayer appearance throughout the next stages of differentiation.

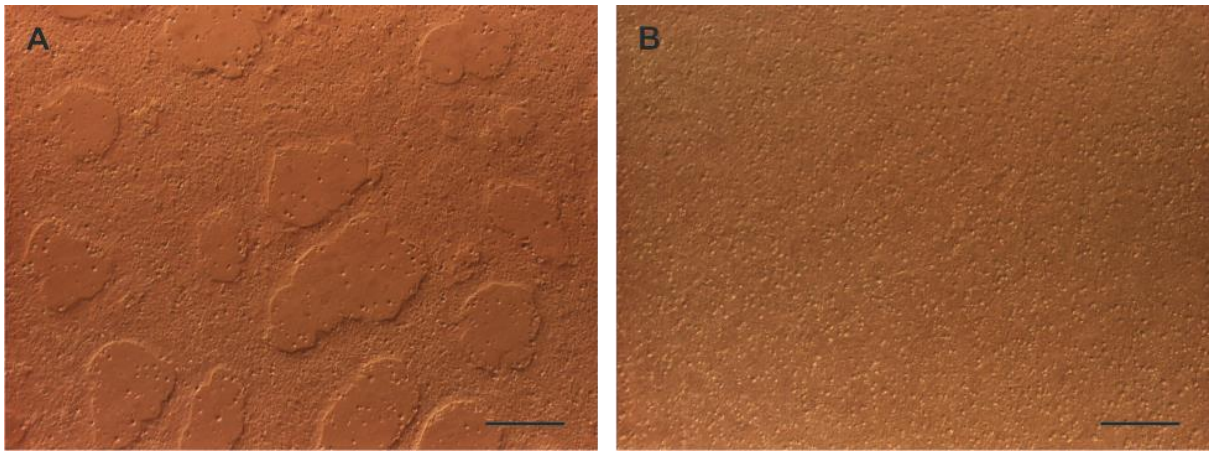


**Figure 102. ReBl-PAT iPSCs in the early stages of differentiation:** (A) On Day 0, after pre-conditioning, the iPSCs were grouped into branching, interconnected colonies with visible empty spaces in between. (B) On Day 2, the iPSCs spread to fill in the gaps and form a dense monolayer. This batch originated with 0.7 million ReBl-PAT iPSCs, seeded in a T25 at 48 hours before commencement of differentiation at Day 0. The scale bar is 250 µm.

The flasks were returned to the incubator for 48 hours, when the medium was exchanged for fresh RPMI medium supplemented with B27, 10 µM KY02111 and 10 µM XAV939. The flasks were returned to the incubator for 48 hours and the medium was exchanged for fresh RPMI medium supplemented with B27. From this point, the medium was exchanged every 48 hours for fresh RPMI medium supplemented with B27 to maintain the culture. During this period, the morphology of the culture gradually transformed from the monolayer to a more complex, fibrous appearance as in Figure 103.

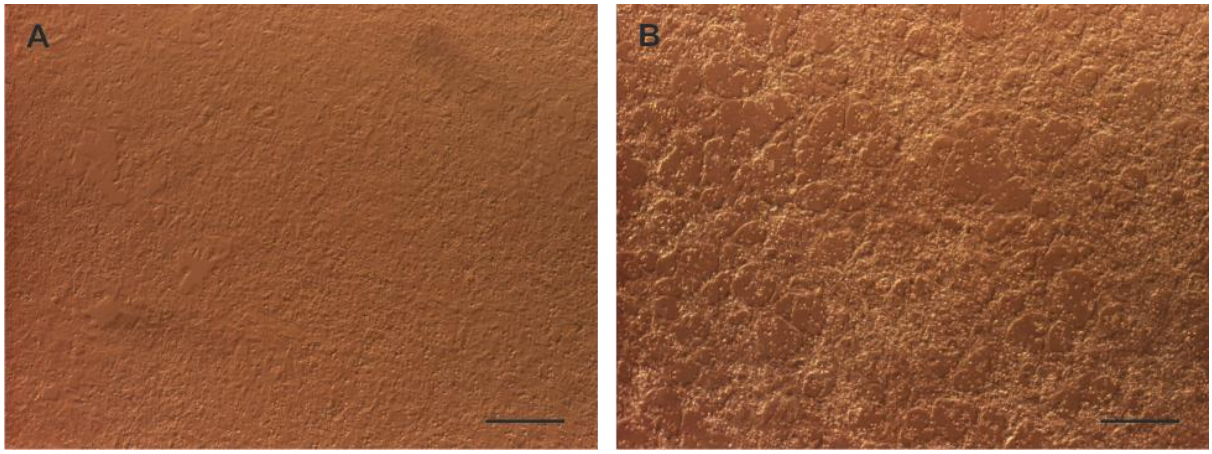


**Figure 103. ReBl-PAT iPSCs towards the end of differentiation, prior to dissociation.** (A) On Day 6, the medium was exchanged to maintain the differentiating cells; at this stage they still had the appearance of a dense monolayer. (B) On Day 9, the cells were pulling together in tight layers to reveal some space between the interconnected clusters of cells. This batch originated with 0.7 million ReBl-PAT iPSCs, seeded in a T25 flask at 48 hours before commencement of differentiation at Day 0. The scale bar is 250 µm.

When cells were observed to be in tight, uniform colonies with spontaneous movement to suggest that the cells were displaying synchronised (but not necessarily regular) beating, they were ready for dissociation. This was expected around Day 12 for ReBl-PAT iPSCs, but could be seen beginning as early as Day 9, as depicted in Figure 104.

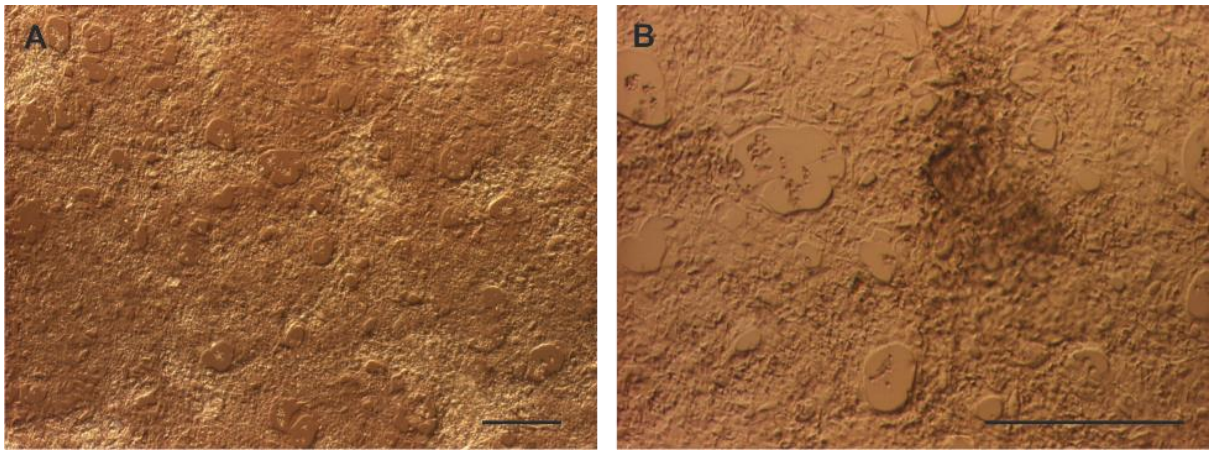


**Figure 104. ReBl-PAT iPSCs post-differentiation, prior to dissociation**. The differentiated cells at Day 9 at: (A) 4x magnification and (B) 10x magnification. The culture formed overlapping bands of cells with a 3D appearance and began to exhibit 'twitching,' suggesting the beginning of spontaneous beating. This batch originated with 0.7 million ReBl-PAT iPSCs, seeded in a T25 flask at 48 hours before commencement of differentiation at Day 0. The scale bar is 250 µm.

The methods for iPSC culture through to differentiation and dissociation were summarised in Table 23. Each stage was carried out according to precise timing, so that no incubation time was reduced or extended. However, after completing the differentiation procedure, the cells were maintained until the appropriate morphology was observed for dissociation, as described above.

#### 8.2.2.3.1 Dissociation of differentiated cells

To analyse the success rate of differentiation into cardiac myocytes, from now on termed 'quality control,' and for other experiments, the cells had to be transferred from the flasks in which they were differentiated to plates. The differentiated cells were maintained in RPMI medium with B27 supplement changed every 3$^{rd}$ day until they had the tight, uniform morphology as shown in Figure 104.

A dissociation solution was made using collagenase II at 200 U/ml in $Ca^{2+}$ free HBSS, supplemented with 10 µm Y-27632, 30 µM N-Benzyl-p-toluene sulphonamide (BTS) and 1 mM HEPES and equilibrated to room temperature. Matrigel coated plates were prepared in advance and warmed in the incubator immediately before use. To begin dissociation of the differentiated cells, the medium was aspirated and $Ca^{2+}$ free HBSS was carefully pipetted in and aspirated twice to ensure no residue of medium remained. Sufficient dissociation solution to cover the base of the flask or plate well (2.5 ml for a T25) was added and incubated for 3.5 hours in the cell culture incubator. The flask was then removed from the incubator and cells gently suspended by slowly pipetting up and down in a 10ml serological pipette. A sample was checked under the microscope to ensure that cells were well separated and no longer clumped together before being transferred to a 50 ml falcon tube.

To inactivate the dissociation solution a pre-warmed (37°C) blocking solution composed of RMPI medium (no B12 supplement) containing 10% FBS, 12 µM Deoxyribonuclease II (DNase II) and 10 µm Y-27632 was used. The DNase II ensured that no free DNA, which is sticky and can cause cells to clump together, was present in the solution. The blocking solution was first used to wash the flask, removing any loosely attached cells, was added to the 50ml falcon tube containing the cell suspension and centrifuged for 15 minutes at 800 rpm. The tube was handled gently upon removal from the centrifuge and medium was aspirated carefully to avoid dislodging the loose pellet created by the relatively slow centrifugation. The blocking buffer was replaced with 5-10 ml (depending on the size of the pellet) of pre-warmed RPMI medium (with B12 supplement and 10 µm Y-27632) and passed through a 100 µm cell strainer for the removal of any clumped cells, or debris. The number of the cells in the filtered solution was counted and subsequently divided amongst Matrigel coated plates for experiments at an appropriate seeding density. The differentiated iPSC-CMs were expected to continue proliferation far more slowly than iPSCs. For some experiments, iPSC-CMs

were supposed to be kept for a prolonged period, so their proliferation had to be taken into account when seeding the cells.

#### *8.2.2.4 Effect of cell density on successful differentiation*

To test at which density the differentiation to iPSC-CMs is most successful, iPSCs were seeded four densities, ranging from 25,000 to 65,000 cells per well of a 12 well plate, and differentiated.

#### *8.2.2.5 Determining the success of differentiation into cardiac myocytes: Quality control*

To determine the success of the differentiation, the proportion of cardiac myocytes in the population of differentiated cells was calculated. α-actinin, an actin-binding protein expressed in skeletal and cardiac muscle, was used as a marker for cardiac myocytes. It is absent in undifferentiated iPSCs.

For fixation, the medium was removed from the wells and exchanged for PBS to dilute and wash away any residual medium. The PBS was then exchanged for ice-cold PFA solution (4% PFA in PBS) and incubated for 15 minutes at room temperature. All following steps were carried out at room temperature. All washes were performed with 200 µl of the respective solution. The PFA solution was carefully removed, and the PBS wash repeated. To permeabilise the cells, PBS containing 0.1% Triton X-100 was added to the wells and incubated for 15 minutes. Following this, the cells were washed again, this time with a wash buffer comprised of 0.1% Tween 20 in PBS, which was used for all subsequent wash steps. A blocking buffer of 5% Human Serum Albumin (HSA) in PBS, was then added to the wells and incubated for 30 minutes. The primary antibody was diluted to 1/1000 in blocking buffer. The blocking solution was exchanged for 50 µl of antibody-solution in each wells and incubated for a further 45 minutes. The primary antibody was monoclonal anti-α-actinin (sarcomeric), produced in mouse (Sigma A7811) diluted 1/1000 in blocking solution. The cells were then washed three times with wash buffer, and the solution replaced with a FITC-labelled secondary antibody, diluted 1/500 in blocking solution.

The cells were washed twice more with wash buffer, which was then exchanged for PBS. Finally, the cells were stained with DAPI, sealed and incubated for 45 minutes before the plate was read and analysed using the Operetta confocal plate reader and software. The quantification of iPSC-CMs in the cell population was based on the percentage of all cells (quantified as number of DAPI stained nuclei) that were positive for α-actinin (antibody stained cardiac specific marker).

As controls, cells were fixed in the same way and underwent the same staining protocol with the following modifications: (1) only the secondary antibody was added (2) neither a primary nor a

secondary antibody were added. Images were captured under identical conditions to provide information about unspecific staining of the antibodies.

## 8.3 Results

### 8.3.1 Culture of iPSCs

The main aim for the culture of iPSCs was to expand and freeze each cell line, while avoiding contamination or spontaneous differentiation. The ReBl-PAT iPSCs were successfully cultured during training at The University of Nottingham, using the feeder-free culture method. The feeder-free protocol was therefore set up at The Open University, as described in sections 8.2.1.1 and 8.2.1.2., and the following iPSC lines were cultured at The Open University: ReBl-PAT, and the CRISPR engineered iPSC pair of CLN3 Q352X and A13777 WT.

Necessary troubleshooting to achieve a successful culture was needed to prevent poor attachment of iPSCs. Two potential reasons for this were identified: cell confluency and the Matrigel coating.

The culture protocol recommends to passage iPSCs when they reach 80% confluence to prevent the detachment of cells. Here, it was observed that flasks with 60% confluency at the end of a day would reach 80% confluency overnight and start to detach before passaging. Therefore, passaging was performed when cells reached a confluency of >60%. This prevented the loss of cultures due to detachment.

Matrigel can polymerise during handling, causing an uneven coating which is an inferior cell attachment surface. When it was observed that iPSCs showed poor attachment after passaging, they were transferred into a new batch of Matrigel-coated flasks. On each occasion the iPSCs attached to the surface as expected. This indicated that the Matrigel coating deteriorated and caused the low level of attachment. If this was observed, all plasticware from this batch of Matrigel-coating was disposed of. After these steps, the three feeder-free iPSC lines were grown successfully at The Open University, expanded and stocks were frozen for future use. These cell lines were expanded and frozen to generate early passage stocks, which were found to recover well from storage in liquid nitrogen. Troubleshooting steps were further discussed in section 8.4, below.

Three iPSC lines, the control line CTRL NHDF and the CLN3-patient derived lines PA 338 and 417 PB had to be cultured on feeder cells. These lines were of special interest because they include the most frequent mutation in the *CLN3* gene. However, culturing them proofed difficult because the colonies were lost through a combination of spontaneous differentiation or failure to attach to the iMEFs in culture.

The iPSCs initially formed colonies with the appearance of healthy undifferentiated iPSCs, but as the colonies expanded the iPSCs rapidly underwent spontaneous differentiation, as shown in 8.2.2, Figure 101. To prevent differentiation of all the cells in the culture, small colonies that still had the appearance of undifferentiated iPSCs were picked and transferred to a fresh plate of iMEFs. However, many of the iPSCs did not adhere to the flask and remained in suspension at the time of medium change the following day. The iPSCs that attached to the iMEFs were generally the larger fragments of the original colonies, which rapidly deteriorated in condition and spontaneously differentiated again.

Several steps were performed to prevent this spontaneous differentiation and address any problems with attachment:

- Testing different densities of iMEFs for the layer of feeder-cells
- Testing different length of time for separating the colonies by pipetting to have a better dispersal of cells, enabling a better attachment

None of these steps prevented the spontaneous differentiation observed. Therefore, the culture of feeder-dependent iPSCs were abandoned in favour of the feeder-free iPSC lines which had demonstrated reliable growth.

All cell lines were free from any visible contamination and negative for mycoplasma each time they were tested. The feeder-free iPSC lines were most vulnerable to contamination as they were cultured in the absence of antibiotics, but this also meant that contamination was unlikely to be masked.

### 8.3.2 Differentiation of iPSCs to iPSC-CMs

The differentiation of iPSCs to iPSC-CMs was carried out when iPSCs reached an appropriate density. The density of iPSCs had an effect on the differentiation capabilities of the culture, with the optimal density known to differ between iPSC lines. When setting up for differentiation, the dissociated iPSCs were counted and seeded in the wells of a 12-well plate at a range of densities. After differentiation and dissociation, the cells were transferred to a 96-well plate for analysis. The results were used to advise on the appropriate density of seeding when seeding a T25 flask, set out in Table 24.

**Table 24. The range of iPSC seeding densities tested on a 12-well plate, per $cm^2$.** Each number of iPSCs per $cm^2$ was scaled to calculate the number of iPSCs for a T25 (25 $cm^2$ cell surface) flask.

| Number of iPSCs /$cm^2$ | Total number of iPSCs / T25 |
|---|---|
| 25,000 | 625,000 |
| 40,000 | 1,000,000 |
| 50,000 | 1,250,000 |
| 65,000 | 1,625,000 |

Post-differentiation and transfer to a 96-well plate, the cells in each well were fixed and immunostained for α-actinin, followed by staining with DAPI before imaging on the Operetta confocal plate reader (Figure 105). To judge the success of the differentiation, the % of cell population positive for the cardiac myocyte marker α-actinin was quantified (Figure 106). The images in Figure 105 clearly showed the presence of α-actinin surrounding the majority of DAPI stained nuclei at the two lower densities (Figure 105 A and B), indicating that the culture was comprised of a predominantly iPSC-CMs. At 50 k/$cm^2$ (Figure 105 C) there were noticeably fewer cells with α-actinin staining present, indicating a drop in differentiation efficiency. However, at the highest density used for differentiation (Figure 105 D) the smaller number of cells is lower and the proportion of α-actinin positive cells is smaller. This suggests two things: the majority of these cells had failed to correctly differentiate to iPSC-cardiomyocytes, and that the differentiated cells had difficulty in adhering to the new plate after dissociation. This was possibly a result of stress from over-confluency during culture and differentiation, or the unknown morphology of the incorrectly differentiated cells.

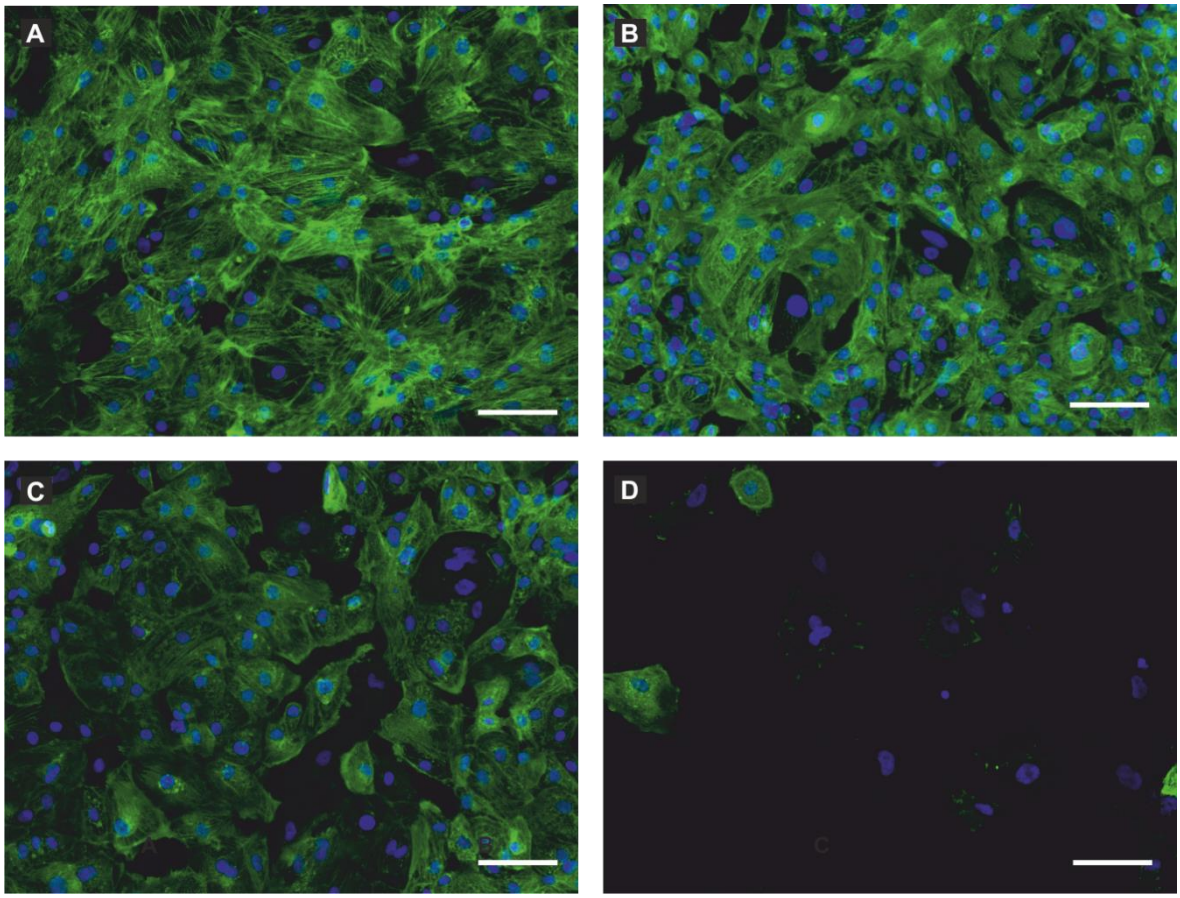


**Figure 105. Quality control for seeding density: to determine the percentage of cells that were successfully differentiated to iPSC-CMs**. The seeding densities were: (A) 25 k/cm$^2$, (B) 40 k/cm$^2$, (C) 50 k/cm$^2$ and (D) 65 k/cm$^2$ 48 hours prior to differentiation. All nuclei were labelled with DAPI (blue) regardless of cell type, while the presence of α-actinin (green) selectively indicated iPSC-CMs. The images were taken with the Operetta confocal plate reader. The scale bars are 100 µm.

The cells imaged and presented in Figure 105 were also quantified by the plate reader software. The DAPI-staining identified all cells. The software then quantified the % of cells positive for α-actinin, which represented the % of iPSC-CMs in the culture. As plotted in Figure 106, the results confirmed a successful differentiation of almost all cells in the populations seeded at the two lowest densities. A slightly lower but still good differentiation (88.98 %) was achieved at a density of 50 k/cm$^2$. The highest density resulted in a low success rate for the differentiation. Therefore, a density of 25-40 k/cm$^2$ iPSCs was considered optimal based on the range tested, translating to 0.625-1 million iPSCs in a T25 flask when setting up a differentiation.

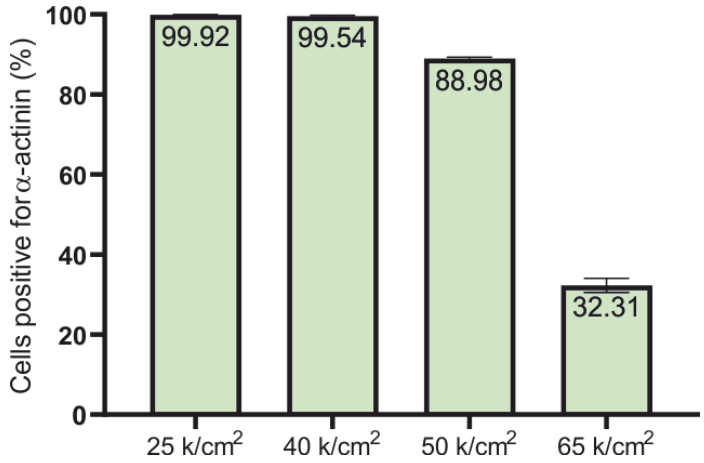


**Figure 106. The percentage of iPSC-CMs in the cell population., indicated by α-actinin staining**. The cells were plated from wells initially seeded with iPSCs at 25, 40, 50 or 65 k /cm$^2$ prior to differentiation. Staining was performed with DAPI and the cardiac marker α-actinin. Each bar represents the mean percentage ± S.E.M. and n = 4 wells on 1 plate.

Control experiments tested if the staining shown in Figure 105 was specific for α-actinin. For these experiments, cells were incubated with DAPI to label the nuclei. The immunostaining was performed either without the primary antibody, or without any antibody addition. Using identical setting to those for imaging the iPSC-CMs shown in Figure 105, virtually no cells were found to be positive for α-actinin (Figure 107). This confirms that the specificity of the α-actinin antibody.

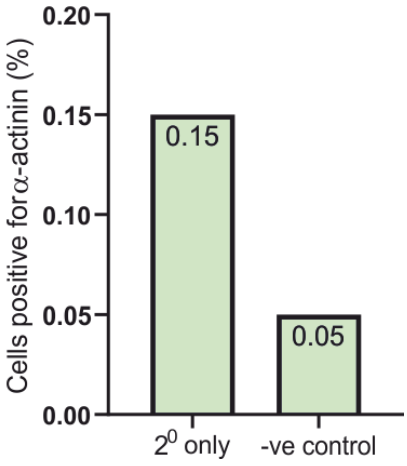


**Figure 107. Control for specificity of the staining protocol.** iPSC-CMs were stained with DAPI. No primary antibody was added. Cells were either incubated with the secondary antibody only (secondary only), or without any antibody (-ve), and imaged under identical conditions to those used for the α-actinin immunostaining. This control was only performed once.

The differentiation described above was performed in wells of a 12-well plate. To test if it can be scaled up and be performed in a T25 flask, two batches of ReBl-PAT iPSCs were seeded at 0.7 million and 1 million iPSCs per T25 flask (the densities that gave the best differentiation in the 12-well plate). These were cultured for 2 days and differentiated. After dissociation, a sample of each batch was placed in a 96-well plate for quality control. The images (Figure 107, quantified in Figure 109) showed the majority of cells to be positive for α-actinin, indicating that they had been successfully differentiated to iPSC-CMs.

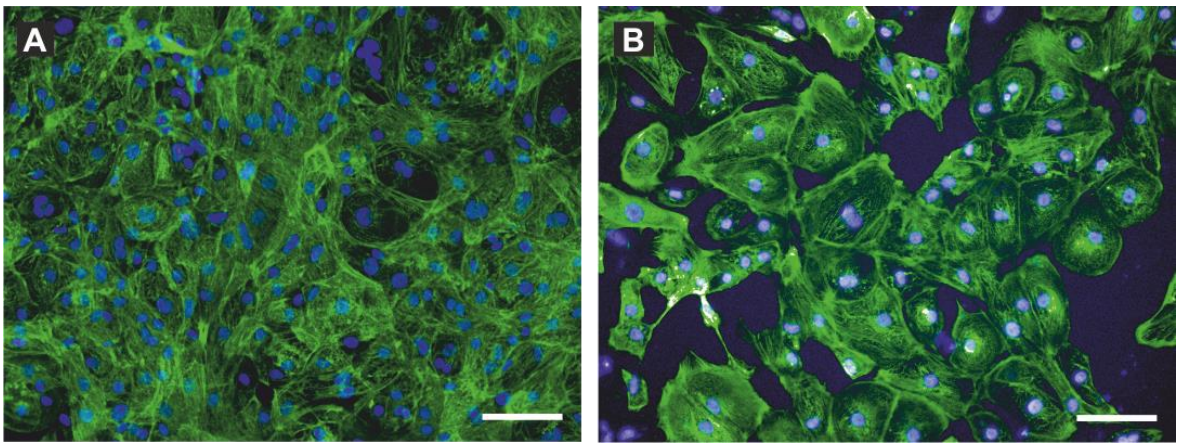


**Figure 108. Quality control for iPSC-CM differentiation: to determine the percentage of cells that were successfully differentiated to iPSC-CMs**. Batch 1 (A) and Batch 2 (B), were differentiated during training at The University of Nottingham. All nuclei labelled with DAPI (blue) regardless of cell type, while the presence of α-actinin (green) selectively indicated iPSC-CMs. The images were taken with the Operetta confocal plate reader. The scale bars are 100 µm.

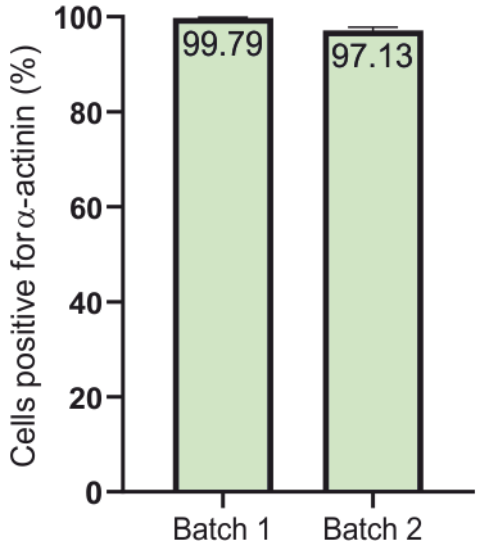


**Figure 109. Quality control: Percentage of cells positive for α-actinin, indicating successful differentiation to iPSC-CMs**. (a) ReBl-PAT iPSCs post-differentiation, training batch 1 and 2, presented as a mean ±S.E.M. and n = 4 wells on 1 plate.

After successfully differentiating the ReBl-PAT iPSCs, the next step was to differentiate iPSCs carrying mutations in the *CLN3* gene. First, differentiation of the CLN3 Q352X and A13777 WT iPSCs was attempted, as these cells were conditioned for feeder-free culture. The cells were plated at the density that was found to be optimal for the ReBl-PAT iPSCs.

In contrast to the ReBl-PAT iPSCs, these cells changed their phenotype after the initial pre-conditioning on Day 0. Instead of growing and spreading to form a monolayer, as shown in 8.2.2.2. Figure 102, the iPSCs contracted to a 'string-like' appearance of long, connected colonies and began to detach from the Matrigel. By Day 2, the differentiation was abandoned due to the detached iPSCs and the failure to form a monolayer.

It was shown for ReBl-PAT iPSCs that the plating density affects the differentiation success (Figure 106). To test if plating at a different density prevents the change in phenotype observed above, a fresh batch of each iPSC line was plated at a range of seeding densities on a Matrigel coated 12-well plate. The string-like morphology was more pronounced at very low seeding densities, probably due to the less dense and therefore thinner groups of iPSCs linking the colonies. Conversely, at higher densities, the iPSCs had an improved appearance of monolayer formation, but a large number of iPSCs detached and the stress of over-confluent iPSCs put them at high risk for spontaneous differentiation. In these experiments, no seeding density could be identified that provided a good compromise between a successful monolayer formation without the problems of a high confluency, indicating that the difficulties with the differentiation might not only be caused by the cell density.

In addition, when recovering and culturing the CLN3 Q352X and A13777 WT iPSCs at the same time, it was observed that despite being an isogenic pair, they had different growth rates. Therefore, the iPSCs reached considerably different densities when seeded at the same original number. This was potentially problematic, as any difference between the two lines may have had a knock-on effect on differentiation efficiency. Furthermore, the introduction of variation between the two cell lines that could modify any readout in subsequent experiments may have rendered them less suitable as a matched pair to study CLN3 disease.

To determine whether the difficulty related to the cell lines or the method in general; further troubleshooting was carried out using the ReBl-PAT iPSCs, which had proven capability for differentiation to iPSC-CMs. However, the ReBl-PAT iPSCs also failed to form a monolayer and had a high proportion of iPSCs detach after pre-conditioning. Therefore, the most likely issue was in either the preparation of the iPSCs for differentiation, the execution of the method or the reagents used for pre-conditioning.

Changing the Stem-Pro24 medium to a new batch did not improve the attachment. One critical component that has been shown to affect the attachment was Matrigel. A new batch of Matrigel was tested, with careful examination of the flasks to check for polymerisation of the Matrigel. A uniform coating with no appearance of polymerisation was not sufficient to improve attachment alone, suggesting that this was not the underlying cause of the poor attachment.

During differentiation, plasticware is not only coated with Matrigel, but Matrigel is also used to form another layer, forming a 'sandwich' between which the iPSCs grow and differentiate. Matrigel, as described in section 8.2.1.1, required careful handling to avoid warming the solution above freezing before it was ready to polymerise. This was achievable when coating flasks, as they could be refrigerated or cooled in the freezer prior to use. However, the addition of a Matrigel-containing solution to a flask of iPSCs which had previously been in the 37°C incubator appeared to cause premature polymerisation and a failure to form a matrix. The suspected polymerisation was observed as lumps of foreign substance in the medium after pipetting into the flask. The Matrigel addition was practised and tested on many flasks and plates, but usually with the presence of polymerisation. A second batch of Matrigel was trialled to ensure that polymerisation had not already occurred in the original stock, but this did not resolve the issue. With practise, the polymerisation appeared less prominent and this may have been a combination of allowing the flask time to cool from 37°C to room temperature and taking care to ensure that the medium and all pipettes were chilled to control temperature. Additionally, gently but firmly pipetting the medium into the flask, avoiding disrupting the iPSC layer but rapidly covering the cell surface and allowing the flask to sit flat to encourage formation of the matrix in a layer.

When growing iPSCs in the Matrigel 'sandwich', fewer iPSCs detached. However, by Day 4 or 6 of the differentiation, the majority of cells were in suspension at the time of medium change and the differentiation had to be re-started. To test the protocol in full at The Open Universities laboratories, with no intention to use the cells for experiments, some flasks with high detachment were carried through to dissociation. However, the few remaining cells did not appear to survive the dissociation procedure and failed to adhere to the new plate for quality control. Due to the appearance of stressors and the incorrect morphology of the culture, it was unlikely that these cells had differentiated to iPSC-CMs.

## 8.4 Discussion

The training for feeder-free iPSC culture and differentiation to iPSC-CMs at The University of Nottingham culminated in the successful differentiation of the ReBl-PAT iPSCs. The differentiation of iPSCs at a range of densities (Figure 105 and Figure 106) provided valuable information for the optimal differentiation of ReBl-PAT iPSCs. Additionally, the results in Figure 106 showed that iPSC density had a great impact on the success of differentiation. The differentiation of ReBl-PAT iPSCs was >97% iPSC-CMs for each batch (Figure 108) indicated that the protocol was successfully carried out. The result indicated a good foundation for experimental work, as there was <3% risk of analysing a cell type that was not a iPSC-CM. By analysing a field of cells per experiment, with repeats, the presence of incorrectly differentiated cells was unlikely to affect the results in a significant way. Furthermore, results of undifferentiated cells may have been removed from analysis if they could be excluded from the analysis due to exhibiting a different morphology to the surrounding iPSC-CMs, or from the data set during outlier analysis if applicable.

As the culture and differentiation had been successfully carried out during training, the next aim was to transfer the protocols to The Open University, and to apply them to the feeder-free and feeder-dependant iPSC cell lines with mutations in *CLN3*. The transfer of the iPSC culture and differentiation protocols involved three stages:

i. Setting up a dedicated laboratory space, ordering all plasticware, medium and reagents and making aliquots of all supplements and reagents such as small molecules.
ii. Receipt and growth of iPSCs: expansion of cultures to generate a large number of early-passage stock vials to be stored frozen.
iii. Differentiation of iPSCs to cardiac myocytes, troubleshooting and quality control.

A dedicated laboratory space was set up for iPSC culture at The Open University and all reagents were purchased, prepared and stored as aliquots suitable for use with the culture and differentiation protocols. Once this was complete, after considerable investment of time but no other hinderance, the iPSC lines were received at The Open University.

The CRISPR-engineered iPSC line carried a rare point mutation in the *CLN3* gene (Q352X). Using this cell line offered the advantages associated with the use of an isogenic control, with the limitation that this rare mutation may not be comparable to the more common CLN3 mutations. As our differentiation protocol uses a feeder free culture methods, it was an advantage that this cell line was conditioned to feeder-free methods in the originating laboratory. However, we also decided to use cells carrying the most common CLN3 mutation, the Δex7/8 deletion. At the time of this study, these were only available as patient-derived cells. The collaborators we received the cells from, grew them in a feeder-dependent culture. So, in addition to the differentiation, we also had to condition these cells to feeder-free culture, which is not always successful.

As described in section 8.3.1, several feeder-free iPSC lines were successfully cultured and expanded to achieve viable stocks. Some troubleshooting steps were required when subsequent passages had a high level of iPSC detachment, but after finding a suitable cell density and solving issues with Matrigel this part was accomplished.

Although the feeder-free iPSC lines expanded rapidly and appeared to retain a healthy morphology, this was not the case with the feeder-dependent iPSCs. These showed high rates of spontaneous differentiation and high levels of detachment. Troubleshooting steps included using different densities of feeder cells and trying to more efficiently breaking up the colonies before replating, to improve cell attachment. However, these attempts did not resolve the problems encountered. Scientists in the labs that provided the cells were contacted for remote troubleshooting, but without achieving significant improvements. Therefore, the feeder-dependent iPSCs were abandoned in favour of the feeder-free iPSC lines which had demonstrated reliable growth.

After creating a large number of stocks, the feeder-free CLN3 Q352X and A13777 WT iPSCs were trialled for differentiation, as these cell lines would have provided a model of CLN3 disease for subsequent experiments. However, these cells changed their morphology and growth pattern during the pre-conditioning, growing in strings instead of forming a monolayer. For ReBl-PAT iPSCs it was shown that the differentiation success was highly dependent on the plating density (Figure 105). Troubleshooting for the CLN3 Q352X and A13777 WT iPSCs therefore included using various plating densities. High plating densities achieved the cells forming a monolayer, but the cells quickly detached from the surface. No density could be found that offered a viable compromise that allowed to carry the cells through the differentiation process. An additional challenge was the fact that WT and *CLN3* mutated cells grew at different rates, making it difficult to proceed with the differentiation process in parallel. It also raised questions if the different rates of proliferation would affect the cell responses independent of the differences in *CLN3*. As the CLN3 Q352X and A13777 WT had not been differentiated to iPSC-CMs by any laboratory, it was possible that these lines may be particularly difficult to differentiate to iPSC-CMs.

To determine whether the difficulty related to the cell lines or the method in general it was attempted to differentiate the ReBl-PAT iPSCs at The Open University. These cells had proven capability for differentiation to iPSC-CMs during the training at Chris Denning's laboratory. However, the ReBl-PAT iPSCs also failed to form a monolayer and had a high proportion of iPSCs detach after pre-conditioning. Therefore, the most likely issue was in either the preparation of the iPSCs for differentiation, the execution of the method or the reagents used for pre-conditioning. During differentiation, Matrigel is used to 'sandwich' the iPSCs, which helps with their differentiation to cardiac myocytes. Because problems with Matrigel has been shown earlier to contribute to poor cell attachment, extensive troubleshooting was performed to test if the Matrigel

coating of the plasticware affected the attachment, which it did not, and to improve the formation of an even layer of Matrigel on top of the cells. Whilst it was possible perfect this technique, the cells in the sandwich did not differentiate successfully, but still detached during the process.

Although the Matrigel step was suspected to be the cause of failure in the differentiation process, the troubleshooting was challenging, as there were a large number of variables which the iPSCs could have been sensitive to. It was possible that some stages took longer or were carried out slightly differently, for example the amount of force used to detach iPSCs passaged with EDTA or Accutase. The iPSCs may have failed to respond correctly to differentiation if they had been detrimentally affected by the culture methods previously used. As the ReBl-PAT iPSCs had differentiated correctly under supervision in a different laboratory, inexperience may have been part of the difficulty with the protocol. The handling of tricky reagents such as Matrigel, and the identification of visual cues in an iPSC culture (e.g. stress or spontaneous differentiation) may have been improved with more time learning from iPSC experts. Additionally, although the protocol was strictly followed, any of the aliquots of medium or supplements used in culture may have inadvertently differed from the stocks from the originating laboratory. Finally, it was possible that the iPSCs were infected despite being negative for mycoplasma and having no obvious contaminants in the medium. However, as the lack of antibiotics allowed uninhibited growth, it was unlikely that an infection would have been remained invisible under the microscope.

With the failure of differentiation, the planned experiments to characterise structural and functional differences in iPSC-derived cardiac myocytes with mutations in CLN3 could not be performed in this study. These included: contraction, number/volume of organelles including nuclei and mitochondria, calcium release from the sarcoplasmic reticulum and staining for the Troponin isoform expressed. Once these experiments were completed in an iPSC-CM model of CLN3 disease with appropriate paired controls, they would also have served to inform where further study could investigate any potential CLN3 disease phenotype.

To further utilise these experiments, additional readouts would have been incorporated, such as a more in-depth assessment of calcium signalling, measurement of lysosome number and dynamics and autophagosome accumulation. Therefore, the maturity study had the secondary objective of identifying the development of any CLN3 disease phenotype, in addition to assessing the structure and function of cells for a matured phenotype as reported in literature. The experiments aimed to establish the extent to which iPSC-CMs were affected by the *CLN3* mutation in comparison to a matched control.

These experiments are explained in Future Work as they are still critical to understand the effects of mutations in the CLN3 gene on the heart. Despite the setback encountered, the system of iPSC-

derived cardiac myocytes offers a lot of promise to perform this work but needs more local expertise in iPSC culture and differentiation to succeed.

## 8.5 Future Work

Despite the challenges, the generation of an iPSC-CM model of CLN3 disease would have been an excellent addition to the study of the heart, to address the gap in CLN3 disease research. The experiments planned for the iPSC-CMs (Table 25) were carefully selected. The first experiment, α-actinin staining as detailed in section 8.2.2.5 was important for quality control.

Next, a number of readouts for the comprehensive characterisation of iPSC-CM maturity over time in culture, as discussed in section 8.1., aimed to inform an appropriate window for experiments in which the iPSC-CMs no longer mostly resembled foetal cardiac myocytes. It was planned to assess the following parameters a 20-day intervals whilst culturing the iPSCs. 100 days was set as the end date, because at this time iPSCs have been described as reaching a mature state regarding their (Dai et al., 2017).

These experiments included the identification of the Troponin isoform expressed, number of nuclei per cell as markers for structural changes during maturation. The number of mitochondria has been demonstrated to increase with iPSC-CM maturity (Dai et al., 2017), and we intended to quantify the number of mitochondria and use this as a marker for maturity.

To measure the function of the iPSC-CMs, overall size and contraction capability, alongside readouts for calcium ($Ca^{2+}$) signalling, responses to electrical field stimulation (EFS) were planned. Immature, foetal-equivalent iPSCs lacked a sarcoplasmic reticulum $Ca^{2+}$ store which developed over time in culture (Hwang et al., 2015). The extent of the SR $Ca^{2+}$ store was supposed to be used as a marker for maturity.

Although lysosomes were not specifically identified as a marker of iPSC-CM maturity in literature, they are an organelle of interest in CLN3 disease and experimental work. Therefore, the confirmation of lysosome presence and measurement of number, size or localisation with time would be provide useful results. Likewise, a pathological change in autophagy has been linked to CLN3 disease and therefore, although autophagosomes are not specifically a marker of age, as with lysosomes they are of interest to measure over time (Chandrachud et al., 2015).

This combination of experiments would provide a systematic and comprehensive understanding of the timeline of maturation for iPSC-derived cardiac myocytes, and thus help the cardiac field. But, more importantly for this work, it would provide knowledge on changes observed in cells with mutations in CLN3, that could help to explain the cardiac defects seen in individuals with CLN3 disease.

**Table 25. Planned experiments for CLN3 model and matched control iPSC-CMs.** A combination of analysis from different imaging methods including fluorescence plate reader (CX5), fluorescence microscope (Fluo), electron microscope (EM) and brightfield microscope (BF).

| Experiment | Reagent(s) | Method |
|---|---|---|
| **Structure: proteins** | | |
| α-actinin | α-actinin antibody | CX5: imaging & quantification |
| Troponin I cTNI (cardiac adult) | cTNI antibody | |
| Troponin I ssTNI (slow/ fetal) | ssTNI antibody | |
| **Structure: organelles** | | |
| Number of nuclei /cell | DAPI + WGA | Fluo: Count DAPI per cell |
| Mitochondria number | MitoTracker | Fluo: Measure % coverage of cell |
| Mitochondria size | | Fluo: Measure average lengths |
| Lysosome number | LysoTracker or LAMP2 antibody for electron microscopy (EM) | Fluo: Count per cell |
| Lysosome size | | EM: measure size (area) |
| Lysosome localisation | | EM: distance from nucleus |
| **Function: live cell experiments** | | |
| Contraction | Brightfield, no stain | BF: Musclemotion plugin (ImageJ) |
| Cell size | | BF: Measure average lengths |
| $Ca^{2+}$ EFS response | Cal-520 | Fluo: EFS pacing changes |
| $Ca^{2+}$ ER release | Cal-520 | Fluo: Caffeine induced release |
| Autophagy (basal) | CytoID | Fluo: (1) complete medium + count |
| Autophagy (starvation) | | Fluo: (2) starvation medium + count |
| ROS/superoxide | Cell ROX/ MitoSOX | Fluo: count |

Following the maturity study (Table 25) it may have been possible to identify any emerging CLN3 disease phenotypes. Therefore, these would inform the most pertinent areas of study for a more thorough set of experiments to fully investigate the phenotype. If no phenotype was found during the experiments detailed above, this would indicate that either: culture conditions should be extended or improved to establish a greater maturity to capture a phenotype emerging with time, that the cells might need challenging to reveal any changes, or the cardiac symptoms of CLN3 disease may be a result of extracellular changes, such as within the conduction system. If the latter is true, this would be an important result in itself which may be verified with a combination of studies involving primary cardiac myocytes isolated from an animal model of CLN3 disease.

To improve maturity, there are a number of published strategies if the cells do not mature quickly enough in time. These include co-culture, 3D culture and electrical stimulation amongst other strategies to improve markers of cardiac myocyte maturity (Besser et al., 2018). Thus, there is considerable scope for improving upon any immaturity apparent in the iPSC-CM cultures, which may allow the identification of any CLN3 disease phenotype that was otherwise masked by the immaturity of the iPSC-CMs. By making a detailed characterisation to inform both the extent of comparability to adult cardiac myocytes and the identification of any CLN3 disease phenotype, the use of iPSC-CMs would be a valuable addition to the study of CLN3 disease.

# 9 General Discussion

This thesis aimed to explore the effects of the CLN3 mutation on organelle activity and structure using cell models of CLN3 disease. The methodology for the assessment of these live cell models forms an important part of this thesis, and these robust and carefully designed assays can be applied to future studies. In particular, the novel lysosome tracking assay (Chapter 4) presented the opportunity for a detailed investigation of lysosome movement, with a high number of tracked lysosomes per sample. The assays described in this study were principally carried out using HeLa and fibroblast cells and primarily explored the activities of lysosomes and mitochondria in CLN3 disease. The final chapters of the thesis detail the assessment of CLN3 mouse heart tissue and the attempt at establishing an iPSC derived cardiac myocyte model of CLN3 disease to further investigate the cardiac phenotype in CLN3 disease. The assays developed and described throughout the thesis would have been applied to the iPSC-CM model had this been feasible, but this is now future work.

Chapter 3 detailed the use of lysosome probes and their appropriateness for experimental purposes. The fluorescent labelling of lysosomes using LysoTracker, CellLight and immunofluorescence of a LAMP2 antibody showed a high degree of co-localisation, which pointed to their comparative specificity for lysosomes. The comparison of these lysosome probes also revealed a large number of characteristics, which were of relevance for the selection of the most appropriate probe for imaging experiments. These characteristics included a tendency towards photobleaching, signal bleed-through and background noise. The use of background subtraction in ImageJ, with the rolling ball radius set to 5 pixels, was also introduced and this method was used with all subsequent experiments in which lysosomes were imaged.

LysoTracker was used to label lysosomes in the experiments presented in Chapter 4, which introduced methods for automated image analysis that were explored and compared to manual methods. In particular, a novel method for the analysis of lysosome movement was presented. Lysosome movement was observed first in a qualitative manner before application of the quantification to establish the most informative readouts. Important considerations, such as the extent of cell 'background' movement and the effect of temperature on lysosome movement, were discussed as critical controls for the lysosome movement assay. The type of lysosome movement (short or long trajectories) was examined and it was surprisingly found that even long trajectories did not have a smooth and continuous profile, with the distance varying on a frame-by-frame basis. The measurement of lysosome movement pathways was calculated based on the sum of the total path (the addition of all frame-to-frame distances), which allowed for velocity of movement to be determined. This 'sum of distance' (and velocity) readout did not provide information on whether

the lysosome had travelled within the cell or continuously moved at the same fixed point. Therefore, the 'maximum distance' was calculated to determine the distance which the lysosome had travelled in the cell body during imaging. The maximum distance differentiated clearly between lysosomes with long trajectories that had travelled in a relatively linear, directional manner and those with short trajectories that had moved around an apparently fixed point within the cell (or had undergone major directions changes). It was therefore the maximum distance that showed the clearest change in response to microtubule depolymerisation, suggesting that the inhibition of microtubule-dependent travel of lysosomes could be induced as a phenotype in live cell models. The correlation between maximum distance and sum of distance was not as close as might be expected, and the microtubule depolymerisation had relatively little influence on the sum of distance compared to the maximum. The lack of correction suggests that lysosome movement is not always dependent upon a directionality. Based on the work to characterise the lysosome probes in Chapter 3 and the attention to robust techniques of imaging and analysis in Chapter 4, the lysosome tracking assay was developed as a sensitive and reliable tool for the investigation of lysosome movement.

The assays established in Chapter 4 were followed up in Chapter 5 and applied to the study of CLN3 disease using the cell models available. In addition to the comparison of the WT and CLN3 cells, the sensitivity of the lysosome tracking assay was tested in cells with microtubules depolymerised through treatment with nocodazole, which induced a phenotype of reduced lysosome movement distance. The key finding of this chapter was that there was no significant change to lysosome movement between the WT and CLN3 KO HeLa cells, but when the WT fibroblasts were compared to the two patient cell lines (Δex7/8 and D416G) there was a significant reduction in lysosome movement in CLN3 patient cells. This highly significant effect on lysosome movement distance in fibroblasts was not replicated with a comparable change to velocity, although there was a trend towards slower lysosome movement in the D416G cells. The fact that the assay revealed a phenotype in the fibroblast cell models of CLN3 disease and not in the HeLa was of interest. The comparison of lysosome movement in untreated WT HeLa and fibroblast cells revealed that lysosomes travelled far greater distances overall in HeLa cells compared to fibroblast cells. This observation suggests an effect of cell type on lysosome movement. In the context of CLN3 disease, it is the more highly differentiated and sensitive cell types, such as neurons and cardiac myocytes that are more severely affected in the disease, and it would be of considerable interest for the assay to be applied to primary cells from patients or robust models.

Following the investigation lysosome movement, the next organelles of interest were the mitochondria, and assays relating to the function of these were set out in Chapter 6. Overall, these experiments suggested no significant functional change to the mitochondria in the CLN3 KO HeLa cells compared to the WT. The mitochondrial membrane potential was comparable, with no

difference in response to the control treatment. ROS production also appeared to be comparable, with no difference between WT and CLN3 KO in ROS production during imaging, or in response to the response to oxidising agents that were used as control treatments. Finally, there was no significant difference in the calcium sequestration measurements in the WT and CLN3 KO HeLa cells, or the response of these cells to the agonist treatment.

Chapters 7 and 8 presented the cardiac aspect of this project. Heart tissue from the mouse model of CLN3 disease was available from mice sacrificed at 6, 12 and 18 months, with tissue from the matched WT mice at each age. This presented an opportunity to investigate the ultrastructural changes within these tissues. Quantitating information within images is not always straightforward. To avoid an impressionistic interpretation of the EM images, a series of analysis protocols were developed that enabled the images to be systematically quantitated. Moreover, the samples were randomised at the imaging stage and the analysis was performed blinded. There appeared to be a tendency for variation in the appearance of the mitochondria with ageing, but few statistically significant findings. It is plausible that more data sets are required.

Each of these experimental chapters could be expanded in future work, as described in the individual chapter discussions. In general, the expansion of this project would incorporate a greater number of cell models of CLN3 disease and apply the assays (e.g., lysosome tracking) to specialised cell types such as neurons and cardiac myocytes that are known to be highly affected. There is great scope for the expansion of the cardiac aspect to this project. A detailed exploration of the cardiac CLN3 phenotype would be possible via the use of animal models, and through the differentiation of iPSCs carrying the CLN3 mutation to cardiac myocytes. However, these future studies should proceed with caution as animal models, such as the CLN3 mice, may not faithfully capture the cardiac phenotype seen in human patients, and the use of iPSC derived cardiac myocytes come with many challenges such as establishing an adequate maturity of these cultures to examine the phenotype.

CLN3 disease involves a terrible, progressive degradation that is devastating for affected individuals and their families. It is of huge importance to understand the cellular consequences of the disease-causing CLN3 mutations. It is frustrating that the clearly vital function of this lysosomal protein is still so elusive. The development and characterisation of CLN3 models, such as those used in this study, will hopefully shed increasing light on the processes affected by CLN3 mutations, as well as those that are not affected. It is hoped that this growing body of knowledge will one day lead to a better prognosis, or even curative options, for the children that receive a diagnosis of CLN3. It is in that spirit that the work described in this study was undertaken and is offered to all who might benefit from it.

**References**


ANDERSON, G. W., GOEBEL, H. H. & SIMONATI, A. 2013. Human pathology in NCL. *Biochimica et Biophysica Acta (BBA) - Molecular Basis of Disease,* 1832**,** 1807-1826.

ANESTI, V. & SCORRANO, L. 2006. The relationship between mitochondrial shape and function and the cytoskeleton. *Biochimica et Biophysica Acta (BBA) - Bioenergetics,* 1757**,** 692-699.

ARMSTRONG, D., LOMBARD, C. & ELLIS, A. 1986. Electrocardiographic and histologic abnormalities in canine ceroid-lipofuscinosis (CCL). *J Mol Cell Cardiol,* 18**,** 91-7.

BA, Q., RAGHAVAN, G., KISELYOV, K. & YANG, G. 2018. Whole-Cell Scale Dynamic Organization of Lysosomes Revealed by Spatial Statistical Analysis. *Cell Rep,* 23**,** 3591-3606.

BALDWIN, S. A., BEAL, P. R., YAO, S. Y., KING, A. E., CASS, C. E. & YOUNG, J. D. 2004. The equilibrative nucleoside transporter family, SLC29. *Pflugers Arch,* 447**,** 735-43.

BALLABIO, A. 2016. The awesome lysosome. *EMBO Molecular Medicine*.

BANDYOPADHYAY, D., CYPHERSMITH, A., ZAPATA, J. A., KIM, Y. J. & PAYNE, C. K. 2014. Lysosome transport as a function of lysosome diameter. *PloS one,* 9**,** e86847-e86847.

BARAVALLE, G., SCHOBER, D., HUBER, M., BAYER, N., MURPHY, R. F. & FUCHS, R. 2005. Transferrin recycling and dextran transport to lysosomes is differentially affected by bafilomycin, nocodazole, and low temperature. *Cell and Tissue Research,* 320**,** 99-113.

BEDADA, F. B., WHEELWRIGHT, M. & METZGER, J. M. 2016. Maturation status of sarcomere structure and function in human iPSC-derived cardiac myocytes. *Biochim Biophys Acta,* 1863**,** 1829-38.

BERRIDGE, M. J. 2014. Calcium regulation of neural rhythms, memory and Alzheimer's disease. *J Physiol,* 592**,** 281-93.

BERS, D. M. 2008. Calcium cycling and signaling in cardiac myocytes. *Annu Rev Physiol,* 70**,** 23-49.

BESSER, R. R., ISHAHAK, M., MAYO, V., CARBONERO, D., CLAURE, I. & AGARWAL, A. 2018. Engineered Microenvironments for Maturation of Stem Cell Derived Cardiac Myocytes. *Theranostics,* 8**,** 124-140.

BOENGLER, K., KOSIOL, M., MAYR, M., SCHULZ, R. & ROHRBACH, S. 2017. Mitochondria and ageing: role in heart, skeletal muscle and adipose tissue. *Journal of Cachexia, Sarcopenia and Muscle,* 8**,** 349-369.

BOOTMAN, M. D., CHEHAB, T., BULTYNCK, G., PARYS, J. B. & RIETDORF, K. 2018. The regulation of autophagy by calcium signals: Do we have a consensus? *Cell Calcium,* 70**,** 32-46.

BOOTMAN, M. D., RIETDORF, K., COLLINS, T., WALKER, S. & SANDERSON, M. 2013. Ca2+-sensitive fluorescent dyes and intracellular Ca2+ imaging. *Cold Spring Harb Protoc,* 2013**,** 83-99.

BOOTMAN, M. D., RIETDORF, KATJA, HARDY, HOLLY, DAUTOVA, YANA, CORPS, ELAINE, PIERRO, CRISTINA, STAPLETON, ELOISE, KANG, ESTHER, AND PROUDFOOT, DIANE 2012. Calcium Signalling and Regulation of Cell Function. *eLS*.

BOOTMAN, M. D., SMYRNIAS, I., THUL, R., COOMBES, S. & RODERICK, H. L. 2011. Atrial cardiomyocyte calcium signalling. *Biochim Biophys Acta,* 1813**,** 922-34.

BORGER, D. K., MCMAHON, B., ROSHAN LAL, T., SERRA-VINARDELL, J., AFLAKI, E. & SIDRANSKY, E. 2017. Induced pluripotent stem cell models of lysosomal storage disorders. *Dis Model Mech,* 10**,** 691-704.

BRENNEMAN, D. E., PEARCE, D. A., KOVACS, A. & DEFREES, S. 2017. Pharmacological Effects on Ceroid Lipofuscin and Neuronal Structure in Cln3 (ex7/8) Mouse Brain Cultures. *J Mol Neurosci,* 63**,** 100-114.

BURLAKOV, V. M., TAYLOR, R., KOERNER, J. & EMPTAGE, N. 2010. Analysis of microscopic parameters of single-particle trajectories in neurons. *Biophysical journal,* 99**,** 1368-1376.

CABUKUSTA, B. & NEEFJES, J. 2018. Mechanisms of lysosomal positioning and movement. *Traffic (Copenhagen, Denmark),* 19**,** 761-769.

CADET, J. S. & KAMP, T. J. 2017. A Recipe for T-Tubules in Human iPS Cell-Derived Cardiomyocytes. *Circ Res,* 121**,** 1294-1295.

CALCRAFT, P. J., RUAS, M., PAN, Z., CHENG, X., ARREDOUANI, A., HAO, X., TANG, J., RIETDORF, K., TEBOUL, L., CHUANG, K. T., LIN, P., XIAO, R., WANG, C., ZHU, Y., LIN, Y., WYATT, C. N.,

PARRINGTON, J., MA, J., EVANS, A. M., GALIONE, A. & ZHU, M. X. 2009. NAADP mobilizes calcium from acidic organelles through two-pore channels. *Nature,* 459**,** 596-600.

CAMACHO, P., FAN, H., LIU, Z. & HE, J.-Q. 2016. Large Mammalian Animal Models of Heart Disease. *Journal of Cardiovascular Development and Disease,* 3**,** 30.

CAO, Y., ESPINOLA, J. A., FOSSALE, E., MASSEY, A. C., CUERVO, A. M., MACDONALD, M. E. & COTMAN, S. L. 2006. Autophagy is disrupted in a knock-in mouse model of juvenile neuronal ceroid lipofuscinosis. *J Biol Chem,* 281**,** 20483-93.

CHAN, C. H., MITCHISON, H. M. & PEARCE, D. A. 2008. Transcript and in silico analysis of CLN3 in juvenile neuronal ceroid lipofuscinosis and associated mouse models. *Hum Mol Genet,* 17**,** 3332-9.

CHANDRA, N., BASTIAENEN, R., PAPADAKIS, M., PANOULAS, V. F., GHANI, S., DUSCHL, J., FOLDES, D., RAJU, H., OSBORNE, R. & SHARMA, S. 2014. Prevalence of Electrocardiographic Anomalies in Young Individuals: Relevance to a Nationwide Cardiac Screening Program. *Journal of the American College of Cardiology,* 63**,** 2028-2034.

CHANDRACHUD, U., WALKER, M. W., SIMAS, A. M., HEETVELD, S., PETCHERSKI, A., KLEIN, M., OH, H., WOLF, P., ZHAO, W. N., NORTON, S., HAGGARTY, S. J., LLOYD-EVANS, E. & COTMAN, S. L. 2015. Unbiased Cell-based Screening in a Neuronal Cell Model of Batten Disease Highlights an Interaction between Ca2+ Homeostasis, Autophagy, and CLN3 Protein Function. *J Biol Chem,* 290**,** 14361-80.

CHENG, Z., ITO, S., NISHIO, N., THANASEGARAN, S., FANG, H. & ISOBE, K.-I. 2013. Characteristics of cardiac aging in C57BL/6 mice. *Experimental Gerontology,* 48**,** 341-348.

CIALONE, J., ADAMS, H., AUGUSTINE, E. F., MARSHALL, F. J., KWON, J. M., NEWHOUSE, N., VIERHILE, A., LEVY, E., DURE, L. S., ROSE, K. R., RAMIREZ-MONTEALEGRE, D., DE BLIECK, E. A. & MINK, J. W. 2012. Females experience a more severe disease course in Batten disease. *J Inherit Metab Dis,* 35**,** 549-55.

COLE, L. W. 2016. The Evolution of Per-cell Organelle Number. *Frontiers in cell and developmental biology,* 4**,** 85-85.

COLLINS, T. J., BERRIDGE, M. J., LIPP, P. & BOOTMAN, M. D. 2002. Mitochondria are morphologically and functionally heterogeneous within cells. *The EMBO Journal,* 21**,** 1616-1627.

COLLINS, T. J., LIPP, P., BERRIDGE, M. J. & BOOTMAN, M. D. 2001. Mitochondrial Ca(2+) uptake depends on the spatial and temporal profile of cytosolic Ca(2+) signals. *J Biol Chem,* 276**,** 26411-20.

CONNOLLY, N. M. C., THEUREY, P., ADAM-VIZI, V., BAZAN, N. G., BERNARDI, P., BOLAÑOS, J. P., CULMSEE, C., DAWSON, V. L., DESHMUKH, M., DUCHEN, M. R., DÜSSMANN, H., FISKUM, G., GALINDO, M. F., HARDINGHAM, G. E., HARDWICK, J. M., JEKABSONS, M. B., JONAS, E. A., JORDÁN, J., LIPTON, S. A., MANFREDI, G., MATTSON, M. P., MCLAUGHLIN, B., METHNER, A., MURPHY, A. N., MURPHY, M. P., NICHOLLS, D. G., POLSTER, B. M., POZZAN, T., RIZZUTO, R., SATRÚSTEGUI, J., SLACK, R. S., SWANSON, R. A., SWERDLOW, R. H., WILL, Y., YING, Z., JOSELIN, A., GIORAN, A., MOREIRA PINHO, C., WATTERS, O., SALVUCCI, M., LLORENTE-FOLCH, I., PARK, D. S., BANO, D., ANKARCRONA, M., PIZZO, P. & PREHN, J. H. M. 2018. Guidelines on experimental methods to assess mitochondrial dysfunction in cellular models of neurodegenerative diseases. *Cell Death & Differentiation,* 25**,** 542-572.

COOPER, G. M. 2000. *The Cell: A Molecular Approach. 2nd edition.*, Sunderland (MA): Sinauer Associates.

CORDONNIER, M. N., DAUZONNE, D., LOUVARD, D. & COUDRIER, E. 2001. Actin filaments and myosin I alpha cooperate with microtubules for the movement of lysosomes. *Mol Biol Cell,* 12**,** 4013-29.

CORSETTI, G., PASINI, E., D'ANTONA, G., NISOLI, E., FLATI, V., ASSANELLI, D., DIOGUARDI, F. S. & BIANCHI, R. 2008. Morphometric Changes Induced by Amino Acid Supplementation in Skeletal and Cardiac Muscles of Old Mice. *The American Journal of Cardiology,* 101**,** S26-S34.

CORTESE, A., TUCCI, A., PICCOLO, G., GALIMBERTI, C. A., FRATTA, P., MARCHIONI, E., GRAMPA, G., CEREDA, C., GRIECO, G., RICCA, I., PITTMAN, A., CISCATO, P., NAPOLI, L., LUCCHINI, V., RIPOLONE, M., VIOLANO, R., FAGIOLARI, G., MOLE, S. E., HARDY, J., MOGLIA, A. & MOGGIO,

M. 2014. Novel CLN3 mutation causing autophagic vacuolar myopathy. *Neurology,* 82**,** 2072-6.

COTMAN, S. L. & STAROPOLI, J. F. 2012. The juvenile Batten disease protein, CLN3, and its role in regulating anterograde and retrograde post-Golgi trafficking. *Clin Lipidol,* 7**,** 79-91.

COTMAN, S. L., VRBANAC, V., LEBEL, L. A., LEE, R. L., JOHNSON, K. A., DONAHUE, L. R., TEED, A. M., ANTONELLIS, K., BRONSON, R. T., LERNER, T. J. & MACDONALD, M. E. 2002. Cln3(Deltaex7/8) knock-in mice with the common JNCL mutation exhibit progressive neurologic disease that begins before birth. *Hum Mol Genet,* 11**,** 2709-21.

DAI, D. F., DANOVIZ, M. E., WICZER, B., LAFLAMME, M. A. & TIAN, R. 2017. Mitochondrial Maturation in Human Pluripotent Stem Cell Derived Cardiomyocytes. *Stem Cells Int,* 2017**,** 5153625.

DEMERS-LAMARCHE, J., GUILLEBAUD, G., TLILI, M., TODKAR, K., BÉLANGER, N., GRONDIN, M., NGUYEN, A. P., MICHEL, J. & GERMAIN, M. 2016. Loss of Mitochondrial Function Impairs Lysosomes. *J Biol Chem,* 291**,** 10263-76.

DEUS, C. M., YAMBIRE, K. F., OLIVEIRA, P. J. & RAIMUNDO, N. 2020. Mitochondria-Lysosome Crosstalk: From Physiology to Neurodegeneration. *Trends Mol Med,* 26**,** 71-88.

DILAVERIS P, K. I., AGGELI C, SIDERIS S, GATZOULIS K, STEFANADIS C. 2014. Severe sinus node dysfunction in a patient with juvenile neuronal ceroid lipofuscinosis. *Int J Cardiol,* 174**,** 143-146.

DISTELHORST, C. W. & BOOTMAN, M. D. 2019. Creating a New Cancer Therapeutic Agent by Targeting the Interaction between Bcl-2 and IP(3) Receptors. *Cold Spring Harb Perspect Biol,* 11.

DUTTA, S. & SENGUPTA, P. 2016. Men and mice: Relating their ages. *Life Sciences,* 152**,** 244-248.

EISELE, J. C., SCHAEFER, I.-M., RANDEL NYENGAARD, J., POST, H., LIEBETANZ, D., BRÜEL, A. & MÜHLFELD, C. 2008. Effect of voluntary exercise on number and volume of cardiomyocytes and their mitochondria in the mouse left ventricle. *Basic Research in Cardiology,* 103**,** 12-21.

EISENBERG, E., DI PALO, K. E. & PINA, I. L. 2018. Sex differences in heart failure. *Clin Cardiol,* 41**,** 211-216.

EISNER, D. A., CALDWELL, J. L., KISTAMAS, K. & TRAFFORD, A. W. 2017. Calcium and Excitation-Contraction Coupling in the Heart. *Circ Res,* 121**,** 181-195.

ESKELINEN, E.-L. 2006. Roles of LAMP-1 and LAMP-2 in lysosome biogenesis and autophagy. *Molecular Aspects of Medicine,* 27**,** 495-502.

FEARNLEY, C. J., RODERICK, H. L. & BOOTMAN, M. D. 2011. Calcium signaling in cardiac myocytes. *Cold Spring Harb Perspect Biol,* 3**,** a004242.

FENG, X. & YANG, J. 2016. Lysosomal Calcium in Neurodegeneration. *Messenger (Los Angel),* 5**,** 56-66.

FIDZIAŃSKA, A., WALCZAK, E. & SZWOCH, M. 2013. Remodeling of Mitochondrial Interior in Cardiac Lipofuscinosis. *Ultrastructural Pathology,* 37**,** 52-55.

FOSSALE, E., WOLF, P., ESPINOLA, J. A., LUBICZ-NAWROCKA, T., TEED, A. M., GAO, H., RIGAMONTI, D., CATTANEO, E., MACDONALD, M. E. & COTMAN, S. L. 2004. Membrane trafficking and mitochondrial abnormalities precede subunit c deposition in a cerebellar cell model of juvenile neuronal ceroid lipofuscinosis. *BMC Neurosci,* 5**,** 57.

GETTY, A., KOVACS, A. D., LENGYEL-NELSON, T., CARDILLO, A., HOF, C., CHAN, C. H. & PEARCE, D. A. 2013. Osmotic stress changes the expression and subcellular localization of the Batten disease protein CLN3. *PLoS One,* 8**,** e66203.

GILBERT-BARNESS, E. 2004. Review: Metabolic cardiomyopathy and conduction system defects in children. *Ann Clin Lab Sci,* 34**,** 15-34.

GOEBEL, H. H., ZEMAN, W., PILZ, H. 1975. Significance of muscle biopsies in neuronal ceroid-lipofuscinoses. *Journal of Neurology, Neurosurgery, and Psychiatry,***,** 985-993.

GOMEZ-GIRO, G., ARIAS-FUENZALIDA, J., JARAZO, J., ZEUSCHNER, D., ALI, M., POSSEMIS, N., BOLOGNIN, S., HALDER, R., JÄGER, C., KUPER, W. F. E., VAN HASSELT, P. M., ZAEHRES, H., DEL SOL, A., VAN DER PUTTEN, H., SCHÖLER, H. R. & SCHWAMBORN, J. C. 2019. Synapse alterations precede neuronal damage and storage pathology in a human cerebral organoid

model of CLN3-juvenile neuronal ceroid lipofuscinosis. *Acta neuropathologica communications,* 7**,** 222-222.
GROMNICOVA, R., DAVIES, H. A., SREEKANTHREDDY, P., ROMERO, I. A., LUND, T., ROITT, I. M., PHILLIPS, J. B. & MALE, D. K. 2013. Glucose-Coated Gold Nanoparticles Transfer across Human Brain Endothelium and Enter Astrocytes In Vitro. *PLOS ONE,* 8**,** e81043.
HAGAN, C. 2017. When are mice considered old? *The Jackson Laboratory* [Online]. Available from: www.jax.org/news-and-insights/jax-blog/2017/november/when-are-mice-considered-old [Accessed 6th November 2017 2020].
HARR, M. W. & DISTELHORST, C. W. 2010. Apoptosis and autophagy: decoding calcium signals that mediate life or death. *Cold Spring Harbor perspectives in biology,* 2**,** a005579-a005579.
HOEKSTRA, M., MUMMERY, C. L., WILDE, A. A., BEZZINA, C. R. & VERKERK, A. O. 2012. Induced pluripotent stem cell derived cardiomyocytes as models for cardiac arrhythmias. *Front Physiol,* 3**,** 346.
HOLLANDER, J. M., THAPA, D. & SHEPHERD, D. L. 2014. Physiological and structural differences in spatially distinct subpopulations of cardiac mitochondria: influence of cardiac pathologies. *American journal of physiology. Heart and circulatory physiology,* 307**,** H1-H14.
HOPPEL, C. L., TANDLER, B., FUJIOKA, H. & RIVA, A. 2009. Dynamic organization of mitochondria in human heart and in myocardial disease. *Int J Biochem Cell Biol,* 41**,** 1949-56.
HWANG, H. S., KRYSHTAL, D. O., FEASTER, T. K., SÁNCHEZ-FREIRE, V., ZHANG, J., KAMP, T. J., HONG, C. C., WU, J. C. & KNOLLMANN, B. C. 2015. Comparable calcium handling of human iPSC-derived cardiomyocytes generated by multiple laboratories. *Journal of molecular and cellular cardiology,* 85**,** 79-88.
JAHOOR, F., TAFFET, G. E. & SEKHAR, R. V. 2019. GLUTATHIONE DEFICIENCY AND OXIDATIVE STRESS IN AGING: METABOLIC MECHANISM AND TARGETED INTERVENTION. *Innovation in Aging,* 3**,** S416-S416.
JAHREISS, L., MENZIES, F. M. & RUBINSZTEIN, D. C. 2008. The itinerary of autophagosomes: from peripheral formation to kiss-and-run fusion with lysosomes. *Traffic (Copenhagen, Denmark),* 9**,** 574-587.
JANSSEN, B., DEBETS, J., LEENDERS, P. & SMITS, J. 2002. Chronic measurement of cardiac output in conscious mice. *Am J Physiol Regul Integr Comp Physiol,* 282**,** R928-35.
JOHNSON, T. B., STURDEVANT, D. A., WHITE, K. A., DRACK, A. V., BHATTARAI, S., ROGERS, C., COOPER, J. D., PEARCE, D. A. & WEIMER, J. M. 2019. Characterization of a novel porcine model of CLN3-Batten disease. *Molecular Genetics and Metabolism,* 126**,** S81.
JOUAVILLE, L. S., PINTON, P., BASTIANUTTO, C., RUTTER, G. A. & RIZZUTO, R. 1999. Regulation of mitochondrial ATP synthesis by calcium: Evidence for a long-term metabolic priming. *Proceedings of the National Academy of Sciences,* 96**,** 13807.
KARBASSI, E., FENIX, A., MARCHIANO, S., MURAOKA, N., NAKAMURA, K., YANG, X. & MURRY, C. E. 2020. Cardiomyocyte maturation: advances in knowledge and implications for regenerative medicine. *Nature reviews. Cardiology,* 17**,** 341-359.
KATZ, M. L. & ROBISON, W. G. 2002. What is lipofuscin? Defining characteristics and differentiation from other autofluorescent lysosomal storage bodies. *Archives of Gerontology and Geriatrics,* 34**,** 169-184.
KIM, Y. Y., KU, S. Y., HUH, Y., LIU, H. C., KIM, S. H., CHOI, Y. M. & MOON, S. Y. 2013. Anti-aging effects of vitamin C on human pluripotent stem cell-derived cardiomyocytes. *Age (Dordr),* 35**,** 1545-57.
KITZMULLER, C., HAINES, R. L., CODLIN, S., CUTLER, D. F. & MOLE, S. E. 2008. A function retained by the common mutant CLN3 protein is responsible for the late onset of juvenile neuronal ceroid lipofuscinosis. *Hum Mol Genet,* 17**,** 303-12.
KOIVUMÄKI, J. T., NAUMENKO, N., TUOMAINEN, T., TAKALO, J., OKSANEN, M., PUTTONEN, K. A., LEHTONEN, Š., KUUSISTO, J., LAAKSO, M., KOISTINAHO, J. & TAVI, P. 2018. Structural Immaturity of Human iPSC-Derived Cardiomyocytes: In Silico Investigation of Effects on Function and Disease Modeling. *Front Physiol,* 9**,** 80.

KOMINAMI, E., EZAKI, J., MUNO, D., ISHIDO, K., UENO, T. & WOLFE, L. S. 1992. Specific storage of subunit c of mitochondrial ATP synthase in lysosomes of neuronal ceroid lipofuscinosis (Batten's disease). *J Biochem,* 111**,** 278-82.

KOUSI, M., SIINTOLA, E., DVORAKOVA, L., VLASKOVA, H., TURNBULL, J., TOPCU, M., YUKSEL, D., GOKBEN, S., MINASSIAN, B. A., ELLEDER, M., MOLE, S. E. & LEHESJOKI, A. E. 2009. Mutations in CLN7/MFSD8 are a common cause of variant late-infantile neuronal ceroid lipofuscinosis. *Brain,* 132**,** 810-9.

KOVACS, A. D. & PEARCE, D. A. 2015. Finding the most appropriate mouse model of juvenile CLN3 (Batten) disease for therapeutic studies: the importance of genetic background and gender. *Dis Model Mech,* 8**,** 351-61.

KOWALD, A. & KIRKWOOD, T. B. L. 2011. Evolution of the mitochondrial fusion-fission cycle and its role in aging. *Proceedings of the National Academy of Sciences of the United States of America,* 108**,** 10237-10242.

KUPER, W. F. E., VAN ALFEN, C., RIGTERINK, R. H., FUCHS, S. A., VAN GENDEREN, M. M. & VAN HASSELT, P. M. 2018. Timing of cognitive decline in CLN3 disease. *J Inherit Metab Dis,* 41**,** 257-261.

KYTTALA, A., LAHTINEN, U., BRAULKE, T. & HOFMANN, S. L. 2006. Functional biology of the neuronal ceroid lipofuscinoses (NCL) proteins. *Biochim Biophys Acta,* 1762**,** 920-33.

LEON, L. J. & GUSTAFSSON Å, B. 2016. Staying young at heart: autophagy and adaptation to cardiac aging. *J Mol Cell Cardiol,* 95**,** 78-85.

LI, H., HASTINGS, M. H., RHEE, J., TRAGER, L. E., ROH, J. D. & ROSENZWEIG, A. 2020. Targeting Age-Related Pathways in Heart Failure. *Circ Res,* 126**,** 533-551.

LICCHETTA, L., BISULLI, F., FIETZ, M., VALENTINO, M. L., MORBIN, M., MOSTACCI, B., OLIVER, K. L., BERKOVIC, S. F. & TINUPER, P. 2015. A novel mutation af Cln3 associated with delayed-classic juvenile ceroid lipofuscinois and autophagic vacuolar myopathy. *Eur J Med Genet,* 58**,** 540-4.

LIU, Y. J., MCINTYRE, R. L., JANSSENS, G. E. & HOUTKOOPER, R. H. 2020. Mitochondrial fission and fusion: A dynamic role in aging and potential target for age-related disease. *Mechanisms of Ageing and Development,* 186**,** 111212.

LLOYD-EVANS, E. 2016. Acidic Ca(2+) stores in neurodegeneration. *Messenger (Los Angel),* 5**,** 37-55.

LOJEWSKI, X., STAROPOLI, J. F., BISWAS-LEGRAND, S., SIMAS, A. M., HALIW, L., SELIG, M. K., COPPEL, S. H., GOSS, K. A., PETCHERSKI, A., CHANDRACHUD, U., SHERIDAN, S. D., LUCENTE, D., SIMS, K. B., GUSELLA, J. F., SONDHI, D., CRYSTAL, R. G., REINHARDT, P., STERNECKERT, J., SCHOLER, H., HAGGARTY, S. J., STORCH, A., HERMANN, A. & COTMAN, S. L. 2014. Human iPSC models of neuronal ceroid lipofuscinosis capture distinct effects of TPP1 and CLN3 mutations on the endocytic pathway. *Hum Mol Genet,* 23**,** 2005-22.

LUIRO, K., KOPRA, O., BLOM, T., GENTILE, M., MITCHISON, H. M., HOVATTA, I., TORNQUIST, K. & JALANKO, A. 2006. Batten disease (JNCL) is linked to disturbances in mitochondrial, cytoskeletal, and synaptic compartments. *J Neurosci Res,* 84**,** 1124-38.

MA, J., GUO, L., FIENE, S. J., ANSON, B. D., THOMSON, J. A., KAMP, T. J., KOLAJA, K. L., SWANSON, B. J. & JANUARY, C. T. 2011. High purity human-induced pluripotent stem cell-derived cardiomyocytes: electrophysiological properties of action potentials and ionic currents. *Am J Physiol Heart Circ Physiol,* 301**,** H2006-17.

MACKENZIE, L., RODERICK, H. L., BERRIDGE, M. J., CONWAY, S. J. & BOOTMAN, M. D. 2004. The spatial pattern of atrial cardiomyocyte calcium signalling modulates contraction. *Journal of Cell Science,* 117**,** 6327-6337.

MARANI, E., USUNOFF, K. G. & FEIRABEND, H. K. P. 2009. Lipofuscin and Lipofuscinosis A2 - Squire, Larry R. *Encyclopedia of Neuroscience.* Oxford: Academic Press.

MASOUD, S. 2018. *The Ultrastructural and Abnormal Calcium Handling in Pulmonary Vein Sleeve Cells, Atrial and Ventricular Myocytes During Ageing.* PhD, The Open University.

MATTEONI, R. & KREIS, T. E. 1987. Translocation and clustering of endosomes and lysosomes depends on microtubules. *J Cell Biol,* 105**,** 1253-65.

MICHIELSEN, P., MARTIN, J. J., VANAGT, E., VRINTS, C., GILLEBERT, T. & SNOECK, J. 1984. Cardiac Involvement in Juvenile Ceroid Lipofuscinosis of the Spielmeyer-Vogt-Sjögren Type: Prospective Noninvasive Findings in Two Siblings. *European Neurology,* 23**,** 166-172.

MITCHISON, H. M., BERNARD, D. J., GREENE, N. D., COOPER, J. D., JUNAID, M. A., PULLARKAT, R. K., DE VOS, N., BREUNING, M. H., OWENS, J. W., MOBLEY, W. C., GARDINER, R. M., LAKE, B. D., TASCHNER, P. E. & NUSSBAUM, R. L. 1999. Targeted disruption of the Cln3 gene provides a mouse model for Batten disease. The Batten Mouse Model Consortium [corrected]. *Neurobiol Dis,* 6**,** 321-34.

MOHAN, N., SOROKINA, E. M., VERDENY, I. V., ALVAREZ, A. S. & LAKADAMYALI, M. 2018. Detyrosinated microtubules spatially constrain lysosomes facilitating lysosome–autophagosome fusion. *Journal of Cell Biology,* 218**,** 632-643.

MOLE, S. E. 2017. *CLN3 mutation table* [Online]. ucl.ac.uk. Available: http://www.ucl.ac.uk/ncl/CLN3mutationtable.htm [Accessed 03/04/2018 2018].

MURPHY, M. P. 2009. How mitochondria produce reactive oxygen species. *The Biochemical journal,* 417**,** 1-13.

NELSON, T., PEARCE, D. A. & KOVACS, A. D. 2017. Lack of specificity of antibodies raised against CLN3, the lysosomal/endosomal transmembrane protein mutated in juvenile Batten disease. *Biosci Rep,* 37.

ONG, S. B., KALKHORAN, S. B., HERNÁNDEZ-RESÉNDIZ, S., SAMANGOUEI, P., ONG, S. G. & HAUSENLOY, D. J. 2017. Mitochondrial-Shaping Proteins in Cardiac Health and Disease - the Long and the Short of It! *Cardiovasc Drugs Ther,* 31**,** 87-107.

OSELLAME, L. D. & DUCHEN, M. R. 2013. Defective quality control mechanisms and accumulation of damaged mitochondria link Gaucher and Parkinson diseases. *Autophagy,* 9**,** 1633-5.

OSTERGAARD, J. R. 2016. Juvenile neuronal ceroid lipofuscinosis (Batten disease): current insights. *Degener Neurol Neuromuscul Dis,* 6**,** 73-83.

OSTERGAARD JR, R. T., MØLGAARD H. 2011. Cardiac involvement in juvenile neuronal ceroid lipofuscinosis (Batten disease). *Neurology,* 76**,** 1245-51.

OUSEPH, M. M., KLEINMAN, M. E. & WANG, Q. J. 2016. Vision loss in juvenile neuronal ceroid lipofuscinosis (CLN3 disease). *Ann N Y Acad Sci,* 1371**,** 55-67.

PALMER, D. N., BARRY, L. A., TYYNELA, J. & COOPER, J. D. 2013. NCL disease mechanisms. *Biochim Biophys Acta,* 1832**,** 1882-93.

PARK, J.-S., DAVIS, R. L. & SUE, C. M. 2018. Mitochondrial Dysfunction in Parkinson's Disease: New Mechanistic Insights and Therapeutic Perspectives. *Current Neurology and Neuroscience Reports,* 18**,** 21.

PENG, W., WONG, Y. C. & KRAINC, D. 2020. Mitochondria-lysosome contacts regulate mitochondrial Ca<sup>2+</sup> dynamics via lysosomal TRPML1. *Proceedings of the National Academy of Sciences,* 117**,** 19266.

PERRY, S. W., NORMAN, J. P., BARBIERI, J., BROWN, E. B. & GELBARD, H. A. 2011. Mitochondrial membrane potential probes and the proton gradient: a practical usage guide. *BioTechniques,* 50**,** 98-115.

PINTON, P., GIORGI, C., SIVIERO, R., ZECCHINI, E. & RIZZUTO, R. 2008. Calcium and apoptosis: ER-mitochondria Ca2+ transfer in the control of apoptosis. *Oncogene,* 27**,** 6407-6418.

PU, J., GUARDIA, C. M., KEREN-KAPLAN, T. & BONIFACINO, J. S. 2016. Mechanisms and functions of lysosome positioning. *J Cell Sci,* 129**,** 4329-4339.

PU, J., SCHINDLER, C., JIA, R., JARNIK, M., BACKLUND, P. & BONIFACINO, J. S. 2015. BORC, a Multisubunit Complex that Regulates Lysosome Positioning. *Developmental cell,* 33**,** 176-188.

QIAN, H., SHEETZ, M. P. & ELSON, E. L. 1991. Single particle tracking. Analysis of diffusion and flow in two-dimensional systems. *Biophysical journal,* 60**,** 910-921.

RESKE-NIELSEN E, B. U., BJERREGAARD P, BRUUN I. 1981. Cardiac involvement in juvenile amaurotic idiocy - a specific heart muscle disorder. *Acta Pathol Microbiol Scand A,* 89**,** 357-65.

RIETDORF, K., COODE, E. E., SCHULZ, A., WIBBELER, E., BOOTMAN, M. D. & OSTERGAARD, J. R. 2019. Cardiac pathology in neuronal ceroid lipofuscinoses (NCL): More than a mere co-morbidity. *Biochim Biophys Acta Mol Basis Dis***,** 165643.

ROBSON, A., BURRAGE, K. & LEAKE, M. C. 2013. Inferring diffusion in single live cells at the single-molecule level. *Philos Trans R Soc Lond B Biol Sci,* 368**,** 20120029.

RODERICK, H. L., HIGAZI, D. R., SMYRNIAS, I., FEARNLEY, C., HARZHEIM, D. & BOOTMAN, M. D. 2007. Calcium in the heart: when it's good, it's very very good, but when it's bad, it's horrid. *Biochem Soc Trans,* 35**,** 957-61.

RONALDSON-BOUCHARD, K., MA, S. P., YEAGER, K., CHEN, T., SONG, L., SIRABELLA, D., MORIKAWA, K., TELES, D., YAZAWA, M. & VUNJAK-NOVAKOVIC, G. 2018. Advanced maturation of human cardiac tissue grown from pluripotent stem cells. *Nature,* 556**,** 239-243.

ROSCA, M. G., TANDLER, B. & HOPPEL, C. L. 2013. Mitochondria in cardiac hypertrophy and heart failure. *Journal of Molecular and Cellular Cardiology,* 55**,** 31-41.

RUAS, M., RIETDORF, K., ARREDOUANI, A., DAVIS, L. C., LLOYD-EVANS, E., KOEGEL, H., FUNNELL, T. M., MORGAN, A. J., WARD, J. A., WATANABE, K., CHENG, X., CHURCHILL, G. C., ZHU, M. X., PLATT, F. M., WESSEL, G. M., PARRINGTON, J. & GALIONE, A. 2010. Purified TPC isoforms form NAADP receptors with distinct roles for Ca(2+) signaling and endolysosomal trafficking. *Curr Biol,* 20**,** 703-9.

SARPONG, A., SCHOTTMANN, G., RUTHER, K., STOLTENBURG, G., KOHLSCHUTTER, A., HUBNER, C. & SCHUELKE, M. 2009. Protracted course of juvenile ceroid lipofuscinosis associated with a novel CLN3 mutation (p.Y199X). *Clin Genet,* 76**,** 38-45.

SAXTON, M. J. & JACOBSON, K. 1997. Single-particle tracking: applications to membrane dynamics. *Annu Rev Biophys Biomol Struct,* 26**,** 373-99.

SBALZARINI, I. F. & KOUMOUTSAKOS, P. 2005. Feature point tracking and trajectory analysis for video imaging in cell biology. *J Struct Biol,* 151**,** 182-95.

SCHULZ, A. & KOHLSCHUTTER, A. 2013. NCL Disorders: Frequent Causes of Childhood Dementia. *Iran J Child Neurol,* 7**,** 1-8.

SCHULZ, A., KOHLSCHUTTER, A., MINK, J., SIMONATI, A. & WILLIAMS, R. 2013. NCL diseases - clinical perspectives. *Biochim Biophys Acta,* 1832**,** 1801-6.

SCHWAKE, M., SCHRÖDER, B. & SAFTIG, P. 2013. Lysosomal Membrane Proteins and Their Central Role in Physiology. *Traffic,* 14**,** 739-748.

SHAW, P. J. & FESKE, S. 2012. Physiological and pathophysiological functions of SOCE in the immune system. *Front Biosci (Elite Ed),* 4**,** 2253-68.

SHIRAKABE, A., IKEDA, Y., SCIARRETTA, S., ZABLOCKI, D. K. & SADOSHIMA, J. 2016. Aging and Autophagy in the Heart. *Circulation Research,* 118**,** 1563-1576.

SKULACHEV, V. P. 2001. Mitochondrial filaments and clusters as intracellular power-transmitting cables. *Trends Biochem Sci,* 26**,** 23-9.

STAROPOLI, J. F., HALIW, L., BISWAS, S., GARRETT, L., HOLTER, S. M., BECKER, L., SKOSYRSKI, S., DA SILVA-BUTTKUS, P., CALZADA-WACK, J., NEFF, F., RATHKOLB, B., ROZMAN, J., SCHREWE, A., ADLER, T., PUK, O., SUN, M., FAVOR, J., RACZ, I., BEKEREDJIAN, R., BUSCH, D. H., GRAW, J., KLINGENSPOR, M., KLOPSTOCK, T., WOLF, E., WURST, W., ZIMMER, A., LOPEZ, E., HARATI, H., HILL, E., KRAUSE, D. S., GUIDE, J., DRAGILEVA, E., GALE, E., WHEELER, V. C., BOUSTANY, R. M., BROWN, D. E., BRETON, S., RUETHER, K., GAILUS-DURNER, V., FUCHS, H., DE ANGELIS, M. H. & COTMAN, S. L. 2012. Large-scale phenotyping of an accurate genetic mouse model of JNCL identifies novel early pathology outside the central nervous system. *PLoS One,* 7**,** e38310.

STERNBERG, S. 1983. Biomedical Image Processing. *Computer,* 16**,** 22-34.

TAKAHASHI, K. & YAMANAKA, S. 2006. Induction of pluripotent stem cells from mouse embryonic and adult fibroblast cultures by defined factors. *Cell,* 126**,** 663-76.

TANDLER, B., DUNLAP, M., HOPPEL, C. L. & HASSAN, M. 2002. Giant mitochondria in a cardiomyopathic heart. *Ultrastruct Pathol,* 26**,** 177-83.

THERMOFISHER. 2021a. *CellLight™ Lysosomes-RFP, BacMam 2.0* [Online]. ThermoFisher. Available: www.thermofisher.com/order/catalog/product/C10504#/C10504 [Accessed 18/05/2021 2021].

THERMOFISHER. 2021b. *LysoTracker™ Red DND-99* [Online]. www.thermofisher.com. Available: www.thermofisher.com/order/catalog/product/L7528#/L7528 [Accessed 18/05/2021 2021].

TINEL, H., CANCELA, J. M., MOGAMI, H., GERASIMENKO, J. V., GERASIMENKO, O. V., TEPIKIN, A. V. & PETERSEN, O. H. 1999. Active mitochondria surrounding the pancreatic acinar granule region prevent spreading of inositol trisphosphate-evoked local cytosolic Ca2+ signals. *The EMBO Journal,* 18**,** 4999-5008.

TOMIYASU, H., TAKAHASHI, W., OHTA, T., YOSHII, F., SHIBUYA, M. & SHINOHARA, Y. 2000. An autopsy case of juvenile neuronal ceroid-lipofuscinosis with dilated cardiomyopathy. *Clinical Neurology,* 40**,** 350-357.

TUXWORTH, R. I., CHEN, H., VIVANCOS, V., CARVAJAL, N., HUANG, X. & TEAR, G. 2011. The Batten disease gene CLN3 is required for the response to oxidative stress. *Hum Mol Genet,* 20**,** 2037-47.

VIDAL-DONET, J. M., CÁRCEL-TRULLOLS, J., CASANOVA, B., AGUADO, C. & KNECHT, E. 2013. Alterations in ROS activity and lysosomal pH account for distinct patterns of macroautophagy in LINCL and JNCL fibroblasts. *PLoS One,* 8**,** e55526.

WAGER, K., ZDEBIK, A. A., FU, S., COOPER, J. D., HARVEY, R. J. & RUSSELL, C. 2016. Neurodegeneration and Epilepsy in a Zebrafish Model of CLN3 Disease (Batten Disease). *PLoS One,* 11**,** e0157365.

WALKLEY, S. U. 2009. Pathogenic cascades in lysosomal disease-Why so complex? *J Inherit Metab Dis,* 32**,** 181-9.

WATANABE, K., UENO, M., KAMIYA, D., NISHIYAMA, A., MATSUMURA, M., WATAYA, T., TAKAHASHI, J. B., NISHIKAWA, S., NISHIKAWA, S., MUGURUMA, K. & SASAI, Y. 2007. A ROCK inhibitor permits survival of dissociated human embryonic stem cells. *Nat Biotechnol,* 25**,** 681-6.

WILEY, L. A., BURNIGHT, E. R., DRACK, A. V., BANACH, B. B., OCHOA, D., CRANSTON, C. M., MADUMBA, R. A., EAST, J. S., MULLINS, R. F., STONE, E. M. & TUCKER, B. A. 2016. Using Patient-Specific Induced Pluripotent Stem Cells and Wild-Type Mice to Develop a Gene Augmentation-Based Strategy to Treat CLN3-Associated Retinal Degeneration. *Human gene therapy,* 27**,** 835-846.

YANG, C., AL-AAMA, J., STOJKOVIC, M., KEAVNEY, B., TRAFFORD, A., LAKO, M. & ARMSTRONG, L. 2015. Concise Review: Cardiac Disease Modeling Using Induced Pluripotent Stem Cells. *Stem Cells,* 33**,** 2643-51.

ZOROV, D. B., JUHASZOVA, M. & SOLLOTT, S. J. 2014. Mitochondrial reactive oxygen species (ROS) and ROS-induced ROS release. *Physiol Rev,* 94**,** 909-50.

ZUPPINGER, C., GIBBONS, G., DUTTA-PASSECKER, P., SEGISER, A., MOST, H. & SUTER, T. M. 2017. Characterization of cytoskeleton features and maturation status of cultured human iPSC-derived cardiomyocytes. *European Journal of Histochemistry : EJH,* 61**,** 2763.